AlxGa1-xN and AlN nanowires : a solution for efficient UV-C light emitting diodes

Alexandra-Madalina Siladie

Communauté
UNIVERSITÉ Grenoble Alpes

THÈSE

Pour obtenir le grade de

DOCTEUR DE LA COMMUNAUTE UNIVERSITE GRENOBLE ALPES

Spécialité : **Physique de la matière condensée et rayonnement**

Arrêté ministériel : 25 mai 2016

Présentée par

Alexandra-Madalina Siladie

Thèse dirigée par **Bruno DAUDIN**
et co-dirigée par **Julien PERNOT**

préparée au sein du **Laboratoire PHotonique, ELectronique et Ingéniérie QuantiqueS (PHELIQS)**
dans **l'École Doctorale Physique**

Nanofils $Al_xGa_{1-x}N$ et AlN pour la réalisation de diodes efficaces émettant dans l'UV-C

Thèse soutenue publiquement le **8 Novembre 2019**,
devant le jury composé de :

Dr. Bruno DAUDIN
Chercheur, CEA Grenoble, Directeur de thèse
Dr. Dr. Lutz GEELHAAR
Chercheur, PDI Berlin, Examinateur
Prof. Nicolas GRANDJEAN
Professeur, EPFL Lausanne, Rapporteur
Prof. Julien PERNOT
Professeur, Université Grenoble Alpes, Co-directeur de thèse
Dr. Maxime RICHARD
Chercheur, CNRS Grenoble, Président
Dr. Martin STUTZMANN
Chercheur, Walter Schottky Institute and TU Munich, Examinateur
Dr. Maria TCHERNYCHEVA
Chercheuse, C2N Paris, Rapporteur

Abstract

Solid-state deep UV Light emitting diodes (LEDs) based on $Al_xGa_{1-x}N$ material are nowadays gaining particular attention due to their potential for replacing mercury lamps, currently used for sterilization and water disinfection applications. However, the realization of planar efficient emitting devices is limited by a high density of extended defects and difficult efficient dopant incorporation affecting both optical and electrical properties. As a strategy to alleviate this difficulty, I have focused on the study of nanowire based heterostructure devices, due to their advantage of elastically relaxing the strain during growth, coupled with a higher dopant solubility limit and an eased light extraction coming from their particular morphology.

First, correlated experiments of Atom Probe Tomography (APT), Energy Dispersive X-ray Spectroscopy (EDX) or Raman spectroscopy performed on GaN pn junctions grown by plasma assisted molecular beam epitaxy (PA-MBE) have shown that both n-type and p-type dopants, namely Si and Mg, respectively, exhibit an inhomogeneous radial distribution, with dopant incorporation upper limits attaining 10^{21} atoms/cm^3 at the periphery, higher than in 2D layers. The study of Mg incorporation by APT concluded on the understanding of the incorporation mechanism, preferential on the m-plane side-wall and assisted by H due to the high stability of the Mg-H complex in N rich conditions.

The second part of the work is dedicated to the study of the more challenging Mg dopant incorporation and activation in AlN alloy, successfully attained in this PhD by In-Mg co-doping. The efficient incorporation of this dopant in AlN nanowires assisted by small concentration of In has been assessed by a series of techniques (EDX, Raman). Ab-initio theoretical calculations have shown that the efficient incorporation of Mg in an Al-substitutional site is due to a process involving the nitrogen vacancies forming an In-V_N complex. The formation of AlN NW p-n junction has been concomitantly assessed by electron beam induced current (EBIC) experiments putting in evidence the electrical field associated with the junction. An extensive study of the electrical activation of acceptor impurities has been further achieved by electron beam irradiation of the samples and characterized in EBIC experiments.

Résumé

Les diodes électroluminescentes (LED) à semi-conducteurs à base de matériau $Al_xGa_{1-x}N$ font actuellement l'objet d'une attention particulière en raison de leur potentiel pour remplacer les lampes à mercure, utilisées pour des applications de stérilisation et de désinfection de l'eau. Cependant, la réalisation de dispositifs émetteurs efficaces en géométrie planaire est limitée par une densité élevée de défauts étendus et par une incorporation des dopants difficile, notamment de type p, ce qui affecte les propriétés optiques et électriques. Pour surmonter ces difficultés, je me suis concentrée sur l'étude des hétérostructures à base de nanofils, en raison de leur capacité à relaxer élastiquement la contrainte pendant la croissance, associée à une limite de solubilité des dopants plus élevée et à une extraction de lumière facilitée par leur morphologie particulière.

En premier lieu, des expériences corrélées de tomographie par sonde atomique (APT), d'analyse dispersive en énergie des rayons X (EDX) ou de spectroscopie Raman effectuées sur des jonctions p-n de GaN développées par épitaxie par jets moléculaires assistée par plasma (PA-MBE) ont montré que les dopants de type n et p, à savoir Si et Mg, respectivement, présentent une distribution radiale non homogène, avec des limites d'incorporation atteignant 10^{21} atomes/cm^3 en périphérie, plus élevées que dans les couches 2D. L'étude de l'incorporation du Mg par l'APT a permis de comprendre le mécanisme d'incorporation, qui a lieu préférentiellement sur la paroi latérale des nanofils correspondant au plan m et est assistée par l'hydrogène en raison de la grande stabilité du complexe Mg-H dans les conditions de la croissance.

La deuxième partie du travail est consacrée à l'étude plus complexe de l'incorporation et de l'activation des dopants Mg dans l'alliage AlN, réalisées dans cette thèse par co-dopage In-Mg. L'incorporation efficace de ce dopant dans des nanofils d'AlN, assistée par une faible concentration d'In, a été évaluée par une série de techniques (EDX, Raman). Les calculs théoriques ab initio ont montré que l'incorporation efficace du Mg dans des sites substitutionnels d'Al est due à un processus impliquant les lacunes d'azote formant un complexe In-V_N. La formation d'une jonction p-n dans les nanofils AlN a été évaluée de manière concomitante par des expériences de courant induit par faisceau d'électrons (EBIC), mettant en évidence le champ électrique associé à la jonction. Une étude approfondie de l'activation électrique des impuretés acceptrices a également été réalisée par irradiation par faisceau d'électrons des échantillons et caractérisée par des expériences EBIC.

Acknowledgements

My PhD was a great collaboration between CEA Grenoble and CNRS-Néel Institute, two of the biggest research centers in France, during which I had the great opportunity of meeting and working with world-renown people in the field of nitrides and semiconductors. Thus, the acknowledgements list will be long and was written in the beginning of my thesis writing journey, because finding words to express my gratitude and support was the easiest task of the process of this PhD manuscript writing. Since the "PhD life" is not just about work, but about personal development, my acknowledgements will be directed towards all of the great people I have met and who have supported me throughout this journey. If I forgot someone, I would like to thank you now.

From a professional point of view, I would like to express my gratitude towards the jury of my PhD defense that I have already had the great opportunity of meeting during several workshops and conferences. I would like to especially thank the reviewers: Dr. Maria Tchernycheva and Prof. Nicolas Grandjean for taking the time to review the partial results of these three years of research. Equally, great thanks to my PhD examination committee, Prof. Martin Stutzmann, Dr. Lutz Geelhaar and Dr. Maxime Richard for accepting to be a part of the jury and examine the PhD defense and the manuscript.

After succeeding in accomplishing one internship and one PhD under his supervision, I would like to thank particularly my PhD director, Bruno. Words cannot express my gratitude towards him and towards the chance he has offered me while accepting me as a part of the team. I am grateful for the endless support and for encouraging me when needed. This continuous "montagne-russe" of PhD ends on a high note thanks to his trust and ambition of always pushing me higher. The scientific discussions we have had will be missed and I hope this will not be our last collaboration.

I have had the chance of having a great working environment and team during my PhD, an equal role for this thesis being played by my co-director, Julien, to whom I am thankful for receiving me in the "diamond group" (even though I was more of a "team GaN" person). I thank him for knowing how to encourage me and for his support and availability every time I needed. I greatly appreciated his understanding as well as optimism when announcing him "unexpected" results. Sitting down with me with nothing but a piece of paper, for hours, trying to understand the physics behind my results, taught me much about his knowledge and I am thankful for the opportunity of having him as a professor and PhD co-director.

Still in the "diamond group" at CNRS, I would like to thank Gwénolé (the other "team GaN" in our wide band gap semiconductors group in Neel Institute). From a more serious point

of view, I would like to thank him for fruitful scientific discussions and a CL efficiency never seen before (even on "unremarkable" samples), as well as for playing an important role in my PhD meetings.

Special thanks to all of my collaborators that were interested in my work and that brought their great knowledge in their respective fields: Fabrice Donatini, for being a part of my scientific group meetings and for his help in EBIC experiments, Ana Cross and Nuria Garro, with whom it was a pleasure collaborating for Raman and KPFM experiments, Lynda Amichi, Bastien Bonef, Adeline Grenier and Catherine Bougerol for results on APT, Yann and Yoann for their technical support and knowledge when MBE was "in trouble".

Huge thanks to all the great researchers that were a part of the EMOUVAN project: Catherine Bougerol and Jean-Luc Rouvière for the TEM studies, Eric Robin for EDX experiments that always brought great results, Pierre Lefebvre for interesting PL experiments, Mathieu Kociak and Luiz Tizei for nanoscale CL, Damien Caliste and Pascal Pochet for theoretical calculations.

By this mean, I would also like to thank Jean-Michel Gerard for welcoming me in the PHELIQS group at CEA. Also, I would like to especially thank Régis André and Bruno Gayral for welcoming me in the NPSC team and for their great help, support and suggestions while preparing a conference, a regular presentation or even the defense of this PhD (for which I am grateful to Catherine, Fabrice and Gwénolé in an equal measure). I have deeply appreciated the scientific discussions and ideas we have been talking about in order to better orient my PhD. I always knew that despite your (sometimes tough) remarks, the aim of our discussions was to help me reach an exceptional level because of your trust in my abilities.

I have appreciated every minute that I have spent both in CEA and in CNRS. In CEA I have had the chance to be a part of the coffee breaks and to assist to enriching politics, climate, scientific and "team" management debates in the company of Bruno, Regis, Yann, Joel E., Joel B., Samuel, Henri, Eva, Christophe and Yoann. The more organized, "3 times a day" coffee breaks at CNRS were a mean of bringing together all the SC2G team and to have short meetings and discuss about the advancements of the different projects (… but not only). By this mean I would like to thank especially my office colleagues Cédric and Khaled, but also the rest of the SC2G team (and DIAMFAB affiliates) Juliette, Martin, Etienne, Timothée, David, Jesus, Charlotte, Aurelian, Gauthier and Loto.

I have spent most of my PhD time with my CEA colleagues and of course, spending that much time with people must be cherished. I would like to thank Marion, Amine, Akhil, Lynda, Anjali, Akanksha, Romain, Nathaniel, Victor, Rémy, Guillerme, Alexandre, Rodrigo, Caroline, David, Saptarshi, Ioanna, Vincent, Camille, Farsane, Saransh, Sergi, Raouia, Bala, Jane, Matthias, Zhihua, Tobias, Jonas, Maria, Martin (hoping I did not forget anyone from this long list…). Some of you became a part of my personal life (and I thank you for being there for me), some of you my all-time best friends and I can't be more grateful for having the opportunity to have met you.

From a personal point of view, I would like to now thank the people that have supported me during these last 3 years from outside. For this, I thank my best friend Bouchra, for her constant support, as well as my friends from Lyon that are my "Romanian family" in France: thank you Loredana Baboi, Lorena, Sorin and Emily Perisanu, Dana, Lucian and Pierre Roiban. I would like to thank Filippo, Fadoua, Ahlam and Kaoutar, for their friendship and support I have always found in them.

Last but not least, there are always people that come, go and some that stay throughout the years, and that help us become who we are, paving the way towards our future. I would like to express my endless gratitude towards people who encourage us to arrive far even if our paths separate at some point in life. Also, I am extremely grateful towards those people who believed I will go very far in life and helped me attain the confidence and the knowledge I have acquired today: all of my professors, most especially my math teachers, Prof. Steluta Monea and Prof. Lia Vasile.

I will end the acknowledgement list by thanking the most precious people I have in my life, my family, for their constant support and for always being by my side, even in my most difficult decisions:

Vă mulțumesc infinit pentru tot ceea ce ați făcut pentru mine, pentru susținerea și suportul moral pe care l-am găsit mereu în voi. Mulțumesc mami, tati, Buni Cica, Lavi, Ali, bebe Matei, bunici, unchi, mătuși și verișori.

A ma famille, pour avoir toujours été là et pour m'avoir soutenu et encouragé pour arriver si loin…

Familiei mele, care mi-a fost mereu alături, susținându-mă și încurajându-mă să ajung departe...

Table of Contents

Acronyms

APT	Atom Probe Tomography
CB	Conduction Band
CL	Cathodoluminescence
DNA	Deoxyribonucleic Acid
DUV	Deep Ultraviolet
EBIC	Electron Beam Induced Current
EBL	Electron Blocking Layer
EDX	Energy Dispersive X-Ray Spectroscopy
EIE	Carrier (electron) Injection Efficiency
EL	Electroluminescence
EQE	External Quantum Efficiency
FIB	Focused Ion Beam
HEMT	High Electron Mobility Transistors
HFET	Heterostructure Field Effect Transistor
HR-EDX	High Resolution Energy Dispersive X-Ray Spectroscopy
HVPE	Hydrogen Vapor Phase Epitaxy
IQE	Internal Quantum Efficiency
ITO	Indium Tin Oxide
IV	Current versus voltage characteristic
JV	Current density versus voltage characteristic
KPFM	Kelvin Probe Force Microscopy
LED	Light Emitting Diode
LEE	Light Extraction Efficiency
LPE	Liquid Phase Epitaxy
MBE	Molecular Beam Epitaxy
MOCVD	Metal-Organic
NBE	Near Band Edge
NH3-MBE	Ammonia Molecular Beam Epitaxy
NW	Nanowire
PA-MBE	Plasma Assisted Molecular Beam Epitaxy
PINLED	Polarization Induced Nanowire Light Emitting Diodes
PVD	Physical Vapor Deposition
QCSE	Quantum Confined Stark Effect
QMAS	Quantum MAterials Simulator
QW	Quantum Well
RF-MBE	Radio Frequency Molecular Beam Epitaxy
RHEED	Reflection High Energy Electron Diffraction
RS	Rock-Salt
SAW	Surface Acoustic Wave
SCR	Space Charge Region
SEM	Scanning Electron Microscopy
SRH	Schokley-Read-Hall
TE	Transverse Electric
TEM	Transmission Electron Microscopy
TM	TransverseMagnetic
UHV	Ultra-high Vacuum
UV	Ultraviolet

VB	Valence Band
VPE	Vapor Phase Epitaxy
WPE	Wall Plug Efficiency
WZ	Wurzite
ZB	Zinc-Blende

"There comes a point in your life when you need to stop reading other people's book and write your own."

A. Einstein

Introduction

The 21st century is one of the most beneficial in terms of technological development. Nowadays, access to high speed internet and high-tech devices is becoming increasingly available. Paradoxically, one third of the global population uses a contaminated drinking water source and almost one billion lack easy access to drinking water, in an era when access to water and sanitation was declared a human right by the United Nations General Assembly (United Nations 2010).

Contaminated water is responsible for transmission of a series of diseases such as diarrhea, cholera, dysentery, hepatitis A. Otherwise preventable and curable, in low-income countries these diseases are still widely spread. In this context, it is crucial to improve water treatment techniques and develop water systems and purifiers.

World Health Organization statistics stress out that by 2025, half of the world's population will be living in water stressed areas. Increasing water scarcity due to current climate changes and population growth demands strategies such as re-use of wastewater. This justifies the need of intensive research in the water purification domain. Therefore, the development of a highly efficient technique is required (World Health Organization and UNICEF 2017).

However, water treatment is not an anodyne process. Different groups of disease-causing germs have to be considered, such as viruses, bacteria, fungi, algae and protozoa. An affordable and widely-used method for water disinfection is the use of chemical oxidants such as chlorine or ozone, due to their capability for deactivating microorganisms' DNA (for planktonic bacteria (Bois et al. 1997)) and oxidation (micro pollutants elimination, taste and odor control). Unwanted side effects can be induced during this water treatment, by reaction with water matrix and micro pollutants, leading to unwanted byproducts (Cancho et al. 2000). Moreover, some microorganisms from contaminated water are resistant to a series of chemical oxidants. Therefore, in industrial applications, high-power mercury, deuterium or Xenon lamps are nowadays used, DNA being highly sensitive to UV-radiation.

Ultraviolet light and genetic material

The ultraviolet (UV) light is a band of the electromagnetic spectrum (illustrated in Figure 1a) with wavelength ranging from 10 nm to 400 nm. The UV spectral range can be divided in 4 corresponding regions depending on the wavelength: the vacuum-UV from 10 to 200 nm, UV-C from 200 to 280 nm, UV-B from 280 to 315 nm and UV-A from 315 to 400 nm. The spectral range comprised between 200 and 300 nm will be further referred to as deep ultraviolet or DUV range. Genetic material, more precisely deoxyribonucleic acid (DNA) has an absorption spectrum in the UV-C range. The maximum of the absorption spectrum of nucleic acid and protein varies between 255 and 265 nm (Held 2001; Charak et al. 2012) as shown in Figure 1b.

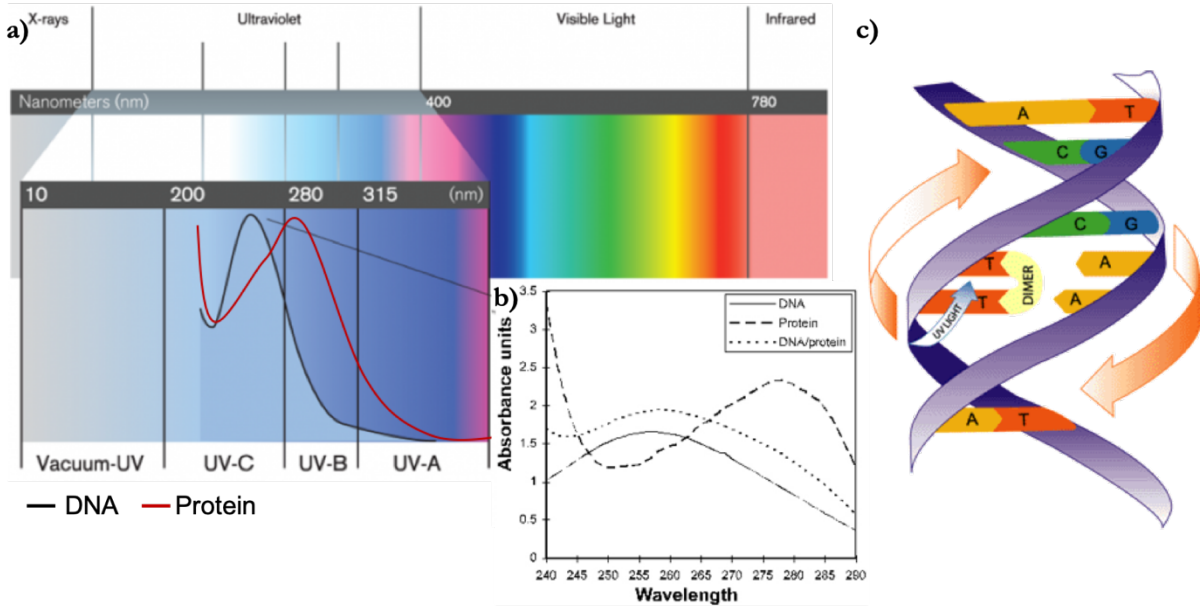

Figure 1. a) Electromagnetic spectrum with specific ranges. UV-C range is represented in zoom-in view with DNA and protein specific absorbance spectra. b) Optimized absorbance spectra of DNA and protein. c) Illustration of the DNA strand and dimerization of thymine bases under UV-radiation process.

The genetic genome of a DNA is formed from a unique sequence of combined bases amongst adenine, guanine, thymine and cytosine. DNA thymine bases are sensitive to UV-radiation. When exposed to UV-light, bonds between thymine and adenine break and thymine bases are dimerizing and binding together (mechanism illustrated in Figure 1c). When exposed to UV-C light, radiations exert adverse effects on the DNA genome stability. This mechanism affects the DNA strand ability to replicate leading to apoptosis (or programmed cell death), if repairing mechanisms are not efficient enough to counteract the lesions. For this reason, the UV light is known as germicidal beyond a certain dose after which the damage is considered irreversible. This mechanism is responsible for deactivation of genetic material of microorganisms from water and air exposed to a specific radiation wavelength rendering them harmless (Rastogi et al. 2010). The closer the light emitting device to 265 nm wavelength, the better the deactivation efficiency.

The degree of inactivation of the DNA by UV radiation depends on the UV dose and the reduction of microorganisms in water is defined by using a deactivation degree logarithmic scale. Thus, the deactivation percent corresponding to one log reduction or deactivation of microorganisms is 90%, two log reduction is 99% and so on. In order to have a stable and permanent deactivation, 4-log reduction corresponding to 99,99% is needed (Kwok-Keung and LeChevallier 2013), else the genetic material is able to reconstruct the broken bonds and thus lead to an ineffective process. Studies have been carried out on different types of microorganisms and a summary of typical UV fluences required for 4-log inactivation of some of them is given in Table 1 (Chevrefils et al. 2006). After a 4-log deactivation, germicidal action of UV-C light is lethal for microorganisms, furnishing a non-chemical water and food disinfection as well as medical sanitization method (Rastogi et al. 2010). It can be seen that for a 4-log reduction of combined microorganisms, a UV fluence higher than 165 mJ/cm^2 is required.

Microorganism	UV Dose (Fluence) (mJ/cm^2)	
	3-Log reduction	4-Log reduction
Bacillus subtilis (virus) (Sommer et al. 1999)	60	81
Adenovirus (virus) (Thompson et al. 2003)	122	165
Escherichia coli (bacteria) (Wu et al. 2005)	9	10
Salmonella typhimurium (bacteria) (Maya et al. 2003)	22	50
Cryptosporidium parvum (protozoan) (Clancy et al. 2000)	6	16
Giardia muris (protozoan) (Belosevic et al. 2001)	25	60

Table 1. Microorganisms deactivation dose summary

Another important application of UV light is phototherapy for psoriasis disease cure. A narrowband of the UV-B spectra, centered at around 310 nm, was found to lead to apoptosis of a variety of relevant cells in psoriasis such as T-lymphocytes from epidermis and dermis of psoriasis lesions (Ozawa et al. 1999) and keratinocytes (Krueger et al. 1995).

Mercury lamps and regulations

Even if other methods such as chlorine disinfection are equally effective, the UV-radiation process has been found to be extremely efficient with protozoa oocysts and cysts (Hijnen et al. 2006), whereas other techniques are not effective in their elimination.

Current water purification techniques mostly use germicidal ultraviolet lamps produced by using short-wavelength low-pressure mercury vapor tubes that emit at the resonance line of 253.7 nm. Even if this is a widely spread, efficient way of purifying water, mercury, used for manufacturing lamps, is also a very toxic element that presents a series of side effects on human health and environment. This chemical element is widely used in a broad range of everyday products and is released to the atmosphere, soil and water from different sources. While using it as a tool for water purification, it becomes extremely polluting for the environment once it becomes a waste.

Besides the toxic character of mercury, these low-pressure lamps have an efficiency of 30%, demanding a high operating voltage of 100 to 400 V and have low functioning lifetime of between 2,000 up to 10,000 h with a high warm-up period required to reach full light output.

Therefore, the use of these devices and of all mercury-based components will be forbidden starting with 2020, following the Minamata Convention on Mercury treaty signed by the Unites Nations and in place since August 2017 (United Nations 2017). In fifteen years, the extraction of mercury from mercury mines will phase-out and a need for ecologically-friendly and more economically competitive alternative urges.

Sustainable development issues require low energy and low-cost components and devices that deliver high-performances and high-power efficiency. Research centers are investigating the actual need of replacing polluting materials with eco-friendly or less polluting and recyclable alternatives, as well as miniaturization of components and devices, without compromising on efficiency.

$Al_xGa_{1-x}N$ based LEDs as an alternative solution

An efficient solution for satisfying the actual demands would be the production of high efficiency light emitting devices (LED) in the UV-B and UV-C range by using direct band gap semiconductors allowing for an efficient light emission. One option for such devices is the use of the semiconductor alloy $Al_xGa_{1-x}N$ that allows for emission wavelength modulation as a function of aluminum composition. Wide band gap semiconductors with a direct band gap such as GaN and AlN present the advantage of allowing the tuning of the emission in a wide wavelength range. Indeed, $Al_xGa_{1-x}N$ material is of high interest in the research community and great progress has been made in the past years as far as light output power and device efficiency is concerned. The study of its properties is of main importance for this project.

State of the art of $Al_xGa_{1-x}N$ based UV-LEDs

2D $Al_xGa_{1-x}N$ based DUV LEDs

Development of $Al_xGa_{1-x}N$ based DUV devices and improvement in efficiency are highly interesting domains for industrial research. Industry groups including RIKEN, Nichia, Nikkiso, LG, Philips or Panasonic have been publishing innovative advances that allow increasing the wall-plug efficiency (WPE) and external quantum efficiency (EQE) of devices. Professor Michael Kneissl from Technische Universität Berlin is summarizing the EQE in DUV LEDs obtained by various research groups throughout the world, as a function of the emission wavelength.

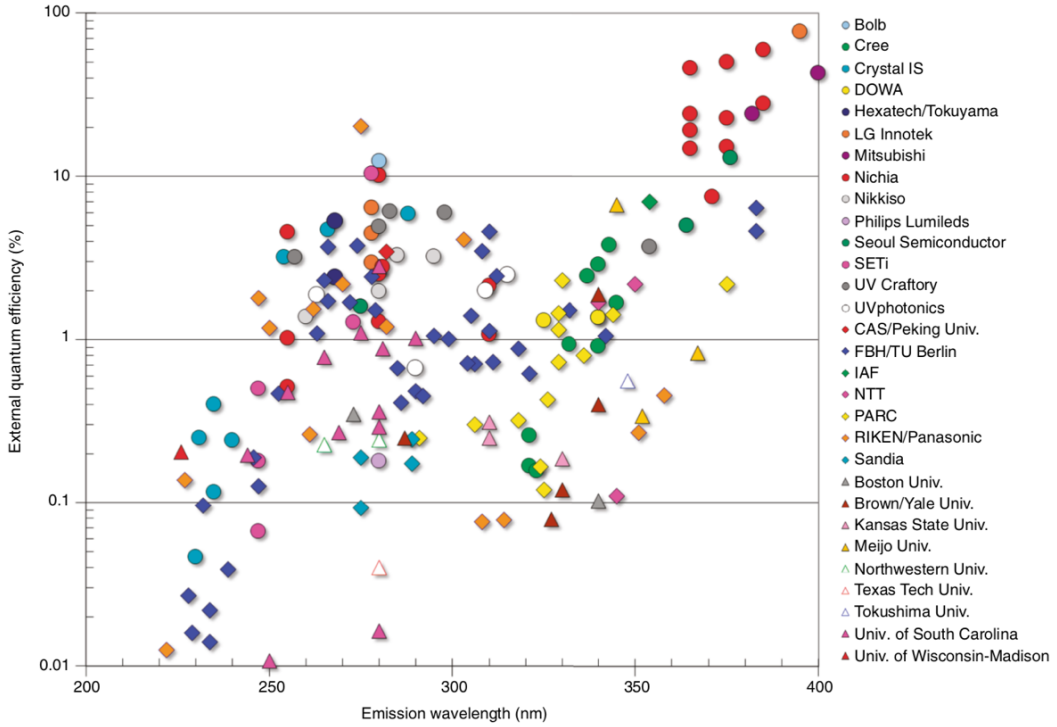

Figure 2. External Quantum Efficiency of $Al_xGa_{1-x}N$ based DUV LEDs as a function of emission wavelength as obtained by different research groups. Summary done by Professor Michael Kneissl from TU Berlin (Kneissl et al. 2019).

The up to date evolution is shown in Figure 2 (Kneissl et al. 2019). The most important milestones that led to significant efficiency improvement will be further discussed.

Overall, GaN based LEDs show an efficiency as high as 90% for emission wavelengths going from 365 to 400 nm. The discoveries made on GaN blue LEDs have led to Nobel prize accorded to three Japanese researchers in 2014: Professor Isamu Akasaki and Professor Hiroshi Amano from Nagoya University and Professor Shuji Nakamura from Nichia Corporation research center. One of the main difficulties while working with GaN material came from the difficult p-type doping. Their combined research and discoveries on Mg-doping activation by electron beam irradiation in 1989 (Amano et al. 1989; Isamu Akasaki et al. 1991) and by thermal annealing in 1992 (Nakamura et al. 1992b) have led to highly efficient doping in light emitting devices and to the further development of the LEDs used nowadays.

The milestone of the difficulty in doping of III-N materials overpassed, between 1996 and 2001 research has started on $Al_xGa_{1-x}N$-based UV LEDs with wavelengths below 360 nm (Han et al. 1998; Kinoshita et al. 2000; Nishida et al. 2001). Nevertheless, 20 years later, the external quantum efficiency (EQE) of $Al_xGa_{1-x}N$ LEDs is still too low in the 255-265 nm wavelength range to answer the demands for replacing mercury lamps.

An $Al_xGa_{1-x}N$ based LED emitting at 280 nm was reported by a group from University of South Carolina in 2004 (Sun et al. 2004). First emitting AlN LED done by Tanyiasu et al from Nippon Telephone and Telegraph Corporation (NTT) was published in 2006 in Nature (Taniyasu et al. 2006). The 2D LED was made by using a simple *pn* junction AlN material and showed emission at 210 nm. The low carrier concentration of p-type AlN was the limiting factor of the efficiency of the diode, due to a high activation energy of Mg acceptors. Nonetheless, the low emission wavelength of the device presented in the paper overpassed an important limit when working with AlN.

The first commercially available LED was developed by Sensor Electronic Technology in 2012. The devices showed emission with wavelengths ranging from 240 to 360 nm and a maximum EQE at 273 nm of 11% (Shatalov et al. 2010, 2012; Mickevičius et al. 2012, 2013; Moe et al. 2012). The internal quantum efficiency (IQE) was improved by growing low density of threading dislocations $Al_xGa_{1-x}N$ layers on c-plane sapphire by metal-organic chemical vapor deposition (MOCVD) as well as UV transparent p-type cladding and contact layers and frontside reflecting ohmic contact.

A record 20.3% for an $Al_xGa_{1-x}N$ LED emitting at 275 nm has been presented by Hirayama et al from RIKEN/Panasonic group. The work was later published in 2017 (Takano et al. 2017). The device's structure was improved by crystal growth techniques limiting the threading dislocations in 2D AlN grown on a patterned sapphire substrate, allowing an optimized internal reflection of light. The issues caused by low doping in $Al_xGa_{1-x}N$ material were suppressed by using a stack of multiple quantum wells (QW) and an electron blocking layer (EBL) to confine carriers in the QW region, while increasing the electron injection efficiency (EQE). The UV-absorbing top

contact electrode normally done by p-type doped GaN was replaced by a transparent p-$Al_xGa_{1-x}N$ contact layer (Hirayama et al. 2014). Instead of a Ni/Au top metal electrode, a highly reflective photonic crystals contact layer improved the light extraction, considerably.

Nichia Corporation launched in April 2019 their first commercially available UV-C LED emitting at 280 nm in a packaging able to resist significantly harsh environmental conditions (Nichia 2019). Nikkiso and Meiju University have also improved the efficiency of their $Al_xGa_{1-x}N$ based LED's by introducing a UV-C resisting resin that encapsulates the device. Their emission wavelength ranges between 250 to 280 nm with EQEs higher than 10% (Pernot et al. 2010; Inazu et al. 2011; Yamada et al. 2014).

Diodes grown directly on AlN substrates theoretically yield higher efficiencies than that grown on a foreign substrate such as sapphire or Si. Crystal IS is an American enterprise providing single crystal AlN substrates and have developed LED devices with high lifetime and high light output in the 250-280 nm range, that also present improved thermal performance (Grandusky et al. 2011, 2013).

2D LEDs vs NW LEDs

One promising way in going further with optimization of devices is the use of nanostructures. Nanostructurization of materials eases some of the issues when dealing with $Al_xGa_{1-x}N$ material, nanowires (NW) occupying an important place in research. Light extraction efficiency (LEE) is considerably improved by the use of nanowires. The first 250 nm UV-LED based on semiconductor nanowires was demonstrated in 2013 by a research group at Ohio State University and University of Illinois in Chicago (Carnevale et al. 2013). The team used a radio frequency Molecular Beam Epitaxy (RF-MBE) growth on p-type Si substrate for device fabrication. The use of these nanostructures allowed the compositional variation of $Al_xGa_{1-x}N$ in a wide range without the formation of dislocations from strain relaxation, using the polarization induced nanowire light emitting diodes (PINLEDs). They used the polarization contrast of chemical bonds of differing Al content $Al_xGa_{1-x}N$ to reduce the need for p-type doping.

Ultra-low threshold electrically injected $Al_xGa_{1-x}N$ nanowire ultraviolet lasers on Si, operating at low temperature as well as the controlled coalescence of $Al_xGa_{1-x}N$ nanowires during growth to reduce dislocations, and to considerably improve the efficiency of $Al_xGa_{1-x}N$ LEDs were reported by researchers at McGill University in Canada (Li et al. 2015; Le et al. 2016).

As far as NW industry is concerned, no major progress was done in the field of DUV LEDs. CryoNano® is a company based in Trondheim, Norway, founded in 2015, that specializes in nanostructures grown on graphene substrates. However, the LEDs developed so far do not exhibit performances in the sub-365 nm range (Høiaas et al. 2019). More recently, NS Nanotech company was founded in 2019 by Prof. Mi, and aims at developing light emitting devices covering the entire electromagnetic spectrum, including DUV for water purification and medical sanitization (NS Nanotech 2019). However, no NW based UV LED product was yet commercialized.

Path towards improvement of efficiency

Currently, the efficiency of $Al_xGa_{1-x}N$ DUV LEDs is still very low compared to that of standard mercury lamps. The path towards improvement of efficiency is assiduous and innovative ideas have allowed the constant increase of efficiency. Still, the low devices performance is due to mainly three limiting factors:

1. Low hole concentration in p-type $Al_xGa_{1-x}N$ caused by a low carrier injection efficiency (EIE);
2. Unsuited metal contact layer and light absorption by p-GaN top contact layer, decreasing the LEE of devices;
3. Low internal quantum efficiency (IQE) due to unsuitable substrate and threading dislocations decreasing the recombination efficiency inside the devices.

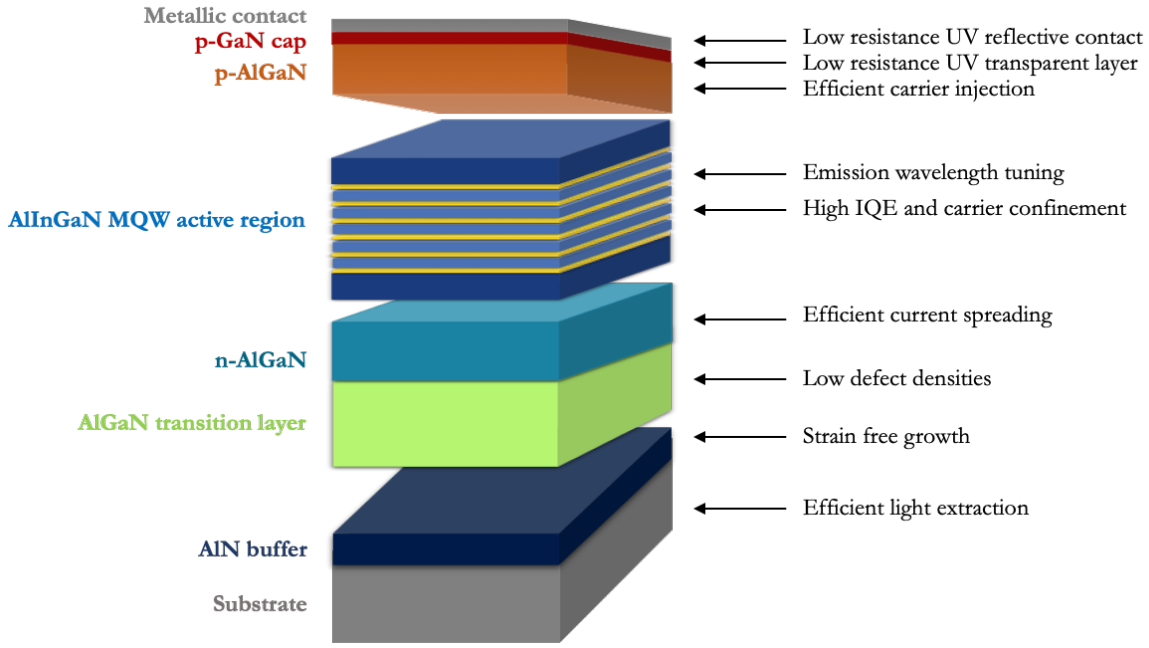

Figure 3. Illustration of the structure of a complete DUV LED device with respective issues associated to each cladding (adapted after (Kneissl et al. 2019)).

Figure 3 illustrates the basic structure of a 2D $Al_xGa_{1-x}N$ based UV LED. Even if some of the above limitations can be more easily overpassed, research is needed to improve some of the issues regarding the carrier concentration in high Al content $Al_xGa_{1-x}N$ structures as well as the metallic top-contacts.

The aim of my PhD was to understand and answer some questions related to physical concepts of nanowire-based UV-LEDs. The research I have done during this PhD concerns $Al_xGa_{1-x}N$ NWs, exploring the whole range of Al content (from x=0 in the case of GaN NWs to x=1 in the case of AlN NWs). My PhD is mainly focused in solving one of the most important problems when dealing with $Al_xGa_{1-x}N$ material: the biggest challenge is the control and characterization of doping in AlN material for further developing *pn* junctions for LEDs. Following questions were still not answered at the beginning of this project:

- Is the NW doping a specific mechanism?
- How can we incorporate acceptors in $Al_xGa_{1-x}N$ and moreover, how can we activate them?
- How can we measure the activation and doping level?
- What are the transport mechanisms in high Al content and AlN structures?
- What other solutions would allow one to improve the metallic contacts for DUV LEDs?

Organization of the manuscript

Therefore, the manuscript will be divided in four chapters, organized as follows:

Chapter 1 starts with a presentation of the state-of-the-art background and concepts on III-N materials regarding structural, optical and electronic properties necessary for the understanding of future results. The physics behind a *pn* structure will be developed further, with a special focus on recombination mechanisms.

Chapter 2 presents the methods and experimental details that allowed the development and characterization of $Al_xGa_{1-x}N$ UV LEDs. The epitaxial growth technique by molecular beam epitaxy with the growth mechanisms and sample growth process will be described in the first part of this second chapter. Further, characterization techniques such as Scanning Electron Microscopy (SEM) will be detailed. A full description of experimental set-up for electrical characterization (JV, different configurations for electron-beam induced current-EBIC set-up) will be given, together with theoretical concepts needed for data modelling.

Chapter 3 is focused on GaN nanowires. In particular, we are interested in optimization of p-type doping as well as on explaining the incorporation mechanisms in nanowires. Another interesting part of the study concerns vacancies formation as a function of doping in GaN nanowires. Finally, electrical characterization and EBIC experiments on GaN NW *pn* junctions have helped us conclude on the importance of studying as-grown nanowires.

Chapter 4 can be divided in two parts: first part is dedicated to the study of $Al_xGa_{1-x}N$ NW compositional fluctuations and on the study of $Al_xGa_{1-x}N$ *pn* junctions by EBIC and electrical characterization. The second part deals with the study of AlN nanowires. From p-type doping achieved by In-Mg co-doping mechanisms, to AlN *pn* junctions, we have improved the feasibility of AlN based LEDs. Irradiation has shown an important effect on Mg activation in the *pn* - junctions. Electrical transport properties were studied in detail and transport mechanisms were defined in the samples.

The ultimate aim of my PhD project is to gather the knowledge in terms of physical and electrical phenomena of $Al_xGa_{1-x}N$ nanowire junctions grown by using the MBE technique. This research has been mainly funded by the French National Research Agency ANR-15-CE24-0006-

04, EMOUVAN project. Most of the research was done at the Atomic Energy and Alternative Energies Commission (CEA), but also at the National Center for Scientific Research (CNRS)-Neel Institute in Grenoble, France.

Concerning my contribution to the project, my work was divided between the two laboratories I was a part of:

At CEA Grenoble, I was in charge of the growth of the samples by Molecular Beam Epitaxy (MBE), as well as of the structural characterization by Scanning Electron Microscopy (SEM) and preparation of the samples (identification of the region of interest for different studies, dispersion, annealing, etc…) under the supervision of my PhD director Dr. Bruno Daudin. Regarding the organization of the project, I was in charge of the collaborations by defining the various complementary studies, interacted with the different collaborators and I gathered and participated at the interpretation of results.

The work at CNRS Grenoble was centered around the electrical characterization of the samples: from clean room processing of the samples (electrodes conception, metal and ITO sputtering, annealing) to IV experiments. Electron Beam Induced Current (EBIC) is one of the major techniques I have used for the study of the electrical properties of $Al_xGa_{1-x}N$ materials, under the supervision of my PhD co-director Prof. Julien Pernot.

A big part of the manuscript is dedicated to the doping and study of electrical properties, since my PhD was focused on the growth and optimization of structures for future DUV LED devices. Answering a part of these questions would not be have been possible without the numerous collaborations I have had during these three years:

- Cathodoluminescence experiments have been performed by Dr. Gwénolé Jacopin at CNRS-Neel Institute- in Grenoble;
- Energy Dispersive X-Ray (EDX)-TEM correlated experiments have been done by Dr. Eric Robin at CEA- INAC in Grenoble;
- Raman Spectroscopy experiments were performed by Dr. Ana Cros and Dr. Nuria Garro at the Materials Science Institute at University of Valencia in Spain;
- Theoretical and ab-initio calculations were done by Dr. Damien Caliste and Dr. Pascal Pochet at CEA Grenoble;
- Atom Probe Tomography experiments were done during the PhD of Lynda Amichi and under the supervision of Dr. Catherine Bougerol and Dr. Adeline Grenier at CEA Grenoble.
- Positron annihilation experiments were performed by Prof. Akira UEDONO from the University of Tsukuba, Japan.

"If you can't explain it simply, you don't understand it well enough"

1. Nitrides for light emission: background and concepts

After introducing the motivations for replacing mercury lamps by $Al_xGa_{1-x}N$ based LEDs, we will focus in this chapter on describing the particular properties of this direct band gap semiconductor that make it an outstanding candidate for DUV LEDs development.

1.1. III-N material

III-V materials define an alloy formed by a third (IIIA) column element (B, Al, In, Ga) and a fifth (VA) column element (N, P, As) (see Figure 4). BN, AlN, GaN and InN are the four main III-N materials exhibiting outstanding optoelectronic properties, which make them suitable for integrating different semiconductor application domains. AlN, GaN and InN materials exhibit similar properties and are considered as "standard nitrides", whereas BN material exhibits very peculiar opto-electronic and structural properties and will not be concerned in the following.

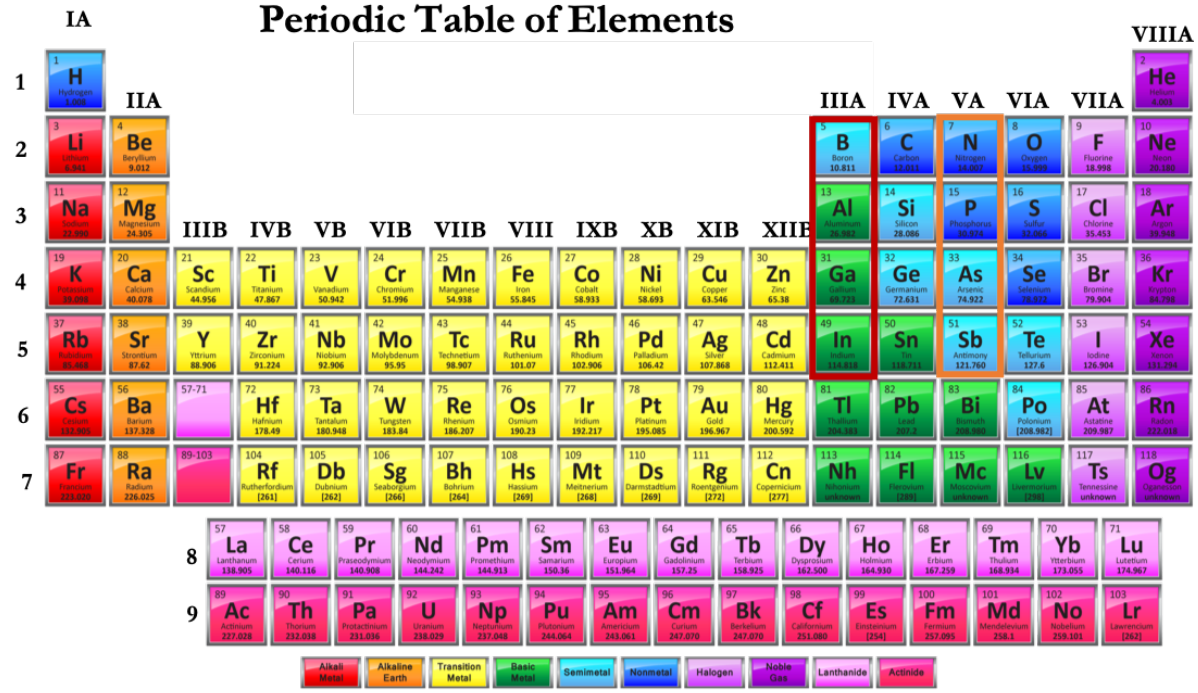

Figure 4. Periodic table of elements evidencing the 3rd and 5th column elements forming the III-V materials category (adapted from (Helmenstine 2016)).

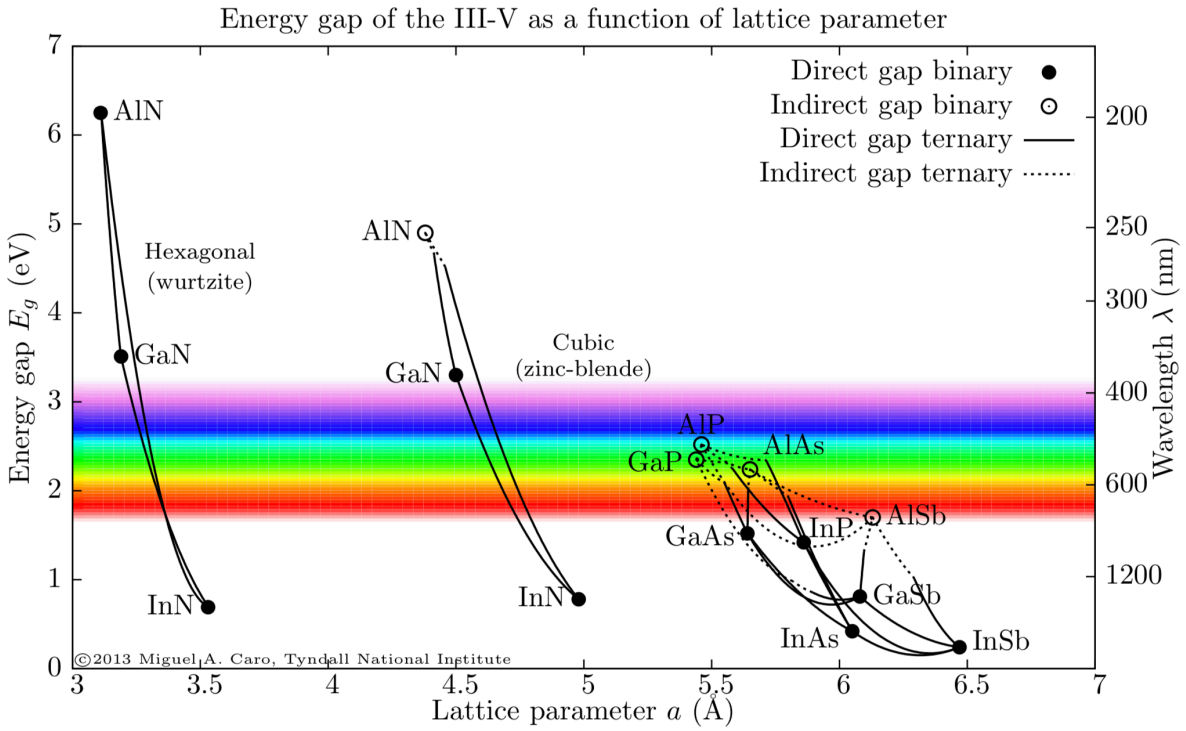

Figure 5. Band gap energy (E_g) variation of the technologically important III-V binary materials with respect to the lattice parameter (in-plane lattice parameter in the case of wurzite nitrides). Image from reference (Caro Bayo 2013)

The emission wavelength and band gap energy (E_g) dependence on lattice parameters for group III-V semiconductor materials is illustrated in Figure 5 (Caro Bayo 2013). The standard nitrides we are interested in have a band gap at room temperature equal to 0.78 eV (near IR) for InN, 3.51 eV (near UV) for GaN and 6.25 eV (extreme UV) for AlN. We will be mostly focusing on the properties of AlN and GaN binary alloys for DUV emission, $In_xGa_{1-x}N$ being an ideal candidate for visible light emission. Therefore, the interest for DUV LEDs based on wide direct band gap semiconductors comes from the possibility of tuning of the emission in a wide wavelength range, from 200 to 365 nm, with both p-type and n-type conductivities in the UV range.

Hence, in order to cover the entire spectral range, intermediate ternary alloys such as $Al_xGa_{1-x}N$, where x is the Al fraction, are synthesized by combining binary alloys. Generally, the band gap energy of an $A_xB_{1-x}N$ alloy for a given composition is given by the empirical equations determined from Vegard's law:

$$E_g^{A_xB_{1-x}N} = xE_g^{AN} + (1-x)E_g^{BN} - x(1-x)b \qquad (1)$$

Where b is the bowing coefficient that corrects the simple linear relation involving the A and B species. For $Al_xGa_{1-x}N$, this empirical parameter is ranging between 0.53 eV and 1.3 eV (Angerer et al. 1997; Ochalski et al. 1999; Jiang et al. 2000; Yun et al. 2002; Dridi et al. 2003), depending on the impurity concentration or Al composition in the studied ternary alloy.

UV LEDs show various advantages with respect to UV mercury, deuterium or Xenon lamps used nowadays. First, a device size of 1 cm^2 could replace the heavy devices that use mercury tubes of more than 1 m of length, without the use of toxic elements and having a single peak emission

with customizable wavelength as a function of their composition. Moreover, $Al_xGa_{1-x}N$ is of high interest in the research community due to the large lifetime of electrical devices and physical hardness. The targeted lifetime of UV LEDs is expected to be of the order of 20,000 hours, 10 times higher than that of UV lamps, with no warm-up time, allowing to reduce the total costs of devices thanks to savings on power supply and packaging costs. On the other hand, the small spot sizes of the surfaces to be illuminated is a disadvantage with respect to large mercury lamps (Kneissl and Rass 2016; Kneissl et al. 2019).

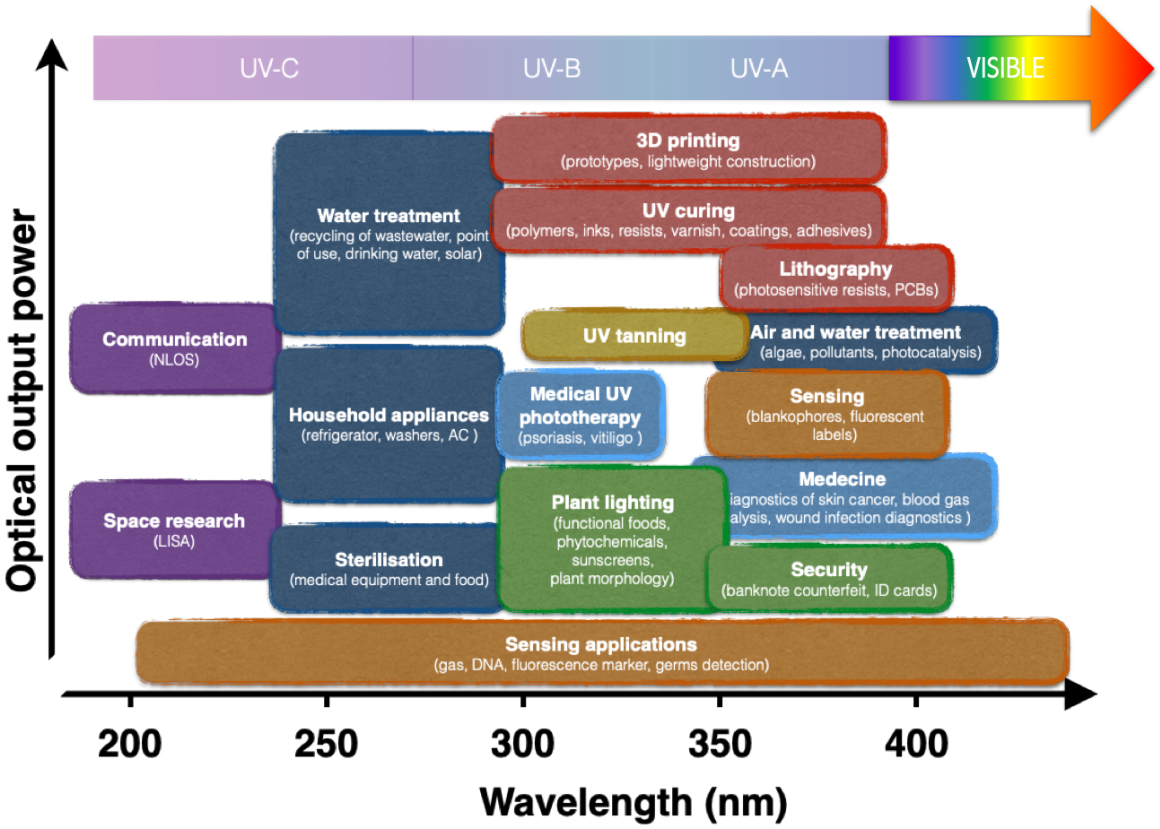

Figure 6. Light output power of UV-LED applications based on $Al_xGa_{1-x}N$ classified with respect to the emission wavelength (image adapted from (Kneissl and Rass 2016)).

In UV-C range, one of the most important application domains is the sterilization of food and medical equipment as well as the water purification, as described previously. At the higher wavelength of 300 nm, $Al_xGa_{1-x}N$ is used for plant lighting in agriculture as well as for medical purposes such as for UV-curing of psoriasis and vitiligo disease. Besides LEDs, more general uses of III-N materials in the optoelectronic field include lasers for applications such as DVD Blue-ray readers (Figure 6). Amongst the general application of III-nitrides we can also mention high power and high frequency electronics such as Heterostructure Field Effect Transistors (HFET) or High Electron Mobility Transistors (HEMT). AlN based devices are used for Surface Acoustic Wave (SAW) devices, signal treatment or for touchscreens in mobile applications because of their piezoelectric properties (Kneissl and Rass 2016).

1.2. Nanowires

The requirement for improved efficiency of actual devices could benefit from the use of nanowire heterostructures. Semiconducting nanowires are one-dimensional nanostructures having a diameter of around 100 nm and a height over diameter ratio higher than 10 (Rigutti 2015). The term "nanowire" has been extended to nanostructures exceeding 100 nm diameter, going up to several micrometers, nevertheless, the term "microwire" is more adapted to define this kind of structures. For structures for which the height over diameter ratio is lower than 10, the common terms "nanorod" or "nanocolumn" is employed.

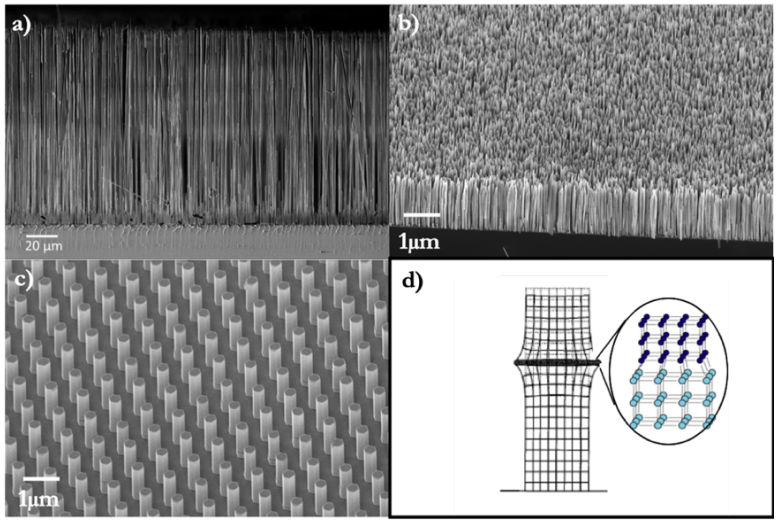

Figure 7. SEM images for GaN nanowires synthesized by different techniques. a) MOCVD (El Kacimi et al. 2018) b) MBE (this work) c) MOCVD by using selective area growth method (Aledia 2019). d) Strain relaxation mechanism on the lateral walls of a nanowire adapted from (Niquet et al. 1997).

Different examples of nanowires synthesized by different techniques are presented in Figure 7a, b and c. The main interest of these nanostructures comes from the high surface to volume ratio that favors surface effects. Elastic strain relaxation during growth considerably reduces the crystallographic extended defects rising from lattice mismatch between materials. Because of the unique boundary conditions, nanowire heterostructures are more effective in relieving mismatch strain coherently, exhibiting defect-free interfaces (Niquet et al. 1997). The crystal quality in nanostructures is also considerably improved because of the small diameter allowing strain to be relaxed laterally, whereas in planar layers the strain could be relaxed only along one dimension (Ertekin et al. 2005).

A critical layer thickness below which no interfacial dislocation should be introduced was determined in literature by evaluating the elastic energy stored in systems (Yoshizawa et al. 1997). Efficient dopant incorporation in nanowires is also worth mentioning as an advantage of studying these nanostructures (Fang et al. 2015). Due to the large area of free surface, which are specific to NWs, the relaxation of tensile strain induced by the presence of dopants is observed. This makes their incorporation easier, while leading to an elastic strain relaxation without cracks formation (Glas 2006). Thus, the solubility limit is expected to increase due to the nanowire relaxed morphology.

1.3. General background on III-N material

The properties of III-N standard materials are similar regarding crystal structure, polarization effects or defects. Therefore, while presenting the state of the art and general properties, I will be talking mainly about $Al_xGa_{1-x}N$ material (from which one understands AlN, GaN as well as the $Al_xGa_{1-x}N$ alloys).

1.3.1. Structural properties of III-N material

1.3.1.1. Crystal structure

Depending on the growth parameters, the III-Nitride semiconductors as well as their ternary alloys such as $Al_xGa_{1-x}N$, exhibit three different crystalline arrangements:

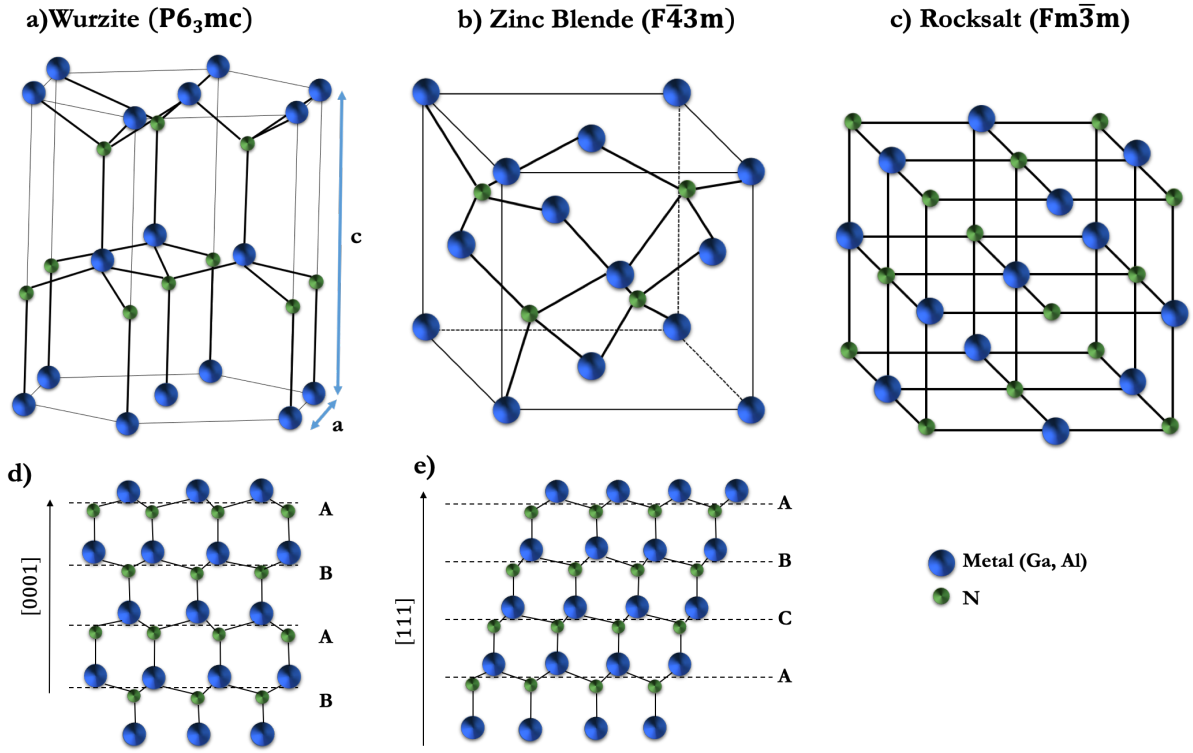

Figure 8. Crystal structure of III-N materials: a) Wurzite, b) Zinc-blende, c) Rocksalt structure d) Plane staking in wurzite structure, e) Plane stacking in zinc-blende structure. Nitrogen atoms are represented in green and metal atoms in blue.

- Wurzite (WZ): or w-phase structure illustrated in Figure 8a belongs to the $P6_3mc$ space group and has an ABAB atomic layer hexagonal stacking pattern, where A and B refer to different in-plane positions of the III-N atoms (Figure 8d). Its primitive unit cell is composed of two hexagonal close-packed sub lattices formed by two metal and two nitrogen atoms. Those sub lattices are shifted one with respect to the other along the [0001] direction (further defined as $\vec{c}$) by a vector $\vec{u} = 3\vec{c}$ with respect to the ideal structure (which can be seen as a tetrahedron where each metallic element is bonded to four N atoms and vice-versa). This is the main phase seen in the samples grown during the PhD.
- Zinc-blende (ZB): cubic or c-phase structure belonging to the $F\bar{4}_3m$ space group is shown in Figure 8b. It exhibits an ABCABC pattern shown in Figure 8e, with the

C plane rotated by 60° with respect to A, in the [111] direction. The unit cell is constituted of two face centered cubic lattices shifted by $\sqrt{3}a$ in the [111] direction. This phase is thermodynamically less stable than the wurzite phase. However, it is possible to obtain it by controlling the growth parameters, for example using a cubic substrate such as 3C-SiC (Okumura et al. 1994, 1997; Wei et al. 2000) or GaAs (Okumura et al. 1991; Lin et al. 1993), or by decreasing the growth temperature, introducing stacking faults in the wurzite segments (Daudin et al. 1998; Hestroffer 2012).

- Rock salt (RS): structure presented in Figure 8c belongs to $Fm\bar{3}m$ space group and the unit cell can be considered as a face-centered cubic structure with secondary atoms in the octahedral holes. This phase can be synthesized only under extreme growth conditions that imply growth at very high pressure, incompatible with MBE growth technique (Christensen and Gorczyca 1994).

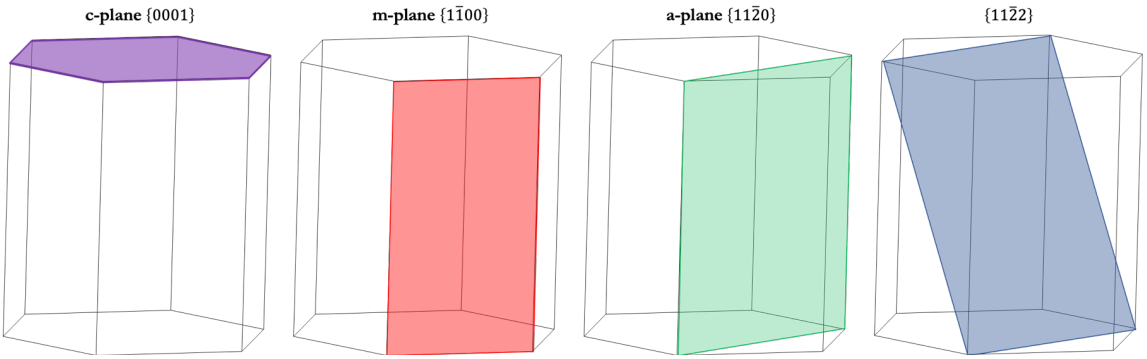

Figure 9. Crystal planes in wurzite lattice structure.

The most common crystallographic structure due to its thermodynamic stability is wurzite. The nanowires grown during this work only show this crystallographic structure. Different crystallographic planes of the hexagonal wurzite lattice are represented in Figure 9 and the description is given in the four indices base notation (h k i l) specific to hexagonal structure. The h, k and l indices are the Miller indices whereas the i parameter is defined as i=-(h+k). This notation allows an easy identification of equivalent planes thanks to indices permutations.

The wurzite lattice structure is defined by 2 main parameters, the length *a* of the hexagonal base and the height *c* of the lattice, as represented in Figure 8a. Table 2 gives *a* and *c* parameters for GaN, AlN and InN at room temperature (300K) and atmospheric pressure (Vurgaftman and Meyer 2003).

Lattice parameters	GaN	AlN	InN
***a* (Å)**	3.189	3.112	3.545
***c* (Å)**	5.185	4.982	5.702

Table 2. Lattice parameters in GaN, AlN and InN materials.

1.3.1.2. Polarity

One particularity of the wurzite crystal structure is the lack of centro-symmetry, due to the presence of a unique polar axis collinear to the $\vec{c}$ axis. Hence, the $[0001]$ (c) and $[000\bar{1}]$ $(-c)$ directions are not equivalent (Hellman 1998). A convention has been adopted to define the polarity of the III-N crystal: the positive direction of the $\vec{c}$ axis [0001] is the vector going from the metallic atom and pointing towards N in the direction of the metal-nitrogen bond, which is collinear to the $\vec{c}$ axis of the wurzite cell.

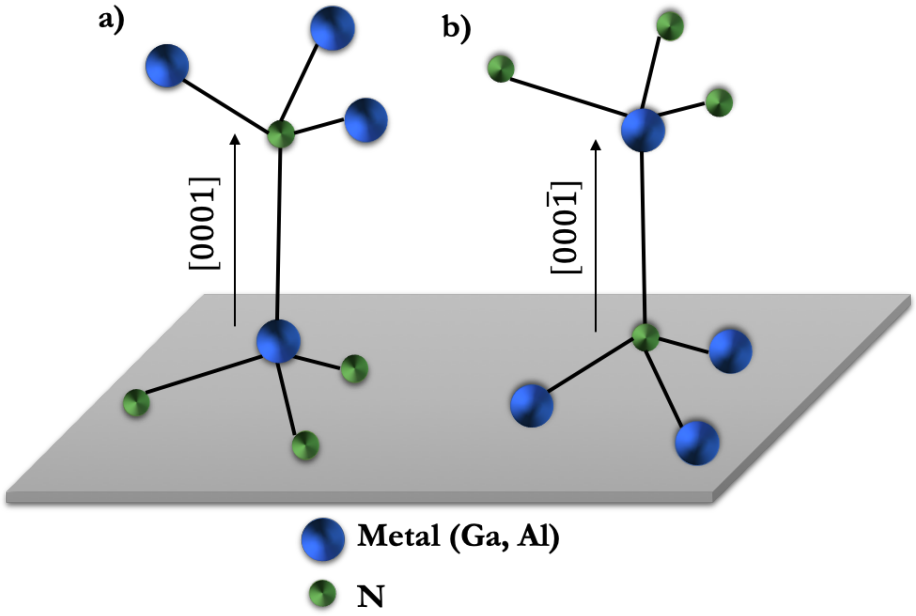

Figure 10. a) metal-polar structure and b) N-polar structure.

The wurzite unit cell and the equivalent directions are illustrated in Figure 10. The growth usually takes place along $\vec{c}$ direction, so the nanostructure or layer polarity is defined by the $+c$ or $-c$ direction, defining also the polarity of the crystal.

Metal-polar: a structure is said to be metal-polar when its growth direction is *c*, with a Ga-N bond directed towards the surface, oriented from a Ga or Al atom towards an N atom.

N-polar: a structure is said to be nitrogen-polar when its growth direction is *-c,* with a Ga-N bond oriented from a N atom towards Ga or Al atom.

The control of polarity is important when working with III-N nanowires, since optical, electrical and morphological properties are depending on it. There are several ways of establishing the polarity of $Al_xGa_{1-x}N$ material, such as the widely used chemical etching by KOH, X-ray diffraction (Hestroffer et al. 2011), KPFM (Minj et al. 2015) or Convergent Beam Electron Diffraction (Largeau et al. 2012).

1.3.1.3. Polarization

A consequence coming from the WZ symmetry is the presence of a macroscopic spontaneous polarization called P_{sp}. The difference between nitrogen and metal atoms, where N atoms have a smaller atomic radius and a higher electronegativity than metal atoms, forms an electrostatic dipole, with negative charges towards N and positive charges towards the metal. Since the -c and c orientations are not equivalent, the charge distribution forms a polarization field P_{sp} along the $\vec{c}$-axis. Conventionally, the P_{sp} vector is oriented (along the $\vec{c}$ axis), from the N atom toward the metal atom, independent of the crystal polarity.

While applying an external force to a III-N material, an additional piezoelectric polarization (P_{pz}) dependent on the crystal polarity has to be considered. Since N atom is more electronegative than metal atoms, crystals' atomic positions are modified by stress and lead to a different spatial distribution of the negative and positive charges, inducing a piezoelectric polarization. This additional polarization is negative on the metal side and positive on the N side. The total polarization P_{tot} in the nanostructure is the sum of the two previous polarizations ($P_{tot} = P_{sp}+P_{pz}$) induced by strain into the band structure during growth.

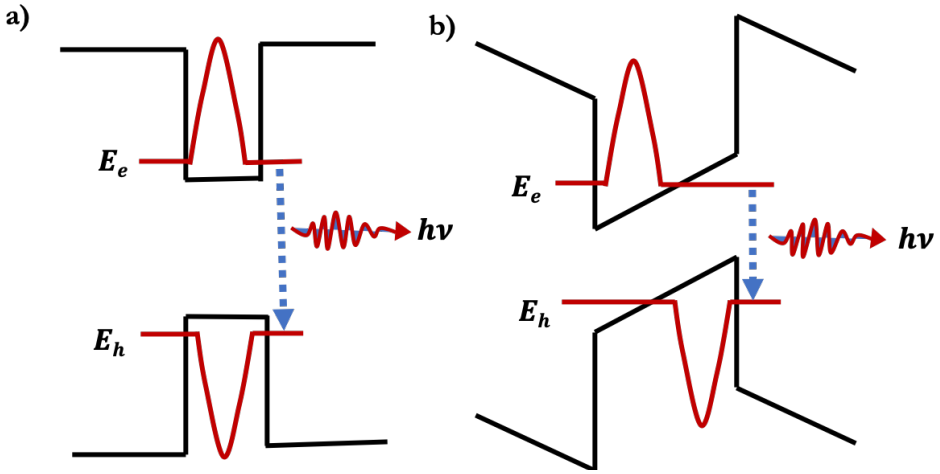

Figure 11. QCSE and wavefunction in $Al_xGa_{1-x}N/GaN$ active region with a) no electric field and b) with electric field.

A direct consequence is the recovering domain for wave functions for the conduction band and for valence band. This limits the efficient radiative recombination probability of electrons and holes, decreasing the optical emission. The phenomenon is known as Quantum Confined Stark Effect (QCSE). Figure 11 illustrates the wave functions of a quantum well under no electric field (a) and under the perturbative effect of an external electric field (b). Undesired effects such as incorporation rate of extra atoms for doping and alloying (Duff et al. 2014) or incorporation of defects (Schuck et al. 2001) can be equally observed.

Moreover, due to the electric field, the planes of a WZ crystal structure are different in terms of charges depending on their orientation with respect to the $\vec{c}$ axis. In consequence, facets (000l) in III-N materials are called polar facets, facets (hkil) with l=0 are non-polar facets. Semi-polar planes are defined by (hkil) facets with a nonzero h, k, or i and a nonzero l Miller index (Romanov et al. 2006).

1.3.2. Opto-electrical properties of III-Nitrides

1.3.2.1. Electronic transitions and light polarization

Being direct band gap semiconductors, the opto-electrical properties of III-N materials are determined by the band structure near the Brillouin zone center at the wavevector $\vec{k} = \vec{0}$, represented as the Γ point. The minima of the conduction band and the maxima of the valence band are both in the Γ point.

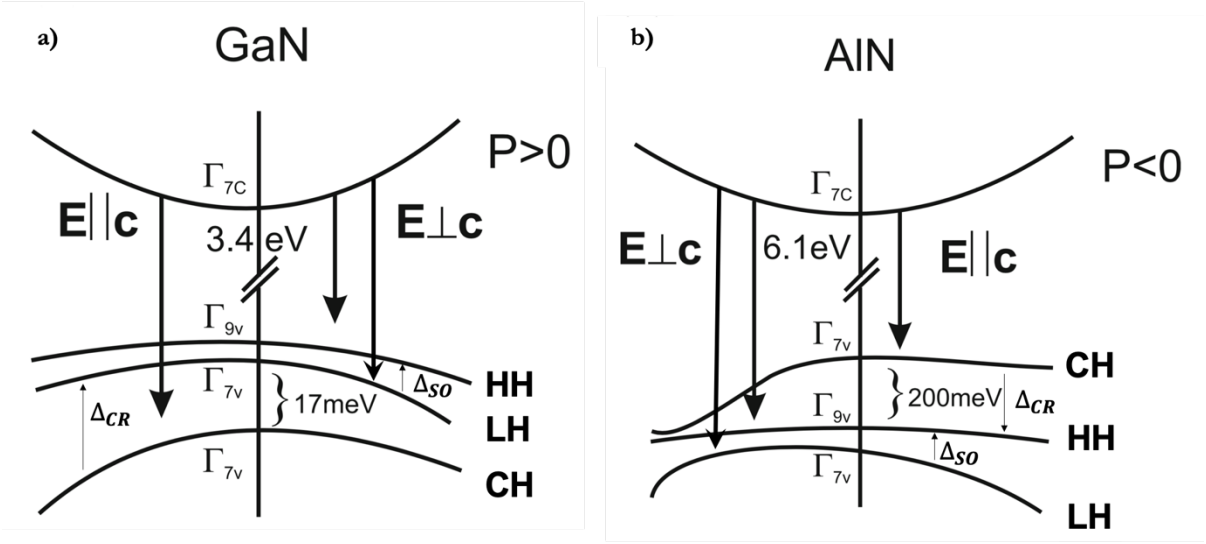

Figure 12. Band structure and transitions for a) WZ GaN and b) WZ AlN (adapted from (Kneissl and Rass 2016))

Both AlN and GaN have one unique conduction band (CB-Γ_{7c}) with atomic *s*-orbital states. However, the valence band (VB) presents a three-level degeneracy (Suzuki et al. 1995). First, due to the asymmetry of the crystal, a partial degeneracy occurs because of the interaction with the crystalline field (of energy Δ_{CR}). Second, the spin-orbit interaction determines an additional degeneracy of the valence band (of energy Δ_{SO}). The valence band is thus formed by a heavy-hole band (HH- Γ_{9v}), a light-hole band (LH- Γ_{7v}) and a spin-off band (CH- Γ_{7v}) represented in Figure 12 for GaN and AlN, respectively.

The valence band (VB) is divided in p_x, p_y and p_z states, depending on the axis of the crystal. The z direction of the orbital state is defined being the axis parallel to the c-axis of the crystal, whereas x and y are perpendicular to this direction and to each other.

There are three possible electronic transitions resulting from recombination of an electron excited into the conduction band and a hole in the valence band coming from *s* states and *p* states. The polarization of light resulting from these recombinations depends on the direction of the *p* orbital states. The light resulted from transitions between orbital states parallel to the c direction is called TM polarized (transverse magnetic), whereas light coming from recombination between the conduction band and the holes in the top-most valence band perpendicular to the c direction is called TE polarized (transverse electric).

The three valence sub-bands are different for AlN and GaN due to the crystal field splitting. For AlN, the top-most band is the CH, followed by the HH and LH band, whereas for GaN, the HH is the lowest energy sub-band, followed by LH and CH (Chen et al. 1996). The transitions in the two crystals between the valence sub-bands and the conduction band are thus not equivalent. Since lower band gap energies are more favorable than other transitions, photons give the maximum luminescence intensity for TM polarized light for AlN (Li et al. 2003), while for GaN it is strongly TE polarized (Chen et al. 1996).

A direct consequence of the different light polarizations is that when working with an alloy, the choice of structure of a LED device should be adapted for an optimized light extraction. The degree of polarization of light emitted from the ternary $Al_xGa_{1-x}N$ alloy is directly related to the composition (Coughlan et al. 2015). Depending on the AlN content, light emitted from a 2D UV LED structure grown along the c-axis can switch from TE polarized to TM polarized, which is an important factor for light extraction from the structure (Kneissl and Rass 2016).

Therefore, light loss is one of the major factors limiting the device efficiency. Depending on the design of the structures, light will be partially reabsorbed in the device, another difficulty arising from extraction efficiency. The AlN material case is even more challenging, since the TM polarized light is in the plane of the structure, favoring extraction through the sides. During this process, the light is partially reflected and re-absorbed in the structure, resulting in poor device performance.

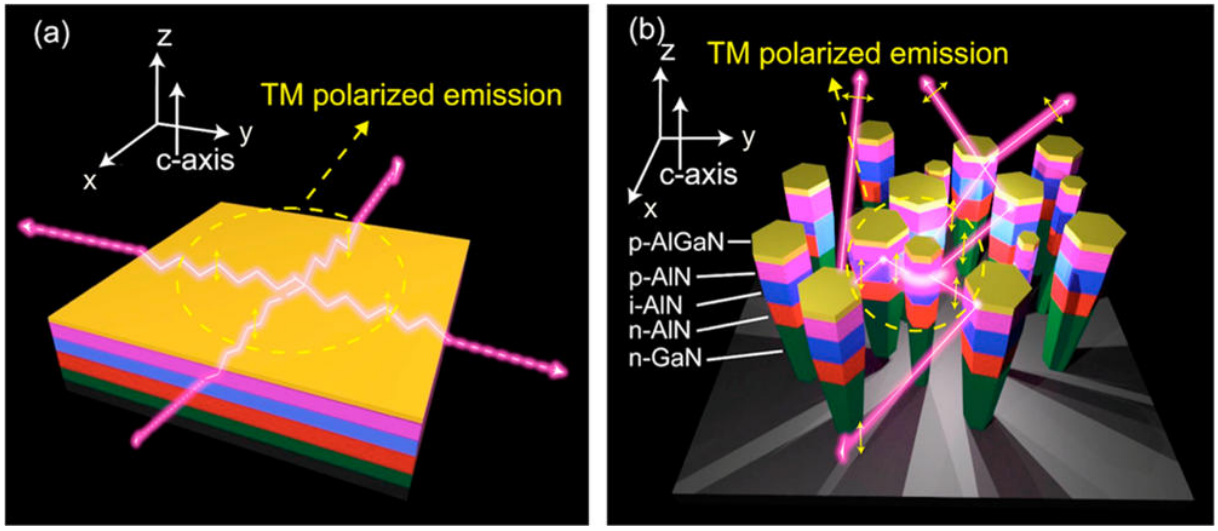

Figure 13. Light emission from a a)2D AlN LED and b) NW-based AlN LED (Zhao et al. 2015c).

Figure 13 illustrates the TM polarized light emission coming from a 2D AlN LED and that coming from a NW based AlN LED (Zhao et al. 2015c). While dealing with nanostructures, this inconvenience is no more a challenge, since light extraction is eased in all directions of the device. The strong light scattering effect in nanowires leads to an enhanced surface emission for TM polarized light. Once again, the NW morphology is one of the strengths of these nanostructures for UV LEDs.

The temperature of the material influences the value of the gap either through the thermal expansion coefficient of the crystal lattice or from the interaction between the electrons and the

acoustic and optical phonons, showing the occupation of these phonon levels.

The values of band structure parameters for GaN, InN and AlN are summarized in Table 3 (Vurgaftman and Meyer 2003):

	GaN	**AlN**	**InN**
$E_g\ (eV)$	3.510	6.25	0.78
$\Delta_{SO}\ (meV)$	17	19	5
$\Delta_{CR}\ (meV)$	10	-169	40

Table 3. Band structure parameters for GaN, AlN and InN

The decrease in the gap energy with temperature of the order of ~100 meV is related to the electron-phonon coupling, according to the Varshini model (Levinshtein, Rumyantsev, and Shur 2001) by the relationship below:

$$E_g(T) = E_g(0K) - \frac{\alpha \cdot T^2}{\beta + T} \qquad (2)$$

With α and β Varshni's thermal coefficients given in Table 4 (Vurgaftman and Meyer 2003).

	GaN	**AlN**	**InN**
$\alpha\ (\boldsymbol{meV.K^{-1}})$	0.909	1.799	0.245
$\beta\ (\boldsymbol{K})$	830	1462	624

Table 4. Varshini thermal coefficients for GaN, AlN and InN

1.3.2.2. Doping of $Al_xGa_{1-x}N$ material

Besides the three electronic transitions defined above, the electron-hole pairs may interact with structural defects and non-ionized impurities in the III-N material, bounding to the latter. These impurities have a different electronic configuration than the intrinsic nitride material, introducing additional energy levels in the band gap. Substitutional impurities and point-defect associated levels can be either close to the conduction band, in which case the impurities behave like donors, or to the valence band, behaving as acceptors. Depending on the position in the band gap, these levels are defined as "shallow" if they are close to either the valence or the conduction band, or "deep" if they are located around the middle of the band gap.

Physical and electrical properties of semiconductor materials are highly influenced by the presence of defects, intentionally or unintentionally created. Defects such as stacking faults, dislocations or point defects are introduced during growth in the material, when growth conditions are not optimized. In LEDs, such defects are mainly responsible for poor performances of the devices, since they are non-radiative recombination centers trapping carriers before recombination (Sugahara et al. 1998).

The main point defects are native defects, impurities, and complexes with the size comparable to the nearest atomic distance. In III-N materials, the most important ones are group II impurities (Zn and Mg), as well as C, Si, H, O, Be, Mn, Cd (Reshchikov and Morkoç 2005). Native defects affect the electrical and optical properties of semiconductors by introducing numerous energy levels in the gap. Usually, this type of impurities is a result of non-stoichiometric growth or annealing, being formed as compensation sources when dopants are introduced. Vacancies, interstitials and anti-sites are isolated native defects, their interaction forming a complex. Their probability of appearing highly depends on their formation energies. Defects with high formation energies such as self-interstitials and anti-sites are unlikely to occur in GaN during growth, however electron irradiation or ion implantation can highly increase their creation probability. Also, Ga vacancies generally occur in n-type $Al_xGa_{1-x}N$ whereas N vacancies are more likely in p-type $Al_xGa_{1-x}N$ (Neugebauer and Van de Walle 1999).

Depending on their electronic configuration and whether they have more or less electrons than the species forming the crystal, impurities in III-N semiconductors are considered as shallow donors or acceptors. Complexes between native defects and impurities introduced unintentionally are usually the dominant type of defects in III-N materials (Mattila and Nieminen 1997; Van de Walle 1997; Van de Walle and Neugebauer 2004).

Physical properties of semiconductor materials such as conductivity, band gap energy or charge carriers are mainly governed by doping. Tuning the electrical conductivity and elaboration of junction devices is acquired by the intermediate of doping. III-N materials are intrinsically n-type doped, unintentional n-type conductivity (doping) in $Al_xGa_{1-x}N$ being due to the incorporation of nitrogen vacancies or oxygen impurities during growth, highly dependent on the growth method.

1.3.2.2.1. n-type doping

To obtain n-type doping of $Al_xGa_{1-x}N$ material, elements from the fourth or sixth column elements of the periodic table are used. C, Si, and Ge on the Ga sites (Figure 14) and sixth column elements such as O, S, and Se on the N sites are considered as shallow donors in GaN (Reshchikov and Morkoç 2005). However, in order to become an electrically active donor of the material under consideration and participate to conduction mechanisms, the charge carriers have to be ionized requiring an ionization energy E_a.

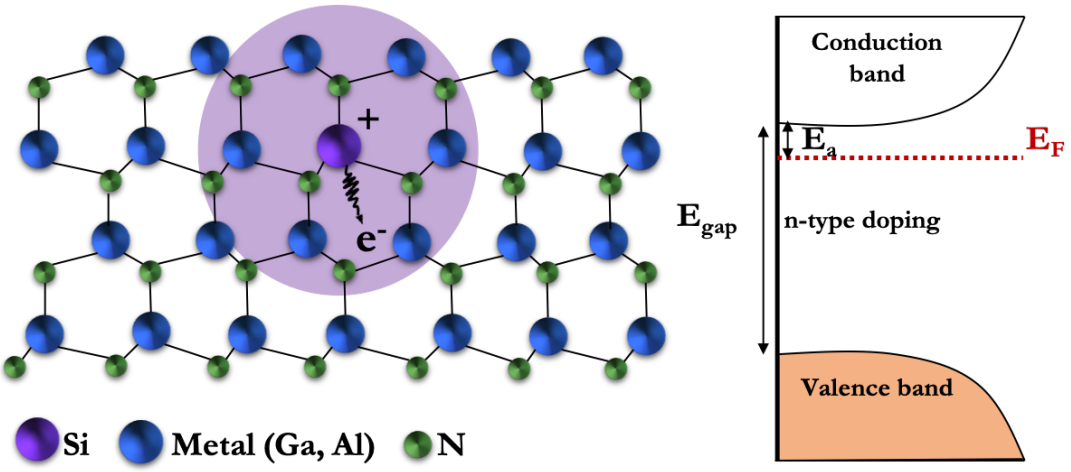

Figure 14. Si atom in substitutional metallic site in $Al_xGa_{1-x}N$ crystal lattice and Fermi level position close to the conduction band for a n-type doped material.

Various studies have determined the ionization energies of impurities for GaN wurzite (Reshchikov and Morkoç 2005). The donor ionization energies in wurtzite GaN are 34.0, 30.8, and 31.1 meV for C, Si, and Ge on the Ga site, and 32.4, 29.5, and 29.5 meV for O, S, and Se on the N sites (Wang and Chen 2000).

In AlN, the same donors present much higher ionization energy. Si is a native donor of AlN with an ionization energy as high as 282 meV (Taniyasu et al. 2006). C in Al site ionization energy is of 200 meV (Lyons et al. 2014). In III-N materials, the metal vacancy is the main defect, substitution of metal atoms from the III-N lattice by fourth column elements being easier than that of nitrogen atoms. The two main candidates for n-type conductivity are Si and Ge. The use of Ge as a n-type dopant of GaN material increased during the last years (Nakamura et al. 1992a; Dadgar et al. 2011; Fritze et al. 2012; Hille et al. 2014; Beeler et al. 2014; Ajay et al. 2017). However, in $Al_xGa_{1-x}N$ materials, clustering of Ge dopants for Al content higher than 0.4 together with a low donor activation has been observed (Ajay 2018). Even though Si and Ge present relatively close activation energies, the small radius of Si as well as the great availability makes it the dominant candidate for AlN and GaN materials. Since in AlN material the Si activation energy is higher than in GaN, the doping activation is expected to be more challenging, with formation of localized deep states (Bremser et al. 1998). In consequence, in $Al_xGa_{1-x}N$ alloys, the Si donor ionization energy increases from 30 meV to 282 meV, depending on the Al content. Increase in Al composition is also accompanied by the increase in the density of defects with energy levels deeper than Si. Combined action of the two above effects leads to the rather challenging n-type doping of AlN material.

1.3.2.2.2. p-type doping

The main p-type doping agents in $Al_xGa_{1-x}N$ are shallow acceptors from second column such as Be, Mg, Zn, Cd, Hg for Ga sites and group four elements C, Si, Ge, Sn for N sites (Reshchikov and Morkoç 2005). The ionization energy of Be on Ga sites of 187 meV is the smallest among these likely acceptors, followed closely by Mg on Ga sites (224meV) (Wang and Chen 2000). Even if, from an energy point of view, conditions are in favor of using Be as a dopant, its small atomic radius favors its incorporation on the interstitial site, acting as a double donor (Stampfl et al. 1999; Van de Walle et al. 2001).

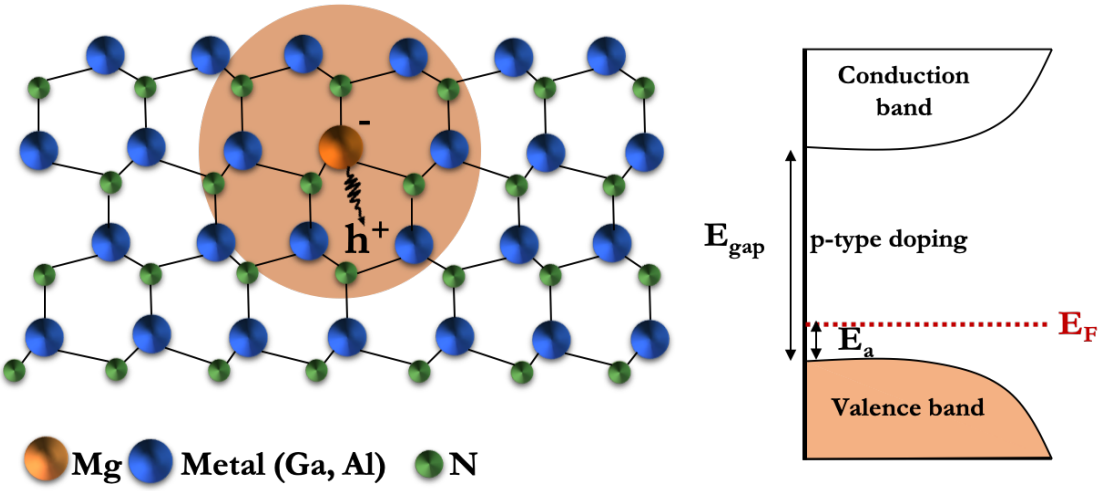

Figure 15. Mg atom in substitutional metallic site in $Al_xGa_{1-x}N$ crystal lattice and Fermi level position close to the valence band for a p-type doped material.

The formation energies of acceptors such as Si_N and Ge_N are relatively high, so that formation of these acceptors is unlikely in GaN under equilibrium conditions, whereas the formation energy of C on N sites could be sufficiently low in Ga-rich conditions, leaving Mg_{Ga} as the best candidate for GaN p-type doping (illustrated in Figure 15). Group I impurities such as K_{Ga}, Na_{Ga}, and Li_{Ga} have high formation and ionization energies, making them unsuitable for p-type doping (Neugebauer and Van de Walle 1999).

Regarding wurzite AlN, C on N site acceptor level is found at 400 meV, whereas Mg on Al site is the best candidate for p-type conductivity (Francis and Worrell 1976). The ionization energy of Mg acceptor in p-type $Al_xGa_{1-x}N$ increases with the concentration of Al, impacting the UV-LED efficiency due to a low conductivity of Mg-doped p-$Al_xGa_{1-x}N$. For Mg-doped AlN layers, the acceptor level has been determined to be of 510 meV above the valence band edge in the work of Nam et al (Nam et al. 2003), and of 630 meV in the work of Taniyasu et al (Taniyasu et al. 2006).

In $Al_xGa_{1-x}N$ materials, acceptors require a very high activation energy, much higher than the thermal energy at room temperature. Therefore, in Mg-doped bulk $Al_xGa_{1-x}N$ layers only a small fraction, around 1% (Ploog et al. 2000), of the Mg acceptors are ionized at room temperature. The device properties of $Al_xGa_{1-x}N$ deep ultraviolet (DUV) LEDs strongly depend on the properties of the p-$Al_xGa_{1-x}N$.

1.3.2.2.3. Complexes

Hydrogen related complexes are commonly observed while synthesizing semiconductor materials in various growth techniques, in particular MOVPE. However, the residual hydrogen in the MBE chamber is also responsible for the formation of complexes in GaN and AlN material (Contreras et al. 2017).

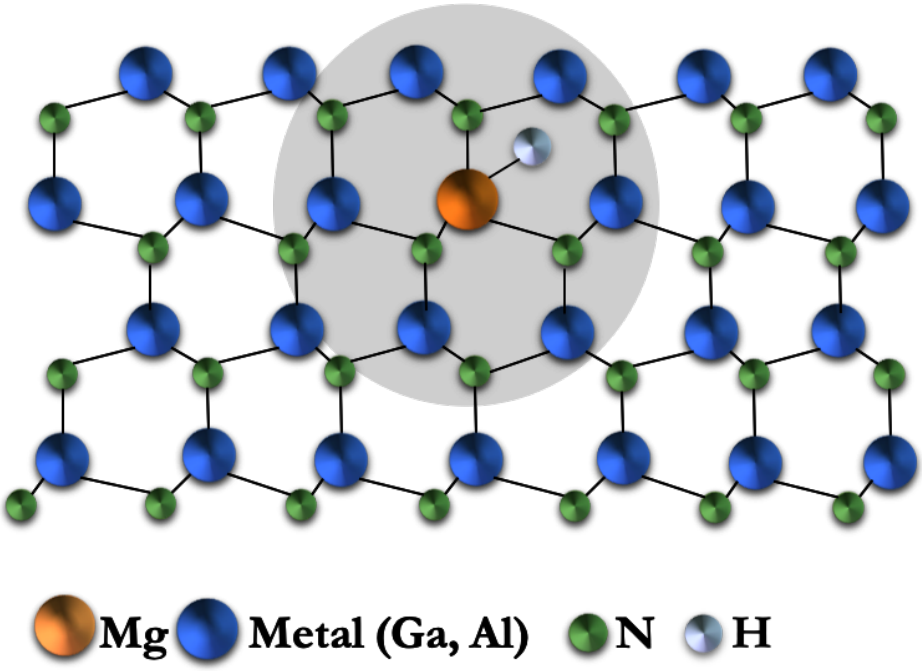

Figure 16. Mg passivated by a H atom due to complex formation in $Al_xGa_{1-x}N$ crystal lattice

The formation energies of the hydrogenated defects are often relatively lower than that of other complexes (illustration of a Mg-H complex is given in Figure 16). The complexes are either associated to Ga vacancies or related to the Mg dominant acceptor in p-type $Al_xGa_{1-x}N$. In the first case, complexes cannot dissociate during post growth thermal annealing because of the large associated binding energies, whereas the Mg–H complex dissociates, and H diffuses either to the surface or to the extended defects. The electrically neutral Mg–H complex has a binding energy of 0.7 eV, with the H atom located in an antibonding site behind the N neighbor of the acceptor (Reshchikov and Morkoç 2005).

Acceptors activation is a crucial step in obtaining p-type doping of III-nitrides. First proof of p-type conductivity in GaN material was published by Amano, Akasaki et al in 1989 (Amano et al. 1989; Isamu Akasaki et al. 1991). The Mg activation was achieved by low energy electron beam irradiation (LEEBI) and was further confirmed in the work of Nakamura et al (Nakamura et al. 1992b) by thermal annealing, a much easier method. Annealing of p-type GaN is done under N_2 atmosphere, at temperatures above 700°C, allowing the Mg-H complex bond breaking. For AlN, the activation mechanisms were not very well studied in the literature. The three researchers (Hiroshi Amano, Isamu Akasaki and Shuji Nakamura) were distinguished in 2014 with the Nobel prize for physics for their major discoveries regarding p-type dopant activation in the field of visible LEDs. Mg efficient incorporation and acceptor activation in AlN NWs will be discussed in Chapter 4 of this manuscript.

1.3.2.3. Optical transitions

Different transitions are taking place in a semiconductor material once excited with a beam of photons or electrons. The incident particle having an energy higher than the band gap, transfers it to electrons from the valence band exciting them to higher energy levels in the conduction band, creating a hole instead. Different types of recombination are possible after thermalizing, either radiative or non-radiative.

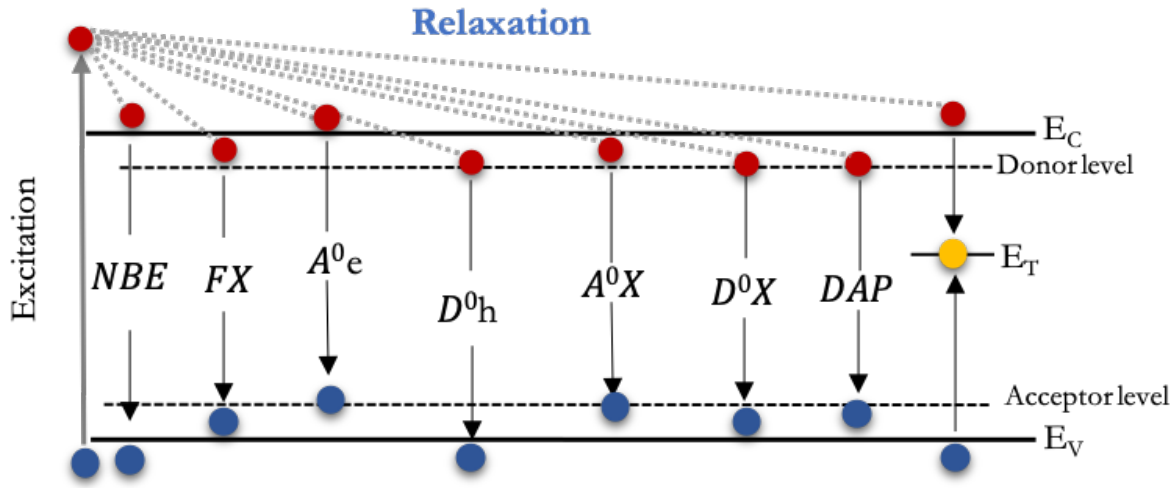

Figure 17. Optical radiative transitions in a nitride semiconductor material.

The main optical transitions taking place in the nitrides are illustrated in Figure 17.

- **NBE - near band edge transition:** corresponding to the direct recombination of an electron from the conduction band with a hole from the valence band of energy:

$$E_{NBE} = E_g + \frac{k_b T}{2} \quad (3)$$

With E_{NBE} the near band edge transition energy, T the temperature (K) and k_b the Boltzmann constant (1.380649×10^{-23} JK^{-1}).

- **FX - free exciton transition:** After thermalizing to lower energy levels in the valence band, the electron loses energy by phonon emission and interacts with a hole by coulombian interaction to form a new quasiparticle called exciton, with a binding energy E_X. The exciton is delocalized within the material diffusing until recombination, for which the energy is given by:

$$E_{FX} = E_g - E_X \quad (4)$$

With E_{FX} the free exciton energy, E_g the gap energy, E_X the exciton binding energy.

- **A^0e and D^0h - free to bound transitions**: correspond to a neutral acceptor or donor recombining to a free opposite charge of transition energy:

$$E_{A^0e,D^0h} = E_g - E_{A,D} + \frac{k_b T}{2} \quad (5)$$

With E_{A^0e,D^0h} the free to bound transition energy, $E_{A,D}$ the ionization energy of acceptors or donors respectively.

D°X and A°X - Donor and acceptor exciton transition: formed by linking to impurities introduced in the material in order to form complexes and minimize the energy of the system. If the level introduced in the band gap of the material is closer to the conduction band then it is called a donor D°X whereas if it is closer to the valence band it is an acceptor A°X. Their emission energy can be determined by:

$$E_{D^0X,A^0X} = E_g - E_X - E_B \quad (6)$$

With E_{D^0X,A^0X} the donor/acceptor to exciton transition energy and E_B the localization energy of exciton on the impurity.

DAP - Donor-acceptor pair transitions: correspond to the recombination between a neutral donor and a neutral acceptor by wave function recovering, with an energy emission depending on their binding energies and on the distance between the donor and acceptor by the coulombian interaction:

$$E_{DAP} = E_g - E_D - E_A + \frac{q^2}{4\pi\varepsilon R} \quad (7)$$

With E_{DAP} the donor-acceptor transition energy, q the elementary electric charge (1.602×10^{-19} C), R the distance between the donor and the acceptor (m), ε the dielectric permittivity of the material ($\varepsilon = \varepsilon_0\varepsilon_r$ where ε_0 =8.854×10^{-12} F.m^{-1} is the dielectric permittivity of vacuum).

Deep level transitions: radiative transitions with deep levels introduced by the impurities in the band gap of the material, usually assigned to complexes of defects and impurities or attributed to complexes formed with vacancies.

Luminescence is used to detect and characterize point defects and stacking faults, as well as various material properties such as crystalline quality, purity or chemical composition in the case of ternary alloys. However, this characterization technique highly depends on temperature, strain and excitation intensity. The surface and structural defects introduce atypical luminescence lines.

Extended defects, such as dislocations, clusters, domains or voids do not contribute to the luminescence, but affect the optical and electrical properties by trapping carriers or gettering the point defects. Threading dislocations behave as deep donors in n-type material and deep acceptors in p-type material, but they are non-radiative recombination centers and do not contribute to luminescence (Wright and Grossner 1998). However, point defects (Ga vacancies, complexes, O_N) can be trapped within them due to the large stress fields near the dislocations, and manifest in luminescence experiments, shifting the spectral line compared to point defects (Elsner et al. 1998). During growth it is thus important to reduce as much as possible all sources of defects in the active region of optical devices.

1.4. Light emitting diodes physics

After discussing the n and p type doping of $Al_xGa_{1-x}N$ material, we will now focus on the physics behind light emitting diodes. Since the main equations have been established in several books and lectures, we will recall in this work the main equations that allow an easy understanding of the future work. For more information, one can refer to the reference book (Schubert 2006).

Under equilibrium conditions, the law of mass action for a semiconductor material relates equilibrium hole concentration p_0 and electron concentration n_0 to the intrinsic carrier concentration n_i, by the law:

$$n_0 p_0 = n_i^2 \quad (8)$$

When injecting a current or exciting with light a semiconductor, excess carriers can be generated. The free electron (hole) concentration $n\ (p)$ in a semiconductor is then the sum of free electron (hole) concentration at equilibrium $n_0\ (p_0)$ and an excess electron (hole) concentration $(\Delta n, \Delta p)$. We establish the equations:

$$n = n_0 + \Delta n \quad (9)$$

$$p = p_0 + \Delta p \quad (10)$$

If considering an ideal case of fully ionized dopants at equilibrium, the free carrier concentration N_D and N_A are n_0 and p_0, respectively (Schubert 2006).

$$N_D = n_0 \quad (11)$$

$$N_A = p_0 \quad (12)$$

1.4.1. Recombination rate in a semiconductor

1.4.1.1. General case

Minority carriers of a given lifetime (τ) recombine over a distance of the order of the diffusion length L, leading to light emission. The recombination rate R at which an electron recombines with a hole can be seen as the rate at which the carrier concentration decreases. Since the number of recombination events depends proportionally to the probability of holes and electrons to recombine, we can express the recombination rate by:

$$R = -\frac{dn}{dt} = -\frac{dp}{dt} = B \times n \times p \quad (13)$$

With B the bimolecular recombination coefficient ($cm^3.s^{-1}$) with typical values comprised between 10^{-11} and 10^{-9} cm^3s^{-1} for $Al_xGa_{1-x}N$ semiconductors (Dmitriev and Oruzheinikov 1996; Ban et al. 2011). Here, n is the free electron concentration (cm^{-3}) and p is the free hole concentration (cm^{-3}).

Recombination processes in a semiconductor can be either radiative, i.e. resulting in a photon emission of energy equal to the band gap energy of the semiconductor and contributing to

the luminescence, or non-radiative, i.e. the electron energy is converted to vibrational energy of phonons.

The hole mobility being lower than the electron mobility, the electron injection coefficient in the p-type region is predominant with respect to the hole injection coefficient in the n-type region. Generally, the p-type region is more radiative than the n-type region. Moreover, to increase the emission intensity, a high doping is required in p and n type regions of the junction, favoring the electron injection.

The carrier distribution is dependent on the diffusion constant of the carriers (D_n and D_p) in the n and p-type regions of the material respectively, which can be extracted from the electron (hole) mobility μ_n (μ_p) by the Einstein relations:

$$D_n = \frac{k_b T}{q}\mu_n \quad (14)$$

$$D_p = \frac{k_b T}{q}\mu_p \quad (15)$$

With k_b the Boltzmann constant (1.380649×10^{-23} J.K^{-1}), T the temperature (K), q the elementary electric charge (1.602×10^{-19} C), μ_n (μ_p) the mobilities of electrons (holes)(cm^2.V^{-1}.s^{-1}). Experimentally, these values can be determined by Hall effect experiments.

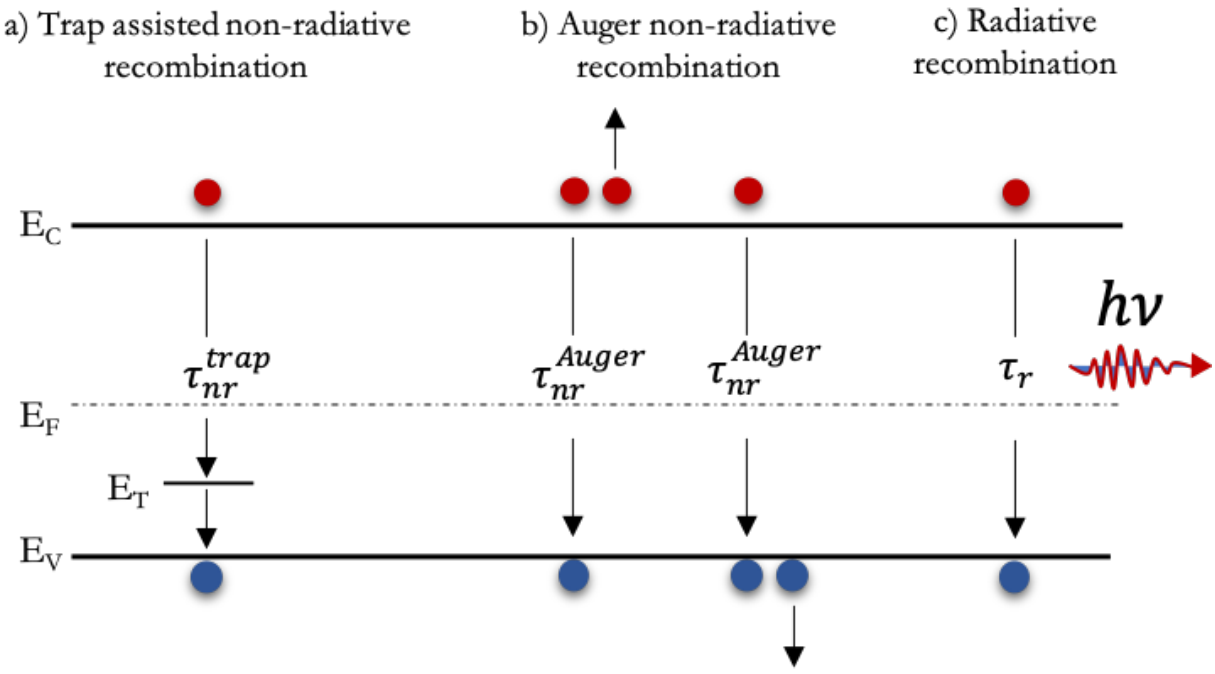

Figure 18. Recombination types in a semiconductor. a) Trap-assisted non-radiative recombination. b) Auger recombination. c) Radiative electron-hole recombination.

The three main recombination mechanisms are illustrated in Figure 18. The equations are given for a p-type semiconductor, but still hold true in the case of a n-type semiconductor, by replacing $\Delta n(t)$ with $\Delta p(t)$ and Δn_0 by Δp_0, respectively:

- **Radiative recombination** of an electron and a hole with emission of a photon of energy equal to that of the band gap. However, if subjected to an external excitation, the recombination rate gives:

$$R = B \times (n_0 + \Delta n(t)) \times (p_0 + \Delta p(t)) \quad (16)$$

With $\Delta n(t)$ and $\Delta p(t)$ the time dependent electron and hole excess concentrations.

We distinguish between:

  - radiative recombination for **low level excitation** (generated excess carrier concentration smaller than majority carriers at equilibrium $\Delta n \ll n_0 + p_0$) for which the recombination rate reads:

$$R = Bn_i^2 + B(n_0 + p_0)\Delta n(t) = R_0 + R_{excess} \quad (17)$$

With R_0 the equilibrium recombination rate and R_{excess} the excess recombination rate.

After ceasing the photoexcitation, the minority carrier concentration decays exponentially during a certain time (minority carrier lifetime):

$$\Delta n(t) = \Delta n_0 \exp(-B(n_0 + p_0)t) \quad (18)$$

The carrier lifetime in a semiconductor is defined as the mean time between generation and recombination of minority carriers and is expressed as:

$$\tau = \frac{1}{B \times (n_0 + p_0)} \quad (19)$$

The majority carriers still recombine, but for low level excitation lifetimes can be considered infinitely long, without impacting the overall recombination.

  - radiative recombination for **high level excitation** (generated excess carrier concentration larger than equilibrium carrier concentration $\Delta n \gg n_0 + p_0$) for which the recombination rate reads:

$$R = -B\Delta n^2 \quad (20)$$

Thus, the carrier concentration decays non-exponentially with time, the carrier concentration being obtained from the equation by the initial conditions $\Delta n(0) = \Delta n_0$:

$$\Delta n(t) = \frac{1}{Bt + \Delta n_0^{-1}} \quad (21)$$

The time constant (carrier lifetime) can be determined by the slope of the decay and reads:

$$\tau(t) = \mathrm{t} + \frac{1}{B\Delta n_0} \quad (22)$$

This shows that the minority carrier lifetime at high excitation levels increases with time, low level excitation conditions being reached after a certain time during the experiments.

Low level excitation is thus favorable for the measurement of the minority carrier lifetime.

- **Auger recombination**: the energy generated following an electron-hole recombination is dissipated through the excitation of an electron into the conduction band or a hole in the valence band, followed by a phonon emission. This mechanism reduces the luminescence efficiency in semiconductors at very high injection currents or very high excitation intensity. The recombination rates are related to the n and p carrier concentrations in the material, since both electron and holes are needed for this process to occur.

$$R_{Auger} = \mathrm{C_p} n p^2 \tag{23}$$

$$R_{Auger} = \mathrm{C_n} n^2 p \tag{24}$$

The C_p and C_n are the Auger coefficients (of unit cm^6s^{-1}) which depend on the band structure of the semiconductor. The Auger recombination lifetime can be determined from the Auger recombination rate and is:

$$\tau_{Auger} = \frac{\Delta n}{R_{Auger}} = \frac{1}{\mathrm{C_n} n^2 + 2n_\mathrm{i}^2(\mathrm{C_n} + \mathrm{C_p}) + \mathrm{C_p} p^2} \tag{25}$$

- **Trap-assisted recombination (Schokley-Read-Hall recombination)**: is a non-radiative recombination mechanism due to the presence of defects in a material, such as dislocations, point defects, complex formation and native defects (vacancies, interstitials or antisite defects) presenting energy levels within the forbidden gap of the semiconductor. The recombination rate is:

$$R_{trap}{}^{p} = An \tag{26}$$

$$R_{trap}{}^{n} = Ap \tag{27}$$

With $R_{trap}{}^{p}$ ($R_{trap}{}^{n}$) the recombination rate through deep levels for holes (electrons) and A the trap recombination coefficient (s^{-1}). The SRH recombination lifetime is expressed as:

$$\tau_{SRH} = \frac{p_0 \Delta n + n_0 \Delta p + \Delta n \Delta p}{(N_T v_p \sigma_\mathrm{p})^{-1}(n_0 + n_1 + \Delta n) + (N_T v_n \sigma_n)^{-1}(p_0 + p_1 + \Delta \mathrm{p})} \tag{28}$$

With N_T the trap concentration, $v_p(v_n)$ the hole and electron thermal velocities, $\sigma_\mathrm{p}(\sigma_n)$ the capture cross section of traps and n_1 and p_1 the electron and hole concentration if the trap level is located at the Fermi level.

It is important to note that generally, most deep-level transitions are non-radiative, but in some cases, there are some exceptions. Deep level luminescence occurs in III-N semiconductors with lower emission energy than the band gap of the semiconductor.

The radiative and non-radiative recombination are in competition in a semiconductor material. Even if non-radiative recombination can be limited by improving the material quality, it cannot be fully eliminated. The carrier lifetime in the bulk semiconductor (τ_{bulk}) is thus defined by considering the contributions from radiative and non-radiative recombination, respectively:

$$\frac{1}{\tau_{bulk}} = \frac{1}{\tau_r} + \frac{1}{\tau_{Auger}} + \frac{1}{\tau_{SRH}} \quad (29)$$

1.4.1.2. Nanowires case

The presence of surfaces and interfaces in a semiconductor device has a detrimental influence on the carrier lifetime. Dangling bonds at the surface of the semiconductors may form bonds with neighboring atoms in the same surface, introducing additional energy states that act as non-radiative recombination centers. Minority carriers arriving at the surface will recombine, decreasing the luminescence efficiency and heating the surface.

The effect of surface recombination introduces an additional second contribution to the recombination rate:

$$\frac{1}{\tau} = \frac{1}{\tau_{bulk}} + \frac{\kappa S}{d} \quad (30)$$

With S the surface/interface recombination velocity (cm.s^{-1}), d the layer/wire thickness (nm) and κ is the surface coefficient (no unit) (Sproul 1994; Schroder 2015). The minority carrier lifetime is thus dependent on the geometrical parameters of the structures.

Surface recombination can be limited by surface passivation.

1.4.2. *pn* junction diodes characteristics

The main function of a LED device is to convert electrical energy injected in the structure into light. The most basic structure of a LED is a *pn* junction. A typical *pn* homojunction band diagram is shown in Figure 19a, with an acceptor concentration N_A and a donor concentration N_D in the p and n parts respectively. We define the forward bias (or direct polarization) as the positive bias applied on the p-type of a *pn* junction (Schroder 2015).

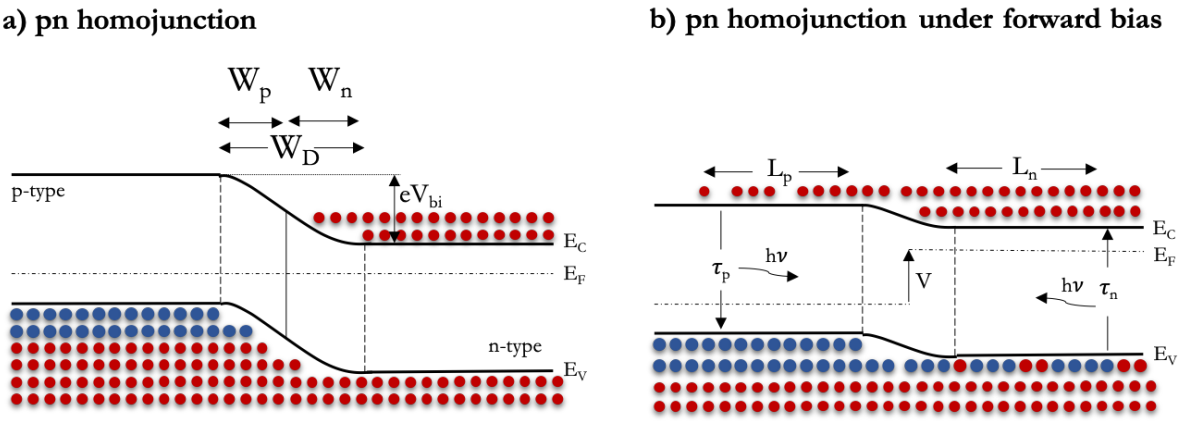

Figure 19. a) pn homojunction band diagram without bias. b) pn homojunction band diagram under forward bias V_{bias}.

Under equilibrium, the Fermi level in the n and in the p-type parts of the junction is constant, with a space charge region width W_D depleted of free carriers, defined by electrons originating from donors diffusing from the n part of the junction on the p side, of width W_p, and inversely, by holes diffusing on the n-side, of width W_n. The built-in potential V_{bi} created by the free charges at the space charge region is the barrier potential that carriers must overcome in order to reach the neutral region of opposite conductivity type. By using Poisson equations, the expressions of the built-in potential V_{bi} and space charge region width W_D can be derived as:

$$V_{bi} = \frac{k_b T}{q} \ln\left(\frac{N_A N_D}{n_i^2}\right) \quad (31)$$

$$W_D = W_p + W_n = \sqrt{\frac{\varepsilon_0 \varepsilon_r}{q}(V_{bi} - V)\left(\frac{1}{N_A} + \frac{1}{N_D}\right)} \quad (32)$$

Where q the elementary electric charge (1.602×10^{-19} C), n_i is the intrinsic carrier density of the semiconductor, V is the applied voltage across the terminals of the diode, $\varepsilon_0\varepsilon_r$ is the dielectric permittivity of the material with ε_0 =8.854×10^{-12} F.m^{-1} the dielectric permittivity of vacuum, k_b the Boltzmann constant (1.380649×10^{-23} J.K^{-1}), N_A the acceptors concentration and N_D the donors concentration (cm^{-3}), T is the absolute temperature (K). At the room temperature of 300 K, $\frac{k_b T}{q}$ value is known as the thermal voltage and is equivalent to 25.85 mV.

The space charge region extension on p and on the n sides is related to the doping levels following the neutrality equation:

$$N_A W_p = N_D W_n \quad (33)$$

1.4.2.1. Ideal diode behavior

By applying a forward bias on the junction, minority carriers are injected (Figure 19b). An excess of carriers over their equilibrium intrinsic values, $np > n_i^2$, is accumulating at the vicinity of the junction. The depletion region being highly resistive, the voltage applied on the *pn* junction is going to decrease (increase) the *pn* junction barrier in forward (reverse) bias.

1.4.2.1.1. Case of forward bias:

By injecting electrons in the p-type region or holes in the n-type region, they become in excess at thermodynamic equilibrium. The electrons are diffusing over an average length called L_p into the p-type region and are recombining with holes, emitting photons. Same mechanism can be observed for holes diffusing in the n-type region over a diffusion length L_n. This diffusion length (m) is directly dependent on the diffusion coefficient of the material as well as on the lifetime of minority carriers:

$$L_n = \sqrt{\tau_n D_n} \tag{34}$$

$$L_p = \sqrt{\tau_p D_p} \tag{35}$$

The current density (A.cm^{-2}) generated in the n and p type regions $j_n(x_p)$ and $j_p(x_n)$ is defined by the Shockley equation in the n and p parts of the junction respectively:

$$j_p(x_n) = \frac{qn_i^2 D_n}{N_D L_n}(e^{\frac{qV}{k_b T}} - 1) \tag{36}$$

$$j_n(x_p) = \frac{qn_i^2 D_p}{N_A L_p}(e^{\frac{qV}{k_b T}} - 1) \tag{37}$$

For ideal diodes, the expression for the total current density variation J (A.cm^{-2}) under a given bias is:

$$J = j_p(x_n) + j_n(x_p) = \frac{qn_i^2 D_n}{N_D L_n}\left(e^{\frac{qV}{k_b T}} - 1\right) + \frac{qn_i^2 D_p}{N_A L_p}(e^{\frac{qV}{k_b T}} - 1) \tag{38}$$

$$J = \left(\frac{qn_i^2 D_n}{N_D L_n} + \frac{qn_i^2 D_p}{N_A L_p}\right)(e^{\frac{qV}{k_b T}} - 1) = J_0(e^{\frac{qV}{k_b T}} - 1) \tag{39}$$

If considering a diode of surface A (cm^{-2}), the current is defined as:

$$I = AJ_0(e^{\frac{qV}{k_b T}} - 1) = I_0(e^{\frac{qV}{k_b T}} - 1) \tag{40}$$

1.4.2.1.2. Case of reverse bias:

In reverse bias, electrons are injected in the n-type region and holes in the p-type region. A saturation current I_S is attained, defined by:

$$I_S = A\left(\frac{qn_i^2 D_n}{N_D L_n} + \frac{qn_i^2 D_p}{N_A L_p}\right) \quad (41)$$

The current is strongly increasing while the diode voltage approaches the diffusion voltage V_{bi}. This value is called the threshold voltage and for highly doped semiconductors, it can be approximated to the band gap energy potential:

$$V_{bi} \approx V_{th} \approx \frac{E_g}{q} \quad (42)$$

Also, since usually the bias voltage is higher than the thermal voltage, the Shockley equation finally becomes:

$$I = I_S e^{\frac{qV - E_g}{k_b T}} \quad (43)$$

1.4.2.2. Real diode behavior

The above considerations hold true for an ideal diode. In the case of real diodes, a couple of parameters have to be considered, coming from parasitic effects caused by device characteristics and quality of the material. The I-V plot of a real diode with respect to an ideal diode is represented in Figure 20 for a GaAs diode at room temperature (taken from (Schubert 2006))

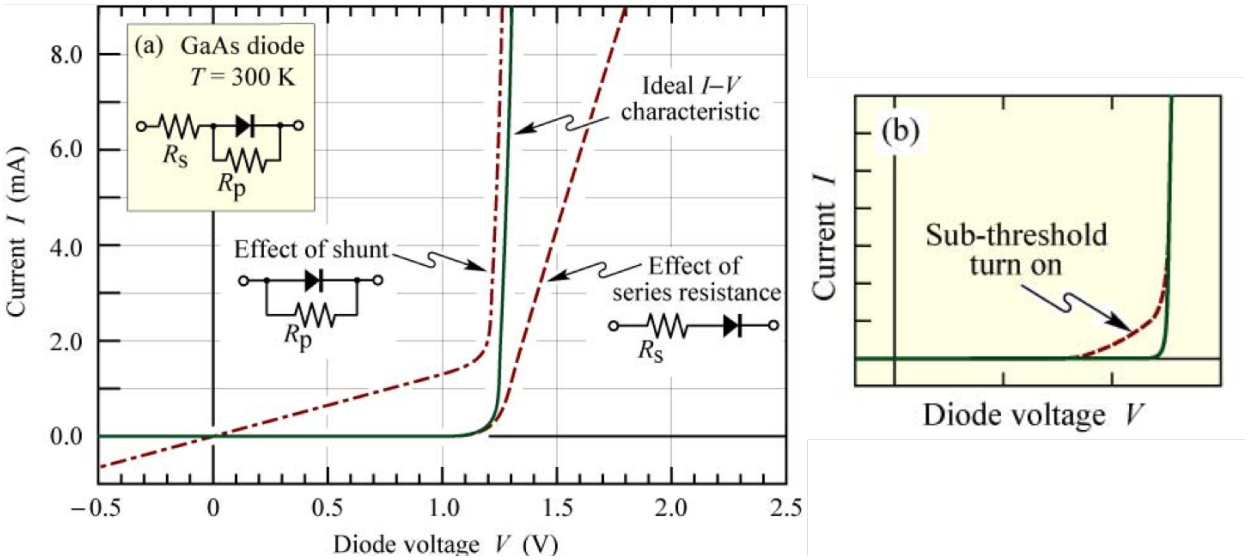

Figure 20. Ideal versus real diode current voltage characteristics (example of a GaAs diode)(Schubert 2006).

- **Ideality factor η_{ideal}:** the behavior of a diode from an ideal case is quantified by the ideality factor which usually takes values between 1 and 2. This factor is related to the quality of the device and characterizes the over-all diode behavior with respect to the ideality.

- **Parasitic resistances**: two types of resistances have to be considered when working with diodes:
    - Series resistance: coming from an unoptimized ohmic contact or from the neutral region resistance due to a low carrier concentration or low carrier mobilities;
    - Parallel (shunt) resistance: coming from any channel by-passing the *pn* junction such as damaged regions or surface imperfections.

Therefore, the Shockley equation (43) for a real diode, including η_{ideal} ideality factor, a parallel resistance R_p and a series resistance R_S becomes:

$$I - \frac{(V - IR_S)}{R_p} = I_S e^{\frac{q(V-IR_s)}{\eta_{ideal} k_b T}} \quad (44)$$

From this expression, the series resistance R_s can be calculated at high voltage ($V > \frac{E_g}{q}$), whereas the parallel resistance R_p is usually calculated near the origin, ($V \ll \frac{E_g}{q}$), where the *pn* junction current can be neglected:

$$R_S = \left.\frac{dV}{dI}\right|_{high\ voltage} \quad (45)$$

$$R_p = \left.\frac{dV}{dI}\right|_{near\ origin} \quad (46)$$

One important aspect that has to be considered when working with diodes is the diode voltage. From the conservation of energy, the energy of an injected electron into the *pn* junction is equal to the optical energy of a photon coming from the electron-hole recombination. Thus, the diode voltage normally equals the band gap energy divided by the elementary charge.

$$h\nu \approx E_g = \mathrm{q}V \quad (47)$$

With h the Plank constant (6.626×10^{-34} $m^2.kg.s^{-1}$) and ν the frequency of the photon (s^{-1}).

While considering the above aspects from a real diode characteristic, it is obvious that the diode voltage is slightly different due to the various mechanisms mentioned before:

- A voltage drop IR_S occurs at the series resistance and is responsible for an increase of the drive voltage;
- Conversion of carrier energy to heat and dissipation of energy by phonon emission increases the drive voltage;
- A sub-threshold turn-on voltage can be sometimes caused by carrier transport through surface states or deep levels in the bulk of the semiconductor.

1.4.2.3. Heterojunctions and carrier confinement

LEDs are usually fabricated by using heterostructures, that is, two type material semiconductors, a wide band gap barrier region (e.g. AlN) and a low band gap active region (e.g. GaN).

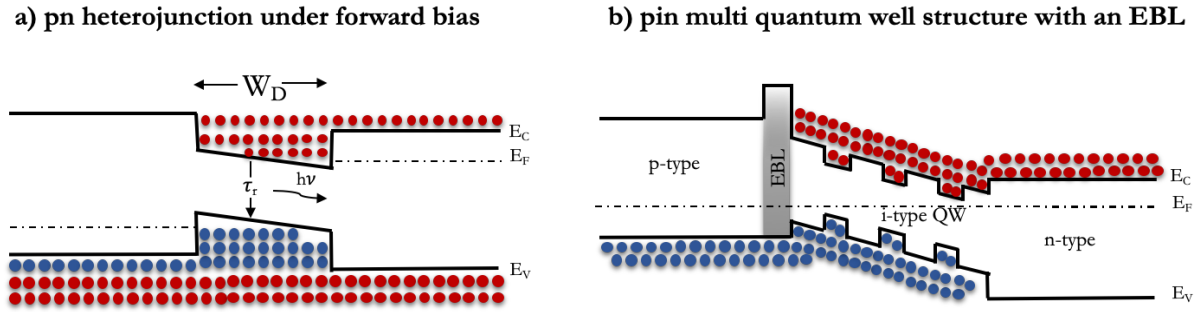

Figure 21. a) Heterojunction under forward bias and b) pin multi-quantum well structure with an EBL.

The confinement of carriers by using a heterojunction in the design of the active region represents a good way of increasing the recombination rates, of decreasing the recombination lifetime and thus yielding a higher efficiency.

By using an undoped layer bound between layers of opposite types, a double-heterojunction design known as *pin* junction (Figure 21a) is formed. The electron-hole recombination length will no longer be defined by the diffusion lengths, since carriers injected into the active region will be confined by the heterojunction barriers. The high carrier density in the active region of a double heterojunction yields higher radiative recombination and lower recombination lifetime than in the case of a homojunction.

Furthermore, the use of quantum wells increases even more the carrier densities, improving the efficiency of a LED such as in the case of a multi QW heterojunction illustrated in Figure 21b.

1.4.2.4. Nanowire *pn* junction

One dimensional nanowire offers several advantages with respect to other material systems, such as carrier confinement in two directions, and, simultaneously, strain relaxation in the axial direction, allowing for a more efficient light emission as well as charge transportation.

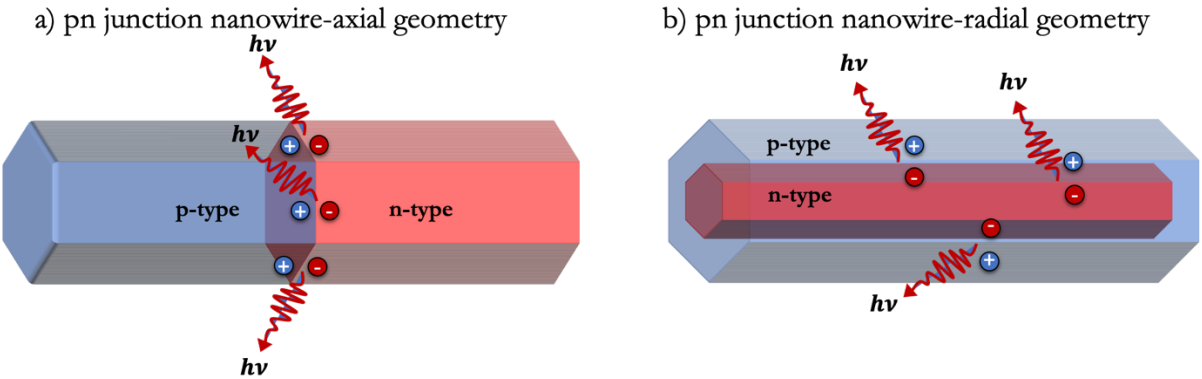

Figure 22. a) Axial and b) radial geometry nanowire pn junction.

Multiple homo and heterojunctions can be synthesized within the nanowires, increasing the optoelectrical properties. Nanowire based junctions generally present two geometries, either axial

(Figure 22a), following the growth direction or radial, more commonly known as core/shell structures, as depicted in Figure 22b. This work will be only concerning *pn* axial junctions, but further in the manuscript we will have to confront to the radial geometry of the *pn* junction.

1.4.2.5. Surface influence on transport properties

The high lateral surface of the nanowires is one of the advantages of working with these nanostructures. However, surface effects can be detrimental to the advantages induced by the high surface (for instance surface recombination or surface depletion). These effects have to be considered when evaluating the performances of UV LEDs (Qu and Duan 2012) (Calarco et al. 2011).

By considering a homogeneous doping (p-type or n-type) of a semiconductor nanowire, free carriers at the surface can be found in three different configurations presented in Figure 23 (Pernot et al. 2014).

When the surface effects are negligible, the carrier density is constant and the flat-band configuration is considered for transport inside of nanowires. The electrical conduction is comparable to that in a bulk layer.

In surface accumulation configuration, the band bending induces higher majority carrier concentration at the surface of the nanowire and an additional conduction path through the surface layer, parallel to that in the core of the nanowire.

In the case of a partially or fully depleted nanowire, the band bending induces the depletion of majority carriers at the surface of the nanowire. The electrical conduction is done through a smaller section of radius r_0 at the core of the nanowire, a full depletion leading to an insulating behavior.

The main reasons of the Fermi-level pinning in the nanowires is the interaction of majority carriers with surface states and species adsorbed at the surface of the nanowires. This creates either a depletion or an accumulation layer depending on the interacting species, but can also result from an inhomogeneous doping.

Fermi level pining and surface effects have been observed previously in GaN nanowires with the creation of a depletion layer and cannot be neglected from the interpretation of the results (Richter et al. 2008; Gurwitz and Shalish 2011; Sanford et al. 2013).

The surface effects issue can be solved by either passivation of the surfaces by chemical methods (Hanrath and Korgel 2004) or coating (Demichel et al. 2010; Dan et al. 2011). However, when working with $Al_xGa_{1-x}N$ nanowires, an AlN outer shell of higher band gap is expected to grow spontaneously, passivating the surface and avoiding surface effects in the core, leading to a better carrier confinement (Pierret et al. 2013b).

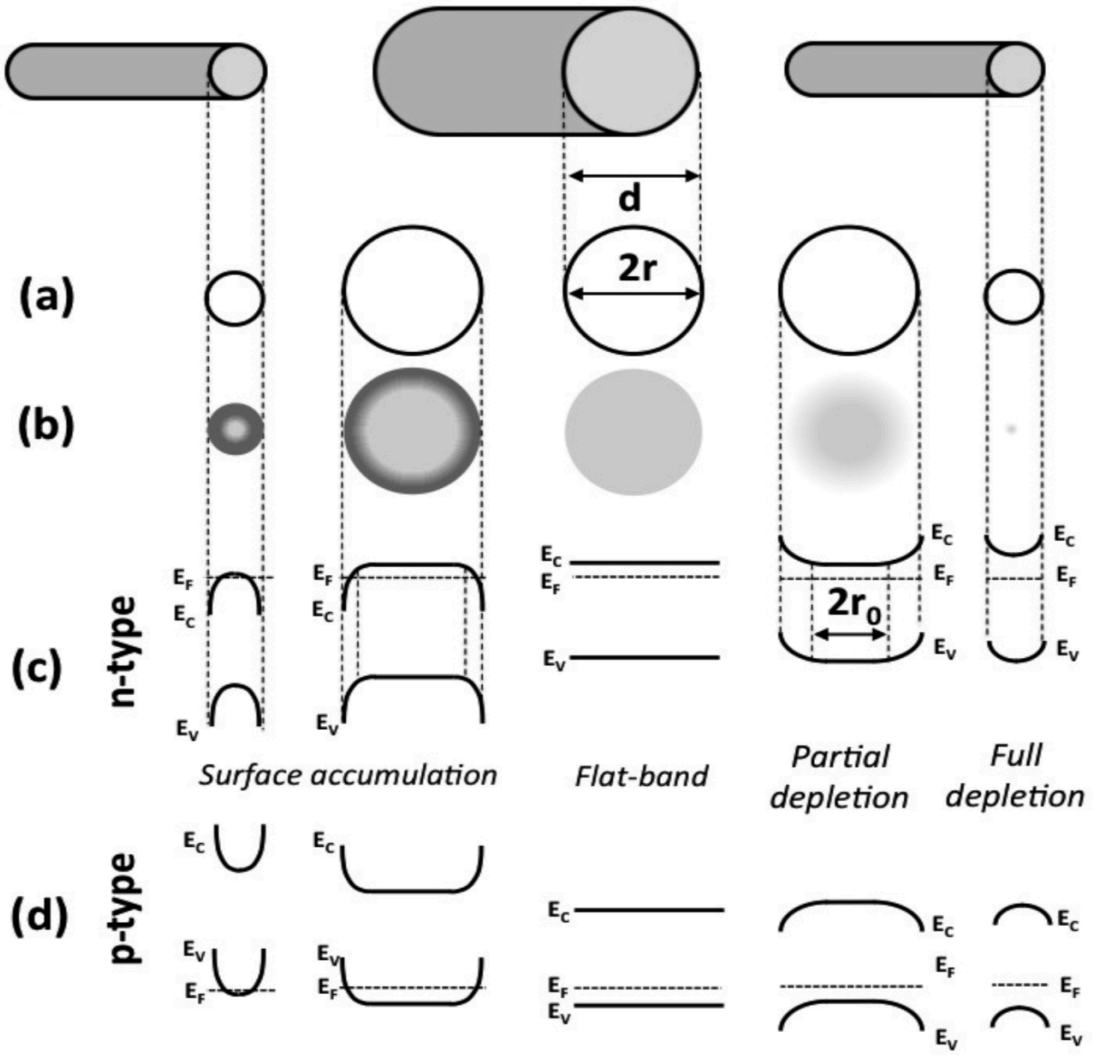

Figure 23. Band bending effects in a nanowire with different sizes: a) sections of the nanowires, b) majority carriers radial distribution and band diagram of the wires for c) n-type and d) p-type semiconductor material.

1.5. Efficiency and optimization

In view of efficiency improvement, intensive research in the field of UV-LEDs has been done recently. Major industrial actors as well as research centers have been optimizing the $Al_xGa_{1-x}N$ based UV-LEDs. Different heterostructures have been developed and optimization of stacks has led to significant improvement. Great progress has been done in the past years as far as light output power and devices efficiency is concerned (Hirayama 2018).

In this section, we recall the different terms of LED efficiency (Schubert 2006). By knowing the origins of these different terms, optimization can be made accordingly.

1.5.1. External Quantum Efficiency (EQE)

The external quantum efficiency of a diode is defined as the number of photons emitted externally from the LED over the number of carriers passing through the device. The EQE is the most important parameter when talking about light emitting devices, since the term considers the influence of the optical efficiency as well as of electrical efficiency.

The external quantum efficiency is defined as:

$$\eta_{EQE} = \frac{number\ of\ photons\ emitted\ externally}{number\ of\ carriers\ passing\ the\ junction} = \eta_{EIE} \times \eta_{IQE} \times \eta_{LEE} = \frac{\mathrm{P}/(h\nu)}{\mathrm{I}/q} \quad (48)$$

With η_{EIE} the carrier injection efficiency, η_{IQE} the internal quantum efficiency and η_{LEE} the light extraction efficiency, P the optical power emitted into free space, I the drive current, $h\nu$ the photon energy. The EQE is greatly impacted by losses during the successive functioning steps: from injection of carriers in the LED, to recombination and extraction of photons from recombined carriers.

1.5.2. Carrier Injection Efficiency (EIE)

The electrons passing through the device coming from the electrical energy have to be injected in the active region and undergo electron-holes recombination to produce photons.

$$\eta_{EIE} = \frac{number\ of\ electrons\ recombining\ in\ the\ active\ region}{number\ of\ electrons\ injected\ in\ the\ device} \quad (49)$$

The active region has to be optimized in order to confine carriers in the active region of the device and increase the electron probability to recombine. The choice of an adapted device structure and use of quantum wells for carrier confinement allow the increasing of η_{EIE}.

1.5.3. Internal Quantum Efficiency (IQE)

The internal quantum efficiency or radiative efficiency of a device, η_{IQE} is the efficiency of converting carrier current to photons.

$$\eta_{IQE} = \frac{number\ of\ photons\ emitted\ internally}{number\ of\ carriers\ passing\ the\ junction} = \frac{\tau_r^{-1}}{\tau_r^{-1} + \tau_{nr}^{-1}} = \frac{\mathrm{P_{int}}/(h\nu)}{\mathrm{I}/q} \quad (50)$$

Where τ_r is the radiative carrier recombination lifetime, τ_{nr} the non-radiative carrier recombination lifetime, P_{int} the power emitted from the active region.

The radiative and non-radiative recombination processes in a device are in competition with each other, either for band to band transitions or for transitions via traps. The η_{IQE} is related to the radiative and non-radiative recombination rates. The carrier lifetime is an important characteristic of the junction that has to be considered when improving the IQE of a device. A low radiative lifetime is necessary to yield a high IQE. The improvement of η_{IQE} can be attained by a good material quality limiting non-radiative recombination centers such as point defects or threading dislocations (Karpov and Makarov 2002; Van de Walle and Neugebauer 2004; Henry et al. 2012).

1.5.4. Light Extraction Efficiency (LEE)

When extracting light from the device, part of it is lost due to reflection inside the structure because of the difference between the refractive indices of the semiconductor and the ambient. Once created from electron-hole recombination, the photons have to escape from the crystal for a light-emitting effect. The light extraction efficiency is defined as the proportion of photons escaping from the device with respect to the photons created in the active region coming from radiative recombination.

$$\eta_{LEE} = \frac{number\ of\ photons\ extracted\ from\ the\ device}{number\ of\ photons\ emitted\ internally} = \frac{\mathrm{P}/(h\nu)}{\mathrm{P_{int}}/(h\nu)} \qquad (51)$$

The optical efficiency of the device mainly depends on the optics around and outside the device, and is not influenced by the electrical phenomena or material properties of the structures. The photonic successive internal reflections inside the structure are limiting the number of photons extracted from the device. Surface structurization allows the optimization of critical reflection angles. The substrate of the device also plays a major role for optimization of the η_{LEE}.

1.5.5. Wall Plug Efficiency (WPE)

Finally, the wall plug efficiency or power efficiency is the ratio between the optical output power over the electrical input power. Normally, the bias applied on a LED is approximately equal to the band gap energy. In a good device, the WPE is thus approximately equal to the EQE.

$$\mathrm{WPE} = \frac{P_{opt}}{IV} = \eta_{EQE} \times \frac{h\nu}{e} \qquad (52)$$

Where V is the operating voltage of the LED.

1.6. Summary of chapter 1

Chapter 1 is focused on the state-of-the-art physics behind the study and fabrication of an UV-LED. The general presentation of the III-N describes the main structural parameters for the materials under study in this manuscript: GaN and AlN, as well as on the ternary alloy $Al_xGa_{1-x}N$, crystallizing in the wurzite structure and showing a N-polarity. Then, the nanowire structures are introduced with a focus on their advantages for light extraction.

Regarding the doping of these materials, literature result shows a high ionization energy of p-type dopants in GaN and AlN material. The best candidate for p-type doping is Mg, whereas n-type doping will be done by using Si. The high Mg ionization energy and difficult incorporation and activation will be one of the main issues at stake in this manuscript.

While working with a LED, the opto-electronic transitions are of high interest. The different transitions taking place in an $Al_xGa_{1-x}N$ can result in radiative or non-radiative electron-hole recombinations. If non-radiative, these opto-electronic transitions are responsible of decreasing the IQE of LED, showing the importance of decreasing their occurrence probability. Another take-away information concerns the deep-level states in a semiconductor, introducing additional luminescence lines and trapping carriers.

I have discussed further the basics of a simple LED functioning principle and presented the general equations of a *pn* junction under bias that we will use further in the studies. Finally, I have dedicated a part of the studies to the interest of considering the surface effects on the transport mechanisms inside the nanowires and concluded with an overview of diode efficiency.

« La théorie, c'est quand on sait tout et que rien ne fonctionne… La pratique, c'est quand tout fonctionne et que personne ne sait pourquoi. »

2. Methods and experimental details

After a detailed description of the background and concepts behind the nitride materials used for the realization of DUV LEDs, the main techniques and experimental details necessary for the growth and characterization of samples are resumed in this chapter. Thus, a major part will concern the exhaustive description of the molecular beam epitaxy growth technique and experimental details, from substrate preparation to final sample. In a next stage, characterization techniques that contributed to the results presented in this PhD will be described. However, I will be mainly insisting on detailed description of the techniques I have worked with. Other characterization techniques will be more briefly presented.

2.1. Growth of III-Nitrides

III-N materials are relatively easy to synthesize. From top-down to bottom-up approach, GaN and AlN material growth has been studied ever since beginning of the 20th century. The main growth techniques mostly used today for III-N material growth will be developed further.

2.1.1. Epitaxial growth

The epitaxial growth (from the Greek "epi" = above and "taxis" = in an ordered manner), is based on growth of a crystalline material on a crystalline substrate in a defined orientation imposed by the substrate and matching of the lattice parameter at the interface. Figure 24 illustrates this principle. One differentiates between *homoepitaxy*, which consists of growing a material on top of a substrate of the same composition with a perfect lattice matching, and *heteroepitaxy* which defines the growth of a material on top of a different composition crystalline substrate with a lattice mismatch at the interface.

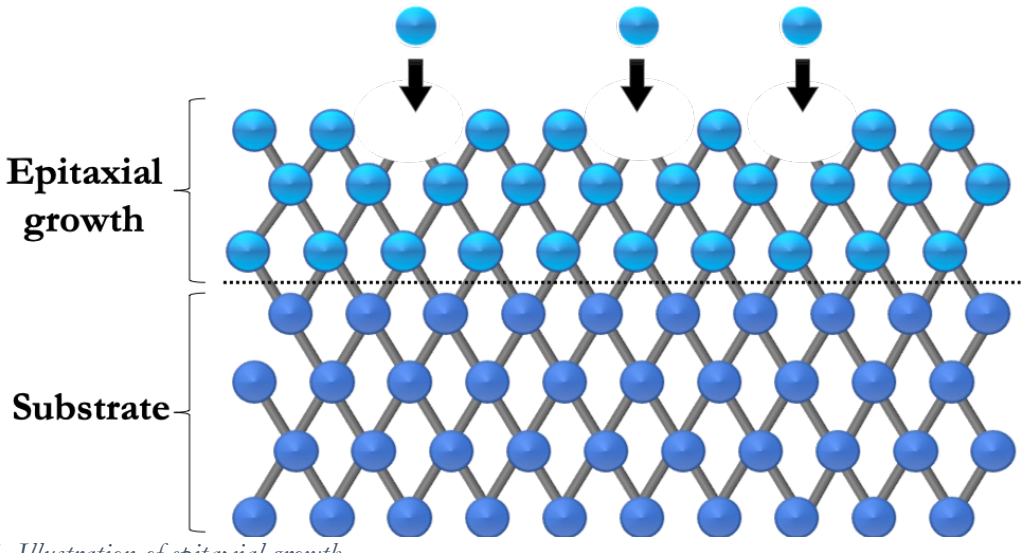

Figure 24. Illustration of epitaxial growth.

High quality material can be obtained by homoepitaxial growth, but the limitations in terms of available growth substrates have highly favored the development of heteroepitaxial growth. However, the compatibility of the substrate with the epitaxial layer is of utmost importance. Indeed, when adapting the lattice parameters of two different materials, the strain relaxation is done either elastically or plastically, introducing defects such as dislocations or cracks that affect the optoelectronic properties of the materials. Thus, the choice of growth substrate as well as of growth parameters are very important for high quality materials growth, epitaxial growth allowing a good control in terms of optical and structural properties.

2.1.2. Growth techniques

Several growth techniques are available nowadays for growth of semiconductor materials, the choice of the growth technique being for a long time a compromise between quality and cost of the final sample.

Liquid Phase Epitaxy (LPE) is a simple growth method that is based on growing a semiconductor material from melted high purity metal sources, with impressive levels of purity of the layers. However, the flexibility in terms of material types and the growth of multi-layer structures with abrupt interfaces is difficult to achieve.

Vapor Phase Epitaxy (VPE) (Stringfellow 2012) the growth species are carried by precursor gases which are either organo-metallic precursors (in the case of MOVPE) or hydrogenated precursors (Hydrogen vapor Phase Epitaxy-HVPE) to a substrate placed in an oven working at a high pressure of several hundreds of mbars (e.g., for GaN growth usually comprised between 400 mbars and atmospheric pressure), resulting in high purity materials and rather abrupt interfaces. The major advantage of MOVPE is the versatility of the technique and the suitability for large scale production, due to the rapid growth process and the ability to grow on large substrates with a high uniformity. However, there are some cons of this technique related to the hazardous precursors and limitations in terms of growth of some materials (high In content InGaN for example).

Molecular Beam Epitaxy (MBE) (Herman and Sitter 2012) growth consists of directing beam fluxes coming from elemental sources at a controlled rate onto a heated substrate, yielding highly crystalline quality materials. The nitrogen source can either be introduced by ammonia gas (NH_3-MBE) or by plasma dissociation of N_2, in which case the technique will be known as plasma-assisted MBE (PA-MBE). The ultra-high vacuum conditions (UHV) aim at obtaining a material with very low residual impurities rate. MBE was the first technique allowing the growth of perfectly abrupt superlattices. However, the low growth rate and expensive cost of growth process and machine maintenance is still one of the disadvantages for industrialization of the technique.

The latter technique was used for growth of the samples presented in this manuscript. The technique as well as the growth process and steps will be further described.

2.1.3. Description of PA-MBE growth technique

2.1.3.1. PA-MBE equipment

The MBE machine used for samples grown in our group is a MECA2000 machine produced by a French supplier for which the schematics of the main parts are illustrated in Figure 25.

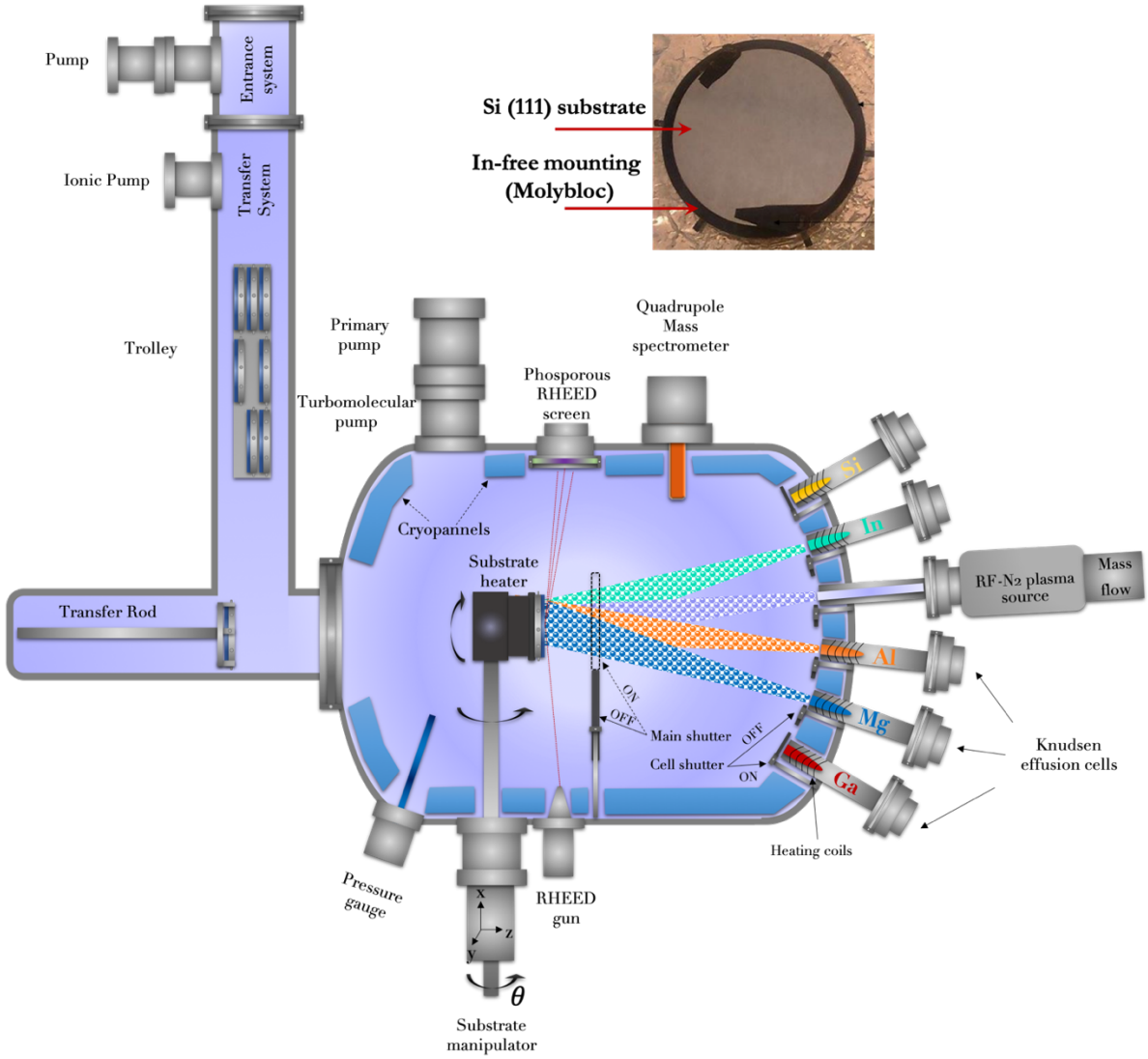

Figure 25. Illustration of the plasma-assisted MBE machine with the respective elements.

2.1.3.1.1. Pre-growth chamber system

The growth substrate is placed on a hollow 2" molybdenum sample holder called "MOLYBLOC" (the so called "In-free" mounting process). The substrate is attached to the substrate holder by 2 pins on the edge of the wafer as shown in Figure 25.

A transfer system is located prior to the chamber and avoids the change of pressure during sample transfer into the growth chamber by exchange with the atmospheric pressure. This provides a way of reducing the number of impurities introduced in the growth chamber, by pumping the air through an ionic pump, maintaining a constant pressure of around 5×10^{-9}-2×10^{-8} mbar. The sample holder is then placed on a transfer rod and then inside the growth chamber.

2.1.3.1.2. Growth chamber and vacuum conditions

The MBE growth process takes place in a chamber under ultra-high vacuum conditions, to limit incorporation of impurity. The high vacuum conditions are controlled by two pumping systems: primary pump coupled to a turbomolecular pump (1700 l.s) that allows to attain vacuum conditions of 10^{-12} up to 10^{-14} mbars depending on the pumping time. Last impurities are trapped inside the chamber by a liquid nitrogen cooling panel (cryopannel) that is also used to cool down the frame around the cells when heated up. The pressure gauge constantly registers the vacuum pressure inside the chamber for optimum vacuum conditions during growth. A Quadrupole Mass Spectrometer allows the analysis of the residual vacuum inside the chamber and identification with mass spectra of different pollutants (if present).

2.1.3.1.3. Manipulator and substrate heater

The MOLYBLOC is placed on a SiC substrate heater inside the chamber, allowing heating temperatures up to 1200°C. The manipulator allows 3-dimensional degrees of freedom allowing the exchange and alignment with the precursor cells inside the growth chamber. A central axis rotation system of the substrate heater allows the homogeneous repartition of incoming atomic beam fluxes on the substrate and plays an important role on the samples homogeneity as described further in this manuscript.

The substrate temperature is controlled through a temperature sensor (thermocouple) in contact with the rear face of the oven. For a more accurate growth temperature control, growth conditions in terms of substrate temperature are determined prior to the growth by using the characteristic desorption time of metallic adatoms (Ga) on bare Si (111) surface, probed by in-situ Reflection High Energy Electron Diffraction (RHEED)(Landré et al. 2008).

2.1.3.1.4. Knudsen cells

The precursors for MBE growth are atomic elements of high purity (6 to 8N-or 99.9999% to 99.999999%) coming from Knudsen effusion cells (shown in Figure 26), radially disposed in the chamber, so that the fluxes converge to the center of the sample. Knudsen cells are usually fit with a removable open-faced crucible made from high temperature resistant BN material. The pure metallic elements charges and crucible are heated up at very high temperature above the sublimation point of the respective elements through a resistively heated filament at a heating up rate of 20°C/min.

Thermocouples in the cell allow feedback control of temperature. Due to the high vacuum conditions, the displacement of atoms coming from the Knudsen effusion cells is in a ballistic regime characterized by a mean free path of atoms greater than 1 m, which eliminates atomic collision in the impinging beams. Limited growth rates of less than 1 monolayer per second (1 ML/s) offer the advantage of precisely controlling the thickness and interfaces of materials during MBE growth.

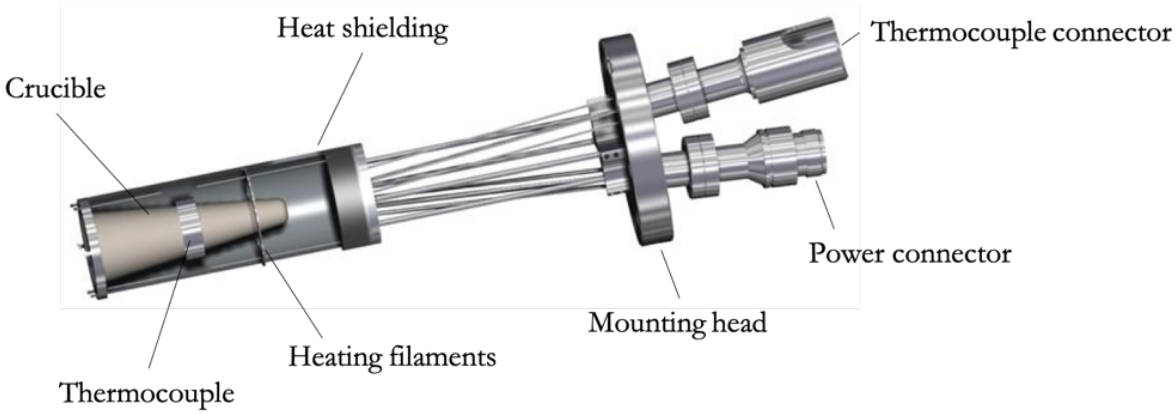

Figure 26. Knudsen cell with respective elements

Individual cell shutters allow the control of the incoming fluxes of precursors during growth and a main shutter is used to protect furthermore the substrate from residual contaminants during heating up phase. Our system is equipped with two Ga, two Al cells and one In cell for $Al_xGa_yIn_{1-x-y}N$ alloys growth and one Mg cell and one Si cell for doping of the alloys. The calibration of the Al and Ga fluxes is done by RHEED oscillations technique through analyzing the surface reflection when growing AlN and GaN layers on a bulk GaN substrate (Joyce et al. 1986). The reflection of the RHEED beam on the growing material is maximal when the last atomic layer is complete and minimal when it is partially filled, leading to oscillation periods equal to the atomic layer completion rate.

2.1.3.1.5. Nitrogen plasma source

The active nitrogen flux in our MBE machine comes from plasma dissociation of N_2 (PA-MBE) by means of radio frequency dissociation (RF PA-MBE). Only 1% of the N_2 primary flux of molecules is dissociated. Two different cells furnishing different fluxes of N_2 are mounted on our MBE system: an ADDON N_2 plasma and a High-Density Radial Source (HDRS) plasma cell designed in the University of Nagoya (Japan) and commercialized by Aakuto Company.

Depending on the plasma cell used for sample growth, the nitrogen flux is regulated through a mass flow at either 0.6 sccm with a radio frequency power of 300W corresponding to a GaN growth rate of 0.25 ML/s, or 2.5 sccm with 600W frequency power corresponding to 1ML/s growth rate, depending on the sample requirements. During growth by using a plasma N_2 source, the pressure inside the chamber rises up to 5×10^{-5} mbar, at the limit of ballistic regime.

2.1.3.1.6. Reflection High Energy Electron Diffraction

The real time in-situ structural characterization in the PA-MBE chamber during growth is done by using a RHEED-Reflection High Energy Electron Diffraction tool. The principle of RHEED technique consists of sending an electron beam emitted from a gun under high accelerating voltage (35 keV in our case) towards a substrate, with a grazing incidence of the order of 2-3°.

After multiple diffractions on the surface of the sample, the diffracted electrons form a diffraction pattern on a phosphorous screen situated on the opposite side of the gun inside the

chamber. These diffracted electrons correspond to the intersection of the surface electronic density Fourier transform with the Ewald sphere of radius $k_0 = \frac{2\pi}{\lambda}$, as illustrated in Figure 27 (Hestroffer 2012).

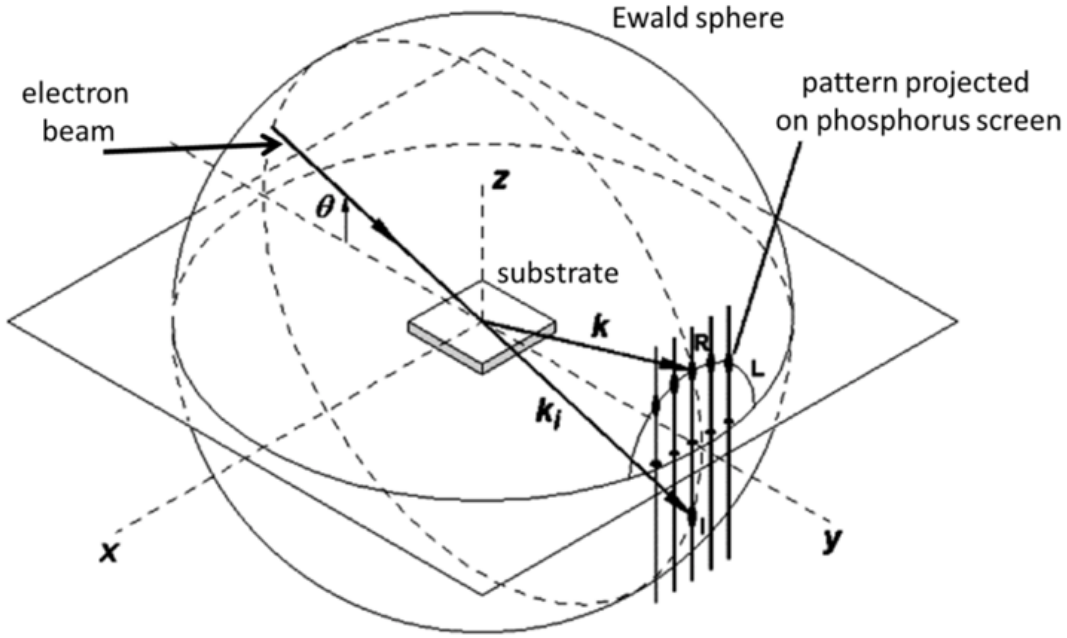

Figure 27. Ewald sphere and RHEED principle.

By interacting with the first atomic layers at the surface of the sample, the RHEED diffraction pattern gives information about the crystallographic plane arrangements, from flatness of the surface to sizes of grains and domains of surface structures, as well as about the epitaxial relationship between grown films and islands with respect to the substrate (Hasegawa 2012). This diffraction pattern is strongly related to the morphology of the samples under study, various cases being represented in Figure 28.

Thus, for an **ideal surface**, the theoretical RHEED pattern should be constituted by infinitesimal spots aligned on a radial arc (Mahan et al. 1990). Because of non-idealities of the surface and due to the fact that the beam is neither perfectly monochromatic nor punctual, the thickness of the Ewald sphere is non-zero and the reciprocal lattice of an ideal surface will be constituted by streaks.

The Ewald sphere is intersected nearly everywhere for a **polycrystal**, because all sorts of in-plane periodicities can be found due to disorder. The pattern has a ring shape and is a sign of a poor crystalline quality with different orientations of the grains.

If there are asperities on the surface of the sample such as in the case of **small surface steps**, the beam is transmitted through the asperities so the diffraction pattern is constituted of spots.

In the case of **islands** such as nanowires, additional lines appear on the RHEED pattern due to the diffraction on the island facets. The RHEED pattern in the case of a nanowires (high 3D islands) will be constituted by lengthened spots, as illustrated in Figure 28 (Nötzel et al. 1992).

One of the main advantages of the technique is that the RHEED diffracted pattern intensities and its evolution during growth can be followed in-situ thanks to a numeric camera, allowing the calibration of different parameters such as substrate temperature and atomic fluxes. The real-time evolution of the surface as well as numerical treatment of the data as registered during growth can be followed on a computer through the AnaRheed program developed in our laboratory by Yoann Curé.

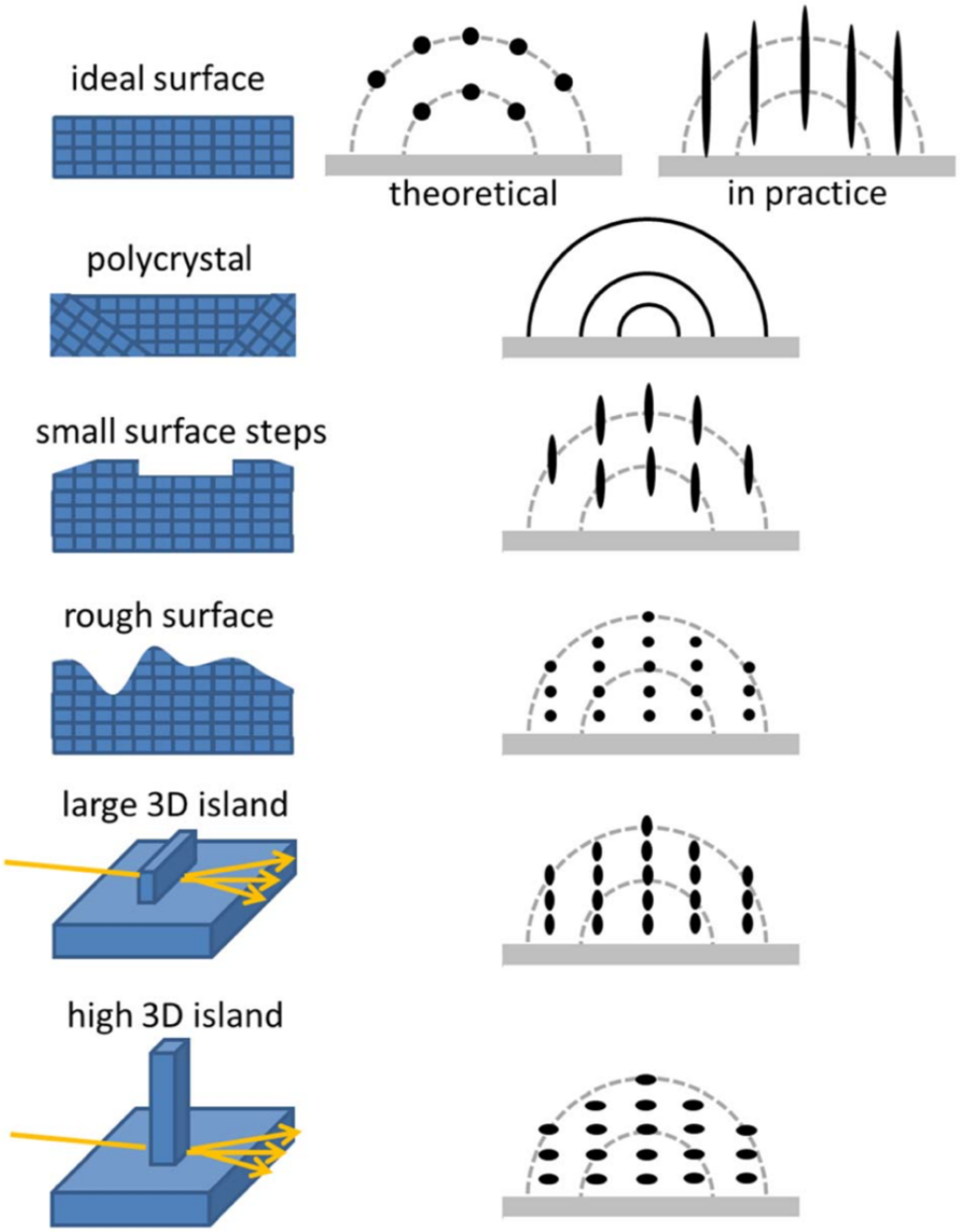

Figure 28. Typical surface morphologies and respective RHEED patterns illustrations and images (taken from (Hestroffer 2012)).

2.1.4. Growth kinetics mechanism

MBE growth conditions are far from thermodynamic equilibrium, governed especially by different kinetic parameters linked to the diffusion and desorption of species on the growth front. Preferential nucleation sites and balance of surface energy are a consequence of the tendency of minimizing the total energy of the system. The kinetic processes that govern the growth in the MBE chamber are illustrated in Figure 29 (Hestroffer 2012).

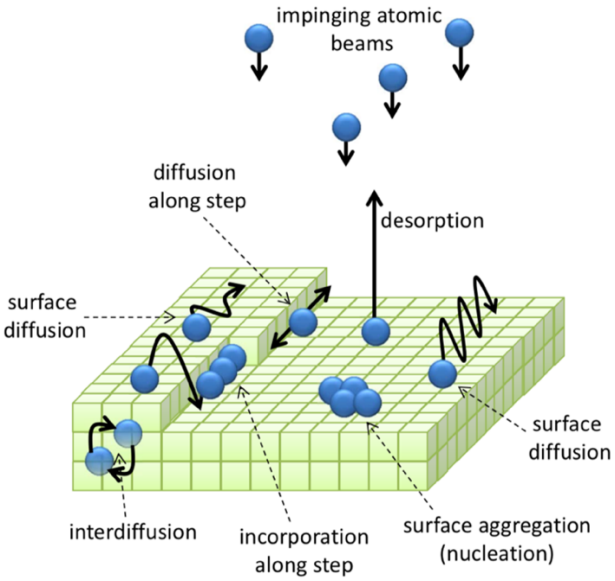

Figure 29. Illustration of processes involved in the MBE growth (Hestroffer 2012).

First, the impinging atoms arriving from molecular beam on the growth surface are physisorbed creating weak Van der Waals bonds with surface atoms. Due to the weak unstable bonds created with the substrate, the adatoms can either desorb or diffuse from the surface depending on the substrate temperature. Atoms that diffused may create chemical bonds between them and with the surface, forming a stable aggregate responsible for further nucleation of material. Following this, preferential sites are created for adatoms incorporation without formation of dislocations or stacking faults, step-edges being the preferential incorporation sites (Madhukar 1983).

Growth specific modes are defined depending on the lattice mismatch with the growth substrate, surface free energy or dislocation formation energy:

a) Frank van der Merwe: 2D growth mode in which the misfit during the growth is released by the formation of dislocations;

b) Volmer-Weber mechanism for materials having a large lattice mismatch with the growth material, the material keeping much of the surface uncovered without wetting;

c) Stranski-Krastanov growth mechanism in which the material wets the surface initially but forms 3D island after a critical height.

The energy balance of the system is responsible for the growth mode, favoring low energies of lateral facets and interfaces.

2.1.4.1. Substrate

2.1.4.1.1. Choice of substrate

As described in Chapter 1, the lattice parameter mismatch between $Al_xGa_{1-x}N$ alloy and available substrates gives place to interface dislocations that appear to relax the strain at the surface, called "misfit dislocations". In wurzite systems, threading dislocations of densities as high as 10^7-10^{10} cm^{-2}, which propagate through the whole layer are most commonly observed. Poor quality interfaces due to a large lattice mismatch influence the efficiency and optoelectronic behavior of heterostructure devices because they are preferred sites for impurities, high-diffusivity paths for dopants, and non-radiative recombination centers (Dridi et al. 2003). The ideal substrate for a heteroepitaxial growth should present a very low lattice mismatch with the grown material and similar thermal expansion coefficient allowing a large temperature range adaptability. In addition, in view of device realization, further requirements are desirable, namely a good electrical and thermal conductivity for heat dissipation, as well as substrate size availability for large scale applications. Ideally, all of these are required for a reasonable cost.

Thus, ideal substrate material candidates for $Al_xGa_{1-x}N$ growth would be AlN bulk crystals, that also present the advantage of UV transparency for UV applications (Carlos Rojo et al. 2001; Kneissl et al. 2007; Bondokov et al. 2008; Kinoshita et al. 2012). Started over 20 years ago, research on these materials intensified lately. Companies such as Crystal IS and Hexatech propose high quality 2" AlN substrates, but still with prohibitive costs for the research field.

Despite these recent developments, epitaxial growth of $Al_xGa_{1-x}N$ layers relies on foreign substrates. At this time, the main candidates for growth of III-Nitrides remain sapphire and silicon substrates.

In the case of sapphire, the (0001) orientated sapphire belongs to the most used amongst various substrates. However, the difference in lattice mismatch is of at least 14% with $Al_xGa_{1-x}N$ alloys, but the material presents good electrical insulating properties and UV transparency (Gupta et al. 2016; Huang et al. 2016; Marini et al. 2016; Sobanska et al. 2016).

Last but not least, the preferences for silicon wafers used as a substrate in the research field comes from a series of advantages of this material: ultra-high-quality wafers can be easily crystallized especially by Czochralski process for a price of as low as 25€/ 2" wafer. Moreover, doping in this type of material is perfectly controlled both for type n and p, allowing electrical conductivity with the growth material. Amongst the disadvantages of growing on Si substrate, we can mention the large thermal expansion coefficient and lattice mismatch with III- N compounds of the order of 17 % with GaN and 19 % with AlN and UV absorbance, making it unsuitable for growth of 2D layers (Reshchikov and Morkoç 2005).

In our case, all the samples will be grown on Si (111) wafer from Siltronix company, highly n-doped with either As or P atoms to ensure a resistivity lower than 0.005 Ohm.cm for electrical conductivity.

The interest of using a Si (111) material comes from the particular diamond geometry of the Si substrate (face centered cubic lattice), compatible to that of wurzite III-N materials. An epitaxial relationship is obtained when the [0001] direction of the wurzite III-N materials is collinear to the [111] direction of the Si substrate

2.1.4.1.2. Substrate preparation

The wafers used as substrates in this manuscript were cleaned prior to the growth following the same chemical procedure described hereafter. Each wafer is thoroughly cleaned for 50s in HF 10%, in order to deoxidize the SiO_2 native layer formed at the surface. The process is stopped using deionized water and then the substrate is blow-dried using nitrogen.

Once fixed on the MOLYBLOC and introduced in the growth chamber, the wafer is outgassed for at least 30 min at a temperature of 250°C in order to eliminate hydrocarbons at the surface, and then heated up to 900°C for around 1 hour (heating up time comprised) at a rate of 20°C/min, until the 7×7 Si surface reconstruction appears clear on the RHEED, an indicator of the residual SiO_2 elimination (Figure 30a).

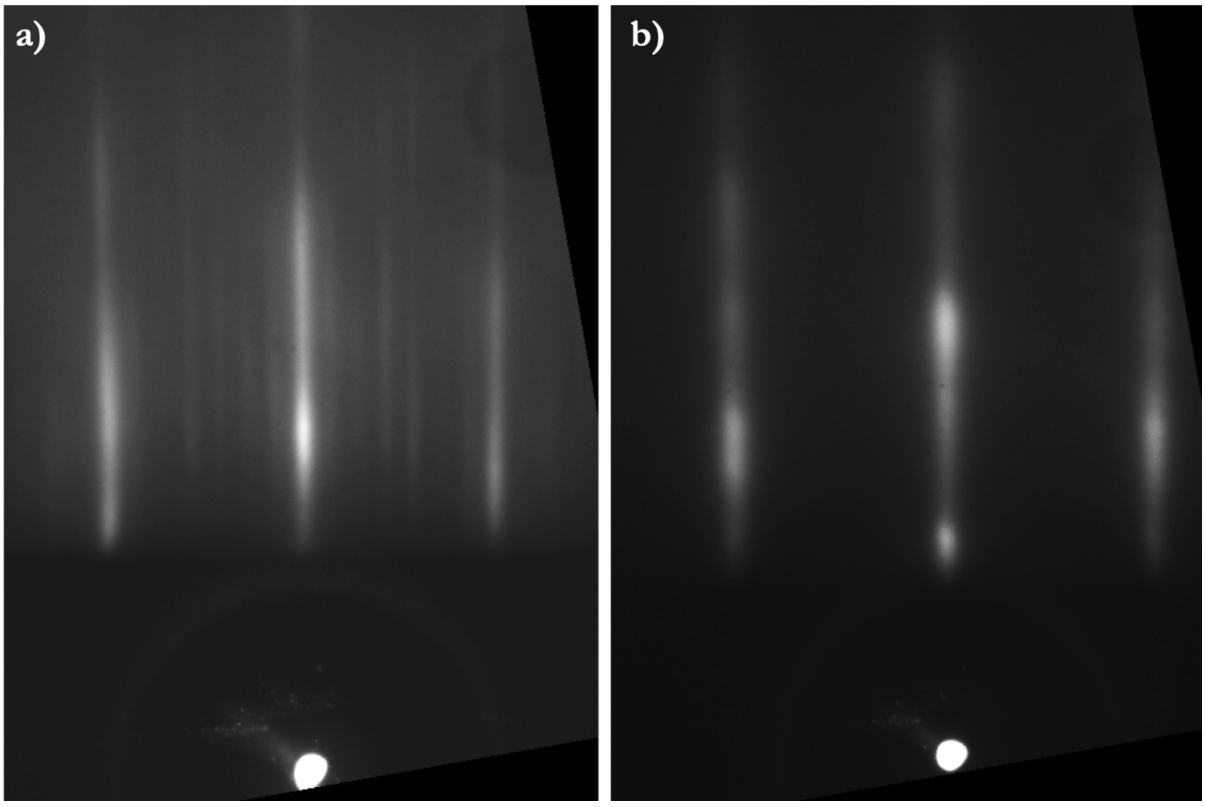

Figure 30. RHEED pattern a) before growth, Si 7×7 surface reconstruction and b) after AlN buffer growth for sample N2551 (60% $Al_xGa_{1-x}N$ NW junction)

2.1.4.2. Buffer layer

Growing a thin AlN buffer layer prior to GaN nucleation on the substrate is known to decrease defects density and increase surface smoothness as well as reduce in-plane rotation of GaN grains (Musolino et al. 2015) (avoiding in-plane tilting and twisting).

It has been previously established that the polarity pattern of an AlN buffer ensures the reproducible nucleation of nanowires as well as controls nanowire density. The buffer layer growth conditions and thickness have been adapted from the PhD of Thomas Auzelle (Auzelle 2015). For additional information about particularities of AlN buffer growth and impact on GaN NW nucleation the lecturer can refer to reference. Around 3 nm of AlN buffer layer was deposited at high Al temperature (growth rate of 0.2 ML/s) and high substrate temperature for some of the samples presented in this manuscript (when mentioned), in an Al-first growth method (Al atoms provided first followed by N atoms). The RHEED pattern after the growth of the buffer layer is presented in Figure 30b.

2.1.4.3. Nanowires growth in MBE

The growth conditions for nanowires are particular since the control of parameters such as substrate temperature or atomic beam incidence angles or III/N flux ratio define the morphology of these nanostructures as well as the limit for obtaining nanostructures instead of 2D growth. The optimized growth conditions for achieving NW structures has been defined by Fernandez-Garrido et al (Fernández-Garrido et al. 2009) in the growth diagram depicted in Figure 31, showing the influence of the substrate temperature and the III/N ratio on the nanowire's morphology.

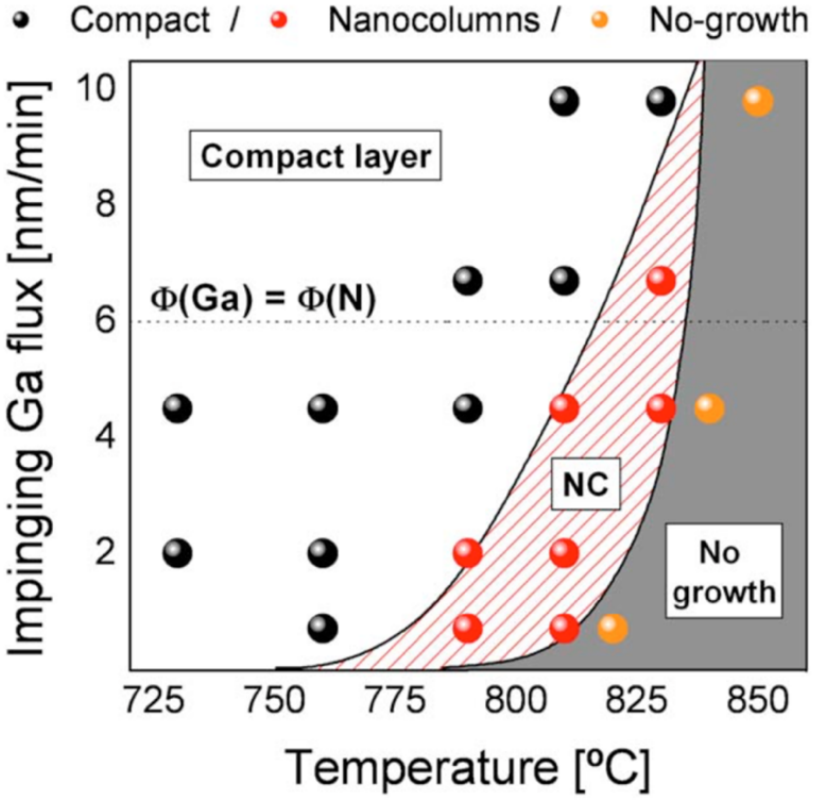

Figure 31. GaN growth conditions diagram and respective growth morphologies (Garrido et al).

It is well known that growth temperature is difficult to compare from one MBE to another. In our case, the substrate temperature for NW growth is usually comprised between 775°C and 850°C, as determined by using a thermocouple close to the rear face of the heater. At quite high temperatures, the metal atoms diffuse towards the top of the nucleation sites, "climbing" on the lateral facets of nanowires and nucleating on top of them. When exceeding a certain temperature,

the desorption rate increases with respect to the diffusion rate, leading to a low nanowires density (Grandjean et al. 1999; Karpov et al. 2000; Fernández-Garrido et al. 2009). Conversely, at low substrate temperatures, nanowires are coalescing, favoring the formation of a 2D compact layer. A suitable couple of Ga/N flux ratio and substrate temperature is needed in order to have a good control of the nanowires' growth. Nitrogen rich conditions allow the formation of nanowires, but even in metal rich conditions and high substrate temperature, columns growth is possible since Ga atoms desorb from the surface leading to nitrogen rich conditions, in the end.

We have discussed, so far, the case of GaN growth on Si (111) substrate. It is important to mention that AlN nanowires nucleation takes place at extremely high substrate temperature, exceeding the working temperature of the substrate heater available in our growth machine. Growth of AlN nanowires was experimentally proved on bare Si (111) and sapphire substrates in previous studies. In this particular III-N alloy, the growth directly on the substrate was previously explored in the PhD of O. Landré (Landré et al. 2010). The density of the AlN nanowires was nonetheless too high to be controlled by the substrate temperature. High temperatures of the order of 1000-1100°C have allowed the growth of AlN NWs directly on the substrate but further studies were limited by oven performances.

Regarding the growth of $Al_xGa_{1-x}N$ material, ternary alloys growth is more difficult to control because of the difference between elements reactivity. $Al_xGa_{1-x}N$ nanowires cannot be directly grown on the substrate, because of the difference in Al-N and Ga-N bonding energies. Ga atoms diffuse more easily than Al atoms, resulting in an AlN-GaN phase separation. Due to the difference between Ga and Al reactivity such as diffusion time and affinity for N bonding, direct growth of $Al_xGa_{1-x}N$ nanowires on Si (111) substrate without the intermediate of a GaN nanowire base shows the formation of a Al rich 2D layer in between the nanowires (Landré et al. 2010).

For these above reasons, the AlN and $Al_xGa_{1-x}N$ nanowires grown in this work will be nucleated on top of GaN stems. In the case of $Al_xGa_{1-x}N$ growth, the Ga atoms form a wetting layer, Al atoms being completely incorporated. Thus, in order to control the Al composition, the ratio $\frac{N_{Al}}{N_{Al}+N_{Ga}}$ (with N_{Al} and N_{Ga} the number of atoms incorporated during growth), is directly given by the flux ratio between Al and N (ϕ_{Al} and ϕ_N). In metal rich conditions, $\phi_{Al} + \phi_{Ga} > \phi_N$, so preferential Al incorporation reads:

$$N_{Al} = \phi_{Al} \text{ and } N_N = \phi_N \tag{53}$$

At stoichiometry, the metal atoms and nitrogen atoms are equal:

$$N_{Al} + N_{Ga} = N_N \tag{54}$$

So, the composition x of Al is determined by the Al/N fluxes ratio from above equations:

$$\frac{N_{Al}}{N_{Al} + N_{Ga}} = \frac{\phi_{Al}}{\phi_N} \tag{55}$$

The doping of nanowires was obtained by introducing Si and Mg impurities during growth. The doping conditions were varied for the different samples with a Mg doping cell temperature between 220°C to 300°C for p-type doping and a Si doping cell temperature between 900°C to 1100°C for n-type doping. These parameters will be specified for each sample in the description of growth conditions.

2.2. Characterization techniques

This section will be dedicated to the description of the main experimental set-up that are used for studying the samples. After mastering the growth of the NWs, the aim of the PhD was to dispose of a complete characterization of the samples. The structural, optical and electrical information about the samples was acquired by a series of different techniques.

2.2.1. Scanning Electron Microscopy

First step in analyzing the growth consists of verifying the morphology of the samples and getting information about the structural parameters by using the Scanning Electron Microscope (SEM).

The working principle of a SEM is based on the interaction between a focused high energy beam of electrons and the surface of the material under study with production of different signals coming from secondary electrons, backscattered electrons and characteristic X-rays collected by detectors. From these signals, different images can be formed and displayed on a computer screen furnishing information about the sample's topography (backscattered and secondary electrons) or composition (X-ray) (Goldstein et al. 2017).

During my PhD, I have used two different SEM systems depending on the specificity of the study:

- The structural and morphological analysis of the samples after growth have been investigated by using the Zeiss Ultra55 SEM from PFNC platform in INAC-CEA Grenoble;
- The electrical characterization, EBIC measurements, electroluminescence and cathodoluminescence experiments were performed inside the FEI Quanta 2000 SEM at Neel Institute in CNRS Grenoble.

2.2.1.1. Morphology and structural characterization

In terms of structural characterization, SEM is of prime interest in visualizing the nanowires structure and morphology. The structural parameters (nanowire diameter, length, identification of different parts of the structure by looking at the chemical contrast, surface coverage) of the different samples grown during this PhD were verified after each growth in the Zeiss Ultra 55 SEM Microscope.

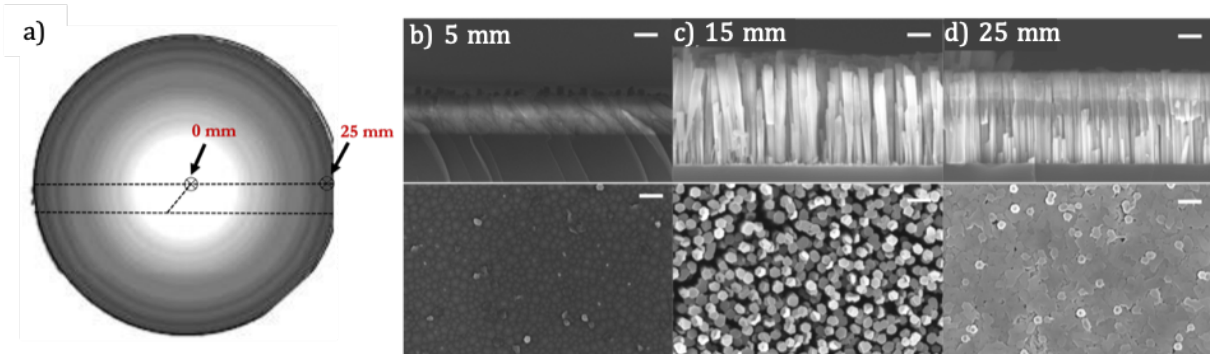

Figure 32. a) Wafer surface inhomogeneity during growth induced by the substrate temperature. Different growth morphologies at b) 5 mm c)15 mm and d) 25 mm from the center of the wafer

Since the growth is done on a 2" wafer, the sample is cleaved as in Figure 32a, using a diamond cutter, under a nanoparticle extraction hood. The sample is examined in edge view and top view, following the observation lines represented in the figure above. In order to have an approximation of the homogeneity of the growth, various SEM images are taken each 5 mm on the radius of the sample, with a low voltage of 5kV to avoid charging effects on the sample. An example of the SEM images at different regions of the wafer is shown in Figure 32b, c, and d. The density of the nanowires, length and diameter vary as a function of the temperature. A large temperature gradient can be observed on a single wafer along the radius leading to inhomogeneity and a restrained exploitable surface on each sample. Depending on the oven characteristics, the deviation of nanowires growth parameters is more or less significant.

The SEM images allow us to determine the exploitable region of each of the samples and adapt it for each study depending on the needs. For example, for the particular growth of sample N3314 which consist of a *pin* AlN NW junction on top of a GaN stem illustrated in Figure 32b, at 5 mm from the center of the wafer there was no growth of GaN stems due to the high temperature at this particular region, leading to the growth of a pure AlN layer.

At around 15 mm from the center of the wafer, the sample presents individual nanowires and a morphology that is convenient for studies demanding dispersion of the nanowires.

Regarding the region toward the end of the wafer, at 25 mm, the nanowires coalescence can be considered as an advantage for metal deposition and electrical measurements, avoiding metal leakage and an eventual short-circuit.

2.2.2. Current voltage characterization

The aim of the electrical characterization of nanowires is to investigate the doping as well as to characterize as fine as possible the electrical conduction properties of nanowires.

2.2.2.1. Sample process

For electrical characterization purpose, samples were processed by depositing metallic electrodes of different sizes on the top surface of the nanowires, taking advantage of the coalescence as seen in the previous section. I have done all of the clean-room work in NANOFAB at Neel Institute. The contacting procedure was respected for all of the electrical characterizations presented further in this manuscript. The recipe for metallic contacts is detailed below:

- Spin-coating of 200 nm of LOR 3A UV positive photoresist at 4000 rpm speed with 4000 rpm/s acceleration for 30s followed by a soft-bake on a hot-plate for 2 min at 200°C;
- Spin-coating of 400 nm of S1805 UV positive photoresist at 6000 rpm speed with 4000 rpm/s acceleration for 30s followed by a soft-bake on a hot-plate for 1 min at 115°C;
- Resist insolation by using laser lithography (DWL 66 fs 405-410 nm laser diode) on a mask with different sizes of squared plots (20x20, 50x50, 100x100 μm^2 and 200x200 μm^2) at an insolation dose of 75% of 120 mA beam current with 3% filters;
- After insolation, the UV resist was developed in a MF26 developer for 1 min and rinsed with deionized water;
- The sample was then exposed to O_2 plasma (PLASSYS plasma etching system) for 10 seconds at 10W and 20 sccm flow prior to metal deposition. This helps reducing the series resistance of p-type ohmic contacts and remove the residual resist on the surface of the nanowires;
- The metal contacts were deposited with an angle tilt of 10° to avoid the direct deposition of metal in the spaces between the nanowires and in consequence, the metal diffusion responsible for short-circuit. Two types of metallic contacts were deposited on the samples: either 100 nm Indium Tin Oxide (ITO) sputtered by physical vapor deposition (PVD) machine, or Ni/Au deposited by metal evaporation;
- Resist lift-off in Remover-PG remover for 2h at 80°C followed by an isopropanol cleaning and nitrogen blow drying;
- Metal annealing at 550°C in nitrogen atmosphere for 10 min in a tubular oven.

The metal conformal deposition was verified by using an optical microscope and the samples were cleaved and studied in I-V and EBIC experiments.

2.2.2.2. Experimental set-up

The electrical characterizations used in this PhD were done inside the FEI Quanta 2000 SEM in vacuum atmosphere. The contacts were taken by using the four probe manipulators presented in Figure 33, developed in our laboratory by Fabrice Donatini.

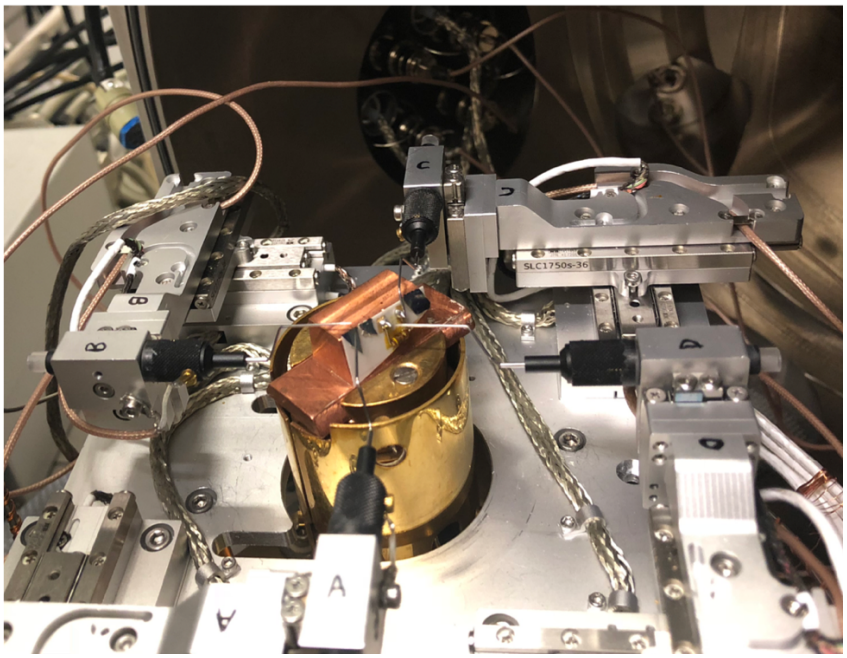

Figure 33. Image of the experimental set-up for electrical studies with respective nanomanipulators on the SEM stage.

The tips used for contacting have a radius of 500 nm and were cleaned by SF_6 plasma at 50W with a flow of 50 sccm for 6 min in the PLASSYS plasma etching system, removing the oxide formed at the tips' surface. Prior to the contacting of the nanowires, a high voltage applied on the tips allows the removal of the oxide, resulting in a more stable contact at the sample surface. The tungsten tips before and after the high voltage are presented in Figure 34.

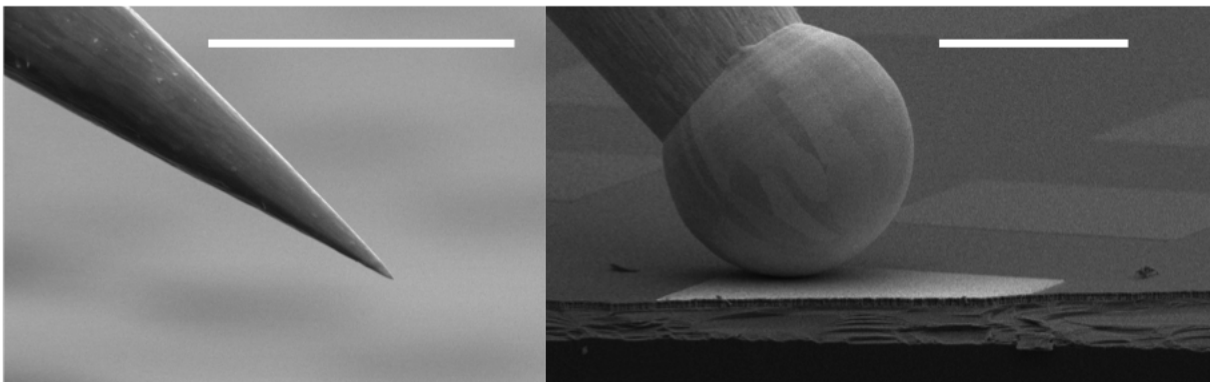

Figure 34. Tungsten tips a) before oxide burning and b) after oxide burning. The scale is of 30 µm for both pictures.

First, samples are characterized in the IV configuration presented in Figure 35a. The direct polarization is applied on the surface contact using a Keithley 2636 source meter. The samples are fixed to a ceramic insulating plate with silver paste to avoid short circuit with the sample holder and the backside contact is taken directly on the Si conductive substrate (Figure 35b).

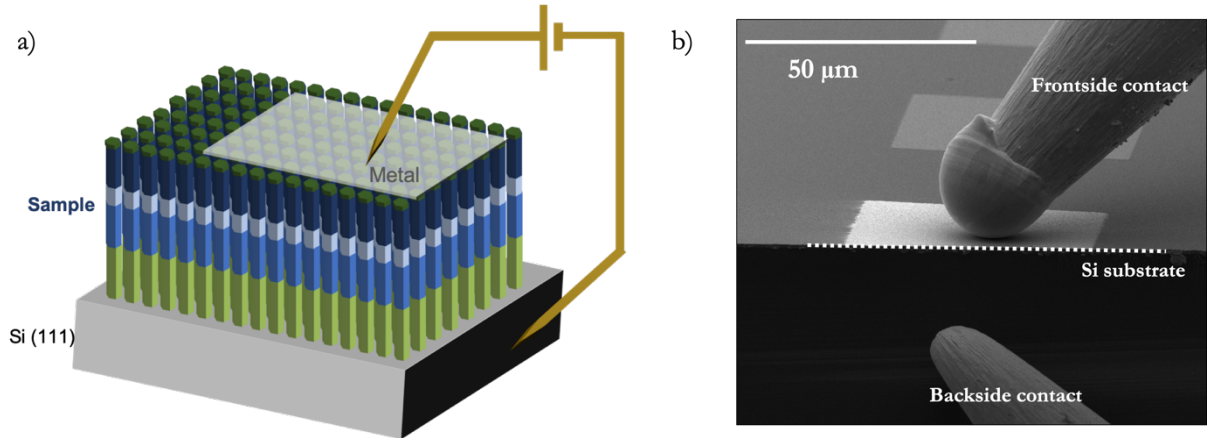

Figure 35. a) Schematics of the IV experimental set-up and b) SEM image of the contacts inside the SEM.

The conformity of the surface contacts can be seen in the SEM images showing a clear contrast when polarizing the surface of the samples (Figure 36b and c). Since we have deposited different electrode sizes (Figure 36a), we have checked the behavior of the metallic patterns by looking at the leakage current.

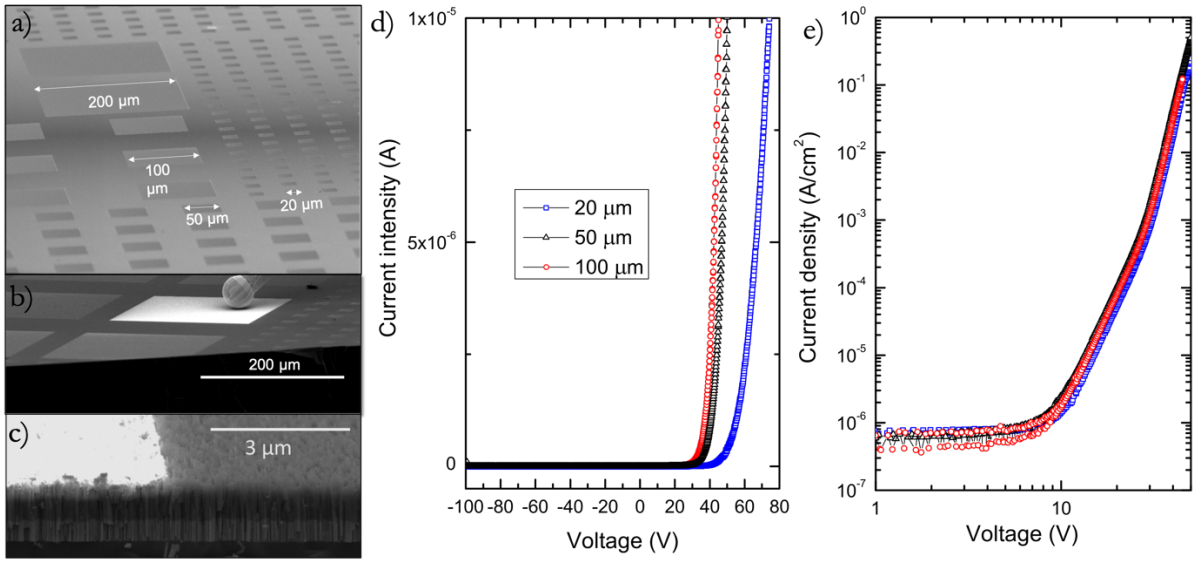

Figure 36. a) SEM image of the surface of electrodes showing different sizes electrodes b) and c) Contacted electrode with a contrast change under bias d) IV characteristics of three different sizes electrodes prior to surface normalization. e) JV characteristics after surface normalization

The current intensity versus voltage characteristics are plotted in Figure 36d for 3 different sizes electrodes. It is important to note that these measurements were done prior to irradiation experiments as detailed later in the manuscript. The electrodes present similar behavior in terms of current density versus voltage characteristics (Figure 36e). On this basis, we conclude that the metal electrode is conformal and the surface of the metallic electrode equals that of the contacted nanowires under the pattern.

However, by looking at the SEM images of the NWs' top surface, a filling factor has to be considered for a correct current density determination. This filling factor is in average 80%, pondering the current density in further electrical studies.

2.2.3. Electron Beam Induced Current technique

One of the major assets I have developed during this PhD regards the use of the Electron Beam Induced Current (EBIC) technique. This powerful tool allows us to visualize the electric field inside of a buried junction, proofing the electrical activity of dopants, as well as to determine the minority carrier or exciton properties.

The EBIC technique is an electrical characterization technique usually performed in a SEM or STEM (in our case, the FEI Quanta 2000 SEM at CNRS-Neel Institute). The physics behind this technique consists in exciting the semiconductor sample with the electron beam inside the SEM, generating electron-holes pairs inside the sample under study. If an electric field is localized in the sample, such as in the case of a junction or at a Schottky contact, the electrons and holes are separated under the electric field. The two carriers will be attracted to their respective n and p parts of the junction, causing a current to flow (called further EBIC current), mapping the electronic activity of the sample as a function of the position of the beam.

The transversal configuration (electric field perpendicular to the electron beam), allows the localization of the electric field in the buried junction or of electrically active defects. Due to the geometry of the sample, this configuration will be preferred and developed further in this work. Two different set-ups were used for the EBIC current imaging.

2.2.3.1. Experimental set-up configuration

2.2.3.1.1. Preamplification set-up

First configuration consists in using a preamplification set-up schematized in Figure 37a. The interest of using the EBIC experimental set-up is that it allows a direct imaging of the EBIC current and an exact in-situ localization of the junction by creating an EBIC current mapping of the sample.

The pre-amplifier permits the modulation of the current range by applying two distinct factors: a sensitivity parameter (A/V) to adapt the EBIC signal to the dynamic range of the video board and an offset current (A) to subtract the offset of the preamplification.

The EBIC current (I_{EBIC}) is then extracted by image treatment (using ImageJ software) by applying those two amplification parameters to the Intensity profile (measured on a greyscale coded on 2^{BITS} corresponding to the number of gray colors in the image):

$$I_{EBIC} = Sensitivity \times \left(\frac{2 \times Intensity}{2^{BITS}} - 1\right) - I_{offset} \quad (56)$$

Figure 37b and c show the SEM image of a *pin* AlN junction and the equivalent EBIC image, respectively, whereas Figure 37d is the superimposition of the two images. This qualitative method applied to an AlN NW *pin* structure is a quick way of visualizing the EBIC current and confirm the existence of an internal electric field.

From the mappings, two kind of studies are interesting for quantitative determination of the junction properties: the EBIC profile of an individual nanowire can be extracted by using a line

scan in the image treatment software Image J (Figure 37e) or a line average EBIC signal can be determined by integrating over the entire image.

Moreover, the SEM contrast image allows an easy alignment of the EBIC current and so an exact identification of the current change.

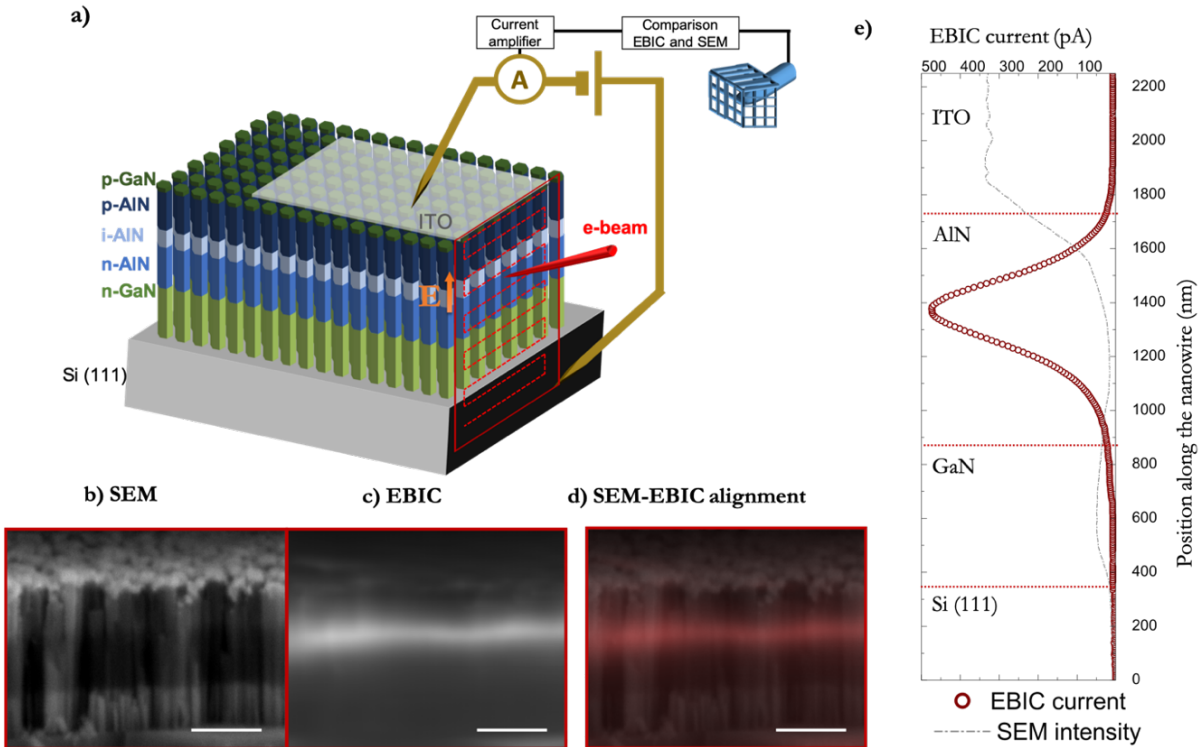

Figure 37. a) EBIC set-up inside the SEM in mapping configuration. b) SEM and c) EBIC signal mapping illustrated on an AlN NW pin sample with the equivalent d) SEM-EBIC alignment showing the presence of a pin junction signature. Scale is of 500 nm for a,b and c. e) EBIC profiling on an individual nanowire

2.2.3.1.2. Ammeter set-up

The second set-up consists in using a scan spot swept over a defined path in order to register the EBIC current flowing through the junction by using a Keithley 6485 pico-ammeter. This configuration allows us to extract and excite an individual nanowire, the EBIC profile with respect to the junction being obtained directly by registering the current variation on the defined path, as illustrated in Figure 38.

The current sensitivity is much higher, due to the pico-amperemeter resolution which is of 10 fA. The EBIC current profile is registered directly in the Labview program developed by Fabrice Donatini for these specific measurements and is illustrated in Figure 38 for the same sample as in the previous case (AlN NW *pin* junction).

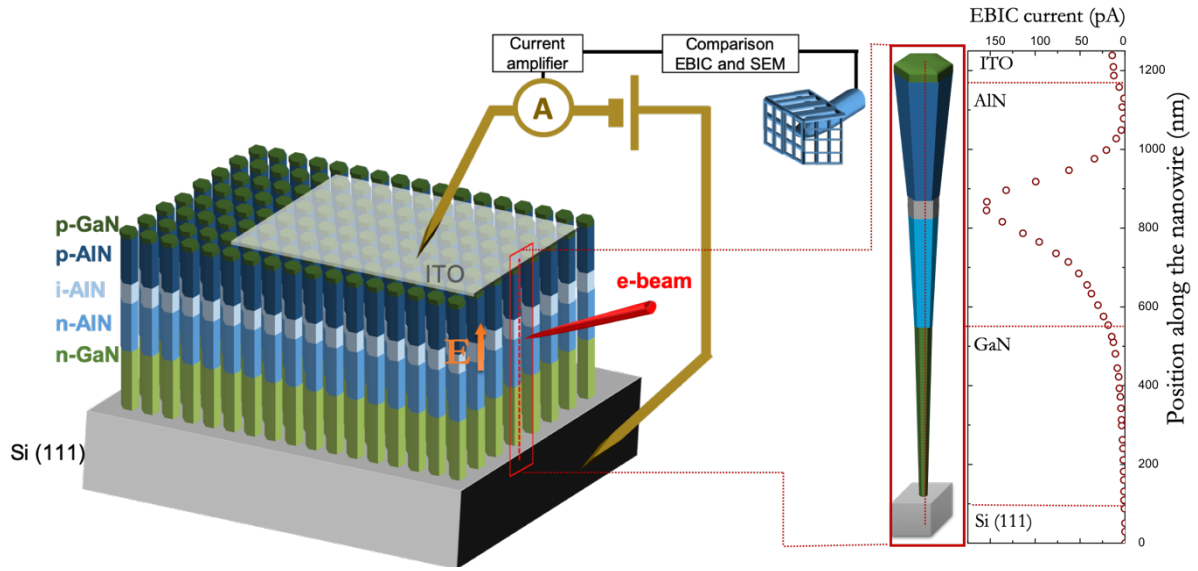

Figure 38. a) EBIC set-up inside the SEM in linescan configuration with the EBIC signal illustrated on an AlN NW pin sample

2.2.3.2. Quantitative EBIC imaging

Direct qualitative information can be obtained from EBIC studies regarding the presence of a junction. However, due to the great influence of the measurement parameters as well as to the sample geometry that may play a role on the recombination mechanisms, only semi-quantitative information about the basic material properties can be determined and it is essential to establish the limits of the experimental conditions. The theoretical considerations as well as the establishment of the experimental limits will be treated further in this section. The general case of a *pn* junction behavior was detailed here. Some of the physical concepts described previously will be used without detailed explanation.

2.2.3.2.1. Injection conditions

The basic principle of the recombination physics of a *pn* junction is based on the generation of minority carriers and diffusion of these carriers over a diffusion length L_n and L_p until a recombination process occurs. However, in EBIC experiments, the equilibrium of the overall system can be perturbated by the injection of excess carriers.

The majority carriers injected into the structure, if in amount larger than the carrier under equilibrium, are responsible for screening effects or carrier gradient creation. These effects modify the minority carriers transport properties. In order to evaluate the injection conditions and estimate the relevance of majority carriers over the system equilibrium one should estimate the amount of the injected charges by looking at the scanning conditions.

When exciting a sample with the electron beam, the beam is scattered losing energy over a certain depth under the sample surface when all of the incident electrons have come to rest. The electron and hole pairs generation take place in the interaction volume defined by considering the lateral spreading of the electron beam. This interaction volume was approximated in literature by Kanaya and Okayama (Kanaya and Okayama 1972) as a sphere of diameter D_{K-O}:

$$D_{K-O} = \frac{0.0276 E_0^{1.67} A}{d \times Z^{\frac{8}{9}}} \quad (57)$$

Where E_0/q is the acceleration voltage (keV), A is the average atomic weight of the material (g/mol), d is the material density (g/cm^3) and Z is the average atomic number of the compound material.

Inside the interaction volume, the number of excess carriers Δn and Δp in the sample is proportional to the beam energy. The Newbury model (Goldstein et al. 2003) has been proposed in order to estimate the electron-hole pair generation:

$$\Delta n, p = \frac{E_0(1-n)}{V} \times \frac{1}{3E_g} \times \frac{i_B \times \tau}{q} \quad (58)$$

Where $\Delta n, p$ are the electron/hole pairs created in the material (excess carriers), $\frac{E_0(1-n)}{V}$ is the energy injected by the beam in the interaction volume V, where n=0.176 is the retro diffusion coefficient determined by Parish and Russel (Parish and Russell 2006). In the model, the energy needed for the creation of one electron hole pair from an initial beam electron has been estimated to $3E_g$, where E_g is the band gap energy (eV).

The $\frac{i_B \times \tau}{q}$ is a ponderation factor estimating the excess carriers amount from the beam energy, with i_B the beam current (A), q the elementary electric charge (1.602×10^{-19} C), τ the recombination time including both radiative and non-radiative processes (s).

The parameters allowing us to determine the electron-hole pairs generation have been calculated in the Table 5 for AlN, GaN and $Al_{0.6}Ga_{0.4}N$ material.

	AlN	**$Al_{0.6}Ga_{0.4}N$**	**GaN**
A (g/mol)	20.5	29.1	41.5
Z (u.a.)	10	13.6	19
d (g/cm3)	3.26	4.41	6.15
E_g (eV)	6.2	5.1	3.43

Table 5. AlN, GaN and $Al_{0.6}Ga_{0.4}N$ parameters

The excess carriers generated for these materials as a function of the electron beam and for different beam voltage acceleration ranging from 5 keV to 30 keV have been calculated and plotted in Annexe 1. These plots can be considered as abacus for further studies.

We have considered a recombination lifetime of 100 ps for the GaN case based on literature (Kumakura et al. 2005), whereas for $Al_{0.6}Ga_{0.4}N$ material and AlN material we have estimated the carrier lifetime ranging between 100 ps to 100 ns, based on the available data (Dmitriev and Oruzheinikov 1996; Chichibu et al. 2010). The different cases allowed us to determine the injection conditions inside the samples.

Since GaN and especially AlN are wide band gap semiconductors having high dopants ionization energies, the doping level and the carrier concentration are not equivalent and depend on the ionization rate of the dopants. The doping of the n-type of the junction n is much lower

than the donor concentration, and the statement is even more true for p-type doping compared to acceptor concentration. Consequently, equations (11) and (12) established in Section 1.4 become:

$$n \ll N_D \tag{59}$$

$$p \ll N_A \tag{60}$$

Under **low injection conditions**, the density of minority carriers is overall lower than the carrier concentration under equilibrium, the diffusion length and recombination lifetime of the minority carriers in the extrinsic semiconductor prevail without perturbation from the excess carriers. In this case, the L_n and L_p can be extracted directly from the EBIC signal.

The excess carrier concentration created in the SCR must be compared to the doping level in order to determine the injection conditions. If the excess carrier concentration (Δn and Δp) is lower than the acceptor and donor concentration, then the electrostatics of the SCR is not disturbed and we are in low injection conditions. However, if the excess carrier concentration is higher than the acceptor and donor concentration, then the electrostatics of the system has been perturbed and we cannot extract the SCR width reliably.

However, under **high injection conditions**, the excess carriers injected in the system are large compared to the carrier concentration under equilibrium in the n and p respective parts of the junction. The charge neutrality equation still has to be respected, electrons and holes injected in the system diffusing together (phenomenon known as ambipolar diffusion), with respective ambipolar diffusion length (L^*) and diffusion coefficient (D^*) directly dependent on both electron and holes diffusion coefficients (D_n and D_p) (Orton and Blood 1990).

$$D^* = \frac{2D_nD_p}{D_n + D_p} \tag{61}$$

$$L^* = \sqrt{D^*\tau} \tag{62}$$

Nevertheless, since the EBIC experiments on the samples are performed in as-grown configuration, the excitation depth should not exceed the diameter of the nanowire, in order to get information about individual nanowires and model the EBIC current. The electrons trajectories when interacting with a given material can be determined by Monte Carlo simulation by using the Casino software. The EBIC experimental conditions will thus be chosen as a compromise between the interaction volume of the sample and creation of excess carriers.

2.2.3.2.2. Experimental fitting of the junction's parameters

From the *pn* junction theory described in Chapter 1 Section 1.4.2, the neutrality equation in the space charge region formed by fixed charges inside the depletion region was expressed as:

$$N_A \times W_p = N_D \times W_n \tag{63}$$

Where N_A and N_D are the doping levels of acceptors and donors (cm^{-3}) and W_p and W_n are the space charge region widths in the p and n part respectively (nm).

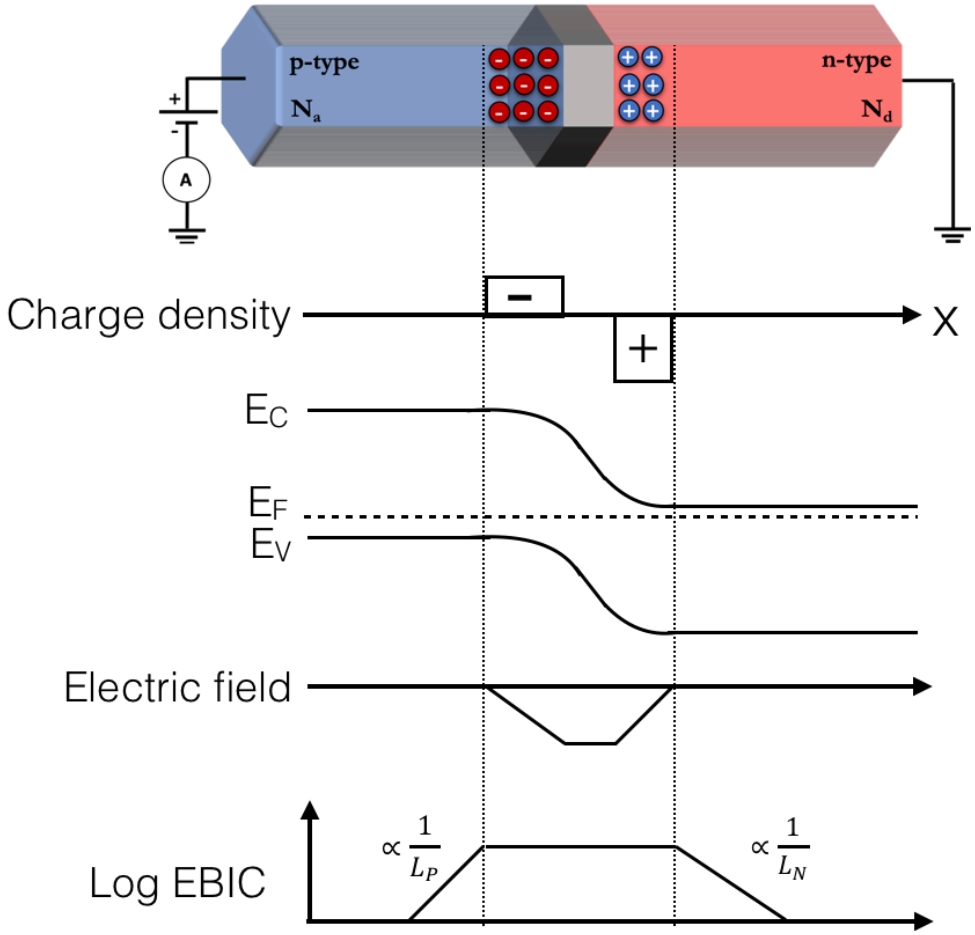

Figure 39. pin junction electrostatics schematization.

The *pin* junction electrostatics is described in Figure 39. It can be seen that the difference in charge density inside a *pn* junction creates an internal electric field inside the junction, which can be directly observed by EBIC studies.

Bonard and Ganière (Bonard and Ganière 1996) established the 2D continuity equation allowing the extraction of the EBIC current profile with respect to the scanning axis x (in our case the position along the nanowire):

$$I_{EBIC}(x) = \int_{-\infty}^{+\infty} d\tilde{x} \int_{0}^{+\infty} h(\tilde{x} - x, \tilde{z})\varphi(\tilde{x}, \tilde{z})d\tilde{z} \tag{64}$$

With $\varphi(\tilde{x}, \tilde{z})d\tilde{z}$ the efficiency of collection of generated carriers. The boundary conditions of this equation in the case of a nanowire is treated in detail by Donalato (Donolato 1994). By

assuming negligible surface recombination effects, the continuity condition in a neutral region situated far from the junction can be simplified to:

$$I_{EBIC}(x) \propto \exp\left(-x/L_{n_{(p)}}\right) \tag{65}$$

This simplified expression for the EBIC current variation can be determined for both n and p sides of the junction by fitting with an exponential dependence of the EBIC current profile as represented in Figure 40.

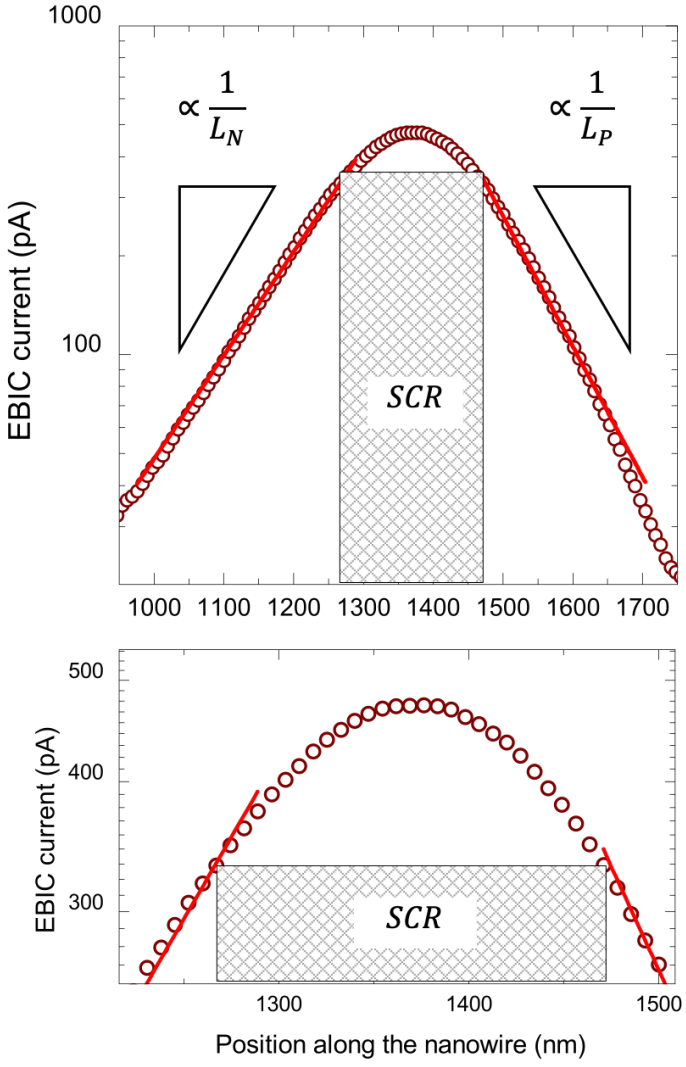

Figure 40. Data fitting example on an EBIC profile for diffusion lengths and SCR limits sketch.

The exponential dependence fitting gives access to the minority carriers diffusion length on both sides of the *pn* junction, in low injection conditions. The space charge region width is determined directly after the fitting of the EBIC profile by the exponential dependence. The space charge region width limits are defined by taking the points of the experimental data after which the fitting diverges.

From equation (32) the total space charge region width in $Al_xGa_{1-x}N$ can be further expressed as:

$$W_D = W_p + W_n = \sqrt{\frac{2\varepsilon_{Al_xGa_{1-x}N}}{qN_{eff}} \times (V_{bi} - V)} \quad (66)$$

With $\varepsilon_{Al_xGa_{1-x}N}$ the relative permittivity of an $Al_xGa_{1-x}N$ material (8.9 for GaN and 9.6 for AlN) ($\varepsilon = \varepsilon_0\varepsilon_r$ where ε_0 =8.854×10^{-12} F.m^{-1} is the dielectric permittivity of vacuum), q the elementary electric charge (1.602×10^{-19} C), N_{eff} the effective doping inside the material $\left(N_{eff} = \frac{N_A \times N_D}{N_A + N_D}\right)$, V_{bi} the built-in potential (V) and V the applied bias (V).

It can be thus observed that studying the space charge region width (W_D) is interesting for estimating the doping levels in the nanowires, since it gives access to the effective doping N_{eff}. By looking at the case of an abrupt junction (that is considering a homogeneous doping), the effective doping gives access to a minimum doping in the sample.

$$N_{eff} = \frac{2\varepsilon_{Al_xGa_{1-x}N}}{qW_D^2} \times (V_{bi} - V) \quad (67)$$

By assuming that either the p or n part of the junction presents a negligible doping (that is $N_A \ll N_D$ or $N_A \gg N_D$), the efficient doping can be expressed as:

$$N_A \ll N_D \; then \; \frac{1}{N_{eff}} \approx \frac{1}{N_A} \quad (68)$$

$$N_A \gg N_D \; then \; \frac{1}{N_{eff}} \approx \frac{1}{N_D} \quad (69)$$

To obtain an efficient LED structure, the recombination lifetimes and, implicitly, the minority carrier's diffusion lengths are essential parameters. However, secondary processes such as surface recombination and trapping of carriers on deep-level states provide an alternative path for recombination processes and play a non-negligible role on the minority carrier radiative recombination. In this simple model, we assume negligible effects regarding surface recombination.

2.2.4. Other techniques and collaboration

This PhD work would not have been complete without fruitful collaborations allowing us to get correlated results from different techniques. The techniques used to present the results have been summarized hereafter. However, experimental details will not be given for these techniques.

2.2.4.1. Luminescence experiments

The cathodoluminescence (Yacobi and Holt 1986) experiments allowed us to get information about a semiconductor material quality by analyzing the electronic transitions and emission coming from defects or impurities by exciting the sample with at a high energy electron beam inside the SEM. When exciting a material with an electron beam, the electrons from the valence band are excited to higher energy levels of the conduction band when the kinetic energy is around three times bigger than the band gap energy of the semiconductor. After thermalizing, electrons recombine with holes in the valence band, releasing photons in the emission range. These photons are captured on a detector imaging the respective CL spectra.

The electroluminescence experiments gave information about the radiative recombination of electrons and holes in the *pn* junction by emission of photons under excitation by an electric current. Cathodoluminescence and electroluminescence experiments have been performed by Dr. Gwénolé Jacopin at CNRS -Néel Institute. The optical properties of the AlN and $Al_xGa_{1-x}N$ nanowires were studied in the FEI Inspect F50 SEM. A Horiba Jobin Yvon ihR 550 spectrometer equipped with a Peltier-cooled charge coupled device detector and a 600 grooves/mm diffraction grating was used for spectral analysis. Low temperature (5K) experiments were obtained by liquid He cooling of the sample.

2.2.4.2. Energy Dispersive X-Ray Spectroscopy

Energy Dispersive X-Ray Spectroscopy (EDX) is a technique that provides information about chemical compositions of specimens by elemental chemical composition quantification. When an incident particle coming from a source of high-energy charged particles strikes an atom from the sample, core electrons from the inner shell are ejected, leaving a hole instead. Electrons from the outer shells with higher energy fill the hole, the difference in energy being released in the form of a X-Ray emission. The unique atomic structure of each element provides characteristic lines corresponding to the K, L, M layers of an element, quantified by using an energy-dispersive spectrometer. The energies of the X-rays are characteristic of the difference in energy between the two shells and of the atomic structure of the emitting element. The integrated intensity is proportional to the element's parameters, allowing the elemental composition of the specimen to be studied.

The EDX experiments presented in this PhD were performed by Dr. Eric Robin in a probe corrected FEI Titan Themis equipped with four windowless silicon drift detectors was.

For a better interpretation of the experiments, the net intensities of N, Al and Ga K-lines were extracted from the X-ray spectra using the QUANTAX-800 software from BRUKER. The X-Ray energies for Al, N, Mg and In are summarized in Table 6 (Deslattes et al. 2005).

Element	$K_{\alpha}(keV)$	$K_{\beta}(keV)$	$L_{\alpha}(keV)$	$L_{\beta}(keV)$	$L_{\gamma}(keV)$	$L_{1,e}(keV)$
N	0.392	-	-	-	-	-
Al	1.486	1.557	-	-	-	-
Mg	1.254	1.302	-	-	-	-
Ga	9.251	10.267	1.098	1.125	-	-
In	24.210	27.275	3.286	3.487	3.82-4.16	2.91-3.11

Table 6. X-Ray energies for different elements

One important parameter that must be considered when analyzing an EDX spectra is the geometry of the specimen. The photons emitted by deep areas of the sample are reabsorbed by the surrounding atoms, modifying the intensity ratios of the spectral lines.

A uniform geometry in terms of thickness is thus needed as well as a simulation of the geometry impact on the spectral lines for a good quantitative interpretation of the analysis. In the case of nanoscale samples, and more particularly nanowires, the lateral spatial extension of the volume probed remains of the order of magnitude of the probe.

2.2.4.3. Raman spectroscopy

Raman Spectroscopy provides information on the vibrational modes of GaN, AlN and $Al_xGa_{1-x}N$ that are sensitive to the crystalline quality, stress and doping level of the samples (Perkowitz 2012). This optical characterization technique is based on the inelastic scattering of light by elementary excitations such as phonons and plasmons. The Stokes-Raman scattering is based on the energy and momentum conservation rule:

$$\omega = \omega_i - \omega_s \tag{70}$$

$$k = k_i - k_s \tag{71}$$

Where ω, the angular speed, is related to the frequency of the incident (i) and scattered (s) photon and k is the wave vector. In order to perform this kind of analysis, spectrometers with high stray-light rejection have to be used because inelastically scattered light and phonon energies are small with respect to elastically scattered light.

The measurements and analysis of Raman data were done by one of this project's collaborators, Dr. Ana Cros from Materials Science Institute at the University of Valencia, Spain. The results provide information mainly on the Mg activation in the GaN and AlN material as well as about the passivation state of this Mg atoms.

2.2.4.4. Atom probe tomography

The Atom Probe Tomography technique gives information about chemical composition and atomic three-dimensional repartition inside the sample (Gault 2012). This time of flight mass spectroscopy consists in applying an electric field on the sample tip ionizing the surface atoms and evaporating them. The evaporated atoms are collected on a detector and by considering the position as well as the chemical nature of the atoms, a 3D reconstruction of the sample after evaporation can be obtained with a precision of 1 nm.

The APT experiments presented in this chapter were done during the PhD of Lynda Amichi under the supervision of Dr. Adeline Grenier and Dr. Catherine Bougerol at the "Plateforme de Nanocharacterizations" department at CEA-INAC Grenoble. The Laser Assisted Atom Probe Tomography experiments were performed by using a FlexTAP equipment at 73K with an ultraviolet laser (λ= 343 nm) with laser frequency of 100 kHz.

2.2.4.5. Positron annihilation

Positron annihilation is the process of collision between an electron (e^-) and a positron (e^+) -electron anti-particle of equal mass but opposite charge- resulting in the emission of two high-energy photons (γ) in the gamma-rays range (around 511 keV, as predicted by Einstein's law of conservation of energy) (Krause-Rehberg and Leipner 1999). The equation illustrating this interaction is:

$$e^- + e^+ \rightarrow \gamma + \gamma \quad (72)$$

The electrostatic interaction of a positron with the annihilation environment gives information on the local electron density and atomic structure of the host material. The positron annihilation radiation spectrum is highly influenced by the interaction with crystal defects in the environment, such as vacancies, clusters or dislocations in the material. Both time and energy parameters characterizing the positron annihilation process are sensitive to these interactions, allowing one to get information on trapping centers concentration and as well as the type of the localization sites.

In collaboration with Professor Akira Uedono from Tsukuba University in Japan, we have performed a series of studies on Si and Mg doped NW samples to determine the influence of doping on vacancy-type defects formation.

2.3. Summary of Chapter 2

This chapter was mainly focused on the description of the main experimental techniques used during this PhD. After presenting the MBE growth technique as well as the sample preparation used further in the manuscript, we have set the experimental conditions for the growth of $Al_xGa_{1-x}N$ nanowires:

To summarize, the growth substrate for the samples presented in this manuscript will be a 2" Si (111) wafer with a resistivity lower than 0.005 Ohm.cm, cleaned by using HF and outgassed prior to the growth inside the MBE chamber. The NW samples will be grown either directly on the Si bare substrate, or by using an AlN buffer layer reducing the in-plane tilt and twist. AlN and $Al_xGa_{1-x}N$ NW growth will be done on top of GaN stems, due to the particular growth conditions of these two materials (high nucleation temperature required for AlN nanowire and formation of a 2D Al-rich layer between $Al_xGa_{1-x}N$ nanowires due to the difference between Ga and Al reactivity). Doping of the samples will be done by using Mg for the p-type and Si for n-type. The morphological and structural characterization of the samples will be done by Scanning Electron Microscopy.

My work implied also sample processing and the study of electrical properties of the junctions by a series of characterization techniques. The procedure for top electrode (ITO or Ni/Au) deposition in the clean room is described in this chapter. The IV experimental set-up is presented in detail allowing also the first analysis of conformity check of the top-metal.

An important part of the chapter was then focused on the different configurations of the EBIC set-up used during the studies of electrical properties. We distinguish between a pre-amplification set-up allowing a direct imaging of the EBIC current and an exact in-situ localization of the junction by creating an EBIC current mapping of the sample and an ammeter set-up with a much higher current sensitivity relevant to extract and excite an individual nanowire.

The experimental conditions used for EBIC studies have a great impact on the results interpretation, the equilibrium of the system being perturbed by the injected carriers. The boundaries between low injection and high injection conditions have been established in the case of wide band gap semiconductors (such as AlN, GaN as well as $Al_xGa_{1-x}N$).

We have concluded that a trade is needed for experimental studies on nanowires, because of the small interaction volume needed to look at an individual nanowire leading to high injection conditions for minority carrier diffusion length. We have also explained the basis of the modelling of the data and concluded on the limits and uncertainties related to quantitative EBIC experiments.

Finally, we have presented other experimental techniques used further in the manuscript, with less exhaustive details. Thus, we will often use correlated TEM-EDX, cathodoluminescence and Raman techniques in order to study the doping of the different materials. Positron annihilation and Atom Probe Tomography (APT) techniques have been used for specific point of the studies.

"I think 99 times and find nothing. I stop thinking, swim in silence and the truth comes to me."

3. Doping problematics in GaN nanowires

This chapter will be dedicated to the study of dopant incorporation in GaN NWs. Doping and characterization of nanowires is one of the important steps in the achievement of NW based LED devices. The mechanisms of dopants incorporation during growth of nanowires not being well defined in the literature, it is crucial to have a better understanding of these mechanisms in order to optimize the doping and thus efficiency of LEDs. Extensive research has been made in our group in the comprehension of dopant incorporation mechanisms in GaN NWs.

These studies were the basis of future work on more complicated systems such as AlN and $Al_xGa_{1-x}N$. The results presented in this chapter have been presented in two publications: (Siladie et al. 2018; Uedono et al. 2019).

3.1. Si and Mg dopant incorporation in GaN

One important aspect of dopant incorporation is that increasing the abundance of the impurity does not necessarily increase its incorporation in the host material as a dopant. Instead, different phases can be favored, such as formation of clusters or complexes. Thus, solubility of dopants is defined as the maximum concentration attained by an impurity in the semiconductor at thermodynamic equilibrium. For instance, the solubility of Mg in GaN is limited at 2×10^{19} at.cm^{-3} by the formation of Mg_3N_2 complexes competing with incorporation of Mg acceptors (Van de Walle and Neugebauer 2004). Concerning Si, theoretical predictions have shown that incorporation of Si in epilayers induces roughness, crack formation and segregation on the surface of the GaN material, limiting the Si incorporation prior to complexes formation to a value of 5×10^{19} at.cm^{-3} (Rosa et al. 2002).

However, state of the art literature shows that Si doping is easily achievable in GaN NW because of the high solubility and low ionization energy in the range of 30 to 60 meV. Mg still presents a couple of difficulties related to the high ionization energy (between 150 to 220 meV) yielding a low ionization rate at room temperature. Moreover, the n-type residual doping of intrinsic GaN compensates the p-type doping, a high incorporation of Mg is thus necessary for p-type conductivity achievement.

Point defects formation such as vacancies (mostly V_N) and complexes (Mg-V_N and Mg-H complexes) is favored for Mg doping, limiting free hole generation. These complexes are compensation centers whose density increases versus Mg concentration (Kaufmann et al. 2000; Vennéguès et al. 2002; Leroux et al. 2002). Thus, growth conditions such as an optimum growth temperature and moderately N rich conditions compensating the V_N formation have to be carefully chosen for a better incorporation of Mg.

It is important to specify that only Mg in substitutional site of the Ga in the wurzite lattice can be ionized becoming electrically active. Most of Mg complexes and clusters, as well as Mg interstitials are not electrically active and thus the probability of formation of such defects should be decreased as much as possible. Furthermore, incorporation of Mg on substitutional N sites is not favorable for p-type conductivity. Extended defects such as pyramidal inversion domains have also been found to affect the Mg activation at high Mg levels (Leroux et al. 2004). The structural and electrical characterization of Mg doped GaN are equally required for p-type conductivity optimization.

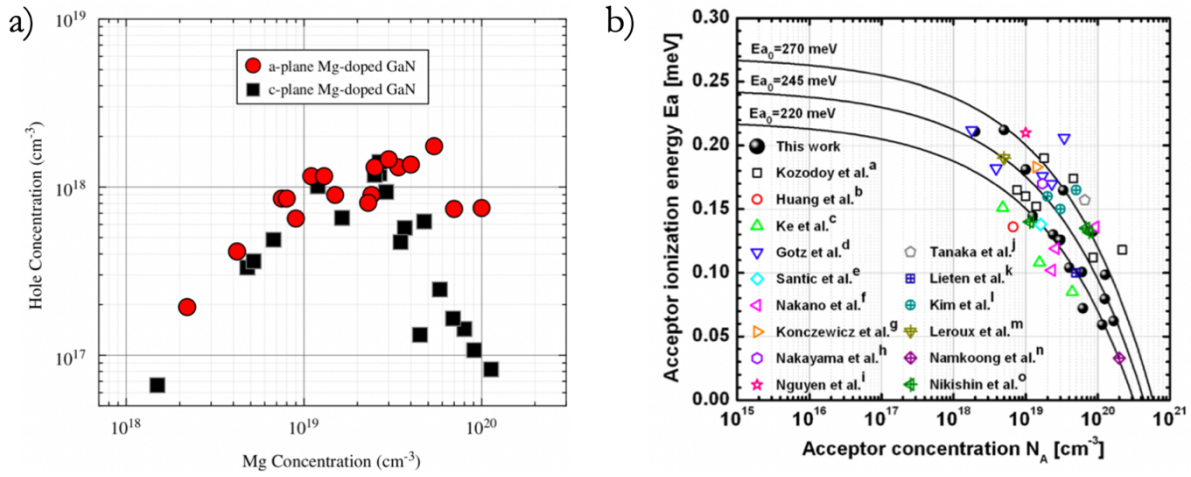

Figure 41. a) Hole concentration variation as a function of Mg concentration on a-plane (red) and c-plane (black) Mg-doped GaN epilayers (Iida et al. 2010). b) Acceptor ionization energy decreasing with acceptor concentration on MBE grown c-plane GaN (Brochen et al. 2013).

Actually, two important studies have evidenced, so far, the Mg acceptor concentration evolution with respect to Mg concentration inside the GaN material. A study on GaN epilayers from the group of Professor Akasaki (Iida et al. 2010) shows that while increasing the Mg concentration in GaN, above the solubility limit, the holes concentration becomes constant, followed by a decrease. This effect was observed both on a-plane and c-plane GaN epilayers, and was assigned to the formation of defects such as clusters or inversion domains, as shown in Figure 41a. On the other hand, Figure 41b shows that while increasing the acceptor concentration in MBE grown GaN epilayers, the acceptor ionization energy decreases from 270 meV down to 30 meV. The study was published by Brochen et al (Brochen et al. 2013). Very high Mg doping could be achieved in NW-based optoelectronic devices (Zhao et al. 2015b) leading to the formation of a defect band instead of an isolated impurity regime, which reduces substantially the effective ionization of Mg with respect to the case of epitaxial layers (Brandt et al. 1994). The presence of such a band of defects could be due to Mg accumulation just below the sidewall surface but is still to be experimentally confirmed (Zhao et al. 2015a).

By considering this two important information, our work will be focused on investigating the Mg incorporation in GaN material as well as answering the crucial question: why do nanowire geometry help increasing the Mg conductivity in standard nitride materials?

3.1.1. Advantages of nanowire structures

As stated before, one of the most important advantages of nanowire structure comes from the large surface bringing two important aspects into play: firstly, the structural strain relaxation on the lateral planes allows the incorporation of a higher concentration of dopants. Secondly, the surface electronic effect is different from the bulk case, due to the surface band bending. Indeed, the formation energies of defects and impurities are dependent on the Fermi level. The space charge carriers and surface states modify the Fermi level with respect to the band edges, known as Fermi level pinning, decreasing the formation energies of defects at the surface (Pernot et al. 2014).

In GaN nanowires, the available surfaces are c-polar plane and m non-polar planes and the exposure to incoming dopant fluxes is done under a certain angle. The absence of extended defects and the eased elastic strain relaxation is expected to favor doping, which is known to result in tensile strain in Si-doped GaN layers (Lee et al. 1998; Sánchez-Páramo et al. 2001; Chine et al. 2006) and NWs (Calarco et al. 2005) or compressive strain in Mg-doped GaN layers (Kirste et al. 2013; Flynn and Lee 2014). However, the question of doping spatial inhomogeneities in NWs is still open.

3.2. Si doping of GaN nanowires: inhomogeneous distribution and solubility limit

The incorporation of Si in GaN nanowires has been studied in detail in our group during the PhD of Zhihua Fang (Fang et al. 2015). The study was done on different GaN nanowires doped at different cell temperatures and gave interesting results regarding Si dopant incorporation in nanostructures.

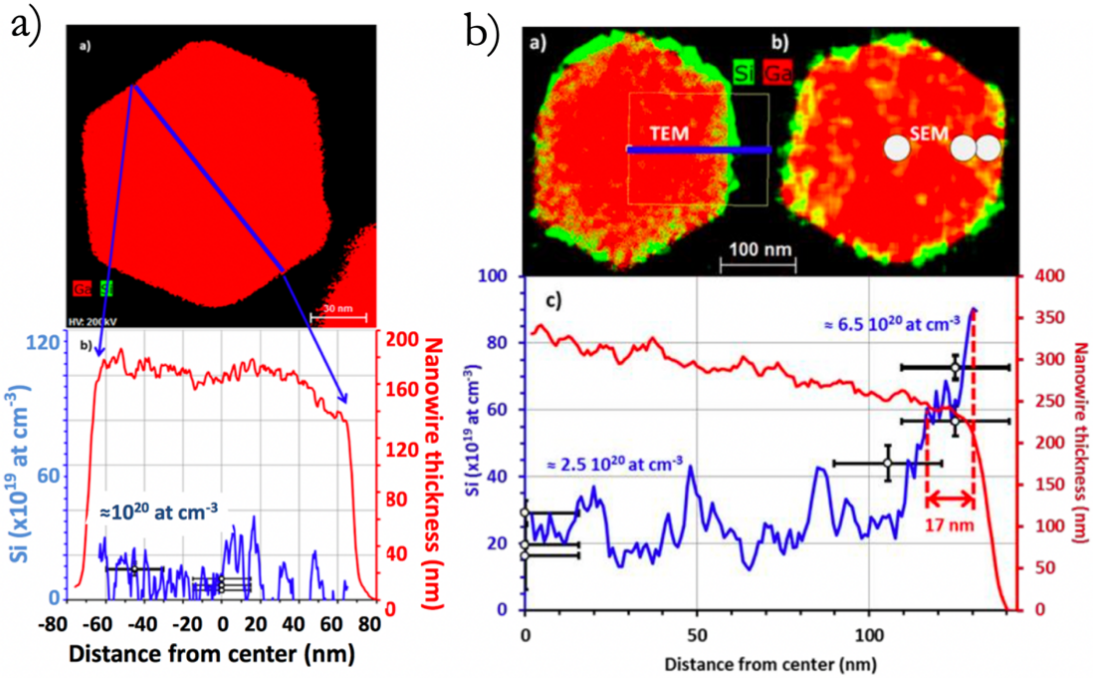

Figure 42. a) Top view cross section HR-EDX on individual Si-doped GaN nanowire doped at a doping cell temperature of 938°C and diametral Si concentration profiling corresponding to Si concentration of 10^{20} at.cm^{-3}. b) Top view cross section HR-EDX in TEM and SEM on individual Si-doped GaN nanowire doped at a doping cell temperature of 950°C and diametral Si concentration profiling showing a Si segregation (Fang et al. 2015).

Figure 42 illustrates a cross-section top view high resolution (HR) EDX profile on individual NWs. First profile (Figure 42a), corresponding to Si and Ga atoms mapping in a NW doped at a Si doping cell temperature of 938°C, shows a homogeneous distribution of Si along the nanowire diameter with a concentration of 10^{20} at.cm^{-3}. However, at a higher Si doping cell temperature (950°C) such as in the case of the NW of Figure 42b, an inhomogeneous distribution of Si atoms was observed. For this particular case, the Si concentration quantified by EDX was determined to vary from 2.5×10^{20} at.cm^{-3} in the core of the nanowire up to 6.5×10^{20} at.cm^{-3} on the outer part of the nanowire on a shell region of around 17 nm. Two remarkable results can be drawn from this study:

Firstly, the segregation of Si on m-planes at high doping cell temperatures was associated to a tensile strain relaxation in nanowires, confirmed by Raman experiments and predicted by theoretical studies for growth in N-rich conditions (Rosa et al. 2002). Secondly, the high Si concentration in the core of the nanowire of 2.8×10^{20} at.cm^{-3} at the plateau region was assigned to a Si solubility limit in NWs, which is higher than the theoretically predicted value of around 5×10^{19} at.cm^{-3} for the case of GaN epitaxial layers (Rosa et al. 2002). Such an inhomogeneous dopant concentration in NWs is of primary importance and is expected to affect their electrical properties.

3.3. Mg-doping of GaN NWs: understanding the incorporation mechanisms

After focusing on Si doping of GaN NWs and elucidating the segregation mechanisms at high doping, our research was oriented towards the understanding of the more complicated Mg doping. Mg tends to segregate on the c-plane (Sun et al. 2006), and slightly N-rich conditions and low growth temperature improve Mg incorporation. This also holds for m-plane, for which enhanced Mg incorporation with respect to c-plane has been demonstrated in N-rich conditions (McLaurin et al. 2005). Since GaN NWs, which are grown in N-rich conditions, are currently exhibiting m-plane side walls, Mg incorporation is expected to be favored on their sides rather than on their top. Similar to the case of Si-doping (Fang et al. 2015), the question then arises to determine if Mg is homogeneously incorporated in the volume of the NWs, an issue of practical importance to fully control the optoelectronic/electrical properties of nitride-based devices, including NW-based LEDs.

3.3.1. Atom Probe Tomography analysis

Such a requirement implies to use a technique which provides three-dimensional maps of doping impurities with atomic scale resolution, similarly to the Si profiling in GaN NWs. However, for the study of Mg homogeneity, we have decided to use laser assisted atom probe tomography (APT), a particularly well adapted technique that has been successfully applied to B content determination in Si NWs (Perea et al. 2008)(Xu et al. 2008) and P in Ge NWs (Perea et al. 2008). Concerning III-nitride materials, the pioneering work of Agrawal et al. has highlighted the experimental challenges faced when analyzing GaN NWs, opening the way to perform quantitative Mg content determination in Mg-doped GaN NWs (Agrawal et al. 2011). The resolution of

detection of Mg atoms in GaN material of this technique is of 1×10^{19} at.cm^{-3}. The APT experiments were done at CEA-Grenoble in collaboration with Lynda Amichi.

3.3.1.1. Samples presentation

3.3.1.1.1. Growth conditions

The GaN NWs studied in this chapter were elaborated by PA-MBE in our epitaxy machine described in detail in Chapter 2. Even if we were mainly interested in Mg-dopant incorporation, the samples structure consists of a *pn* junction grown along the c-axis on a 2" Si (111) wafer, n-doped with As, that was further used for electrical experiments.

The results of these APT experiments were mainly performed on two samples grown under nitrogen-rich conditions with a radio frequency power of 300 W for the plasma cell and a N_2 flux of 0.6 sccm. The Ga/active N flux ratio was 0.31. For n-type doping, a temperature of 900°C was set for the Si effusion cell. For p-type doping, Mg was used with an effusion cell temperature of 240°C.

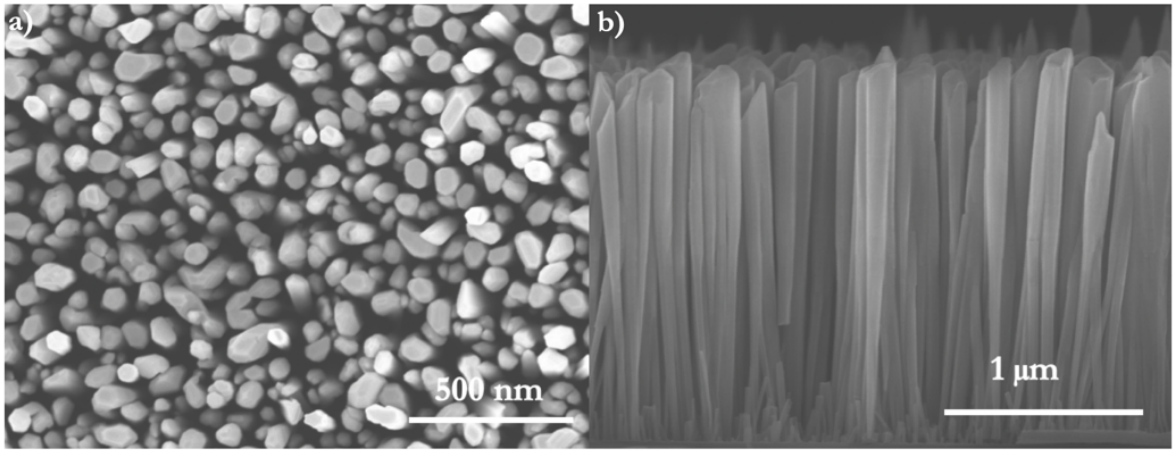

Figure 43. a) Top and b)side view SEM image of sample #1 (N2495).

- Sample #1 (N2495) was grown by Z. Fang during her PhD (INAC, CEA/Néel Institute) and was used for this experiment due to the particular geometry of the nanowires. Substrate growth temperature was changed from 890°C to 840°C for the n and p parts of the junction, respectively, to improve Mg dopant incorporation. The length of sample #1 (N2495) is estimated from SEM images in Figure 43b and is of the order of 2.2 µm, with 1 µm corresponding to the n-doped GaN and 1.2 µm to the upper p-doped section. Diameter varies along the growth direction of the wires ranging from 70 nm for the Si-doped part up to 140 nm in the Mg-doped part, likely assigned to the Mg incorporation effect (Yoshizawa et al. 1997).

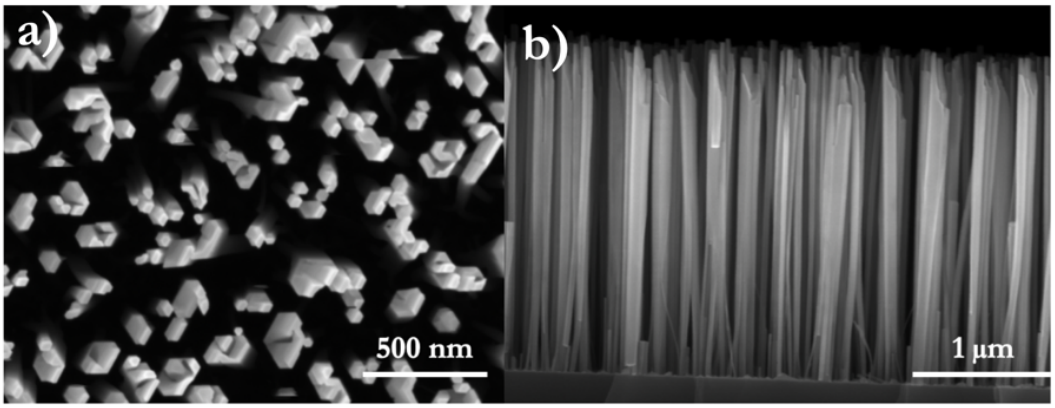

Figure 44. a) Top and b)side view SEM image of sample #2 (N2714)

- Sample #2 (N2714) was grown at a constant substrate temperature of 810°C. A thin AlN buffer layer of around 3 nm was deposited in this case prior to the growth of GaN section to prevent the in-plane tilt and twist of the wires. It has to be noted that with or without AlN buffer layer, it has been previously demonstrated that GaN NWs self-nucleated on Si mostly exhibit N-polarity (Auzelle et al. 2015)(Hestroffer et al. 2011), so that no difference in polarity-dependent Mg incorporation is expected from one sample to another. Unlike sample #1, the rotation during growth of sample #2 was turned off. During a growth without rotation, the nanowire is facing the doping cell in the same configuration, resulting in an inhomogeneous repartition of atoms. Top and side view SEM images of sample #2 are given in Figure 44. Total length of sample #2 is of 2.4 µm, with equal sizes for the n and p parts of the sample, as estimated from SEM images, with a diameter of around 80 nm.

  The summary of the growth conditions is presented in Table 7.

Sample no	Sample name	Ga flux (ML/s)	Mg cell temp (°C)	Substrate T (°C)
#1	N2495	0.1	240	840
#2	N2714	0.09	240	810

Table 7. Growth conditions

3.3.1.1.2. Nanowires preparation prior to evaporation

In order to be evaporated, individual nanowires have to be carefully extracted from the samples and assembled on the APT holder. For each sample, a single NW has been extracted from the substrate by Focused Ion Beam (FIB) preparation in a Strata DB 400S system from FEI, and mounted on an APT holder, following the specific procedure described by Koelling et al (Koelling et al. 2017).

It has to be noted that individual nanowires extraction from the growth substrate is a delicate process and breaking of the nanowires occur often. Since the evaporation process in APT requires a needle-shape of the sample in order to promote the field evaporation of surface atoms, the individual NWs were then milled at low energy. In order to minimize FIB-induced artefacts and Ga contamination during the cleaning process, the final milling voltage was 2 kV, significantly below the 5 kV value identified by Tang et al. as an upper limit of this contamination (Tang, F. et al. 2015). This preparation step was done by Nicolas Mollard from CEA Grenoble and the SEM image of a nanowire from sample #1 is given in Figure 45. An initial tip radius of the specimen of 35 nm and a tilt angle of the nanowire with respect to the APT holder of 5° were measured on the final SEM picture taken during the FIB preparation.

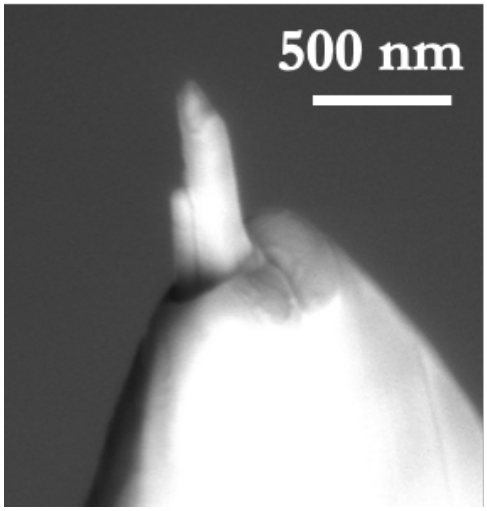

Figure 45. SEM image of the NW prior to evaporation on an APT sample holder after FIB and milling.

3.3.1.2. Results: Mg atoms distribution in GaN NWs

The Laser Assisted APT experiments were then performed by using a FlexTAP equipment at 73K with an ultraviolet laser (λ= 343 nm) with laser frequency of 100 kHz. The applied laser energy was 2.4 nJ and the evaporation flux was maintained constant at about 7×10^{-3} atoms/pulse, with a large field of view of 60°. These conditions were chosen in order to get a low electric field at the sample tip, which ensures the optimum accuracy in the III-site fraction occupancy determination (i.e. Mg/(Mg+Ga) ratio) as well illustrated by Rigutti et al (Rigutti et al. 2016). One of the main advantages of APT experiments comes from the fact that it is possible to get a 3-dimensional reconstruction of evaporated atoms coming from the sample, by using a geometric reconstruction algorithm based on the initial tip radius and the shank angle (tilt) measured prior to the evaporation.

3.3.1.2.1. Atoms distribution analysis in sample #1

APT reconstructions have been obtained using Tap3D software from CAMECA supplier. In this reconstruction, only Mg and 1% of Ga atoms are shown for the sake of visibility.

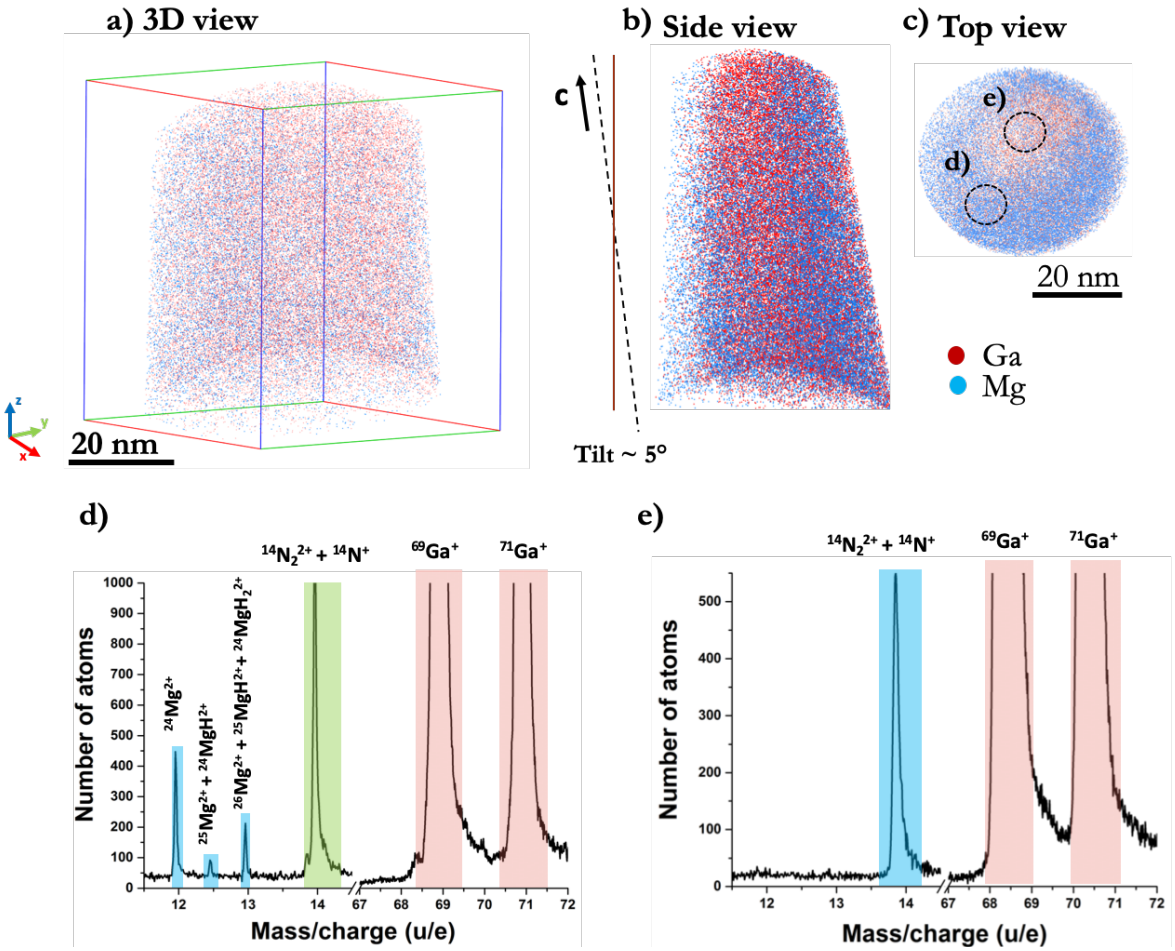

Figure 46. a) 3D b) side and c) top view of atom probe tomography map of Ga (red) and Mg (blue) atoms of sample #1. d) Mass spectra in the shell of the NW showing the presence of Mg atoms and its isotopes. e) Mass spectra in the middle region of the NW showing no presence of Mg isotopes with no noise limit increase.

Figure 46a presents the 3D reconstruction of Mg and Ga atoms after evaporation corresponding to sample #1. The side and top views represented in Figure 46b and c have been extracted from this 3D mapping of atoms distribution. The clear evidence of inhomogeneous Mg atoms distribution along the nanowire is shown by the top view cartography. Due to the increased Mg atoms distribution on the outer part, we have associated the structure of the nanowires to a "core-shell" like. Further investigation was done by manipulating a cylindric volume of the reconstructed 3D mapping in the core and shell regions respectively.

Mass spectra extracted from these respective volumes are given in Figure 46d and e, as indicated by the dashed circles on the top view in Figure 46. In Figure 46d, the mass spectrum corresponding to the shell region of the nanowire is represented for Mg, N and Ga atoms. Besides peaks corresponding to Ga and N species, the 3 peaks observed at 12, 12.5 and 13 a.m.u. respectively are attributed to Mg^{2+} and its isotopes, namely $^{24}Mg^{2+}$, $^{25}Mg^{2+}$, and $^{26}Mg^{2+}$. One important observation related to Mg isotopes peak relative intensities is that they do not reflect those expected from their natural abundance, 78.99%, 10% and 11.01%, respectively. Indeed, the

peak at 13 a.m.u. is greater than expected and is attributed to the formation of $^{24}MgH^{2+}$, which is more thermodynamically stable than $^{24}MgH^{+}$ according to Song et al (Song et al. 2004). The presence of $^{24}MgH^{2+}$ molecular ions and its isotopes is either coming from the sample or from the evaporation chamber. Indeed, hydrogen being inevitably present in the chamber may recombine with Mg during evaporation process. It should also be mentioned that in our experimental conditions, post-ionization of Mg during evaporation is strongly favorable, which explains why only Mg^{2+} but not Mg^{+} are detected (Kingham 1982). The clear Mg atom sub-density in the core of the nanowire in the top-view reconstructed map was also confirmed by mass spectrum taken on the cylindric volume considered in this region. Contrary to the shell region, in the case of the core region (Figure 46e), no Mg^{2+} peaks are detected at their expected positions in the mass spectrum, only peaks corresponding to N and Ga being present. Thus, this does not imply the complete absence of Mg in the core region, but we conclude that the Mg concentration in this region is below the detection limit of the APT technique, and clearly inferior to that found in the shell of the NW.

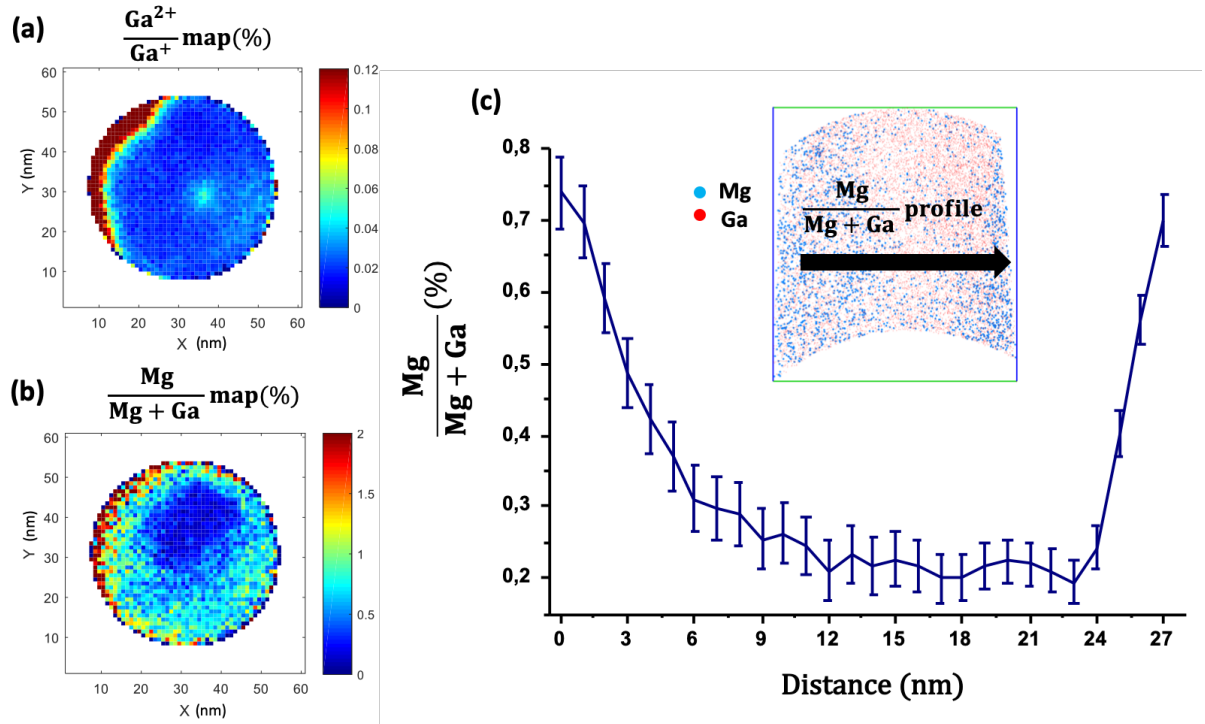

Figure 47. a) Ga2+/Ga+ ratio 2D map of a sampling volume indicated in Figure 46a evaluating the low influence of the electric field during the tip evaporation on the observed inhomogeneity in the Mg distribution. b) Mg/ (Mg+Ga) ratio 2D map, obtained for the same sampling volume evidencing an inhomogeneous distribution of Mg atoms with a Mg-poor region in the core. c) The concentration profile of Mg calculated perpendicular to the NW axis. The black arrow represents both the slice volume in the inset and the direction of the profile.

One important artefact has to be considered when evaporating a semiconductor by APT and analyzing the 3D atoms distribution on the detector. The crystal lattice of the material accommodates to an equilibrium shape during field evaporation, creating a pattern of poles and lines commonly known as "pole effect". The electric field distribution in the material can determine such an effect, changing the atoms reconstruction on the detector linked to the crystallographic orientation (De Geuser et al. 2007; Gault 2012).

In order to exclude this artefact related to APT experimental conditions, the Ga^{2+}/Ga^{+} ratio was mapped in 2D in Figure 47a for the total volume indicated in the 3D reconstruction in Figure 46a. The ratio maps have been calculated from reconstructed volumes using a home-made Matlab program. It has been reported in the case of nitride semiconductors (Rigutti et al. 2016) that this ratio is directly related to the strength of the surface electric field, otherwise not measurable (Bonef et al. 2017)(Mancini et al. 2014). Indeed, important changes in the Ga^{2+}/Ga^{+} ratio allow to evaluate the influence of the surface electric field during the tip evaporation on the observed inhomogeneity in the Mg distribution. Figure 47a shows a homogeneous ratio between Ga^{2+} and Ga^{+} with values below 0.05, which is the criterion reported by Koelling et al (Koelling et al. 2017) for low field conditions suitable for good accuracy in the III-site fraction occupancy determination. However, a thin and elongated area close to the left side of the reconstruction shows a Ga^{2+}/Ga^{+} ratio higher than 1, probably due to the sample tilt from detector axis. This otherwise rather good homogeneity indicates that possible "pole effects" (De Geuser et al. 2007) have been minimized in our experimental conditions and can be neglected.

However, quantification of Mg in the GaN nanowires is difficult because of the field conditions used for this experiment. Indeed, when low field conditions are used for III-nitride evaporation, the metal/N ratio is largely deviated from the nominal value of 1, likely due to the thermal desorption of nitrogen as N_2 neutral molecules (Gault et al. 2016)(Mancini et al. 2014). The doping level can be approximated by considering the III-site fraction occupancy Mg/(Mg+Ga) ratio. This ratio was mapped in 2D in Figure 47b, and confirms an inhomogeneous distribution of Mg atoms with a Mg-poor region in the core. The correlated observations of Figure 47a and Figure 47b allowed us to completely exclude surface electric field effects responsible for unequal evaporation of metal/N species. Indeed, the difference in the field distribution deduced by the Ga^{2+}/Ga^{+} mapping with respect to the Mg/(Mg+Ga) atoms repartition confirms that the Mg spatial inhomogeneity in the evaporated sample is an intrinsic feature of the specimen prior to the evaporation.

We have further quantified the Mg concentration along the radius of the nanowire presented in Figure 47c, by considering a sampling volume given in the inset. The outer region of the sample was not taken into consideration to avoid an overestimation of Mg due to the above-mentioned lack of reliability. From the composition profile shown in Figure 47c, it can be seen that the Mg/(Mg+Ga) ratio reaches 0.8% at the periphery of the NW. If we consider that all Mg atoms are located on substitutional sites, an approximated Mg concentration of 3.4×10^{20} at.cm^{-3} can be deduced. However, in the core of the nanowire, this ratio approaches 0.1%, but no quantitative information can be drawn from the data in this region, since the value of the Mg/(Mg+Ga) is assigned to an upper limit related to the detection limit of the technique.

3.3.1.2.2. Atoms distribution analysis in sample #2

In the same way, an individual nanowire from sample #2 was prepared and evaporated at similar evaporation conditions.

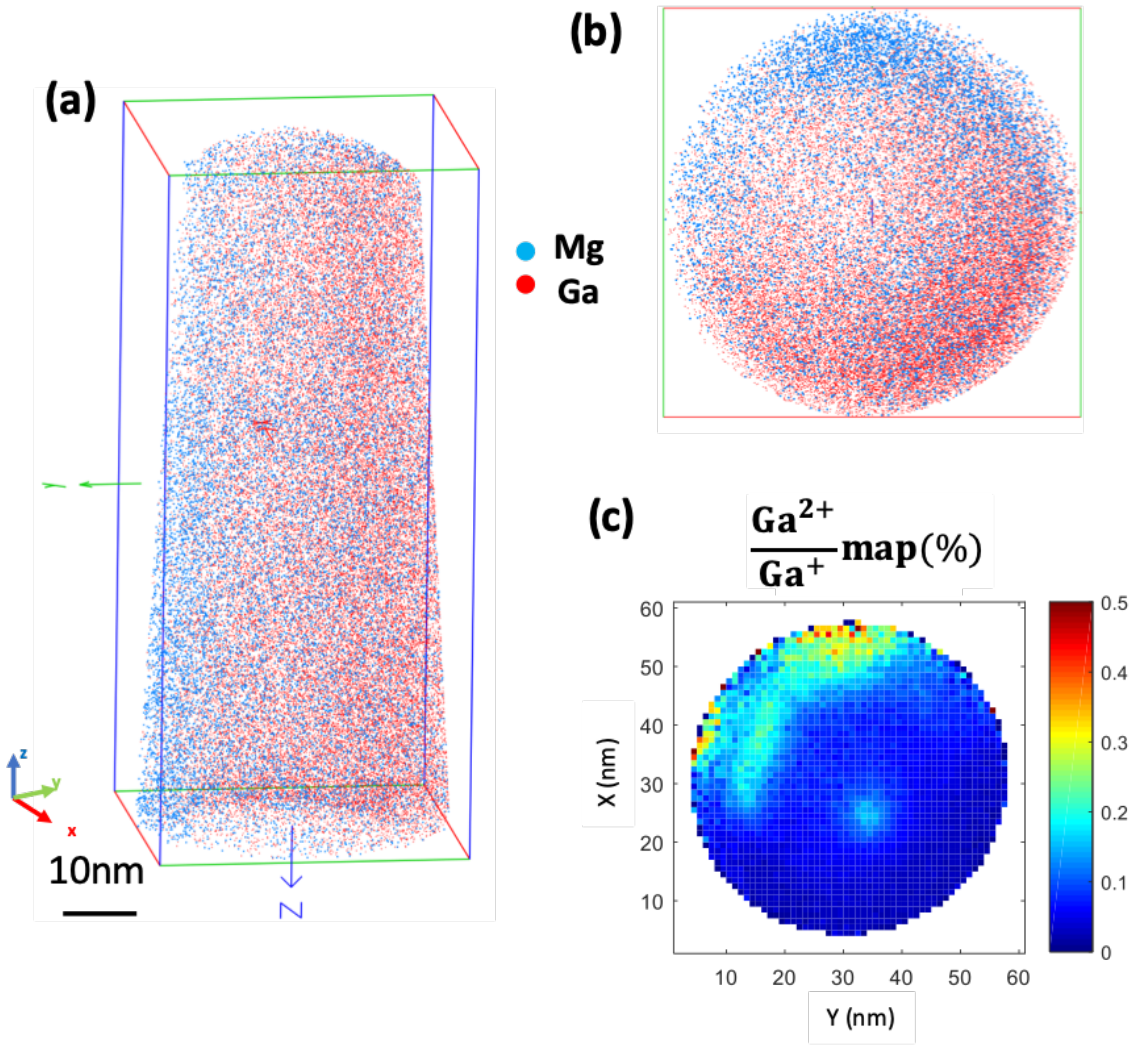

Figure 48. a) 3D volume and b) top view of atom probe tomography of Mg (blue) and Ga (red) atoms in sample #2 (without rotation) showing an inhomogeneous distribution. c) Ga^{2+}/Ga^{+} map ratio showing spatial variations in the evaporation field partially corresponding to the spatial inhomogeneity in the Mg distribution.

The 3D reconstruction of Mg and 1% of the Ga atoms is shown in Figure 48a, whereas the top view map is given in Figure 48b. As in the case of the previous sample, a clear inhomogeneous distribution of the Mg and Ga atoms is evidenced in this sample too. However, contrary to the case of sample #1, a lower Mg content is observed at the bottom part of the top view, corresponding to one side of the sample, without a core-shell distribution as in the case of sample #1. The Ga^{2+}/Ga^{+} map ratio in Figure 48c allows once again the exclusion of an artefact introduced by inhomogeneities in the evaporation field, whereas the comparison between the two mappings in Figure 48b and c reveals that the spatial variations in the evaporation field do not fully correspond to the spatial inhomogeneity in the Mg distribution and therefore cannot account for them. In particular, a Mg content higher on the top right part compared to the bottom part of

Figure 48b is observed whereas no significant variation of the evaporation field is noticed between these two regions in Figure 48c.

Due to the specific growth conditions without rotation of the substrate during sample growth, we assign the higher Mg concentration on one side of the NW to the sample facet exposure to the dopant flux and a preferential incorporation of Mg on the side-walls of the NW structure. This over density of Mg only on one side of the sample should not be observed if the Mg was incorporated only on the c-plane, neither in the case of a dopant segregation as in the case of Si.

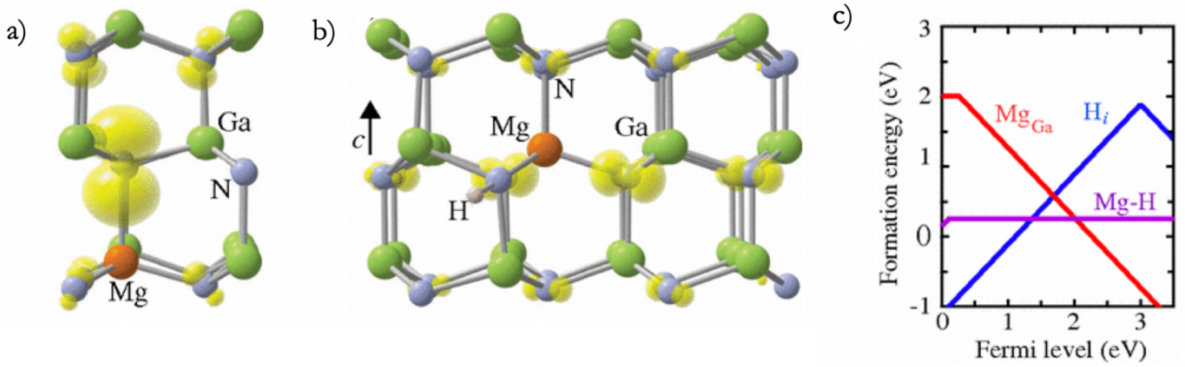

Figure 49. a) Local structure of a wurzite GaN lattice showing the distortion around a Mg atom in substitutional site. b) Mg-H complex in a wurzite GaN lattice. c)Formation energy as a function of the fermi level diagram for Mg, Mg-H and H formation in GaN showing a lower energy of formation for Mg-H complexes with respect to substitutional Mg (Lyons et al. 2012)

The hypothesis that Mg preferentially incorporates on the m-plane of a wurzite NW is reinforced by the theoretical considerations of Northrup (Northrup 2008) in which he states that under nitrogen rich conditions, the Mg rich m-plane surface is stabilized by H.

The dominant surface of GaN NWs being m-planes, these considerations are in good agreement with our observations. In this model, one of the Ga in the Ga-N surface dimers is replaced by Mg, whereas the nitrogen binds to H, the local structure of GaN wurzite being represented in Figure 49b (Lyons et al. 2012). Therefore, it suggests that Mg is incorporated through the m-plane NW sidewalls leading to a higher density of Mg in the periphery while its easy diffusion (Ptak et al. 2001) actually prevents it from accumulating in the vicinity of the surface.

Such a Mg doping mechanism, specific to nanowires, may lead to higher levels of Mg doping than in layers, boosting the potential interest of nanowires for light emitting diodes applications. Nonetheless, this also suggests that H, stabilizing the Mg surface reconstruction, may be simultaneously incorporated. Indeed, the formation energy of Mg-H complex as represented in Figure 49c is lower than that of a Mg atom in a Ga substitutional site, the complex formation being favored with respect to acceptor incorporation.

We then suggest that, as a consequence, the NW morphology, with a large value of m-plane/c-plane surface ratio, is favorable to promote a hydrogen-assisted Mg incorporation mechanism typical of m-plane behavior. The formation of Mg-H complexes is then expected concomitantly with Mg incorporation.

3.3.2.Mg concentration quantification by EDX

Quantification of the Mg concentration inside the samples was also verified by additional Energy Dispersive X-Ray Spectrometry (EDXS) experiments, performed by Eric Robin at CEA Grenoble. The detection limit of this technique for Mg concentration in GaN is of 10^{19} at.cm^{-3} (Robin et al. 2016). Spectra were acquired with a duration of 5–20 min at 250 000 counts per second.

Deconvolution of Mg K-line (1.25 keV) and Ga L-lines (1.1–1.12 keV) were performed by normalizing the spectra to a pure GaN reference spectrum acquired under the same conditions. Mg and Ga concentrations were quantified using pure MgO, GaN and GaP as reference spectra and concentrations are corrected from ZAF effects (standing for atomic number (Z), absorption (A) and fluorescence (F) effects). The entire procedure was tested with Mg-doped 2D GaN layers previously measured by secondary ion mass spectrometry (SIMS) and having concentrations ranging from (1–10)×10^{19} at.cm^{-3} (Robin et al. 2016).

Besides samples #1 and #2, two additional samples were grown on a Si (111) substrate, on which an AlN buffer layer was deposited prior to the growth of the GaN section. A substrate temperature of 810°C was maintained constant throughout the growth. Si-doped stems were grown using a Ga flux of 0.09 ML/s and a N flux of 0.25 ML/s, i.e. a Ga/N nominal flux ratio value of 0.36 and a Si effusion cell temperature of 900°C. However, in steady state conditions, the self-regulation of NW diameter is resulting in a Ga/N ratio value on top close to stoichiometry (Fernández-Garrido et al. 2013). After completion of the Si-doped GaN stem in established steady-state regime, the Mg-doped section was grown using a Mg effusion cell temperature of 240°C, with a Ga flux of 0.06 ML/s (sample #3 N2721) and 0.143 ML/s (sample #4 N2720), i.e. in N-rich and Ga-rich conditions, respectively, in terms of *effective* Ga/N flux ratio value with respect to the Si-doped stem.

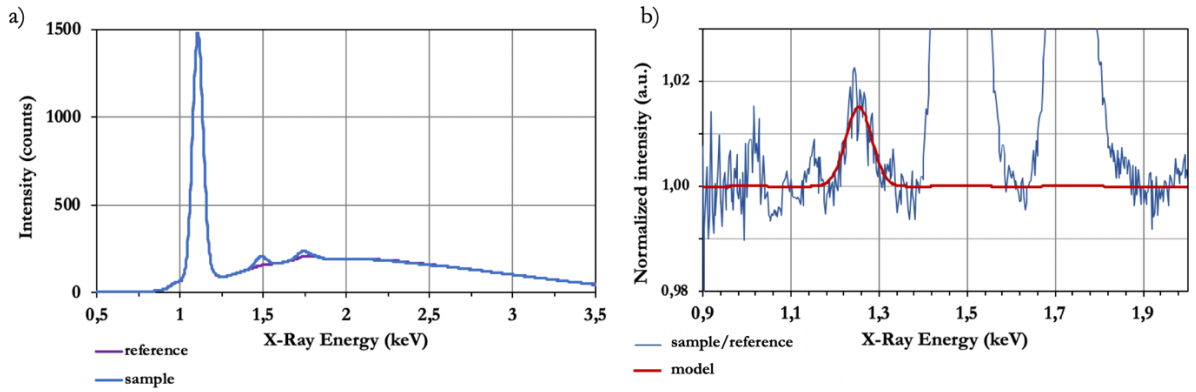

Figure 50. a) EDX intensity spectrum of sample #2 in blue with respect to a reference spectrum b) Normalized intensity of sample #2 with respect to the reference spectra in blue and model fitting the peak at 1.25 keV for Mg concentration quantification.

The X-Ray spectrum of each sample was normalized with respect to that of the reference sample (Figure 50a). After normalization, the peak corresponding to Mg can be directly fitted and appears clearly with respect to the noise in Figure 50b. This fitting allows the quantification of Mg concentration inside the nanowires.

The corresponding Mg average concentration in each of these samples quantized by EDX experiments on individual nanowires is summarized in Table 8.

Sample no	Sample	Ga flux (ML/s)	Mg concentration (at.cm^{-3})
#1	N2495	0.1	$(1.70\pm0.11)\times10^{20}$
#2	N2714	0.09	$(2.17\pm0.32)\times10^{19}$
#3	N2721	0.06	$(4.05\pm0.37)\times10^{19}$
#4	N2720	0.143	$(2.45\pm0.38)\times10^{19}$

Table 8. Summary of estimated Mg concentration

An average value of the Mg concentration of $(1.7\pm0.1)\times10^{20}$ at.cm^{-3} was found by integrating the periphery and the core of the NWs in the case of Sample #1, in good agreement with the quantification given by APT experiments, which was of 3.4×10^{20} at.cm^{-3}. The concentration of in sample #2 was found to be of $(2.17\pm0.32)\times10^{19}$ at.cm^{-3}, whereas that in samples #3 and #4 were estimated at $(4.05\pm0.37)\times10^{19}$ at.cm^{-3} and $(2.45\pm0.38)\times10^{19}$ at.cm^{-3}, respectively.

The increase of Mg incorporation by a factor of 2 for a Ga flux of 0.06 ML/s is consistent with the improved Mg incorporation on c-plane and m-plane GaN layers grown by MBE in N-rich conditions. In particular, it has been established by McLaurin et al. that for m-plane GaN layers Mg incorporation was 5 times higher in moderately N-rich conditions than in Ga-rich conditions (McLaurin et al. 2005).

Although qualitatively in agreement with these results, the Mg incorporation rate improvement found in NWs is significantly small. This can be tentatively assigned to reduced impact of growth conditions on the local stoichiometry of NW sidewalls. Indeed, NW growth is mostly governed by Ga diffusion along the sidewall to the top, which is expected to self-regulate the amount of Ga present on the m-plane sidewalls. Also, the stabilization of Mg-H reconstructed surface is expected to reduce the effect of Ga flux fluctuations resulting in the Mg incorporation rate being poorly dependent on such fluctuations. The investigation of Mg-H complexes present in the sample is required.

3.3.3. Raman characterization

One way of checking the presence of Mg-H modes that validates the hypothesis of simultaneous incorporation of Mg and H in the NWs is by Raman spectroscopy. The experiments on as-grown and dispersed nanowires were performed by Prof. Ana Cros from the Materials Science Institute at the University of Valencia, Spain. The spectroscopy experiments were performed in backscattering configuration using the 532 nm line of a laser diode as excitation source. A Horiba Jobin Yvon Xplora spectrometer equipped with a Peltier-cooled charge coupled device detector and 1800 grooves/mm diffraction gratings was used for spectral analysis. A 100x microscope objective focused the excitation laser on the samples and collected the scattered light to the spectrometer.

Four different additional doped NW samples, grown under similar conditions to that previously described, but with different growth temperatures and Mg doping cell temperatures ranging from 230°C to 250°C have been studied in as-grown configuration and are summarized in Table 9.

Sample no	Sample	Ga flux (ML/s)	Mg cell temp (°C)	Substrate T (°C)
#1	N2495	0.1	240	840
#2	N2714	0.09	240	810
#3	N2721	0.06	240	810
#4	N2720	0.143	240	810
#5	N2689	0.09	240	775
#6	N2676	0.09	230	730
#7	N2686	0.09	240	753
#8	N2671	0.09	250	725

Table 9. Growth conditions summary

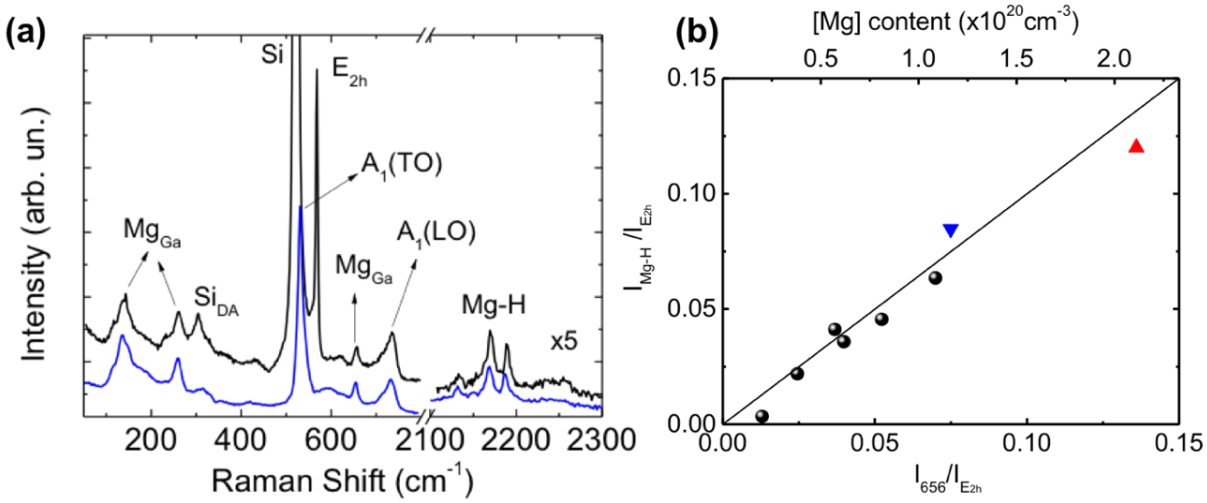

Figure 51. a) Raman spectrum of typical GaN NWs doped with Mg. The upper spectrum (black) is taken from the as-grown ensemble excited along the wurtzite c axis (z direction). The lower spectrum (blue) is obtained from a single NW (or few of them) dispersed on graphite in the x(z,-)-x configuration b) Integrated intensity of the three main Mg-H modes vs. the intensity of the Mg-Ga mode at 656 cm-1. Both intensities have been normalized to that of the E2h mode. Samples #1 and #2 analyzed by APT correspond to the red (up) and blue (down) triangles, respectively. Black dots correspond to the six other samples presented above.

Raman spectra for sample #1 of as-grown ensemble (upper spectrum, black) and dispersed configurations (lower spectrum, blue) are shown in Figure 51a. The Raman E_{2h} and the A_1(TO)

modes assigned to GaN strain appear in the spectra according to the Raman selection rules. However, these modes are different for as-grown and dispersed configurations. Although forbidden in the x(z,-)-x configuration by the Raman selection rules of the bottom spectrum (blue), the A_1(LO) mode is clearly observed, probably due to the disorder introduced in the GaN lattice by the Mg atoms.

The peaks associated to the incorporation of Mg in the GaN lattice are similar in both spectra. They appear at 140, 260 and 656 cm^{-1} for Mg in substitution to Ga (Kaschner et al. 1999)(Kaczmarczyk et al. 2000), while the feature observed around 2170 cm^{-1} is assigned to Mg-H complexes with various configurations (Brandt et al. 1994). These Mg-H modes are of particular interest since they have been previously observed in MBE-grown 2D layers with a Mg content larger than 1×10^{19} cm^{-3} (Brandt et al. 1994)(Kaschner et al. 1999). However, they are absent in MOCVD-grown samples without annealing treatment. After thermal annealing at 700°C, these set of lines built up with a relative intensity similar to what is observed in Mg-doped GaN NWs, associated to an increase of hole concentration according to Harima and coworkers (Harima et al. 1999).

As a matter of fact, it is well established by the literature and we have discussed in Chapter 2 that the formation of Mg-H complexes is responsible for the poor p-type doping levels of MOCVD-grown layers. Activation of dopant by dissociation of these complexes by electron irradiation (Amano et al. 1989; Isamu Akasaki et al. 1991) or thermal annealing (Nakamura et al. 1992b) is required. If considering that dopant activation by thermal annealing of MOCVD layers leads to a rearrangement of Mg-H complexes associated with the building up of a set of lines around 2170 cm^{-1}, the presence of these modes on unannealed NW samples is a clue that the specific structure of associated Mg-H complexes is not detrimental to Mg activation.

Since the intensity of these Mg-H modes is an indicator of Mg activation inside GaN material, the intensity of the 656 cm^{-1} line versus the integrated intensity of the three main peaks related to Mg-H complexes is represented in Figure 51b for the 8 samples. In all cases, the intensity of the peaks has been normalized to that of the E_{2h} mode, giving the bottom axis of the Figure 51b. The linear variation of the Mg-H mode normalized intensity with respect to that of Mg mode at 656 cm^{-1} clearly shows a correlation between H and Mg incorporation. Based on the intensity of the 656 cm^{-1} line associated to Mg, the Mg content in the samples has been estimated. Based on the calibration performed by Kamimura et al (Kamimura et al. 2017) for Mg doped GaN NWs, the Mg concentration can be obtained by multiplying this intensity with the scaling factor $S= 7.8\times10^{20}$ cm^{-3}. Since the Raman intensity is sensitive to the volume of the sample, another precaution has to be taken when quantifying the Mg concentration, which is considering the contribution of the Si-doped lower part of the sample. A factor of 2 has thus been considered, the scaling factor being $2S=15.6\times10^{20}$ cm^{-3}. The values obtained for Mg content are shown in the upper scale of Figure 51b. The Mg content determined by Raman analysis of the Mg associated modes varies from 1×10^{19} cm^{-3} up to 2×10^{20} cm^{-3}, with a major role played by growth conditions, consistent with EDXS studies.

3.3.4. Conclusion

This study of Mg dopant spatial distribution in GaN NWs helped us in understanding the incorporation mechanism of Mg, preferential on the m-plane side-walls. However, this mechanism results in a marked radial inhomogeneity of dopant in NWs, but, thanks to the eased diffusion of Mg atoms, without formation of clusters that could decrease the doping efficiency. Thus, due to this NW-specific feature resulting from their morphology as well as to the high m-plane to c-plane ratio, it is expected to obtain higher levels of Mg doping in NWs than in their thin film counterpart. This feature is consistent with the possible formation of defect bands enhancing the hole conduction and makes NWs of potential interest for the realization of practical optoelectronic devices, in particular for deep UV emission applications.

Another important conclusion of the study is that the Mg incorporation is assisted by H due to this complex' high stability in N rich conditions, coherent with theoretical predictions, with a considerable fraction of Mg dopants forming Mg-H complexes.

3.4. Vacancy defects study by positron annihilation in doped GaN NWs

Increasing the dopants concentration in GaN material also favors point defects formation and most notably, nitrogen vacancies. Even though nitrogen rich growth conditions limit the nitrogen vacancies formation, the probability of formation of vacancies is not totally excluded. One way of probing vacancy-type defects in GaN NW is by positron annihilation (Krause-Rehberg and Leipner 1999; Tuomisto and Makkonen 2013).

The study and understanding of point defects formation is extremely important for GaN-based optical and electrical devices, since they act like non-radiative recombination centers degrading the performance. Indeed, the NWs geometry is beneficial to the reduction of extended defects density as well as to the increase of solubility limit of dopants (Xie et al. 2008; Nguyen et al. 2012a, b; Fang et al. 2015). Because vacancy-type defects act as carrier compensation and recombination centers (Van de Walle and Neugebauer 2004) knowledge on the behavior of vacancies is crucial to improve the crystal quality and optoelectronic properties of GaN NWs, further increasing the external quantum efficiency of GaN NW based devices.

Professor Akira Uedono from Tsukuba University in Japan performed positron annihilation experiments on a series of Si and Mg doped NW samples so that we study the influence of doping on vacancy-type defects.

3.4.1. Positron annihilation technique

The interest of positron annihilation experiments in vacancy-type defects comes from the sensitivity of this particular technique with respect to point defects, allowing low concentrations detection and classification of the vacancy-type based on the positron annihilation radiation spectrum. Free positrons in the crystal lattice of a material are strongly repulsed by positive ion cores and attracted by negative and neutral ones. While vacancy defects act as attractive centers

inside a material, the vacant lattice site in the crystal lattice is responsible of trapping the positron. To annihilate, the positron needs to collide with an electron. The missing valence and core electrons around the vacancy site have a great influence on the electron momentum distribution in the sample as well as on the positron lifetime.

The study of positron annihilation by vacancy-type defects in this section is based on the electron momentum distribution in the sample (known as Doppler-broadening spectroscopy of the 511 keV line) by using a monoenergetic positron beam, with an irradiance of about 10 mW/cm^2 (Krause-Rehberg and Leipner 1999). Throughout this section, two parameters will be constantly evoked when talking about annihilation events:

- The *S* parameter defined as the fraction of annihilation events over the energy range of 510.24–511.76 keV;
- The *W* parameter, defined as the fraction of annihilation events in the ranges of 506.44–508.72 keV and 513.28–515.56 keV.

Information about the annihilation sites of positrons can be determined from the (S,W) parameters. The Doppler broadening spectra for the delocalized state and the trapped states in typical vacancies and vacancy impurity complexes (oxygen and hydrogen) were calculated by using QMAS (Quantum MAterials Simulator) code (Ishibashi et al. 2007; Ishibashi and Uedono 2014). Theoretical (*S*,*W*) values for the annihilation of positrons in the delocalized state (defect-free: DF), vacancy complexes between V_{Ga} and V_N, $[(V_{Ga})_m(V_N)_n]$, V_{Ga} containing hydrogen atoms denoted as $(H_n)_{Ga}$, and vacancy-impurity complexes such as $V_{Ga}O_N$, $V_{Ga}(O_N)_4$ were calculated by Prof. Uedono. The comparison of these theoretical values to those determined by Doppler broadening spectra for each sample is a way of identifying the main vacancy-type defects in the samples.

Since the properties of the hydrogenated V_{Ga} with one or two hydrogen atoms, such as the transition levels in the band gap, are not so much different from those of V_{Ga}, they act as acceptor-type defects. Because the positron trapping rate for donor-type defects is small (Krause-Rehberg and Leipner 1999), we mainly consider hydrogenated V_{Ga} and vacancy clusters in the present work. When hydrogen atoms are located inside of V_{Ga}, the (*S*,*W*) value tends to approach the value for defect-free GaN with the increase in the number of hydrogen atoms in V_{Ga}. The same is true for vacancy clusters coupled with multiple hydrogen atoms, such as $(H_2)_{Ga}(V_N)_2$ and $(H_3)_{Ga}(V_N)_3$.

3.4.2. Samples presentation

For this study, a series of GaN NWs doped with Si and Mg at different cell temperatures were grown by plasma-assisted MBE on a low resistivity 2" Si (111) wafer used as a substrate. The cleaning and annealing processes prior to growth are the same as described in Section 2.1.4.1.2. An AlN buffer layer with a thickness of 3 nm was deposited prior to the growth of the wires. During the growth of the NWs, the substrate temperature was kept at 800°C. Plasma cell radio frequency power was set to 600W with a N_2 flux of 2.5 sccm, with a Ga/active N nominal flux ratio of 0.3. The nanowires were doped by exposing the samples to a Mg or Si flux. For the p-type doping series, the Mg cell temperatures were 220 (Mg1), 240 (Mg2), 260 (Mg3), and 280°C (Mg4), whereas

for n-type, the Si cell temperatures were at 900 (Si1), 920 (Si2), and 945°C (Si3). An undoped sample (U) grown in same conditions was used as a reference sample in the annihilation experiments.

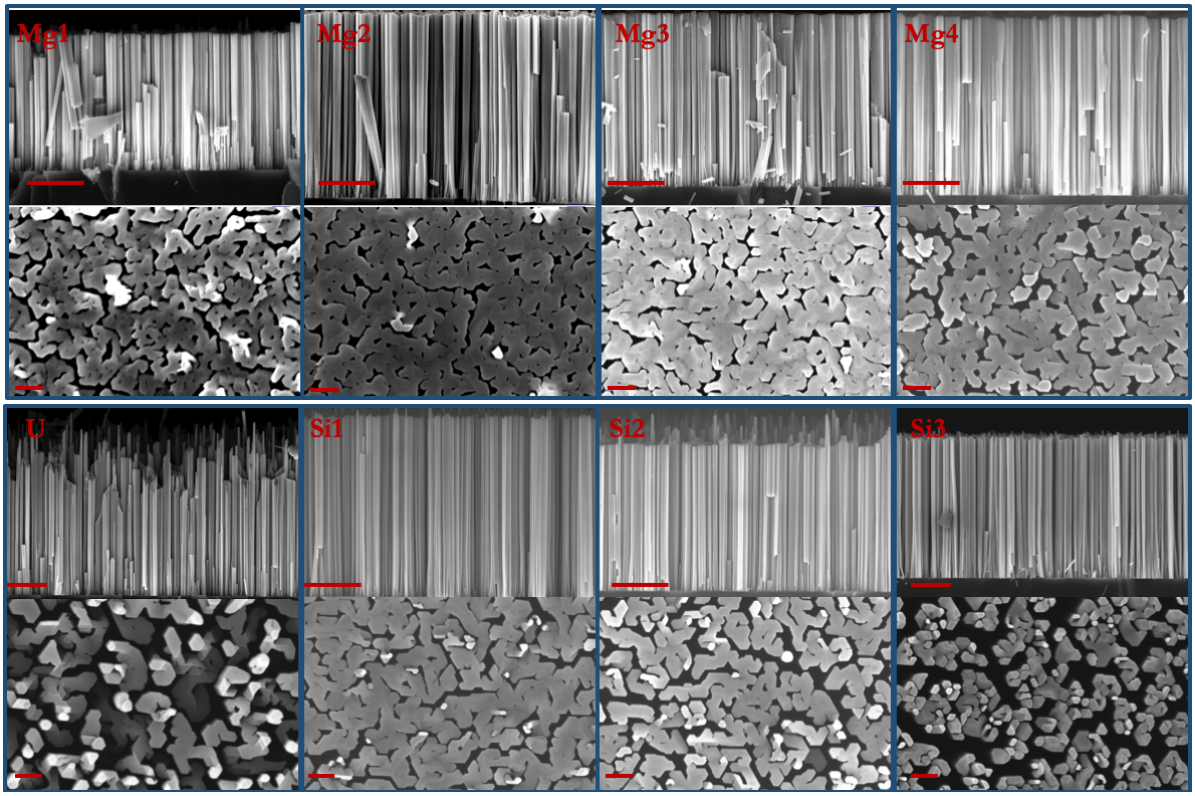

Figure 52. SEM side (upper images) and top views (bottom images) of all samples studied by positron annihilation. The scale line in red corresponds to 1µm for side view and 200 nm for top view.

Top and side-view morphology variations were observed by SEM (ZEISS Ultra 55 microscope). Figure 52 shows side and top views of all of the GaN NW samples. A high density of nanowires is required for high level signal during experimental studies of positrons annihilation. For this purpose, coalesced nanowire region of the samples was chosen. Using the top view of the SEM pictures the surface covering rates of the GaN NWs were calculated and are given in Table 4. After the growth, the samples were annealed at 800°C in N_2 atmosphere for 10 min. From the SEM pictures, the length and diameter of the NWs were estimated to be 2 to 3 µm and about 100 to 200 nm, respectively. Table 10 summarizes the cell doping temperature and the covering rate of each sample used for this study:

Sample	Sample	Cell temp (°C)	Covering rate
U	N2980	-	0.71
Mg1	N3005	220	0.93
Mg2	N3004	240	0.98
Mg3	N3017	260	0.87
Mg4	N2986	280	0.96
Si1	N2997	900	0.89
Si2	N2993	920	0.80
Si3	N3016	945	0.77

Table 10. Doping cell temperature and covering rates

3.4.3.Mg-related vacancies by positron annihilation

The effect of positron energy on the annihilation probability was studied for the undoped sample as well as for two Mg doped samples (Mg2 and Mg4). A HVPE-grown GaN layer was used as a reference for bulk layer, and experiments were performed in darkness and under illumination, to get information about the optically active defects in the nanowires.

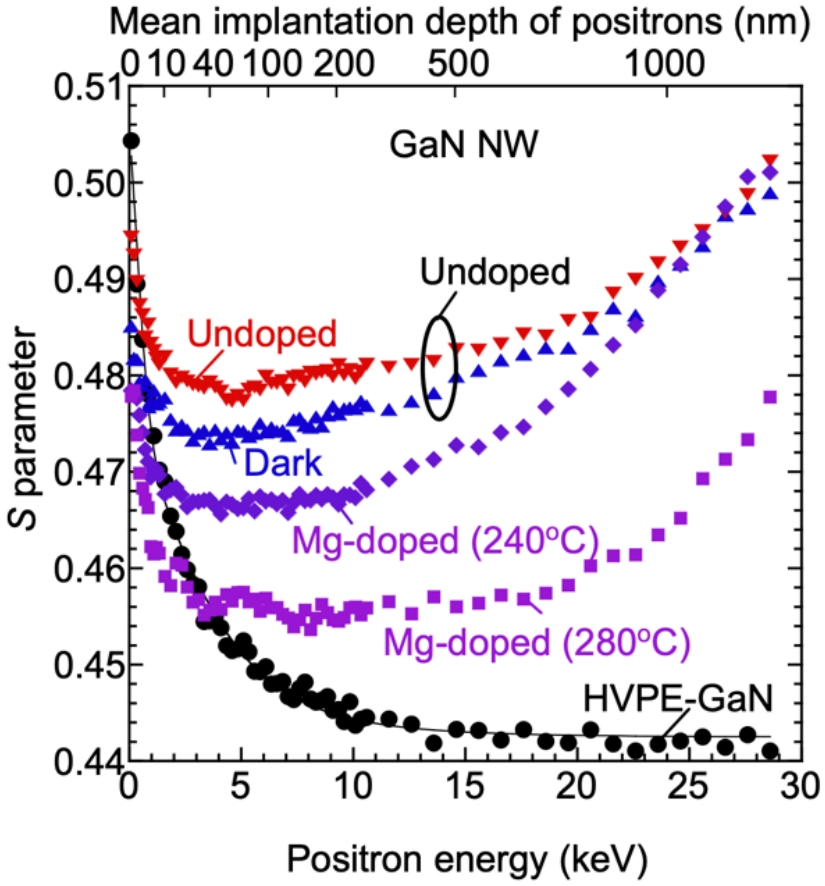

Figure 53. S parameters as a function of incident positron energy E for undoped sample measured in darkness and under illumination (blue and red symbols). S-E curves for Mg doped samples at 240°C and 280°C are given in purple. HVPE-GaN profile is given as a reference in black.

The mean implantation depth of positrons is related to the positron energy, thus information about the annihilation localization can be extracted from this study. Since the covering rate of the nanowires is not 1, the positrons annihilation in the Si substrate has to be considered.

Figure 53 shows the *S* values of the GaN NWs grown on the Si substrates as a function of incident positron energy *E*. When considering the HVPE-GaN, the increase of the *S* value with decreasing implantation energy shows a diffusion of positrons towards the surface. The total annihilation of positrons can be deduced from the experiments at energies higher than 15 keV, yielding a GaN defect-free positron diffusion length of 52±2 nm, typical for defect-free GaN (Uedono et al. 2013; Ishibashi and Uedono 2014).

The behavior of nanowires is thus different from that of bulk layers. Depending on the positrons' energy, the implantation takes place in both the NWs and in Si substrate. When looking at the undoped sample studied under darkness and under illumination, the *S* values saturated as *E*

increased up to 2 keV, followed by a plateau up to 10 keV. However, when increasing the positron energy and consequently the mean implantation depth up to around 1 μm, an increase of the annihilation probability can be observed, assigned to the increased annihilation probability of positrons in the Si substrate. The same behavior is observed in darkness and under illumination. However, the observed increase in the *S* value under illumination with respect to darkness in the 0-20 keV range suggests the presence of optically active defects in NWs. No illumination effect on the *S* value was observed for the Si substrate (E>20 keV). For the two Mg-doped samples, experiments show a decrease of the S value below E=20 keV with increasing doping cell temperature. Two possible explanations for this can be considered : either a decrease of the number of vacancies for increasing doping level or the reduction of positron trapping probability by vacancy-type defects due to the change in the vacancy charge state from negative (neutral) to positive due to a change in the Fermi level position (Uedono et al. 2015, 2018) with increasing doping.

Indeed, as stated before, positive charged vacancies do not attract the positrons as in the case of negatively (neutrally) charged vacancies. The positrons are instead repelled by the vacancies, who become invisible to the different defect related positron detection methods (Krause-Rehberg and Leipner 1999).

3.4.4. Vacancy-type defects in GaN NWs and doping effects

The identification of the annihilation sites can be determined by looking at the (S,W) parameters and comparing them with the calculated values for some of the predominant vacancy-type defects in GaN.

Due to the nanowire geometry, positrons implanted in the samples are expected to partly annihilate at the lateral surface of the NWs. Doppler broadening spectra were measured at E=5.1 keV by using the coincidence technique, since at this specific energy, the positron annihilation at the top surfaces of NWs is negligible and implantation takes place only in the NW, without reaching the Si substrate. The (*S*, *W*) values were obtained from those spectra and are plotted in Figure 54, for as-deposited and annealed samples, in darkness and under illumination conditions.

The different S and W parameter couples for the theoretically calculated vacancy sites are also represented in blue. Since incorporation of O and H impurities is favored on m-plane due to the NW geometry, complexes between these impurities and vacancies are also represented.

3.4.4.1. Darkness condition

The (S,W) values for the 8 samples in darkness conditions and before annealing are represented in Figure 54a (left). From these values, different types of vacancies have been attributed to the different series of samples as follows:

- **Undoped sample:** the major defect species in the undoped sample was identified as vacancy-oxygen complexes such as $V_{Ga}(O_N)_4$;

- **Si-doped samples:** values for (*S*,*W*) parameters have been found to be very close to a couple of vacancy type defects such as V_{Ga}, $V_{Ga}V_N$, $V_{Ga}(O_N)_4$ and H_{Ga}. With increasing of the doping level (Si1 → Si2 → Si3), main vacancy type defects were found to be $V_{Ga}(O_N)_4$, similarly to that in the undoped sample. This was assigned to a recombination between V_{Ga} and Si, similar to the case of Si-doped $Al_xGa_{1-x}N$ (Uedono et al. 2012). The probability of formation of V_{Ga} decreases as the Fermi level position increases (Van de Walle and Neugebauer 2004), thus increasing the defects concentration in Si-doped samples;

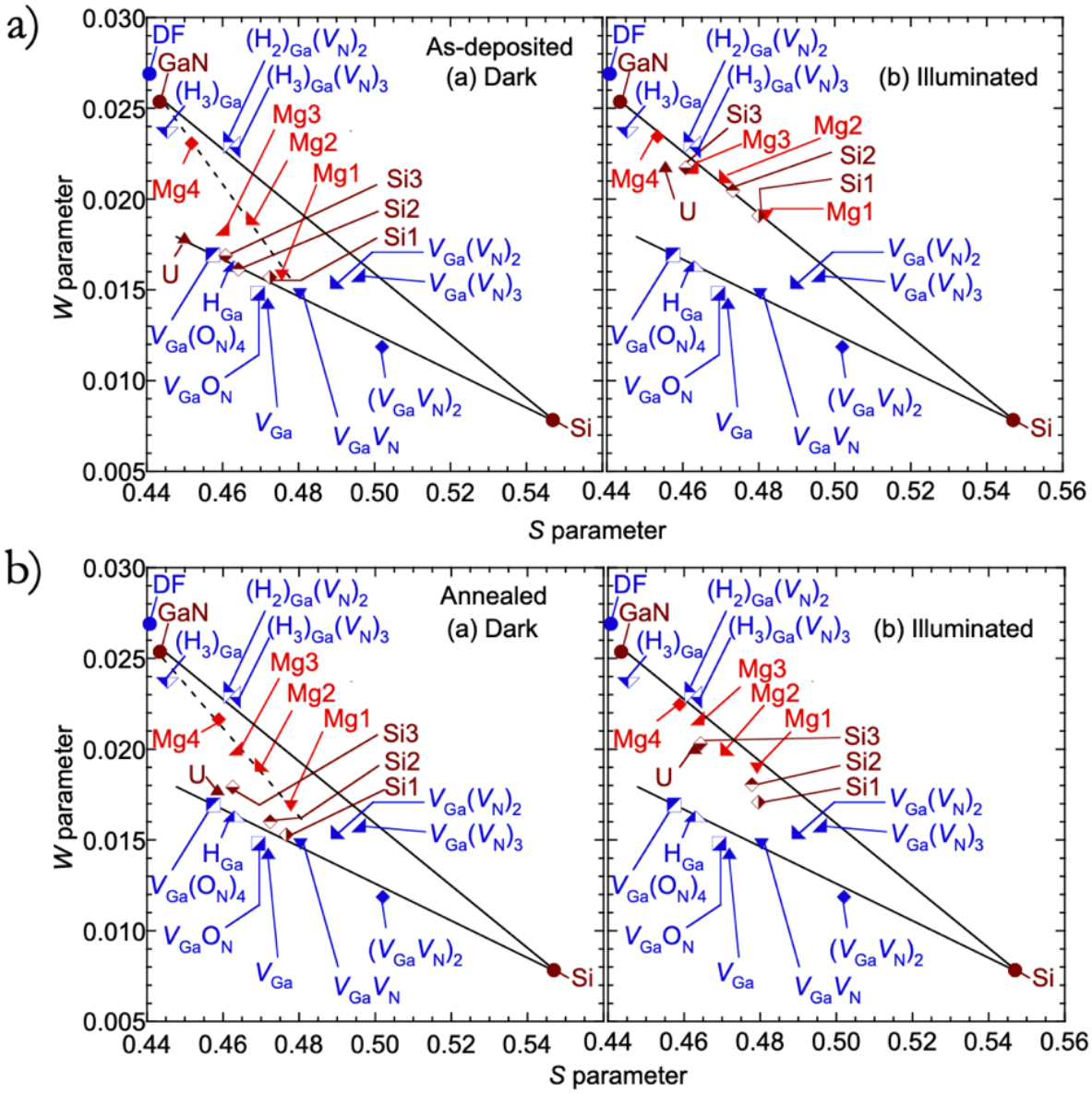

Figure 54. a) (S,W) values (brown and red) corresponding to annihilation of positrons in GaN NWs for undoped (U), Mg-doped (Mg1, Mg2, Mg3, and Mg4), and Si-doped samples (Si1, Si2, and Si3). Measurements were done in darkness (left) and under illumination (right). (S,W) values for HVPE-GaN (denoted as GaN) and Si are shown as references (brown for positron annihilation in defect-free (DF), VGa, VGa(VN)n, (VGaVN)2, and their complexes with oxygen and hydrogen).b)(S,W) values (brown and red) corresponding to annihilation of positrons in GaN NWs after 800°C annealing in darkness (left) and under illumination (right).

- **Mg-doped samples:** at low doping levels (Mg1) the (*S*,*W*) value is close to that of Si doped samples, suggesting that the major defects in this sample were similar to that of the Si-doped sample fabricated with a low T_{cell}. As T_{cell} increased, the (*S*,*W*) values tended to approach the value for defect-free GaN. However, as explained previously, the change in the charge state from neutral to positive reduces the positron trapping probability by vacancy type defects.

3.4.4.2. Illumination effect

Interestingly, the illumination shifted the (*S*,*W*) values, approaching the line connecting the values for GaN and Si, as observed in Figure 54 (right). Under illumination conditions, the transition of the charge state of vacancy-type defects from positive to neutral (or neutral to negative), increases the trapping probability of positrons (Krause-Rehberg and Leipner 1999). Thus, the observed change in the (*S*,*W*) value for all the samples can be attributed to the capture of photon-excited electrons by vacancy-type defects in the GaN NWs. Because the (*S*,*W*) values under illumination is close to the values for vacancy clusters containing hydrogen atoms, such as $(H_2)_{Ga}(V_N)_2$ and $(H_3)_{Ga}(V_N)_3$, these defects are possible candidates for optically active defects observed in the samples.

3.4.4.3. Annealing effect

The same studies were done on the samples annealed at 800°C in N atmosphere and are presented in Figure 54b. After annealing, the (*S*,*W*) values tended to shift towards the lower right, but without a major influence on the vacancy defects reduction. The proximity to $(V_{Ga}V_N)_2$, $V_{Ga}(V_N)_2$, and $V_{Ga}(V_N)_3$, located in the lower right in the *S*–*W* plot suggest a vacancy clustering effect of annealing on the samples.

3.4.5. Conclusion

Positron annihilation experiments in GaN NWs allowed us to identify the main vacancy type defects in these structures, which are predominantly V_{Ga} coupled with impurities such as oxygen and hydrogen. However, experiments become more difficult when considering Mg doping, since the positron trapping probability is reduced due to a change in the charge state repealing the positrons. Illumination experiments suggested the presence of optically active defects in NWs, such as $(H_2)_{Ga}(V_N)_2$ and $(H_3)_{Ga}(V_N)_3$ complexes. Annealing of the samples did not change the overall configuration of predominant vacancies, but clustering of vacancy-type defects was observed.

3.5. *pn*-junction visualization in GaN NWs

We have shown so far that the nanowire geometry is indeed adapted for the achievement of highly doped GaN. However, the behavior of Mg and Si dopants is not as in layers, since it was observed that due to preferential incorporation on m-plane side walls, Mg concentration is higher in the outer shell of the nanowires that in the core. In the case of Si, the dopants tend to segregate towards the shell above a given concentration. To conclude the study of doping of GaN NW, we have performed electrical experiments on a simple *pn* junction, that allowed us to get information about the electrical characteristics through EBIC measurements.

3.5.1. Sample presentation

Sample #2 experimental growth conditions are described in Section 3.3.1.1. As a summary, the Si doping cell temperature for the n-type GaN was set at 900°C, whereas Mg doping cell temperature was 240°C, corresponding to a Mg concentration of $(2.17\pm0.32)\times10^{19}$ at.cm^{-3} as estimated through EDX experiments. Based on the work of Z. Fang concerning Si-doping of GaN nanowires, the Si carrier concentration in this sample can be estimated to be $N_d=(6\text{-}8)\times10^{18}$ cm^{-3} (Fang et al. 2015). The ITO electrical contacts were deposited on a more coalesced part of the sample, avoiding short-circuiting the *pn* junction during direct metal deposition following the procedure described in Section 2.2.2.1.

3.5.2. EBIC on as-grown sample

EBIC characterization inside the SEM in the preamplification set-up (defined in Section 2.2.3.1.1) was performed on as grown nanowires. The aim of this EBIC characterization is purely qualitative, quantitative characterization demanding complementary experiments.

The EBIC studies were performed with an electron beam energy of 30 kV and a beam current of 400 pA. The electron-hole pairs density generated in this experimental configuration for various lifetimes varying between 100 ps and 100 ns is represented in Figure 55. Nonetheless, typical values for carrier lifetime in GaN material vary between 0.1 and 7 ns (Bandić et al. 1998; Grazzi et al. 2001; Kumakura et al. 2005).

Under these experimental conditions, the electron hole pair density generated inside the sample is no higher than 2×10^{16} cm^{-3}, which is lower than the minority carrier concentration under equilibrium inside the sample. The experiment is thus in low injection conditions.

Nevertheless, the Monte Carlo simulations for these specific conditions show a penetration depth of the interaction volume of 3 μm, making the experimental conditions unsuitable for single nanowire studies.

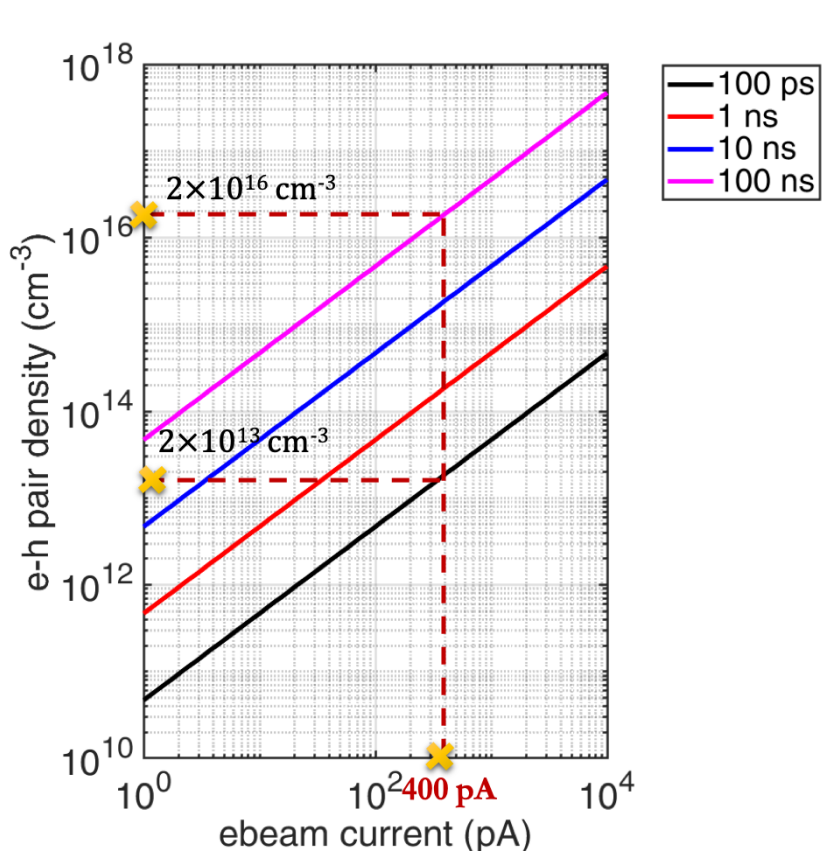

Figure 55. Injection conditions for GaN NW sample.

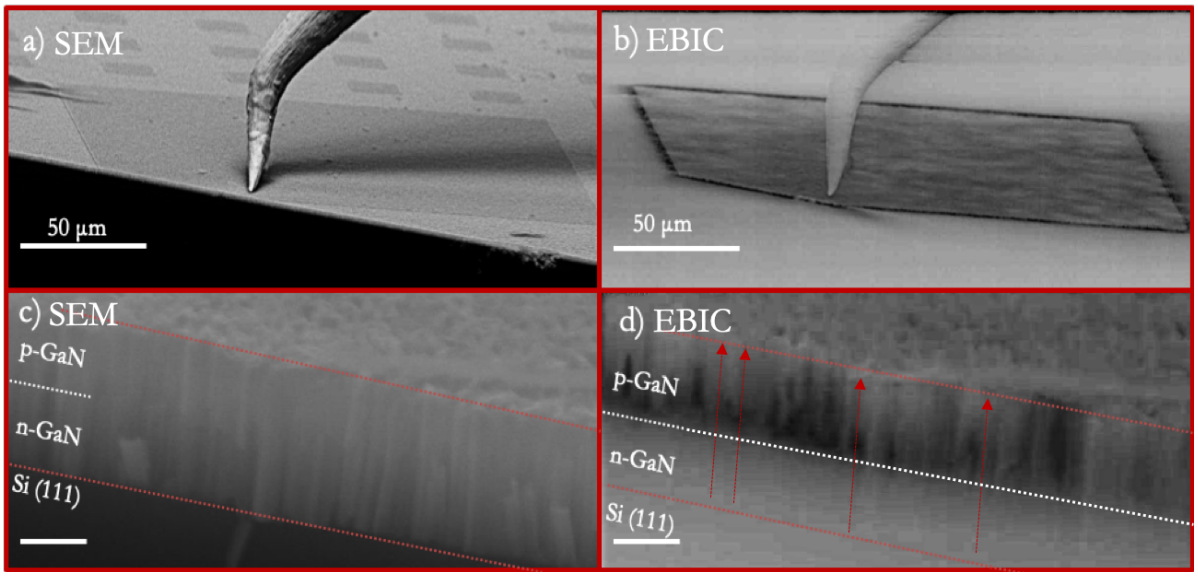

Figure 56. Bird-eye view of contacted electrode of sample N2714 in (a) SEM and (b) EBIC image. Side view of the NWs as seen in (c) SEM and (d) EBIC showing an inhomogeneous signature of the EBIC signal. The bar scale in the side views correspond to 1 µm.

Figure 56 illustrates the SEM (left) and EBIC (right) corresponding images on a cleaved diode of sample #2 without polarization (0V bias). Due to the high interaction volume, since the penetration depth for such a high e-beam current is of the order of 3 µm, the electric field inside of the nanowires under the entire electrode appears clearly in Figure 56b.

The electric field intrinsic to the *pn* junction inside the GaN NWs was investigated in side-view as shown in the SEM image in Figure 56c. The p and n respective parts of the junction are delimited by the red and dashed lines. The equivalent EBIC image of these nanowires at 0V bias (thus without polarization) is illustrated in Figure 56d. The EBIC signal associated with the presence of an electric field at the pn junction does not appear as homogeneous. We have studied the EBIC signal evolution with respect to the position on the nanowire on different individual nanowires as shown by the red arrows in Figure 56d.

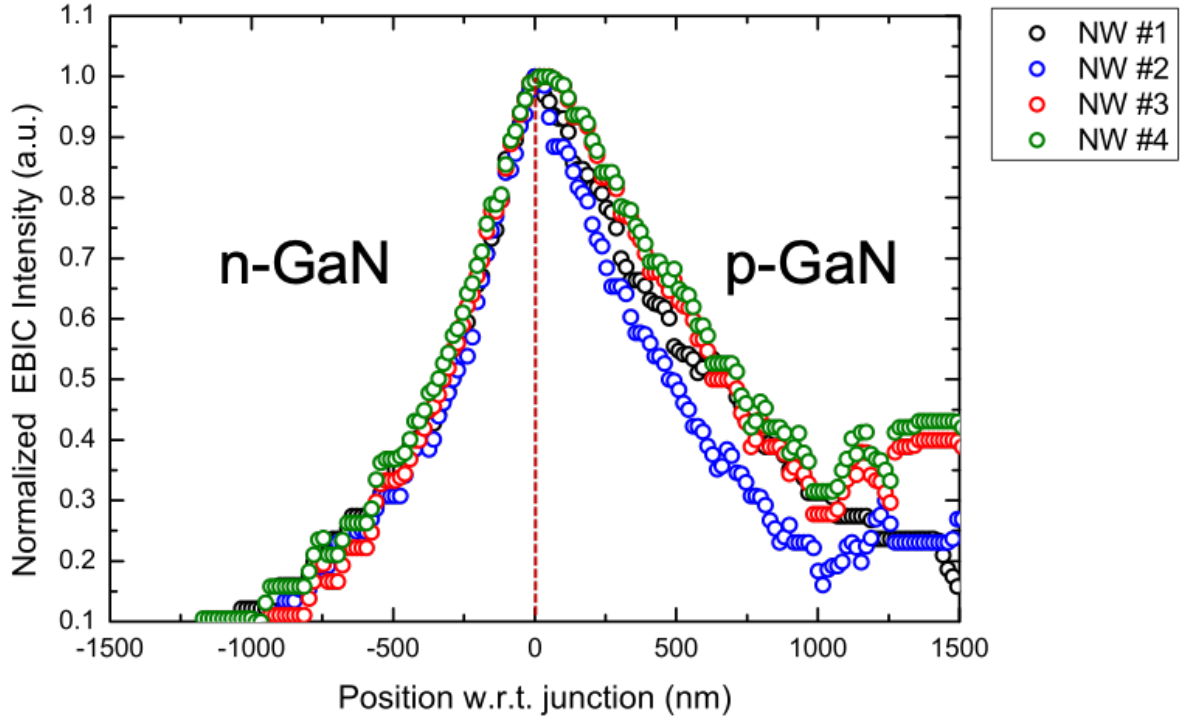

Figure 57. Normalized intensity EBIC profiles in different NWs showing the SCR dispersion on the same sample.

Figure 57 illustrates the normalized intensity of the EBIC signal profiled on four different nanowires from sample #2. The n and p respective regions are delimited by a red dashed line and the origin of the profiles is defined with respect to the position of the junction.

The electrical parameters of the junction such as the minority carrier diffusion length and effective doping level were estimated in Figure 58 for each of the NWs by fitting the EBIC signal using the method described in Section 2.2.3.2.2. Since the experiment takes place in low injection conditions, the exponential dependence fitting was applied for the extraction of the minority carrier diffusion length.

The effective doping (N_{eff}) characterizing the junction can be obtained from the space charge region width (W_D) of the four individual nanowires by assuming a built-in potential approximated to the band gap voltage in GaN (qV_{bi} approximately 3.43eV), from the equation:

$$N_{eff} = \frac{2\varepsilon_{Al_xGa_{1-x}N}}{qW_D^2} \times (V_{bi} - V) \quad (72)$$

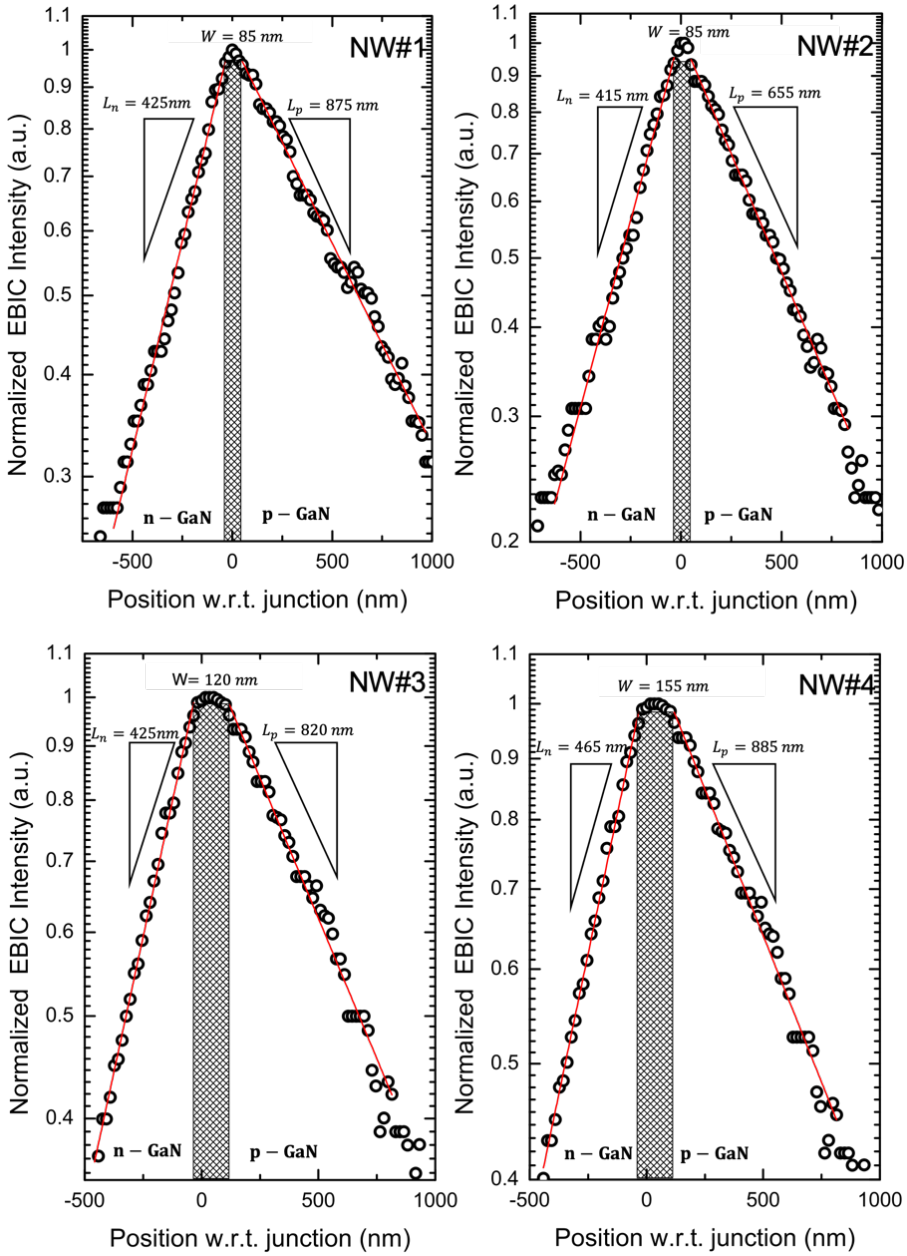

Figure 58. EBIC profile as a function of the position with respect to the junction for a) NW#1 and b) NW#2.

The junction parameters determined for the four nanowires are summarized in Table 11:

NW	SCR (nm)	L_n(nm)	L_p(nm)	N_{eff}(cm^{-3})
#1	85	425±12	875±12	5×10^{17}
#2	85	415±14	655±14	5×10^{17}
#3	120	425±12	820±16	2.5×10^{17}
#4	155	465±12	885±16	1.5×10^{17}

Table 11. Junction parameters of the 4 NW from sample #2

Different information can be drawn from this study. The inhomogeneity of the *pn* junction electrical parameters is clearly evidenced. A qualitative analysis of this images gives an indication with respect to the NWs doping homogeneity. The dispersion of the EBIC current from NW to NW is an indication that the electrical characteristics of the *pn* junction are not uniform.

The space charge region extension is mainly on the Mg-doped part of the NW. From the charge neutrality equation, this information suggests a lower doping in the Mg-doped part with respect to the Si-doped part of the junction. The effective doping gives a lower limit of the acceptors and donors level in the sample. By looking at the space charge region width extension with respect to the junction, we can conclude that the effective doping showing a level of (1-5)×10^{17} cm^{-3} is related to the acceptor's concentration in the nanowires.

These results are in agreement with previous studies on individually contacted nanowires in the work of Z. Fang et al (Fang et al. 2018). The results have shown nanowire to nanowire behavior dispersion in terms of electrical I-V and EBIC response. The conduction mechanism suggested for these nanowires was space charge limited current, with a acceptor concentrations of N_a=(2-3)×10^{17} cm^{-3}, assuming a donor concentration N_d=(2-3)×10^{18} cm^{-3}, as determined by EBIC experiments.

Regarding the minority carrier diffusion length, very large values with respect to literature have been determined for this particular sample. Literature reports on minority carrier diffusion lengths in GaN material show values between 15 nm and several micrometers. Table 12 summarizes different values of minority carrier diffusion lengths in GaN layers and nanowires:

Reference	N_D (cm-3)	L_n (nm)	N_A (cm-3)	L_p (nm)
(Fang et al. 2018) (NW)	(2-3)×10^{18} cm^{-3}	77	(2.8-2.9)×10^{18} cm^{-3}	122
(Fang et al. 2018) (NW)	(2-3)×10^{18} cm^{-3}	40	(2.8-2.9)×10^{18} cm^{-3}	170
(Tchoulfian et al. 2014) (microW)	3.5×10^{18} cm^{-3}	15	3×10^{18} cm^{-3}	57
(Bandić et al. 1998) (bulk)	UID	280		
(Grazzi et al. 2001) (bulk)	5×10^{17} cm^{-3}	248		
(Gonzalez et al. 2001) (bulk)	No data	80	No data	70
(Moldovan et al. 2007) (bulk)	(2-3)×10^{18} cm^{-3}	24	(1-2)×10^{17} cm^{-3}	33.7
(Matoussi et al. 2003) (bulk)	1.35×10^{17} cm^{-3}	720		
(Kumakura et al. 2005) (bulk)	4×10^{17} cm^{-3}	250		
(Kumakura et al. 2005) (bulk)	4×10^{18} cm^{-3}	250		
(Kumakura et al. 2005) (bulk)			4×10^{18} cm^{-3}	950
(Kumakura et al. 2005) (bulk)			1×10^{19} cm^{-3}	700
(Kumakura et al. 2005) (bulk)			3×10^{19} cm^{-3}	220
(Chernyak et al. 2000) (bulk)	2×10^{17} cm^{-3}	350	3-4×10^{17} cm^{-3}	550-1700

Table 12. Literature values for minority carrier diffusion lengths in GaN.

The dispersion of these values comes from the doping levels in the samples, but are also subjected to errors due to the different experimental conditions. For instance, sample preparation could be responsible for the small value of 23 nm found for the diffusion length in the work reported by Moldovan et al (Moldovan et al. 2007), whereas experimental conditions and high beam acceleration voltage could account for the large diffusion length of 720 nm found in reference (Matoussi et al. 2003). Interestingly, the work of Chernyak et al (Chernyak et al. 2000) presents a study of the minority carriers diffusion length under electron beam irradiation. In this study, the increase of the minority carrier diffusion length of electrons in p-GaN from 550 nm to 1.7 μm depending on the irradiation time has been associated to the charging of deep metastable centers associated to Mg doping. The irradiation time had no effect on the minority carrier diffusion length of holes in n-GaN which was insensitive to irradiation effects.

3.6. Summary of Chapter 3

Chapter 3 was dedicated to the study of GaN nanowires in terms of dopant inhomogeneity and related defects. First studies of Mg-dopant incorporation in GaN nanowires were concluding concerning the inhomogeneous repartition of Mg atoms in NWs, with a preferential m-plane incorporation and Mg-H complex formation. Interestingly, a high Mg concentration was determined in the samples under study, with concentrations of the order of $(1\text{-}3)\times10^{20}$ at.cm^{-3}

The study of vacancy defects formation in GaN NWs showed that the main type defect in both Si-doped, Mg doped and undoped samples are V_{Ga} complexes with hydrogen and oxygen. These defects proved to be optically active, with no great impact of annealing.

EBIC experiments performed on as-grown nanowires depicted an effective doping of the *pn* junctions of the order of $(1\text{-}5)\times10^{17}$ cm^{-3} most probably limited by the acceptor concentration. The inhomogeneous doping was qualitatively visualized in the samples and high minority carrier diffusion lengths between 400-500 nm for holes in n-GaN and of the order of 600-800 nm for electrons in the p-GaN have been explained by either charging of deep-defects associated with Mg, experimental conditions or to a low donor/acceptor concentration inside the samples.

"Failure is success in progress."

4. Binary AlN NWs: from doping to UV LEDs realization

Studies on GaN NWs provide additional information about doping and defect formation in nitride materials. However, our main purpose being the realization of DUV LEDs, this chapter will be dedicated to doping of $Al_xGa_{1-x}N$ material. The need for efficient p-type doping of Al-rich $Al_xGa_{1-x}N$-based DUV LEDs has been a point of interest of various research groups in the past decade. Being a well-known issue in the field of nitrides, efforts have been made in order to improve the Mg incorporation in AlN material, as well as to increase the doping level concentration, with the common aim of developing efficient $Al_xGa_{1-x}N$-based DUV LEDs for disinfection purposes. Nonetheless, some of the published results are controversial, the physics behind $Al_xGa_{1-x}N$ doping mechanisms and of electrical current conduction is not fully understood (Mi et al. 2016).

This chapter deals with the major problematics one encounters when studying $Al_xGa_{1-x}N$ *pn* junctions, especially concerning doping and electrical characterization. While the first part is devoted to investigations on $Al_xGa_{1-x}N$ material of 60% Al composition, a complete description of doping and transport mechanisms inside AlN NW junctions is developed in the second part of the chapter. The results presented in this fourth chapter have been partially published in one article (Siladie et al. 2019), and is subjected to one deposited patent.

4.1. $Al_xGa_{1-x}N$ nanowire *pn* junctions for UV-LEDs

Being a ternary alloy, one of the main difficulties we have encountered while studying $Al_xGa_{1-x}N$ NW based DUV LEDs concerns alloy inhomogeneity and control of dopant incorporation in such alloys. As already discussed previously, the maximum EQE obtained on planar LEDs does not exceed 20.3% for an emission wavelength of 275 nm (Takano et al. 2017), whereas the main achievements on NW based $Al_xGa_{1-x}N$ LEDs are coming from results in the group of Professor Zetian Mi (Mi et al. 2015; Djavid and Mi 2016), without in detail studies concerning transport mechanisms.

The growth control of $Al_xGa_{1-x}N$ NWs on GaN stems was previously optimized in our group during the PhD of Matthias Belloeil (Belloeil 2017) and of Aurelie Pierret (Pierret 2013). I have adapted these optimized growth conditions to all of the samples presented in this chapter. Even though a series of samples with different AlN content were grown for optimization of $Al_xGa_{1-x}N$ *pn* junction, this part of the study will be mainly focused on a particular sample with 60% Al composition and properties of this *pn* junction will be presented further.

4.1.1. Growth conditions of $Al_{0.6}Ga_{0.4}N$ NW sample

The 60% $Al_xGa_{1-x}N$ NW *pn* junction sample (N2551) was grown by PA-MBE on a highly n-doped 2" Si (111) wafer cleaned by using the standard cleaning process (Section 2.1.4.1.2). A 3 nm AlN buffer was deposited at high Al temperature (growth rate of 0.2ML/s) and high substrate temperature (Auzelle et al. 2015).

As stated before, ternary alloys growth is more difficult to control because of the difference between elements reactivity. Therefore, $Al_xGa_{1-x}N$ nanowires are grown on a GaN base that ensures the epitaxial relationship with the Si (111) substrate.

The GaN nanowires growth conditions are controlled in order to favor adatoms diffusion on top of the bases. The GaN base has been doped at a Si doping cell temperature of 900°C in order to ensure the electrical conductivity with respect to the substrate. Then, the $Al_{0.6}Ga_{0.4}N$ nanowire growth is obtained by limiting the Ga atoms diffusion with respect to the Al atoms, by controlling the flux. The doping of the $Al_{0.6}Ga_{0.4}N$ *pn* junctions was obtained by using Si at a cell temperature of 900°C and Mg at a cell temperature of 220°C.

The SEM images of the sample after growth is given in Figure 59. The length of the GaN stems is of approximately 700 to 750 nm whereas the length of n and p parts are estimated to be 750 nm for both parts, with a radius varying from 20 nm for the GaN stem up to 80 nm for the $Al_{0.6}Ga_{0.4}N$ p-doped region, as shown in the schematics in Figure 59a.

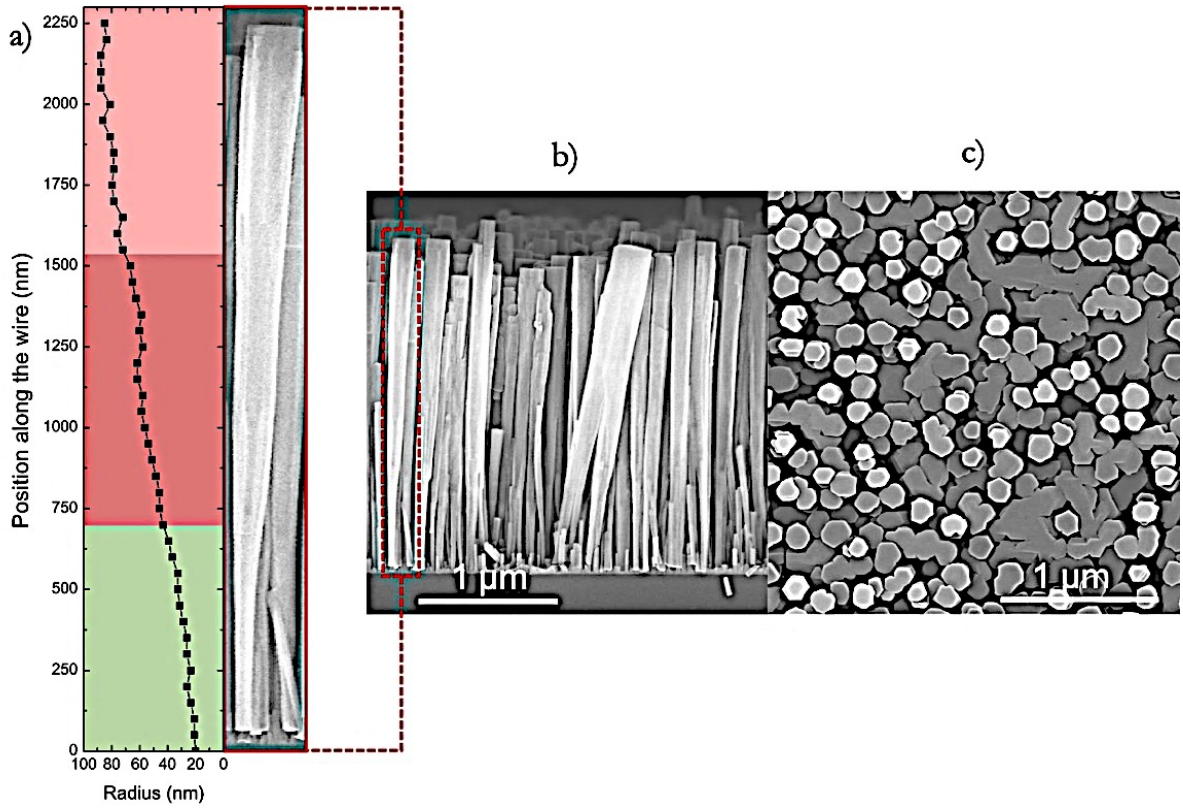

Figure 59. a) Radius dimension of an individual nanowire of the $Al_{0.6}Ga_{0.4}N$ sample (N2551). SEM images in b) side view and c) top view.

4.1.2. Compositional fluctuations inside $Al_{0.6}Ga_{0.4}N$ NWs

To quantify the Al composition in the nanowires, we have performed EDX spectroscopy showing an average of 65% Al composition on individually dispersed nanowires. The Al composition in the nanowires was found to be inhomogeneous, ranging from 55 up to 75% Al composition along the nanowire length, related to the difference between Al and Ga atoms in terms of diffusion time and Al atoms preferential incorporation. The Al composition was found to be higher in the outer-shell of the nanowire, suggesting an $Al_{0.6}Ga_{0.4}N$ core - AlN shell like structure.

These observations agree with previous studies from our group related to inhomogeneous $Al_xGa_{1-x}N$ growth of nanowires for high Al compositions. A pure AlN insertion was observed by STEM analysis in a 85% Al composition $Al_xGa_{1-x}N$ NW (Pierret et al. 2013a). Micro-photoluminescence experiments performed on individual $Al_xGa_{1-x}N$ nanowires have shown a quantum-dot like behavior due to compositional fluctuations (Belloeil et al. 2016).

After assessing the presence of an inhomogeneous Al composition in our sample, more in detail characterization inside the $Al_{0.6}Ga_{0.4}N$ nanowires were achieved by TEM-EDX correlated analysis performed by Dr. Eric Robin in a probe corrected FEI Titan Themis equipped with four windowless silicon drift detectors and are presented in Figure 60.

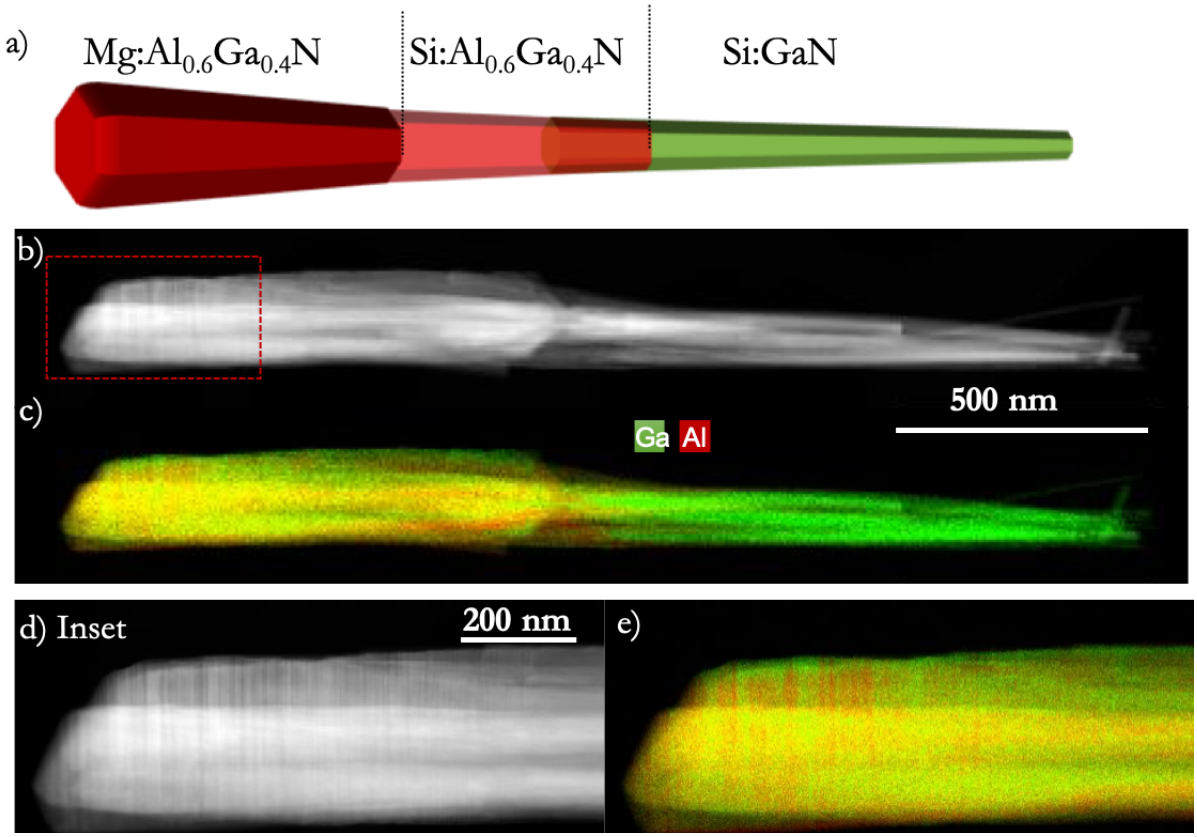

Figure 60. a) Individual nanowire schematic from sample N2551 with identification of the respective regions. b) TEM image of an individual nanowire and c) the correspondent EDX mapping of Ga (green) and Al (red) atoms. d) TEM inset and e) corresponding EDX mapping of Ga and Al atoms on the upper part region of the nanowire corresponding to Mg-doped $Al_{0.6}Ga_{0.4}N$.

Figure 60a shows the schematic of an individual nanowire with the respective regions as determined from EDX-TEM images presented in Figure 60b and c. An inset is done on the upper part of the nanowire corresponding to Mg-doped region and is illustrated in Figure 60d and e. The Ga atoms are represented in green whereas Al atoms appear in red on the corresponding EDX map presented in Figure 60b and Figure 60e.

On one hand, the TEM-EDX correlated images of the individually dispersed nanowire from sample N2551 presented in Figure 60b and c show core-shell inhomogeneous alloy formation at the transition region between n-doped $Al_{0.6}Ga_{0.4}N$ nanowires and GaN stems. The inhomogeneous distribution of Al-Ga atoms is visible in the n-type doped part of the sample where an AlN shell is evidenced around the GaN stems, with distinguishable Al rich and Ga rich regions in the sample.

On the other hand, in the Mg-doped part of the sample, an interesting superlattice-like configuration of AlN and GaN planes seems to be formed (inset in Figure 60d and e). Several TEM and EDX images were taken on the same sample at a region situated in the Mg-doped part of the sample at higher magnification. This region was studied in the inset zoom-in presented in Figure 61 on the edges of the Mg-doped $Al_{0.6}Ga_{0.4}N$ nanowires.

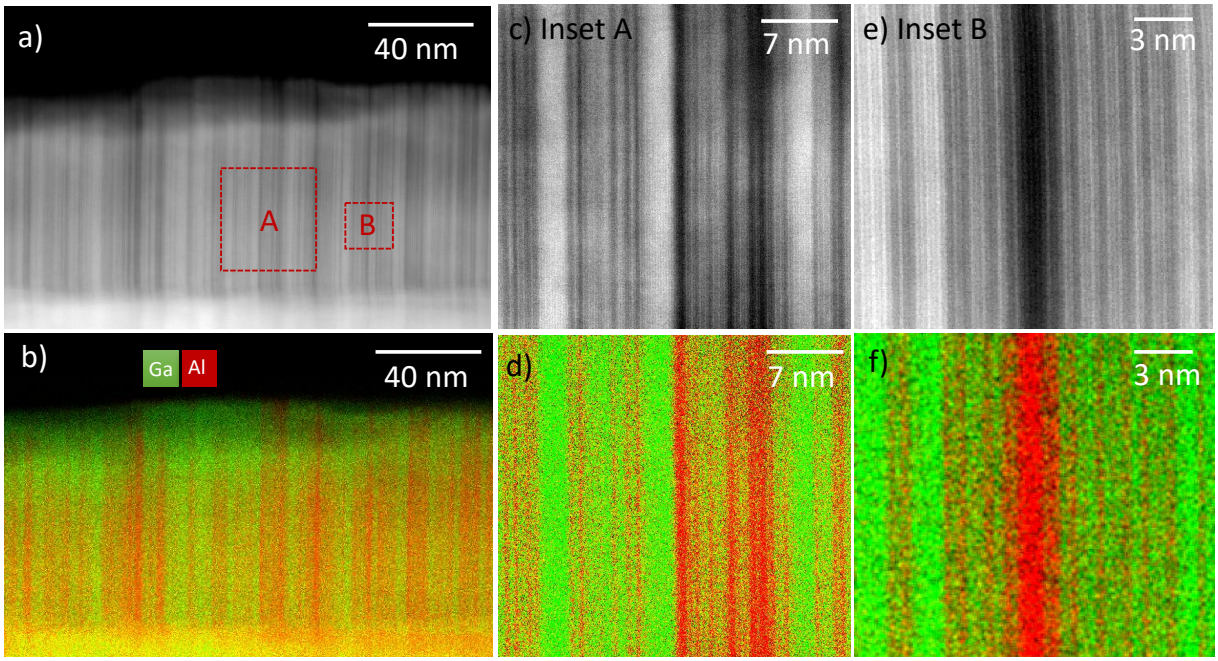

Figure 61. a) TEM image and b) EDX image of a region of the nanowire situated on the edge in the Mg doped part of the sample. C) TEM image and d) EDX image of inset A and e) TEM image and f) EDX image of inset B showing a superlattice arrangement of AlN and GaN planes

The p-doped $Al_{0.6}Ga_{0.4}N$ alloy presents nanoscale in-plane compositional inhomogeneities evidenced further in Figure 61c and d as well as in Figure 61e and f where TEM images and EDX respective maps are taken in the regions from the insets A and B in Figure 61a. The layers thickness is not constant, varying from atomic layer thick AlN and GaN up to 2 nm thick AlN plane. The planes distributions is similar to GaN QW separated by AlN barriers.

Surface kinetics plays an important role in the growth of ternary alloys due to the different Al and Ga adatoms desorption at the growth surface, different surface mobilities and residence times leading to a surface supersaturation of one of the two adatoms. However, apparent phase separation compositional inhomogeneity is not an intrinsic characteristic of $Al_xGa_{1-x}N$ alloys, but can be controlled by the growth conditions. The $Al_xGa_{1-x}N$ phase separation was previously observed also by various groups in the field, in $Al_xGa_{1-x}N$ /AlN nano-disks (Himwas et al. 2014) as well as in $Al_xGa_{1-x}N$ layers (Shen et al. 2006; Bryan et al. 2016).

This phase separation has a big impact on the efficiency of UV LEDs, leading to multiple emission peaks in electroluminescence due to enhanced carrier localization into the quantum well-like structure, linewidth broadening and red shift of the emission.

4.1.3. Optical properties by cathodoluminescence

Cathodoluminescence experiments were performed on dispersed nanowires at 5K in order to study the influence of the disordered alloy on the luminescence of $Al_{0.6}Ga_{0.4}N$ NWs.

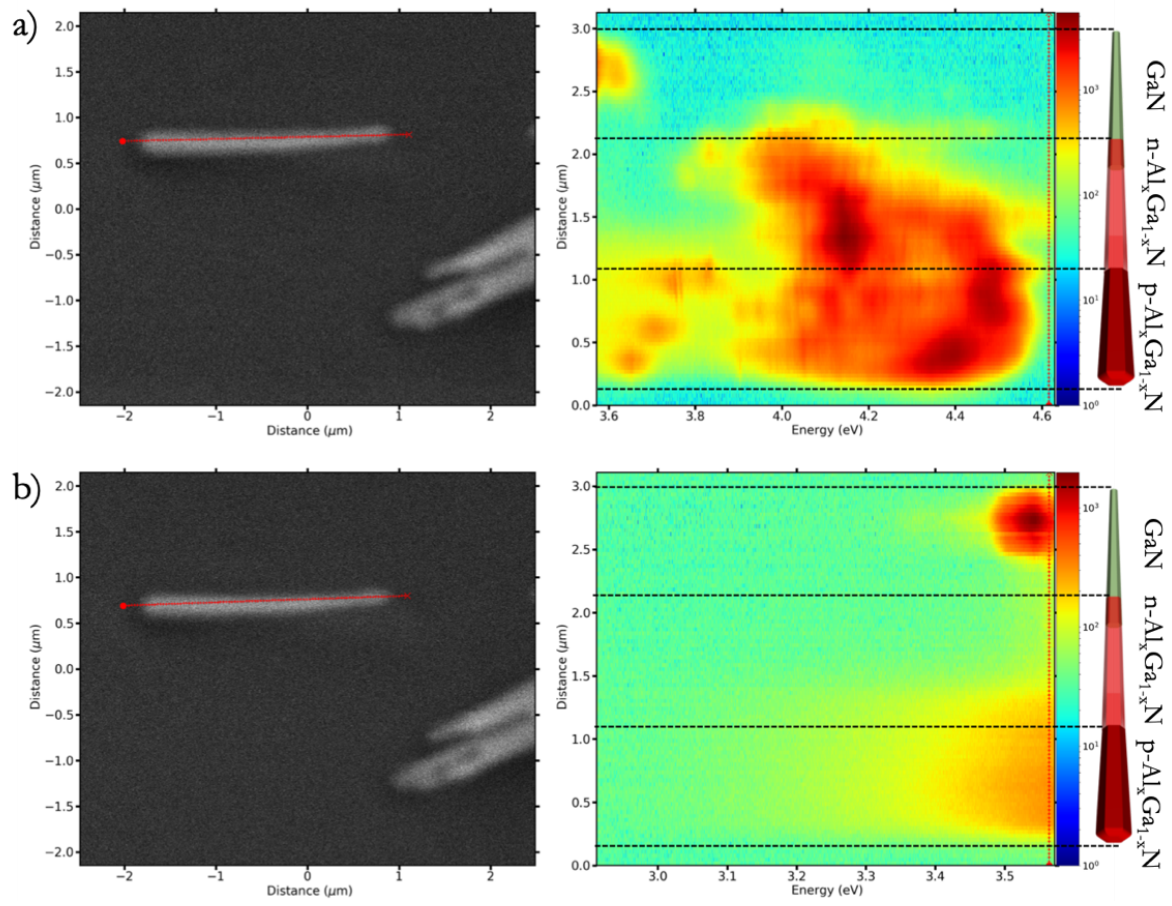

Figure 62. Individual nanowire cathodoluminescence mapping for energies between a) 3.6 and 4.6 eV b) 2.9 and 3.6 eV with associated AlN illustration and respective regions.

The cathodoluminescence mapping in logarithmic scale of one dispersed nanowire from sample N2551 is illustrated for energies comprised between 3.6 eV and 4.6 eV in Figure 62a and between 2.9 eV and 3.6 eV for Figure 62b. The different regions of the $Al_{0.6}Ga_{0.4}N$ nanowire have

been delimited on the mapping and the luminescence regions have been correlated to the respective regions of the nanowire (right side of the figure).

The upper part of the nanowire is identified as being the GaN stem showing an emission signal slightly above 3.50 eV corresponding to GaN band edge. The GaN emission band edge is shifted compared to the expected luminescence of the D^0X_A for strain free GaN at 3.47 eV. This blueshift of the transition may be due to the presence of the $Al_{0.6}Ga_{0.4}N$ shell around the basis. This could compress the GaN core leading to an emission at higher energy (Rigutti et al. 2011).

Regarding the $Al_{0.6}Ga_{0.4}N$ emission, a clear impact of doping is observed on the cathodoluminescence mapping, associated to different emission energies: the n-doped $Al_{0.6}Ga_{0.4}N$ region is emitting at energies between 4 eV and 4.4 eV with an intense signal at around 4.1 eV, whereas the p-type doping is associated to a higher energy emission between 4 and 4.6 eV, with a maximum emission at 4.4 eV corresponding to DAP transitions in the $Al_{0.6}Ga_{0.4}N$ band gap. This DAP transition consists of a relatively broad emission even at single nanowire level assigned to different atomic configuration. This shows that the random distribution of Ga and Al atoms leads to a broad DAP emission band.

Moreover, sharp emission lines associated to deep level luminescence and an extended emission signal at low energies (between 3.4 and 3.8 eV) appear in the Mg-doped $Al_{0.6}Ga_{0.4}N$ material.

4.1.4. EBIC evidence of the *pn* junction

4.1.4.1. Sample processing

Sample N2551 was processed and electrical characteristics of this sample were studied by EBIC characterization following the procedure described in Chapter 2.

Electrodes of different sizes were fabricated on top of as-grown nanowires. Ni/Au metal contacts were deposited with a thickness of 5 and 10 nm respectively and annealed for 10 min at 550°C under N_2 atmosphere.

4.1.4.2. Electrical characterization

The processed sample was studied in the IV configuration presented in Section 2.2.2.2. Tungsten tips of 500 nm diameter were used for contacting in direct mode configuration. The frontside contact was taken directly on the metallic electrode whereas the backside contact was taken on the Si (111) conductive substrate. The study of a diode of 50x50 μm^2 is discussed further.

The results have been normalized in current density by considering a surface filling factor of nanowires of 80%, as discussed previously.

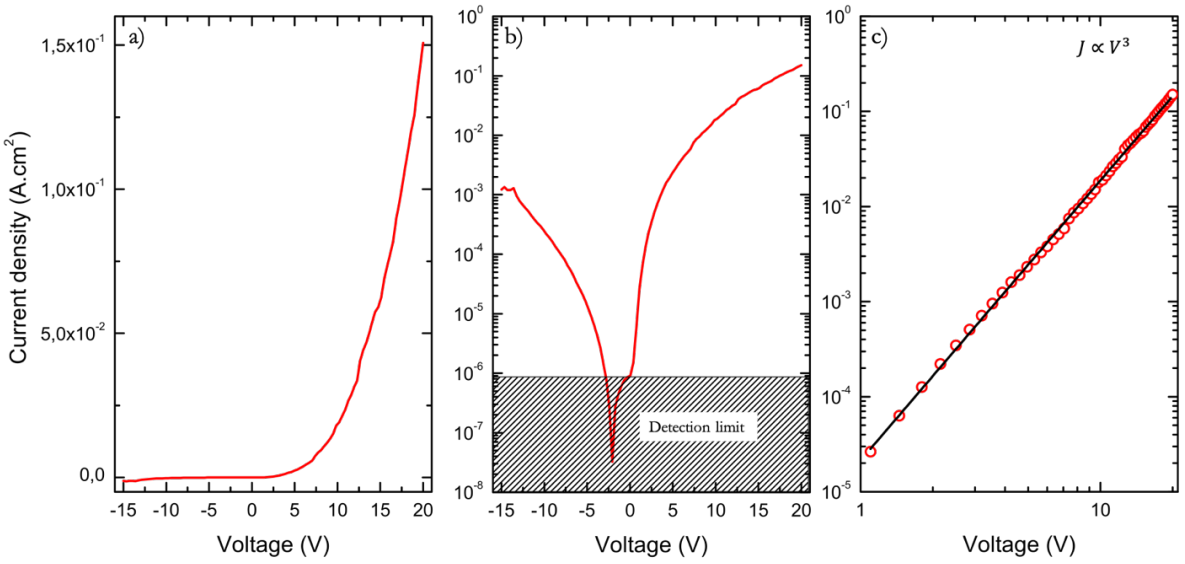

Figure 63. Current density-voltage characteristic of a diode in a) linear b) semi-logarithmic and c) log-log representation of forward regime with a $J \propto V^3$ fitting.

A rectifying behavior similar to that of a diode is obtained in the linear IV characteristic going from -15 V to 20 V, as shown in Figure 63, with a turn-on voltage of the diode at 8.1 V. If we have a look at the semi-logarithmic representation of the current-density variation with respect to the bias, the leakage current in reverse bias appears 2 orders of magnitude smaller that in direct bias under symmetric polarization (-15 V and 15 V). Considering the current limit of detection of the source meter, data below 10^{-6} A/cm^2 will not be considered. However, the sample does not present an ohmic behavior, but a $J \propto V^3$ power law dependence as shown in the log-log representation in Figure 63. This transport mechanism agrees with a SCLC conduction mechanism with a power coefficient of 3 corresponding to trap levels in the material.

In order to investigate the electrical activation of Mg dopant inside the *pn* junction, we have performed EBIC studies in the preamplification set-up (Section 2.2.3.1.1) on as-grown $Al_{0.6}Ga_{0.4}N$ NW. The study was done on a cleaved metallic pattern in side view, allowing the access to the first row of contacted nanowires. The samples were scanned with a beam voltage of 6 kV and a beam current of 30 pA, for which the excess carrier concentration generated by the electron beam with respect to the beam current were represented in Figure 64 for different carrier recombination lifetimes. The excess carriers generated in the sample varies between 2×10^{14} cm^{-3} and 3×10^{17} cm^{-3}. The space charge region width can be safely extracted from the EBIC signal due to the low injection conditions. These quite high excess carrier levels do not allow us to extract safely the carrier diffusion length assigned to minority carriers, since the electrons and holes concentration can be lower than the excess carriers, placing the experiment in high injection conditions for minority carriers.

The Casino Simulated interaction volume for such a low beam energy shows a penetration depth of 200 nm. This allows us to profile individual nanowires even in as-grown configuration.

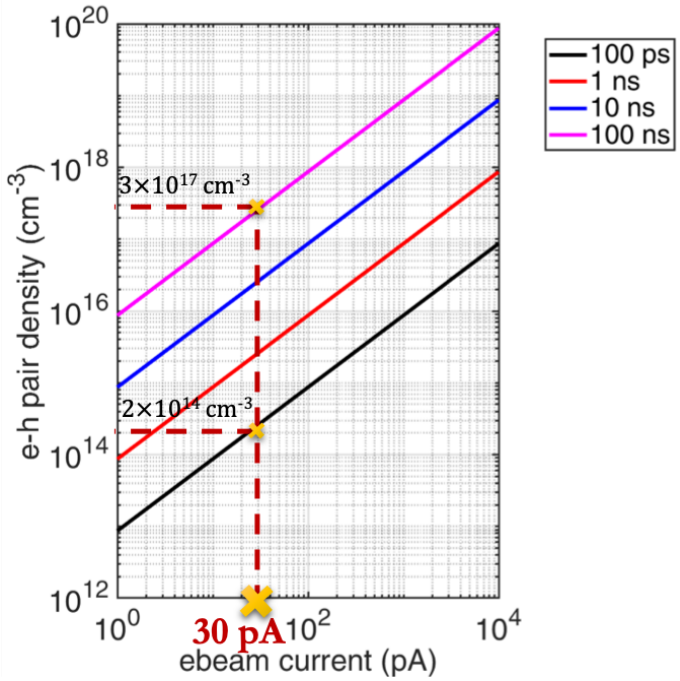

Figure 64. Injection conditions for the $Al_{0.6}Ga_{0.4}N$ sample for 6kV acceleration voltage depending on the lifetime.

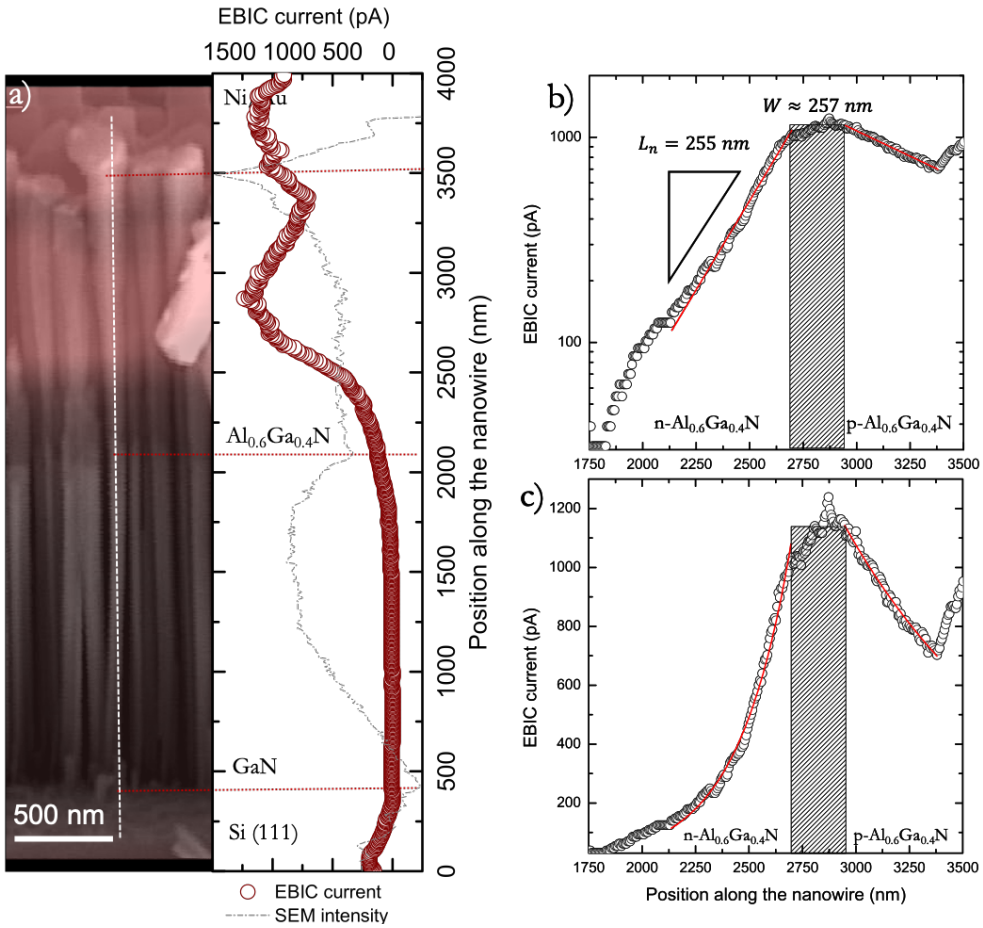

Figure 65. a) SEM and EBIC images superposition aligned with the EBIC signal plotted with respect to the position along the nanowire (red dots) and SEM intensity (grey dot line) showing a clear signal in the $Al_{0.6}Ga_{0.4}N$ region of the nanowire corresponding to the pn junction. EBIC signal variation from the $Al_{0.6}Ga_{0.4}N$ region with respect to the position along the NW in b) semilogarithmic and c) linear scale.

The SEM image of the first row of nanowires is superimposed to that of the EBIC signal under no bias and is given in Figure 65a.

Under no polarization, the EBIC current signal is profiled on an individual nanowire with the respective SEM profile represented as dashed line. The alignment of the image with respect to the EBIC profile is done by aligning the substrate signal visible in both EBIC and SEM characterizations. The different regions of the sample (GaN stems and $Al_{0.6}Ga_{0.4}N$ *pn* junction) are distinguishable from the SEM chemical contrast and are delimited by the red lines in Figure 65a. The high EBIC signal intensity in the $Al_{0.6}Ga_{0.4}N$ region suggests the presence of an intrinsic electric field assigned to a *pn* junction.

The signal in this particular *pn* junction region is extracted in logarithmic and linear scale in Figure 65b and c. The effective diffusion length L_n in the n part of the junction can be extracted from the fit with an exponential dependence and was determined to be of 255 nm. The effective diffusion length in the p part of the junction cannot be reliably determined since the signal coming from the junction is perturbated by the boundary conditions and the drift contribution. However, the exponential dependence fitting gives a value of L_p=800 nm for the diffusion length of electrons in the p-part of the junction. Such large electron diffusion lengths in p-type $Al_xGa_{1-x}N$ were already observed in $Al_{0.1}Ga_{0.9}N$ and $Al_{0.2}Ga_{0.8}N$ material in EBIC experiments and were associated with charging of the deep metastable centers associated with Mg doping (Chernyak et al. 2000). In this paper, the L_p for Mg-doped $Al_{0.2}Ga_{0.8}N$ varies from 100 nm up to 2.5 µm as a function of the irradiation duration in the EBIC experiments.

The space charge region width was extracted after the diffusion length fitting and was found to be roughly around 255 nm, corresponding to an effective doping of $N_{eff}=9\times10^{16}$ cm^{-3}. Even if the donor/accepter levels associated to this effective doping is not high, the EBIC experiments performed on this $Al_{0.6}Ga_{0.4}N$ junction are promising.

We have seen so far that working with a ternary alloy implies considering the different compositional inhomogeneities that are difficult to control. Despite the limitations of a compositional inhomogeneity, these results are valuable in light of understanding the doping of $Al_xGa_{1-x}N$.

One of the questions we are asking ourselves concerns the real definition of an "alloy" and the need of controlling the homogeneity of such a material. Besides this, an inhomogeneous dopant incorporation due to compositional inhomogeneity in the case of the $Al_{0.6}Ga_{0.4}N$ ternary alloy cannot be excluded.

This is very much the key component in future attempts to overcome dopant incorporation issues in AlN material. The strategy of achieving UV LEDs was then redirected towards AlN and solving one of the most important problems concerning this material which is achieving an active p-type doping.

4.2. Controversial AlN p-type doping issues

Results concerning a significant increase of Mg concentration in AlN NWs by using Mg/In co-doping are presented in this section. By means of electron irradiation and annealing, successful activation of acceptor impurities and conduction mechanisms have been obtained. An easy ionization of In-vacancy complex associated with a negative charging of Mg in In vicinity during the growth is proposed as theoretical scenario for the Mg incorporation. Transport mechanisms in a *pn* junction AlN nanowire will be detailed and EBIC studies will reveal acceptor activation mechanisms.

4.2.1. State of the art doping in III-N material

Literature on AlN doping is very scarce due to the difficult incorporation of dopants in this wide band gap semiconductor. One of the main difficulties of improving the carrier concentration in AlN material comes from the high activation energy of dopants.

State of the art results show an ionization energy as high as 630 meV in 2D layers of AlN, as determined by Taniyasu et al in a *pin* AlN-based heterostructure, inferred from temperature dependent electrical characterizations (Taniyasu et al. 2006). Concerning Si doping, an activation energy of 282 meV was determined in the same way (Taniyasu et al. 2006). A binding energy of 510 meV for Mg acceptor in AlN has been previously determined by temperature dependent PL emission in the work of Nam et al (Nam et al. 2003), confirming the high activation energy required for p-type doping of Al. Such high activation energies have been validated by theoretical research for Mg substitutional in Al site of wurzite AlN demanding binding energies as high as 758 meV (Mireles and Ulloa 1998). Hole concentration is thus extremely low, of around 10^{10} cm^{-3}, explaining the poor injection in pure AlN based materials (Taniyasu et al. 2006).

Nonetheless, the group of professor Z. Mi announces in one of its publications a surprising 25 meV ionization energy of Mg in AlN nanowires (Tran et al. 2017). Some assumptions are made in order to determine the Mg activation energy in the structures. First, the AlN segment is grown between an $In_xGa_{1-x}N$ /GaN tunnel junction and an $Al_xGa_{1-x}N$ top contact layer. The resistance of the segment is taken as the difference with respect to that of a reference sample exhibiting the same structure but without the AlN insertion. Also, the resistivity is inferred from the slope of I-V characterizations, without being in purely ohmic regime. The free hole concentration determined in this study is 6 order of magnitude higher than that determined previously and has been assigned to reduced nitrogen-vacancy related defects during growth in nitrogen rich conditions inside the MBE machine, favoring a hole hopping conduction mechanism.

Another paper from the same group has shown the first realization of an AlN nanowire DUV-LED with an emission at 210 nm and a free hole concentration of Mg in AlN nanowires of 10^{16} cm^{-3} or higher at room temperature. The means used for determining the Mg concentration ("The Mg concentration in an equivalent AlN:Mg epilayer was 10^{21} cm^{-3}") is not fully understood, since the paper compares the Mg content in AlN nanowires to an equivalent Mg doping in GaN

nanowires (as inferred from SIMS characterization of Mg-doped epilayers (Kibria et al. 2014)). Needless to say, this method is not accurate enough since it is well known that Mg incorporation in AlN material is more difficult than in GaN material. Also, it has to be mentioned that the low dimensions of the heterostructures withstand extremely high electric fields on p-type segments of width of the order of 15 nm. This point will be discussed further in this manuscript in Section 4.3.4.1. Although exhibiting a very good electroluminescence, it has been previously shown that electroluminescence signal coming from a MIS structure occurs when the unintentionally doped region is large enough (Taniyasu et al. 2006).

This ionization energy decrease was already mentioned for GaN structures. As a brief recall, Brochen et al reported that the ionization energy of Mg substitutional to Ga in the low dopant concentration limit was 245±25 meV (Brochen et al. 2013). Such a high value implies to introduce large quantities of Mg to reach significant hole concentrations at room temperature. The ionization energy of Mg decreased strongly as a function of the Mg content, reaching values as low as 60 meV for acceptor concentrations higher than 10^{20} cm^{-3}. This strong decrease in ionization energies was assigned to a shift from isolated impurity regime to a defect energy band at high Mg concentrations.

However, increasing the Mg concentration is also associated with the risk of Mg clustering and defects formation. As explained more in detail in the previous chapter, the solubility of Mg in GaN layers is limited to about 10^{20} cm^{-3} (Namkoong et al. 2000). Above this concentration, Mg clustering associated with the formation of pyramidal extended defects and partial polarity inversion has been observed (Vennéguès et al. 2002), leading to a marked degradation of surface morphology as well as of the optical and structural properties. The morphology of nitride nanowires is favorable in improving this limit solubility due to the lack of extended defects, as shown in the previous study (Siladie et al. 2018).

Another solution to improve the incorporation of Mg in GaN material comes from co-doping by using In, as shown by Liu et al (Liu et al. 2016). Their theoretical predictions show that through In-Mg co-doping the valence band maximum energy is elevated, increasing the p-type dopant incorporation limit. This was confirmed by SIMS-Hall transport correlated measurements showing hole concentrations as high as 1.4×10^{18} cm^{-3} achieved in GaN MOCVD grown layers. In order to improve the surface morphology and decrease the amount of electrically compensating point defects, the use of In as a surfactant has also been proposed for GaN layers (Kyle et al. 2015). This led to increased p-type conductivity in GaN layers. Although remarkable results have been shown on GaN layer, co-doping by using In in AlN material has not been studied so far. We have thus investigated the doping mechanisms in AlN nanowires grown by PA-MBE.

In this context, the study of physics behind Mg incorporation in AlN material as well as its activation is a subject of high interest. All of the above-mentioned studies on GaN nanowires have led our research towards an interesting strategy to improve the carrier concentration in p-type AlN; We are taking advantage of the nanowire morphology and of the co-doping advantages to increase the Mg incorporation, followed by annealing and electron beam dopant activation.

4.2.2. Growth conditions of AlN NW samples

A series of AlN NW *pn* junctions were elaborated by PA-MBE. As presented in chapter 2, NWs were grown along the c-axis on a low resistivity 2" Si (111) wafer, highly n-doped by using As. The standard process of sample preparation prior to growth was followed (Section 2.1.4.1.2). Nitrogen rich conditions with a plasma cell radio frequency power of 600W and a N_2 flux of 2.5 sccm were chosen. Table 13 summarizes the different growth parameters of the samples used for the In:Mg incorporation studies.

Sample No.	T_{Mg} (°C)	T_{In} (°C)	T_{Al} (°C)
A (N3050)	280	-	1135
B (N3048)	280	700	1135
C (N3059)	300	700	1135
D (N3068)	300	800	1135
E (N3073)	300	800	1150

Table 13. Summary of samples studied for In:Mg incorporation conditions. Corresponding growth parameters varied from sample to sample such as doping cell temperatures (Mg, In, Si) are given in the corresponding fields. Other growth parameters such as substrate temperature, growth time or nitrogen/metal flux ratio were similar for all samples.

We have grown the samples on Si-doped GaN stems that ensure the electrical conductivity with respect to the substrate. GaN NW stems were grown at a Ga/active N nominal flux ratio of 0.3 and a substrate temperature of 800°C. For n-type doping of the stems, a temperature of 900°C was set for the Si effusion cell.

AlN part was grown at a constant Al/active N nominal flux ratio of 0.15 for samples A to D and of 0.2 for sample E, with the aim of studying the growth conditions influence on Mg incorporation. n-type part was grown directly on the stems with a Si-doping cell temperature of 900°C.

Concerning the p-type region, a reference sample (sample A) was grown at a Mg effusion cell temperature of 280°C without In assistance, but keeping identical other growth parameters. p-type doping growth parameters, mainly Mg and In fluxes, were varied during growth of the AlN p-part of the samples in order to have a complete study of co-doping conditions. Indium cell temperature was varied from 700°C to 800°C and magnesium cell temperature was varied from 280°C up to 300°C.

Figure 66 presents the SEM side and top view of one of the samples, the morphology being overall representative of all the samples. This morphology is also assigned to Mg incorporation evidence due to the increased diffusion of Al atoms during Mg doping. In the region of interest, diameter of the NWs along the growth direction and from sample to sample varies from 75 nm to 100 nm, as determined statistically from the SEM images in side view. The total length is of 600 nm for the GaN stems in the region of interest and AlN NW part is around 900 nm.

Further characterization of the Mg concentration level was confirmed by a series of techniques such as EDX and Raman spectroscopy and the results are presented hereafter.

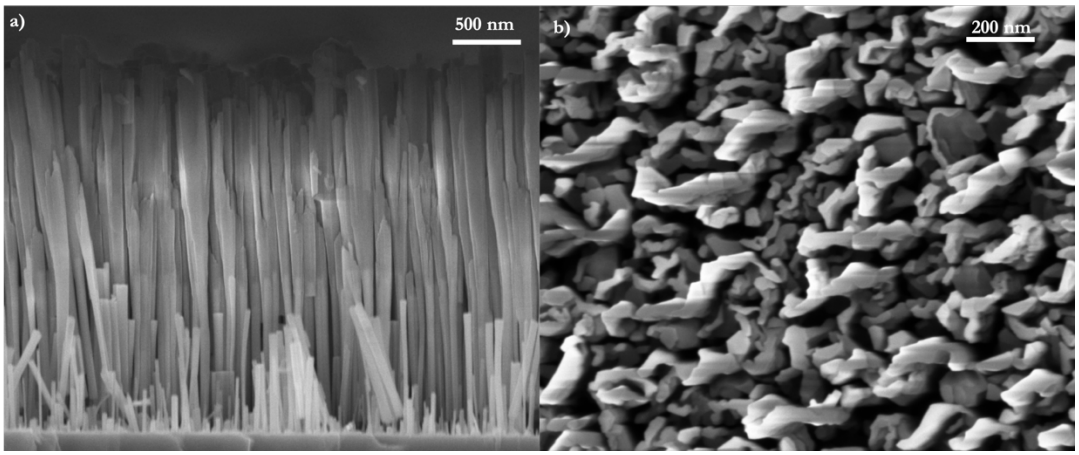

Figure 66. SEM side (left) and top (right) view of co-doped nanowires of sample N3048 ***(200 nm for left)****.*

4.2.3.EDX-TEM correlated results

We have first assessed the presence of Mg as well as the quantification of Mg atoms concentration inside the samples. These experiments were done in collaboration with Dr. Eric Robin by Energy Dispersive X-Ray Spectroscopy. This study was performed on individual AlN NWs, dispersed on a transmission electron microscopy (TEM) carbon grid as represented in Figure 67a (using a scratching technique).

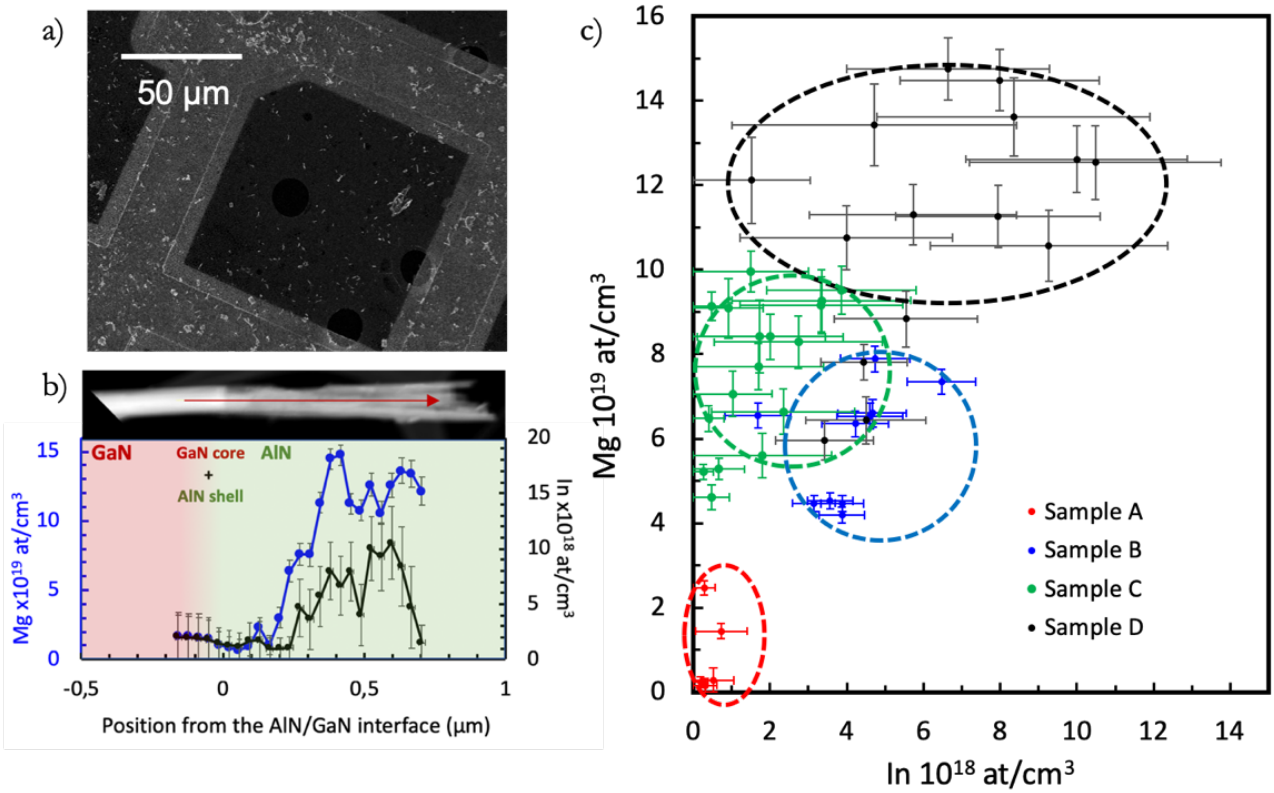

Figure 67. a) TEM grid NW dispersion b) TEM picture of dispersed nanowires from sample D (N3068) and corresponding Mg (blue axis to the left) and In (black axis to the right) profiles along the growth axis. Mg and In profiles follow the same tendency, associated to incorporation of Mg in presence of In atoms. Note that the axis is expressed in 10^{19} at.cm^{-3} for Mg and 10^{18} at.cm^{-3} for In, respectively. c) Mg and In concentration in samples A to D.

A probe corrected FEI Titan Themis equipped with four windowless silicon drift detectors was used for a better detection limit than in a regular SEM set-up and the assessment of Mg was done statistically on several nanowires. For Mg and In profiling, several points along the NWs growth axis were measured.

The acquisition time of X-ray spectra was of 1 to 5 minutes at 200 kV with high probe currents (from 3.5 up to 7.8 nA). This allowed the increase of the counting statistics (> 100 kcps) and the lowering of the detection limit for Mg and In in AlN down to 1-5×10^{18} at.cm^{-3}.

For a better interpretation of the experiments, the net intensities of N, Al and Ga K-lines were extracted from the X-ray spectra using the QUANTAX-800 software from BRUKER. Due to the composition of the samples, the net intensities of Mg K-line and In L-lines in AlN are lower than that of the Al, Ga and N elements. Indeed, the Mg K_α-line appearing at 1.25 keV cannot be extracted directly from the X-Ray spectra since the peak corresponding to this line cannot be directly deconvoluted from the Al K_α-lines. These intensities were thus extracted by normalizing the X-ray spectra to a pure AlN reference spectrum acquired in the same conditions. This AlN reference is unintentionally doped and was grown in similar conditions to those of doped samples.

The conversion of the net X-ray intensities into concentrations was performed using the zeta-factor method allowing correcting intensities from X-ray absorption (Watanabe and Williams 2006). The zeta-factors were directly measured on the same equipment, at the same operating conditions, using reference samples of known composition and thickness. For more information, the lecturer can refer to Lopez-Haro et al (Lopez-Haro et al. 2014).

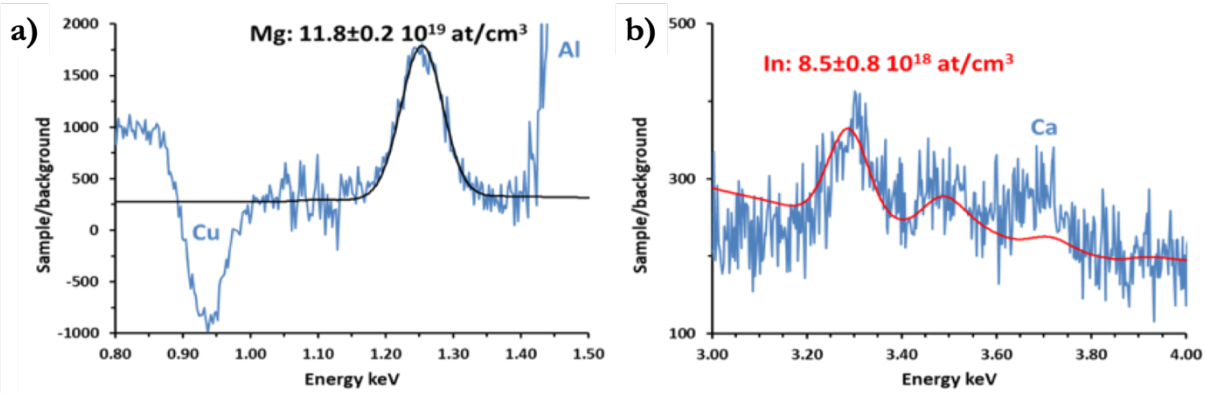

Figure 68. Normalized spectrum of sample D. a) Mg peak intensity is clearly depicted from noise level and can be quantified to a level of around 1×10^{20}at.cm^{-3}. b) In peak intensity can be quantified to a level of around 9×10^{18}at.cm^{-3}.

Normalized spectra of sample D in the low X-Ray energy range are given in Figure 68. When co-doping by using In, the Mg peak intensity is clearly increased such as in the case of sample D (N3068), allowing the extraction of a quantified Mg level (Figure 68a). The average concentration in the p-type doped section was estimated at 1.2×10^{20} at.cm^{-3}. By the same means, the In concentration is quantified in the same sample and is equivalent to 8.5×10^{18} at.cm^{-3} (Figure 68b).

For sample A (N3050), where the AlN p-part of the sample was doped with a Mg cell at a temperature of 280°C, the noise level does not allow a reliable quantification of Mg inside this sample. The Mg concentration level is too low with respect to the limit of this technique. We have thus approximated the Mg concentration inside this sample to be under the detection limit of the technique, that is 5×10^{18} at.cm^{-3}.

Mg-In concentration mapping was plotted in Figure 67b with respect to the position from the AlN/GaN interface on individual nanowires extracted from sample D. Mg and In profiles are found to vary along the Mg-doped part of the sample, with an increasing concentration of Mg related to an increasing In concentration. However, in the Si-doped part of the sample, a low concentration of Mg was detected in all samples. We associate this trend to the diffusion of Mg in the sample during growth as well as to the presence of a slightly Mg-doped AlN shell around the GaN stems. If we refer to the study of Mg incorporation in GaN nanowires, this mechanisms can be associated to the preferential incorporation of Mg on m-planes during growth under N-rich conditions (Siladie et al. 2018).

Figure 67c is showing the Mg concentration variation as a function of In concentration for all the samples. Without In co-doping, such as in the case of sample A (N3050) represented in red dots, Mg concentration equivalent to 280°C was found closely above detection limit. Indium concentration for sample A (N3050) is residual and is found to be at most 1×10^{18} at.cm^{-3}, corresponding to the In detection limit in the EDX set-up. While adding In during growth even at a very low level of 0.08ML/s such as in sample B (N3048) represented in blue, Mg concentration found in this sample is highly increased, with an average of 6×10^{19} at.cm^{-3}. Mg cell temperature increase in sample C N3059, schematized in green, for an equivalent In flux increases the concentration of Mg atoms incorporated, reaching higher levels than previously, whereas In incorporation level decreases, suggesting a competition mechanism as well as a possible surface saturation by Mg. At high doping levels of Mg and In (sample D N3068 represented in black), a maximum value of around 1.5×10^{20} at.cm^{-3} was determined, related to an In content slightly below 1×10^{19} at.cm^{-3}.

These results suggest that In plays an important role in the Mg incorporation in the AlN material. The concentration of In in samples B to D, though higher than in sample A, is still one order of magnitude smaller than that of Mg. These particular results establish a clear correlation between the incorporation of Mg and the presence of In.

Another important point worth mentioning is that given the low In concentration (<0.01%), the formation of an $Al_xIn_{1-x}N$ ternary alloy can be safely discarded for all samples. Even if the flux of In used for these growths is high, the In atoms do not incorporate efficiently at such high substrate temperature, since the desorption mechanism governs the In incorporation, allowing us to associate this enhanced Mg concentration to a co-doping mechanisms.

4.2.4. Raman spectroscopy

The presence of Mg in the samples has also been investigated by Dr. Ana Cros by Raman experiments through the Mg-H complexes formation. The experiment was performed on the samples presented previously in backscattering configuration using the 532 nm line of a laser diode as excitation source. A Horiba Jobin Yvon Xplora spectrometer equipped with a Peltier-cooled charge coupled device detector and 1800 grooves/mm diffraction gratings was used for spectral analysis. A 100x microscope objective focused the excitation laser on the sample and collected the backscattered light to the spectrometer.

The experiment was performed directly on the undispersed NW sample. Since the Raman peaks intensity is sensitive to the volume of the material, a normalization of the spectrum was done with respect to the respective dimensions of the Mg-doped part, allowing one to extract quantitative information.

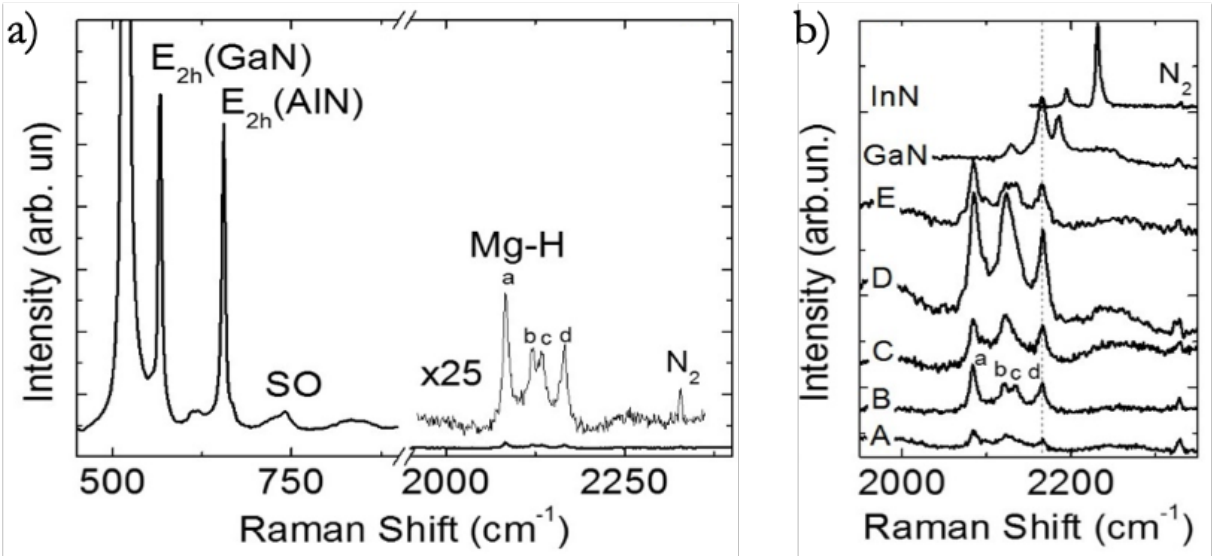

Figure 69. a) Raman spectrum of sample B (N3048) showing the spectral range corresponding to E_{2h} and Mg-H modes. The intensity of the Mg-H modes has been multiplied by 25 for clarity. (b) Detail of the spectral range corresponding to the Mg-H modes of samples A to E. GaN NW and InN bulk Mg doped references have also been included.

Figure 69a shows the Raman spectrum of sample B (N3048). The E_{2h} phonon mode characteristic of the GaN stem and the AlN grown on it can be clearly observed at 567 cm^{-1} and 655 cm^{-1}, respectively. Additionally, the surface optical mode (SO) ascribed to GaN NWs appears as a distinctive feature. At the high frequency range and around 200 cm^{-1} below the stretching mode of the nitrogen molecules from the air, four much weaker peaks are identified, labeled a, b, c and d. These particular modes have not been reported in the literature, but a look-up to the Raman spectra of a Mg-doped GaN NW sample (N2714) suggest the presence of Mg-H related complexes inside the nanowires. For the sake of comparison, this spectrum was illustrated in Figure 69b (Siladie et al. 2018).

High frequency spectral region is displayed in Figure 69b for samples A to E. In this figure, the spectra have been normalized to the intensity of the E_{2h} mode of AlN. Consequently, the intensities of the Mg-H modes reflect the Mg content of the samples and the quantification of Mg becomes possible. The frequencies of modes a (2185 cm^{-1}), b (2123 cm^{-1}), c (2135 cm^{-1}) and d (2166 cm^{-1}) are the same for all samples, and their relative intensities remain similar. The main difference concerns peak b: its intensity is larger in samples C (N3059) and D (N3068), the samples with the highest Mg and In contents. This is an indication that the configuration of Mg and H atoms changes when doping increases. Since they correspond to local modes, Mg-H vibrations are not expected to be very sensitive to the characteristics of the host lattice. However, comparison with the Mg doped GaN indicates that in AlN, most of the local modes appear at a smaller wave number. Interestingly, peak d is shared in both samples, indicating a common configuration of Mg and H in both lattices. Also, a spectrum corresponding to Mg-doped InN (Cuscó et al. 2012) allows us to confirm that no InN-related modes appear to be visible in the samples. The Raman spectrum of Mg doped InN is shown at the top, with two Mg-H related peaks shifted to higher frequency when compared to AlN and GaN. It is obvious that the In content of our samples is too small to detect any Mg-H mode related to InN.

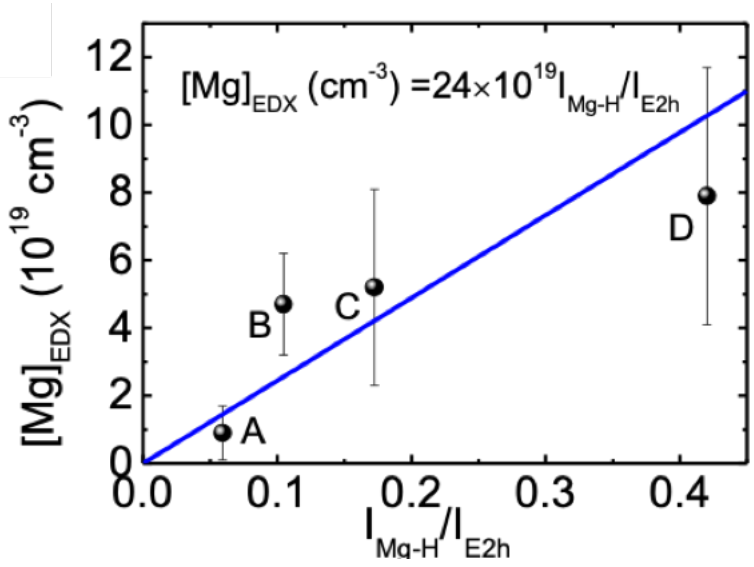

Figure 70. [Mg] content of samples A, B, C and D determined by EDX compared with the normalized Mg-H Raman mode intensities. The full line is a linear fit to the data.

Taking profit of the quantification of the Mg content performed by EDX, Figure 70 shows the comparison between the normalized Raman intensity of the Mg-H modes of samples A (N3050), B (N3048), C (N3059) and D (N3068). The linear relationship extracted from this comparison allows the quantitative assessment of the Mg based on the integrated intensity of these Raman peaks: $[Mg]=(24\pm3)\times10^{19}\times I_{Mg\text{-}H}/I_{E2h}$ ($at.cm^{-3}$). The Mg content of the samples is represented in Figure 70 as obtained from this relation. As shown by the results, the smallest Mg content is found in sample A (N3050), where no In co-doping has been used. The highest Mg content appears in sample D (N3068), doped with the highest Mg and In cell temperatures, consistent with EDX results. This correlation between EDX and Raman does hold after growth

and has to be taken with precaution if the samples are further annealed and/or irradiated since the Mg-H modes rearrange their configuration. The intensity is not directly related to the Mg content in the sample, but to the Mg-H modes.

Concerning sample E (N3073), grown at a higher Al/N flux ratio, it is observed that this sample presents less intense peak intensities compared to sample D (N3068), grown in the same growth conditions. Indeed, nitrogen rich condition favors Mg incorporation in nitrides materials, Mg concentration in sample D (N3068) being higher than that of sample E (N3073).

In the case of AlN reported here, the observation of Raman modes assigned to the presence of Mg-H complexes suggest that the Mg incorporation mechanism could be similar to the case of GaN NWs and possibly favored along the AlN NW sidewalls. Combined to a decreased formation energy and the dramatic enhancement of Mg content experimentally observed in In co-doping conditions, it appears that AlN NW morphology is extremely favorable to high Mg content incorporation. It is likely that such a high Mg content is responsible for a shift from isolated impurity regime towards a regime dominated by the formation of an impurity band and a marked decrease of the effective dopant ionization energy or hopping mechanism leading to a significant p-type conduction.

4.2.5. Ab-initio co-doping mechanism

In order to establish the improvement of Mg incorporation when AlN is Mg:In co-doped, various scenarios were investigated by means of ab initio calculations in the L-SIM laboratory at CEA-Grenoble by Damien CALISTE and Pascal POCHET.

The calculations were performed with BigDFT 12. A simplified 3D orthorhombic supercell containing 360 Al and N atoms in wurtzite structure was used in order to determine the influence of In. Such super-cells are large enough to compute the wavefunctions at Γ point only. The exchange and correlation potential were defined by the Perdew-Burke-Ernzerhof (PBE) approximation (Perdew 1996) and core electrons were described by pseudo-potential formalism using the Hartwigsen-Goedecker-Hutter (Hartwigsen et al. 1998) formulation. Since PBE is under-estimating the gap of AlN, the results provide trends but cannot be taken quantitatively. Indeed, in the simulation, the AlN gap is found to be 4.1 eV in our PBE calculations, while it is experimentally observed at 6.2 eV. Two hypotheses can be postulated regarding the increase of Mg incorporation during growth in the presence of In.

Firstly, the behavior was assigned to a direct electronic or elastic interaction between the two elements. Since both In and Mg atoms are creating a compressive strain into the AlN matrix, a purely elastic effect cannot explain the efficient incorporation of Mg.

The option of a direct electronic interaction favoring Mg incorporation in presence of In was then considered. The calculations giving the energies related to binding energies involving substitutional In and Mg positions on the Al sub-lattice, including 1st and 2nd neighbors along the c-axis or in the [100] and [110] directions have been done for various situations, similar to the case

described by Liu et al (Liu et al. 2016) for a GaN co-doped material. However, it has been found that substitutional In does not affect in a significant way the band diagram of AlN. The top of the valence band is not raised by the In presence since the energy required to transfer one electron from the In atom to Mg is of around 123 meV per transfer. Since no significant binding energies between the two elements have been found, the hypothesis of an increased Mg incorporation mediated by a favorable electronic interaction with In can be discarded.

However, an alternative possibility was considered, namely an indirect inter-play between the two elements, mediated by a third party. Such a scenario is depicted on Figure 71 and relies on the ionization of Mg atom into Mg^- during the growth process, followed by its eased incorporation in Al-substitutional site. We have considered a self-defect of AlN with a negative volume of formation to compensate for the elastic deformation induced by both In or Mg, namely the nitrogen vacancy V_N. Nitrogen vacancy are known defects in III-N materials. As explained previously, this defect is one of the most commonly defect created during GaN nanowires growth.

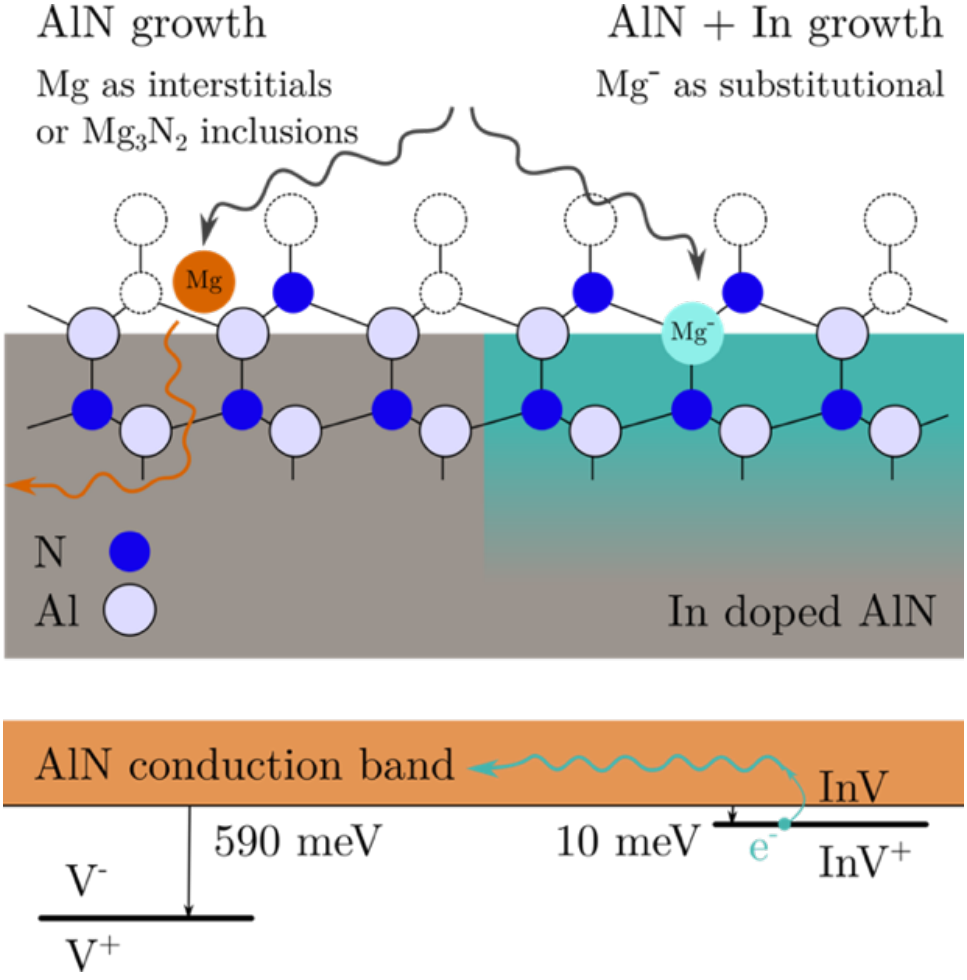

Figure 71. Better Mg incorporation in AlN in presence of indium. The InV complex is a shallow donor, easily sending an electron in the conduction band. The resulting ionization of an Mg atom is expected to ease Mg incorporation in Al-substitutional site in the wurtzite structure.

Its direct link to Mg incorporation has thus been considered. Various charge states for different elements and complexes have been calculated. The most interesting complex, though, is

the one formed between a substitutional In atom with a V_N as 1st neighbor along the c-axis. The InV_N complex is a very shallow donor, located just 10 meV below the conduction band.

We suggest the following incorporation scenario: incoming In atoms are incorporated during growth in the nanowire and then trap a V_N leading to an In-V_N complex formation in order to accommodate the related elastic deformation. This mechanism is similar to that proposed by Haller et al. in the case of InGaN/GaN quantum wells(Haller et al. 2018). Since the growth takes place in out of equilibrium conditions, the In-V_N complex is quickly ionized, releasing an electron in the conduction band (CB) of AlN (right hand side of Figure 71). On the other hand, incoming Mg atoms available in the valence band are ionized into Mg^- with the available electrons. The electronic structure of Mg^- is closer to the one of Al than neutral Mg, facilitating its incorporation in substitutional site in the growing wurtzite structure. By contrast, neutral or positively charged Mg tends to form Mg_3N_2 inclusions or interstitial Mg (Miceli and Pasquarello 2016), decreasing the Mg carriers concentration.

It has to be pointed out that V_N alone is a deep donor located at 590 meV under the conduction band (see left hand side in Figure 71), preventing it to efficiently ionize Mg. In our case, we have only considered the transition from V^+ to V^- without -/0 and +/0 transitions since in the case of AlN this transition level is not allowed.

However, the calculated energy of an InV_N complex is found to be only 10 meV below the conduction band minimum. This highlights the specific role of InV_N complexes as donors, while the nitrogen vacancy alone, if indium is absent, cannot significantly contribute to ionize Mg atoms.

The above calculations are performed at thermodynamic equilibrium and do not consider the kinetics of In-V_N complex formation. For a full comprehension, the Mg and In fluxes should be related to the AlN NW growth rate, since the interaction between the surface V_N reservoir and substitutional In is expected to depend on the local density of reacting species.

Regarding In-V_N complexes, it is possible that the complex neutralizes close to the growth surface of the nanowire due to surface effects, or by interaction with adsorbed species, a recycling mechanism being an eventual explanation for the 1 to 10 ratio between the In and Mg atoms concentration.

This will further be investigated by electrical measurements that aim at proving the electrical activity of Mg incorporated in the samples, as well as studying the conduction mechanism taking place in complete structures in samples grown in similar conditions as the ones presented previously.

4.3. Electrical activation of Mg in AlN doped NWs

Even though we have presented an increased Mg concentration in the nanowires, the electrical activation of these acceptors is not yet investigated. Besides passivation by H during growth in the MBE chamber, the dopant can be passivated by forming Mg-V_N complexes or by clustering, decreasing the hole concentration in the material.

4.3.1. Samples presentation

To study the electrical properties, a sample (N3209) was grown with an AlN intrinsic region to increase the recombination volume in the heterostructure. The growth conditions of this sample were optimized with respect to that determined previously.

The Si cell doping temperature for GaN and AlN NW sections was 920°C and 1000°C, respectively. p-type AlN NW part of the junction was grown at a Mg doping cell of 280°C and at an In doping cell temperature of 800°C. A 20 nm highly p-type doped GaN section (Mg content larger than 10^{19}cm^{-3}) was grown at the top of the sample with a cell temperature of 280°C in order to facilitate the metal deposition.

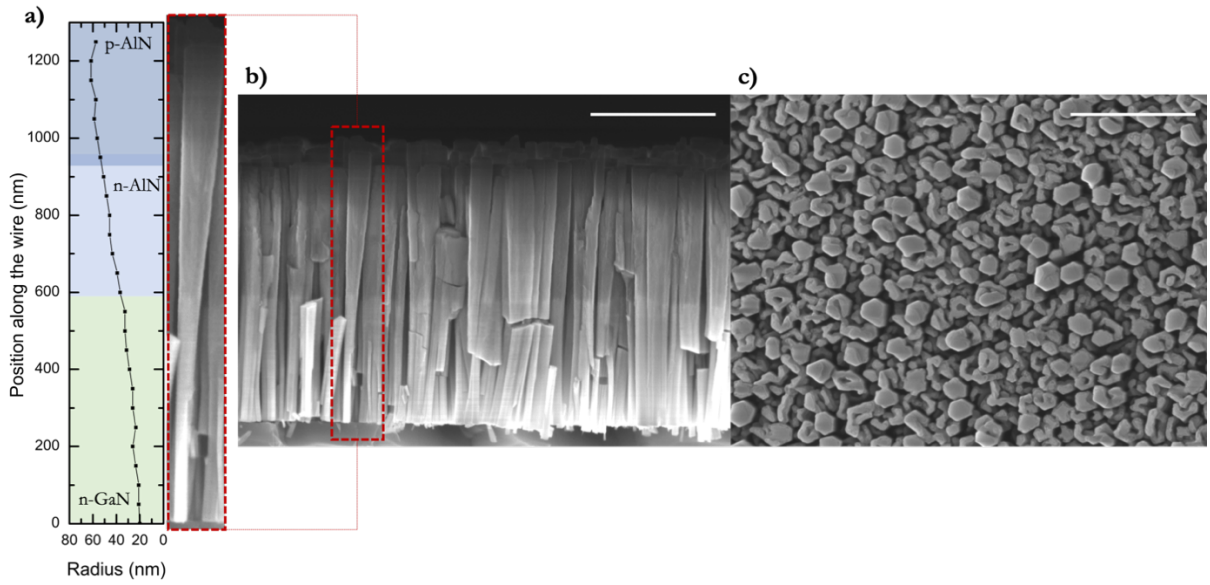

Figure 72. a) Radius dimension of an individual nanowire of sample N3209. SEM images of sample N3209 in b) side view and c) top view. The scale is of 500 nm.

The structure of the sample is presented in the SEM image in side and top view in Figure 72.

The n-type GaN stem of the wire is approximately 600 nm long. Then, the AlN *pin* junction consists of 30 nm of undoped AlN sandwiched between n-type and p-type AlN sections of approximately 300 and 250 nm length, respectively.

4.3.2. Optical properties

We have first investigated the optical properties of the AlN *pin* junction by cathodoluminescence spectroscopy measurements, performed by Gwénolé Jacopin (CNRS, Néel Institute Grenoble). The experiments were performed at room temperature T=300 K in the FEI Inspect F50 SEM. A Horiba Jobin Yvon ihR 550 spectrometer equipped with a Peltier-cooled charge coupled device detector and a 600 grooves/mm diffraction grating was used for spectral analysis.

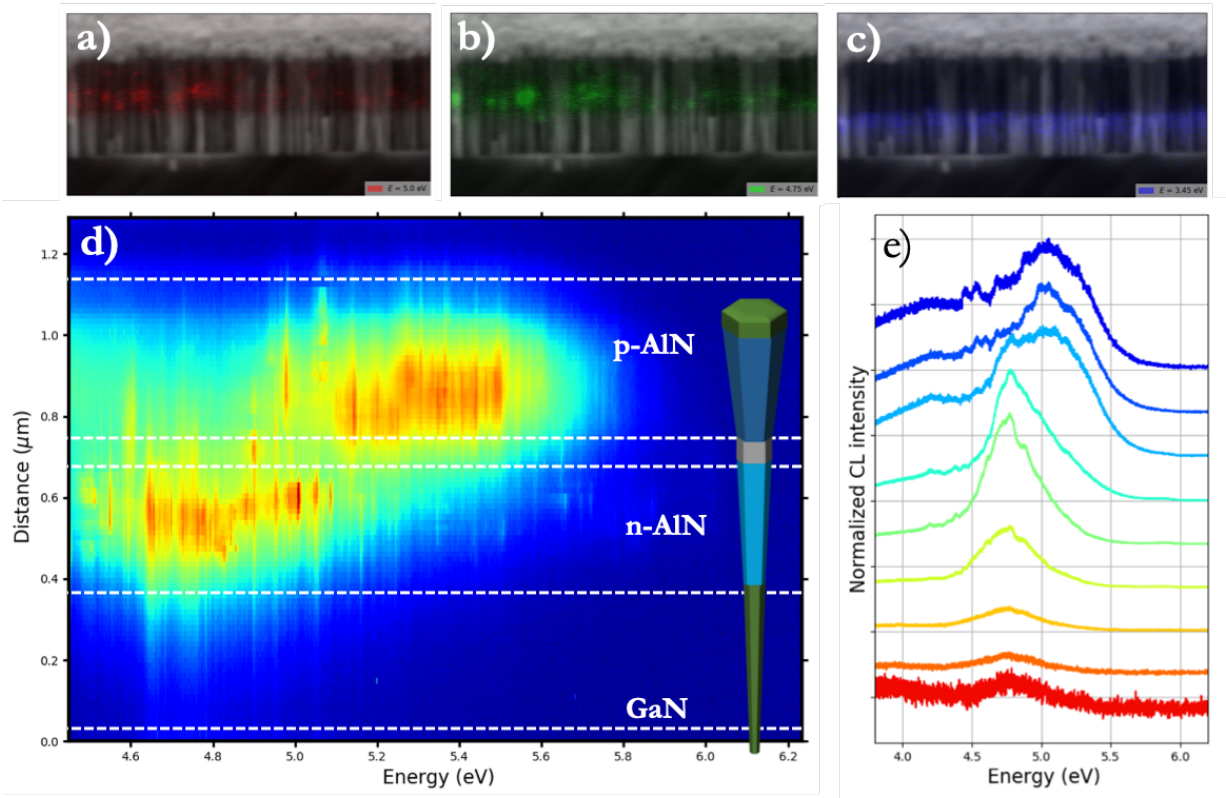

Figure 73. Optical characteristics of the AlN pin junction sample N3209 at T=300 K. a-c) Monochromatic cathodoluminescence mapping at different energies a) 5 eV, b) 4.75 eV, c) 3.5 eV. d) Cathodoluminescence mapping along the pn junction at T=5K and nanowire schematic delimiting the different regions. e) Normalized cathodoluminescence spectra for different position along a nanowire (spectra have been shifted for clarity).

The sample was studied in side view and a mapping of the corresponding cathodoluminescence spectra is shown in Figure 73a, b and c for different energies corresponding to 5 eV (red-a), 4.75eV (green-b) and 3.45 eV (blue-c).

As expected, it can be seen that the bottom part of the wire is mainly emitting at *3.45 eV*, which corresponds to the emission from *n*-GaN region. At room temperature, the AlN part of the wire is emitting at shorter wavelengths comprised between *4.4 eV* and *5.6 eV*, corresponding to defect band transitions in AlN which are different for n-type and p-type AlN parts of the samples. More precisely, we observe that the *n*-doped region of AlN is emitting around 310 nm (4.75 eV) while the *p*-doped region is emitting at a lower wavelength of 225 nm (≈ 5.1 eV).

A mapping of the cathodoluminescence energy as a function of the position along an individual wire is shown in Figure 73d at low temperature measurements of 5K (He cooling). The spectra corresponding to different regions of the sample are also given in Figure 73e.

The emission of *n*-AlN is ranging from 4.4 eV to 5.1 eV while the *p*-AlN mainly emits between 5 eV to 5.6 eV. According to literature (Koppe et al. 2016), the emission coming from 5.0 – 5.5 eV may be assigned to DAP type transitions involving Mg acceptor and nitrogen vacancy, coherent with the model described previously and confirming the Mg incorporation in the p-AlN region. Similar to the $Al_{0.6}Ga_{0.4}N$ case, the DAP transitions consist of sharp lines assigned to different atomic configurations of DAP transitions. The AlN band edge emission does not appear in the spectrum at low wavelengths of 210 nm (6.2 eV).

After assessing the difference in optical properties, which indicates the presence of a physical junction formation, the sample was processed for electrical measurements.

4.3.3. Electrical characterization

ITO electrodes of different sizes were fabricated on top of as-grown NWs on the AlN *pin* junction (N3209), with a thickness of 100 nm. Contacting for electrical characterization was done directly in the FEI SEM using tungsten tips controlled by nanomanipulators, in the configuration presented in Section 2.2.2.2.

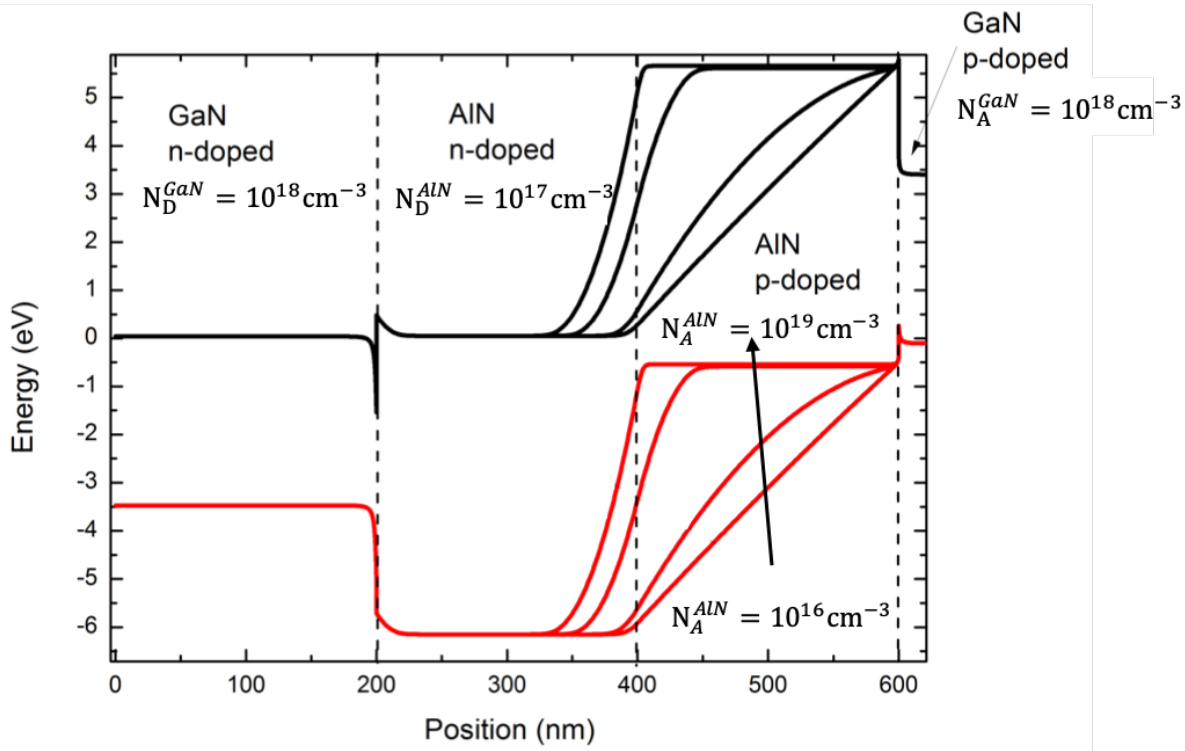

Figure 74. Nextnano simulation diagram for band gap alignment for the pin structure for different levels of doping in AlN p-type region.

The band gap diagram of the structure is given in Figure 74 as determined by Nextnano simulations. We have considered a homogeneous Si doping level in the GaN stem of 10^{18} cm^{-3} and of 10^{17} cm^{-3} in the AlN n-doped section. The Mg doping in the p-doped AlN section was

considered as homogeneous, but different cases with acceptors concentrations varying from 10^{16} cm^{-3} up to 10^{19} cm^{-3} have been considered. The Mg doping level in the GaN p^{++} cap was fixed at 10^{18} cm^{-3}. For low Mg doping levels ($\leq 5\times10^{17}$ cm^{-3}) the electric field appears mainly in the p-type region, whereas for highly doped p-type AlN ($\geq5\times10^{18}$ cm^{-3}), it is predominantly in the n-type region.

However, due to the high ionization energy of Mg in AlN nanowires of 510 meV, we expect a lower ionization rate in the Mg-doped AlN with respect to the Si-doped AlN for which the activation energy is of 282 meV (Nam et al. 2003).

By making the hypothesis that these ionization energies are constant whatever the doping level (which is not necessarily the case, as seen previously in (Brochen et al. 2013) for GaN), further simulations show the carrier concentration and ionization rate variation as a function of temperature in the p and n type AlN material (Figure 75).

The data was calculated by Matlab by taking an effective mass for holes of $2.7m_0$ and of electrons of $0.4m_0$ (Nam et al. 2003). Different doping concentrations have been considered with a decade step, from 10^{15} cm^{-3} to 10^{20} cm^{-3}. One important remark is that in these simulations we have not considered any carrier compensation, which would significantly decrease the hole and electron concentration.

One significant information that we have to consider is the low carrier concentration in the p-type AlN at room temperature (300K). Indeed, due to the extremely high ionization energy, for an equivalent doping level, the hole concentration at high doping levels corresponding to 10^{20} cm^{-3} does not exceed 2×10^{15} cm^{-3}.

On the other hand, the electron concentration for the lowest doping level is of at least 2×10^{14} cm^{-3} and for a moderate doping level of 10^{17} cm^{-3} the carrier concentration exceeds 2×10^{15} cm^{-3} and can attain electron concentration as high as 1×10^{17} cm^{-3} for the most doped case.

Moreover, it can be seen that at room temperature, the ionization rate of donors is more than 100 times higher than that of acceptors, a full ionization of Si being almost immediate for high level of donor concentrations.

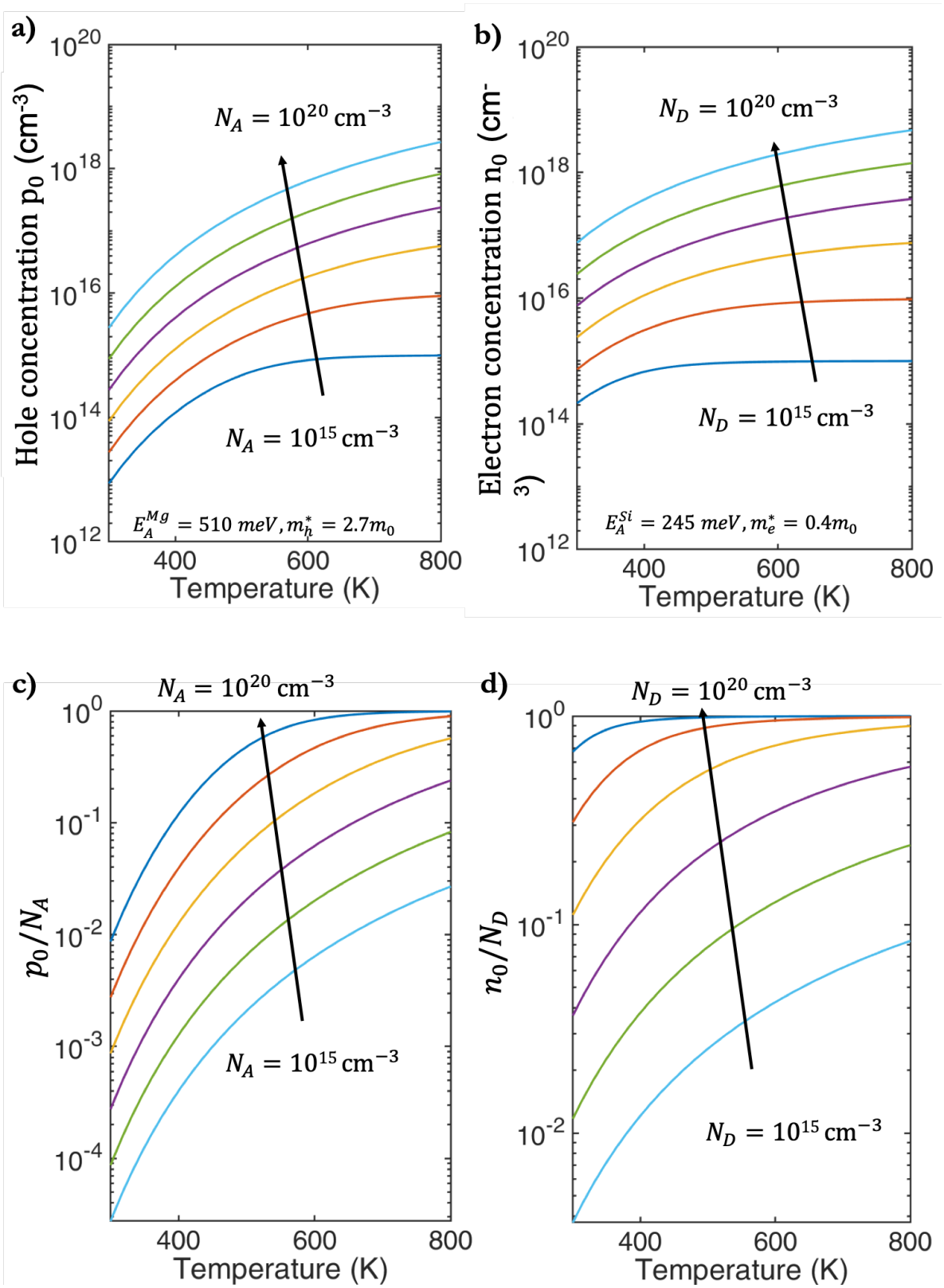

Figure 75. a) Hole concentration and b) electron concentration variation as a function of temperature for different doping levels. Ionization rate dependence on temperature for holes (c) and electrons (d).

4.3.4. Transport properties

While studying the electrical properties of the diode under the SEM beam, the J-V characteristics of the diode appeared to change while exciting the diode with a high voltage beam (higher than 10 keV). The transport properties of the sample were thus studied as a function of the e-beam irradiation in the configuration given in Figure 76. The J-V experiments were done by scanning an entire diode on top-view configuration (that is, the e-beam perpendicular to the sample surface) as shown in Figure 76a. The schematics of the set-up configuration is shown in Figure 76b.

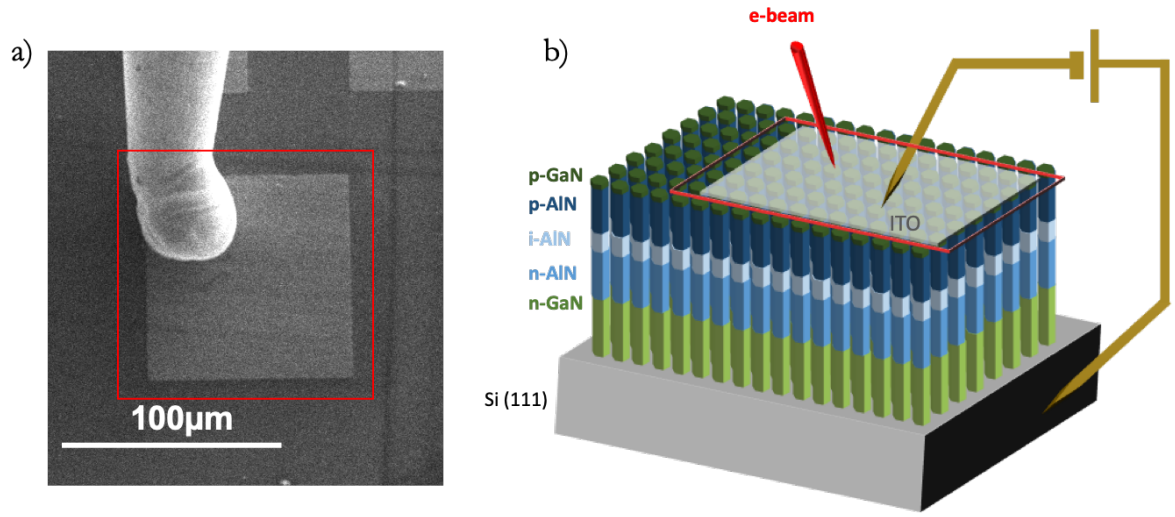

Figure 76. a) Top view SEM image of the sample contacting configuration and b) Set-up schematics for irradiation experiments and IV characterization

One important aspect worth mentioning is the difficulty of defining the experimental conditions due to the irreversibility of the diode behavior when studying the samples. Indeed, the distinction between reversible effects (coming from surface and deep states) and irreversible effects (such as dopants activation under electron beam scanning of the samples) during sequential experiments was a difficult issue.

In the following, we will define as "non-irradiated" state, the characteristics of the structures that have been exposed to an electron beam dose below 5 mC/cm^2. This value is calculated by considering only one scan on the surface of interest, the beam of the SEM being blanked during the experiment. The term "irradiated" corresponds to a continuous scanning of the sample for a given amount of time, receiving a dose higher than that announced previously.

The irradiation dose D (C/cm^2) was calculated from the SEM beam current I_{beam} (A) measured by using a Faraday cage, the irradiated surface of the diode A (cm^2) and irradiation time t, from the expression:

$$D = \frac{I_{beam} \times t}{A} \tag{73}$$

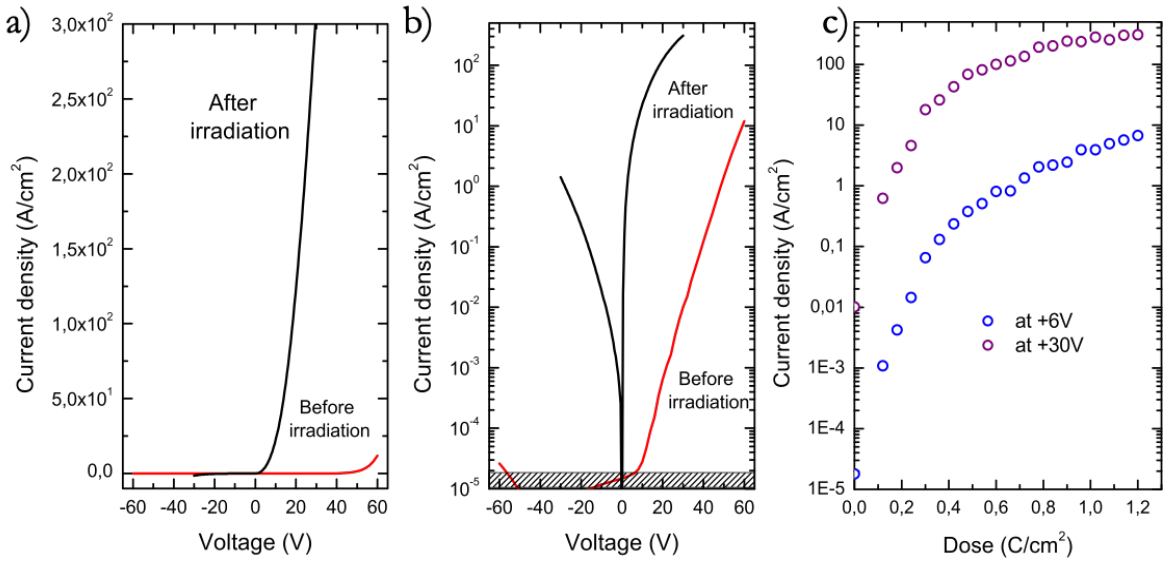

Figure 77. J-V characteristics of sample N3209 in a) linear scale and b) semilogarithmic scale. c) Current density variation as a function of the irradiation dose at +6V and +30V

Typical J-V characteristics of a 100x100 μm^2 electrode corresponding to sample N3209 are reported in Figure 77a and b with a linear scale and semi-log scale, respectively. We have represented in red the I-V characteristics of the diode before irradiation and in black after irradiation. Figure 77c shows the current density variation as a function of the dose taken at +6V and +30V polarization. For an electron beam dose higher than 0.8 C/cm^2, the current density tends to saturate. In the following, the "after irradiation" characteristics refer to a dose of 1.2 C/cm^2.

The J-V characteristics are rectifying whatever the e-beam irradiation dose. The reverse current density before irradiation is below the detection limit of the experimental set-up (dashed area of the Figure 77b) up to -60 V, the real current flowing in the diode in reverse bias being below 1pA.

4.3.4.1. Electrical properties before irradiation: impact ionization in p-type region

Before irradiation, the current density of the diode exhibits a power law dependence versus voltage $J \sim V^{\alpha}$ in forward regime at high polarization bias. The JV characteristics were performed on a sampling of a dozen electrodes of different sizes, all exhibiting a similar behaviour with same power law dependence, but different power law coefficients. The α value is estimated such as $6<\alpha<12$ depending on the diode.

In the example shown in Figure 77 that we will discuss further in this section, the current density dependence on the applied bias follows a power law dependence with an $\alpha=6.8$. However, this power law dependence is not compatible with a *pin* rectifying behaviour since no ohmic regime appears. It has been observed that such strong current increase versus voltage is generally observed in low doped semiconductors where multiplication mechanism occurs by impact ionization (Baliga 2008).

During impact ionization mechanism, an energetic charge carrier loses its kinetic energy by the creation of other charge carriers. This could create multiplication and then avalanche breakdown. In our case, electrons injected in the resistive region and having enough kinetic energy can knock out a bound electron out of its bound state from the valence band, giving enough energy for the electron to attain the conduction band and in consequence create electron-hole pairs. However, in *pn* diodes, this behavior is parasitic and results in poor device performances with low EQE.

Prior to irradiation, we assign the insulating behavior of the J-V characteristics in forward regime to a low carrier concentration in the *p*-type region. Indeed, Taniyasu et al (Taniyasu et al. 2006) reported that Mg is a deep acceptor with an ionization energy of 630 meV. In their epilayer, they measured a hole concentration of around 10^{11} cm^{-3} for a doping level in the range of 2×10^{19} cm^{-3}. If we assume this hole density in the 250 nm long p-type part of the NW with an average radius of 50 nm, the equivalent number of holes in one NW is 1.5×10^{-4}. This is equivalent to 200 holes in the volume corresponding to 250 nm long p-type AlN NW section of a 100 µm×100 µm diode, or, one chance over 10,000 to find a hole inside an individual nanowire.

Moreover, assuming that the applied voltage holds on the most resistive 250 nm p-type part, the electric field can be evaluated between 0.5 and 2.4 MV/cm for a voltage bias ranging between 10 V and 60 V. These values are typical electric fields for impact ionization, which is not unusual in such structures. If we refer to literature, a similar behavior under high electric fields has been shown in a *pin* AlN planar structure by Taniyasu et al (Taniyasu et al. 2006).

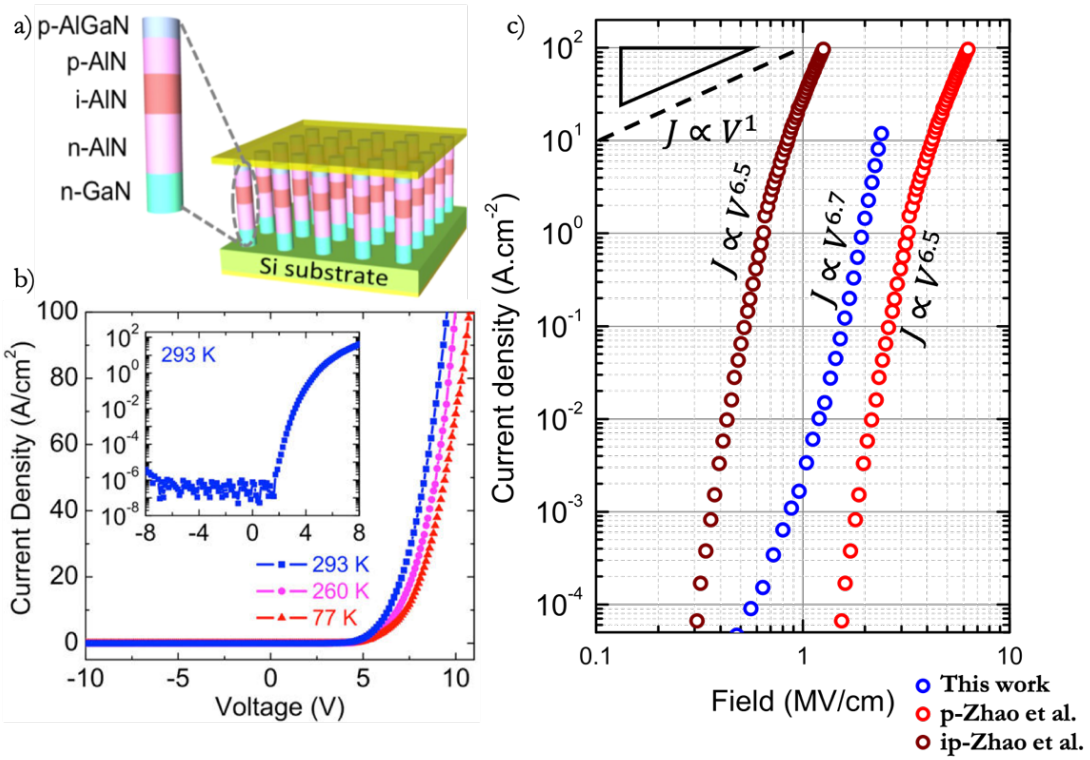

Figure 78. a) Sample structure from the paper of Zhao et al.(Zhao et al. 2015a) b) J-V characteristics of the AlN pin structure as presented in the paper of Zhao et al.(Zhao et al. 2015c) c) J-E variation in the structure N3209 and comparison with the reference paper characteristics.

If we refer to the paper of Zhao et al (Zhao et al. 2015c), the J-V characteristics of a *pin* AlN NW diode represented in Figure 78b does not exhibit an ohmic behavior. The NW based *pin* heterostructure described by the authors is made of 90 nm n-AlN, 60 nm undoped AlN and 15 nm p-AlN, the thin layer AlN withstanding similar electric field as in our case, for a lower bias. An illustration of this diode structure is given in Figure 78a.

Figure 78c presents the current density variation of the diode studied in this work before irradiation (in blue) compared to that reported by Zhao et al (in red and wine colours), taken from Figure 78b. Two cases were considered: in the first case, intense electric field region (most resistive) was considered as being the p-type resistive part of the structure (red curve) and in the second case, both p-type AlN and intrinsic AlN were considered as resistive (wine curve). These assumptions were made by considering the fact that the residual doping of the intrinsic region is n-type.

Whatever the considerations, the similar behavior of the electric field variation suggests a similar impact ionization mechanism in both cases, yielding an inefficient transport mechanism for *pin* junction LED. In the case of Zhao et al, the current variation with the applied bias follows a power law variation of coefficient α=6.5, which is a typical value that we have observed also on our samples. Another conduction mechanism that could be corelated with such a high-power law variation is Space Charge Limited Current (SCLC). However, at such high electric fields the impact ionization mechanism is more probable. At this stage of the analysis, p-type doping cannot be evidenced. An insulating n-type region or p-type region can be at the origin of the impact ionization and electron hole creation. More investigations are needed to establish the p-type behavior as demonstrated by EBIC measurements in the following for our samples. Clearly, for Zhao et al data, the questions of p-type doping are still open.

4.3.4.2. Irradiation impact

After irradiation, the current density in the diodes is 5 orders of magnitude higher than before irradiation, which is compatible with a high density of Mg dopants in the p-part of the AlN.

The intermediate J-V characteristics at different irradiation doses are shown in Figure 79 in logarithmic scale (a) and in semi-logarithmic scale (b). The J-V curves were registered after every 30 sec of surface irradiation, corresponding to a dose of 60 $mC.cm^{-2}$. To simplify the lecture of the data, only some of J-V curves selected for different irradiation doses are represented in Figure 79.

A slope change is clearly observed on the characteristics, indicating a change in transport mechanisms, which appears to be around the threshold voltage of AlN (6.2V) defining two different conduction regimes. The fitting of the curves by two power laws (low injection regime below +6 V and high injection regime above +6V) fit accurately the J-V characteristics as illustrated in Figure 79.

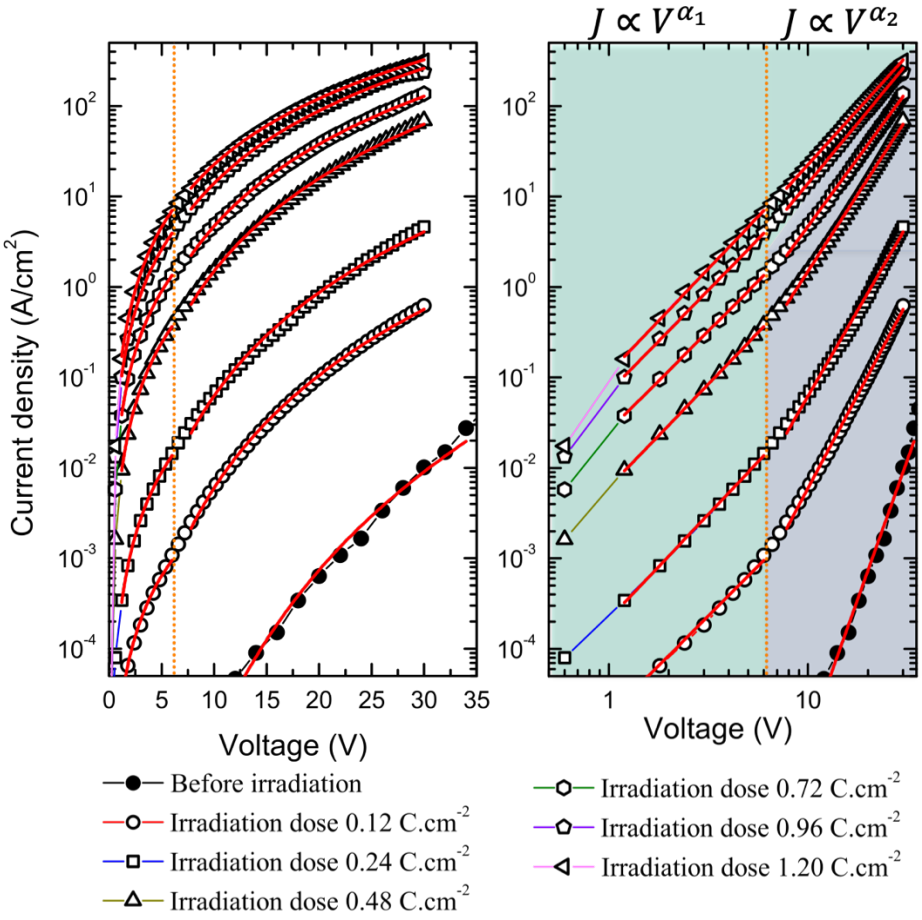

Figure 79. Current density versus voltage variation in a) semi-logarithmic scale and b) log-log scale for different irradiation doses.

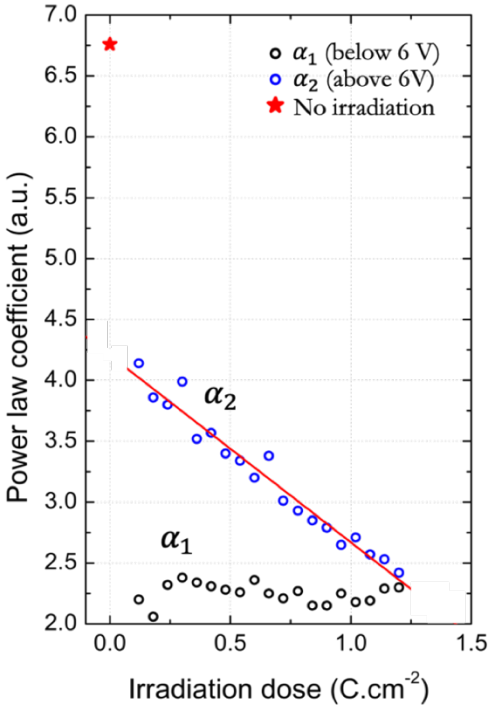

Figure 80. Power law coefficient variation as a function of the irradiation dose for the low injection and high injection regimes.

The power law coefficient for the low injection regimes (black circles) and high injection regime (blue circles) have been represented in Figure 80. The value of the power coefficient before irradiation is represented separately by the red star.

Several information about the transport mechanisms can be drawn from this study. First, at a low bias voltage below the threshold, the transport mechanism seems compatible with a space charge limited current (SCLC) mechanism with a rather constant dependence coefficient ranging between 2 and 2.5. The space charge limited current conduction mechanism occurs when injecting more carriers into a structure than the ones available at thermodynamic equilibrium, leading to a current reduction due to coulombic interaction. The transport inside the structure occurs by carriers moving between the traps.

The expression of the current voltage variation in the case of a trap-assisted SCLC conduction mechanism was established by Rose et al (Rose 1955):

$$J \approx V^{l+1} \tag{74}$$

With l coefficient dependent on the trap temperature T_c such as:

$$l = \frac{T_c}{T} \tag{75}$$

In case of trap-free SCLC, the expression of J becomes (Rose 1955):

$$J \approx V^2 \tag{76}$$

In the case of the structures presenting different defects and structural imperfections, a range of trap energy has to be considered. In the low injection regime, the trap temperature deduced from the l coefficient is comprised between room temperature and 450 K.

Due to the large slopes measured on different diodes and on different samples, additional transport mechanisms such as Pole Frenkel mechanisms can be excluded from the interpretation of the data thanks to the fitting of the JV variation with a SCLC mechanism.

After irradiation, for the highest Mg concentration measured in this work by EDX, N_A, of 1×10^{20}cm^{-3}, the mean distance between dopants, R, can be estimated from the expression:

$$R = \left(\frac{3}{4\pi N_A}\right)^{1/3} \tag{77}$$

Thus, the mean distance is roughly equal to 2 nm, suggesting that the electrical conductivity in the AlN NW section can be hole hopping, which is consistent with SCLC.

Above +6V, the current increases much more rapidly, the power law coefficient fitting this variation being comprised between 2.5 and 4.5 for different irradiation doses. Due to the reduced dimensions of the structure, the field applied on the nanowire is sufficient for impact ionization in the resistive region of the nanowire.

However, after complete irradiation of the structure, the conduction mechanism becomes purely SCLC with a power fitting coefficient of 2.3. This transport change suggests that the irradiation has a clear effect on the defects annealing and on dopants activation. However, given the configuration of the structure (in-series p-type and n-type AlN), additional studies are required in order to establish the potential drop in the structure that limits the conduction.

4.3.5. *pn* junction evidence by EBIC characterization

4.3.5.1. Injection conditions

The set-up using a pico ammeter presented in Chapter 2 (Section 2.2.3.1.2) was readapted on a *pin* AlN junction in Figure 81c. The side view configuration of a cleaved sample allows us to perform in-situ EBIC characterization by accessing the first row of nanowires.

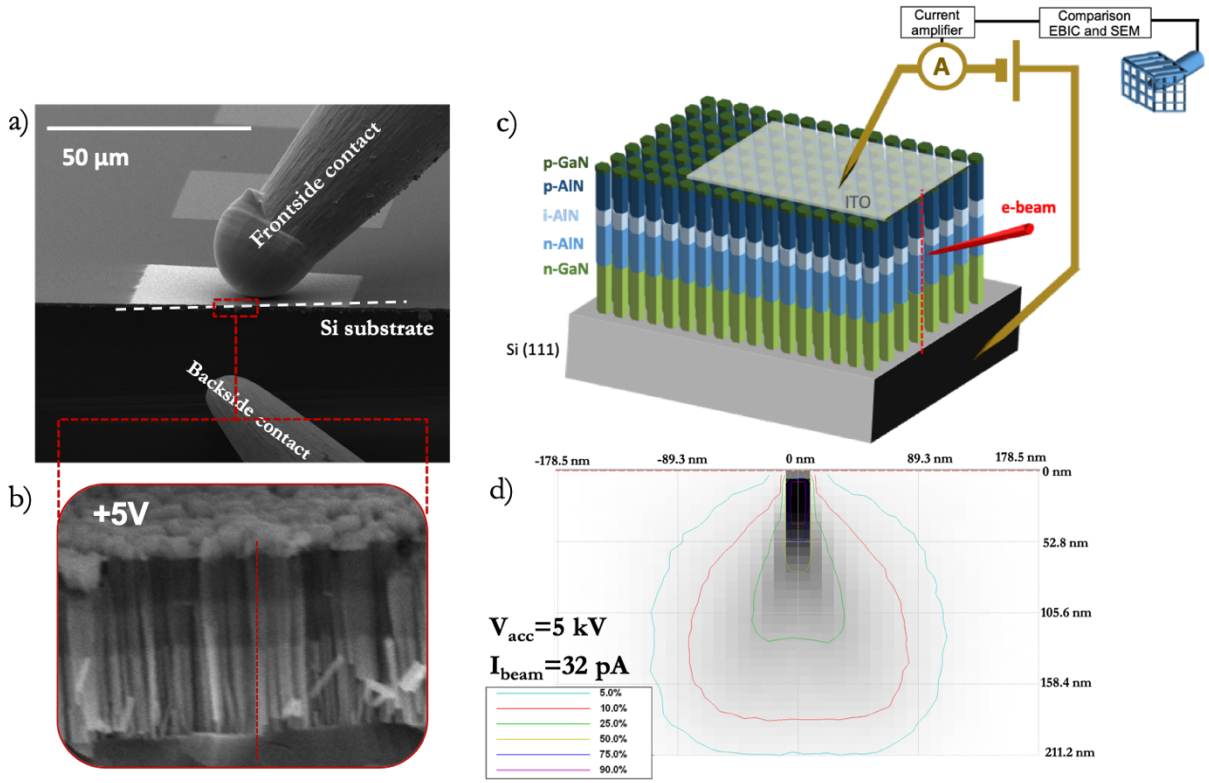

Figure 81. a) Contact configuration in side view for EBIC experiments b) Side view SEM image of the nanowires with a visible potential contrast under +5V polarization. c)Set-up schematics for EBIC experiments. d) Interaction volume as determined from electron trajectory Monte-Carlo simulations.

Figure 81c shows the schematic of the AlN *pin* junction nanowire structure and the experimental setup for electrical measurements. In this specific case, the irradiation was performed using an e-beam configuration parallel to the sample surface in order to study NWs at the edge of the cleaved sample, the scanning profile being done on an individual nanowire (red line in Figure 81b).

In order to visualize and characterize the *pin* junction inside the AlN NW, EBIC measurements have been performed with a beam energy of 5 kV and a beam current of 32 pA as measured by using a Faraday cage inside the SEM. The interaction volume for these particular

conditions are illustrated in Figure 81d by electron trajectory Monte Carlo simulations using the Casino program. These experimental conditions allow us to get information by exciting an individual nanowire, the electron beam penetration depth being of around 210 nm. Moreover, 50% of the electrons are concentrated in the nanowire under study (first row). These individual nanowire experimental conditions would not be fulfilled for higher electron beam acceleration voltage, as we have seen in the case of GaN NW *pn* junction sample in Section 3.5.2.

The localization of the electron hole pairs creation is an important issue, but another one which must not be neglected is the concentration of electron hole pairs created. Indeed, if the injection of excess carriers is larger than the concentration of carriers under equilibrium or of dopants, this will affect the diffusion of carriers in the neutral region and the electrostatics within the SCR, respectively. The injection regime was approximated by looking at the excess carriers generated by the electron beam for carrier lifetimes of 100 ps, 1 ns, 10 ns and 100 ns[1]. The carrier density generated by the scanning of the sample is represented in Figure 82 for an accelerating voltage of 5 kV.

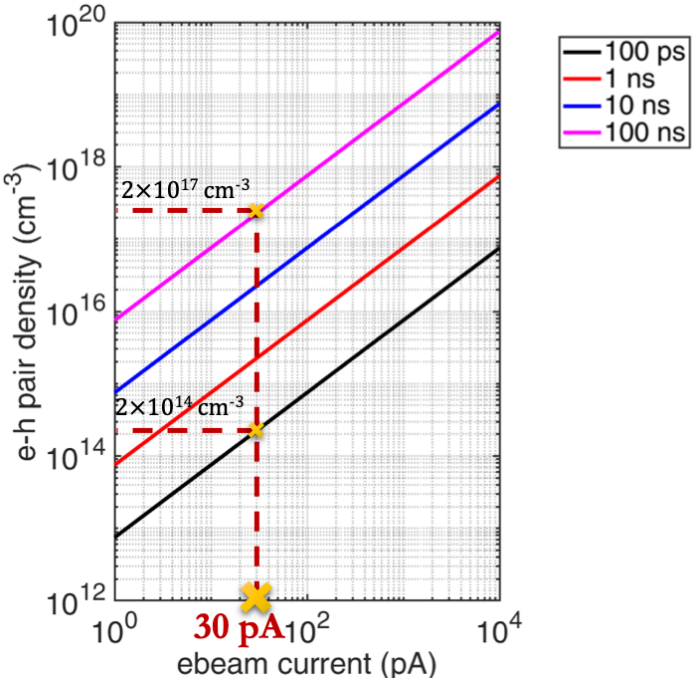

Figure 82. Electron-hole pairs generation in AlN material for a beam current of 30 pA and accelerating voltage of the beam of 5kV.

In any case, the space charge region can be reliably determined since for doping levels higher than $n_0=2\times10^{17}$ cm^{-3} (as in the case of a radiative recombination time of 100 ns) we can safely consider a low injection regime.

[1] Since the carrier lifetime in AlN material is not well established by the literature, different values have been determined so far, going from 530 ps (Chichibu et al. 2010) to 25 ns (Dmitriev and Oruzheinikov 1996)

However, the diffusion lengths cannot be quantitatively determined since the experimental conditions we have used in our study are at the limit of the low injection regime. Thus, even if we can safely extract them from the exponential dependence fitting, they cannot be directly related to the minority carrier diffusion length, but will be given in the following as indicative (ambipolar diffusion length). The compromise between a high injection regime and a low injection regime comes from the need of a small excitation volume in order to keep the spatial resolution of the experiment which is detrimental to low injection regime conditions for which higher excitation voltage (20-30 keV) would be needed. Due to the small NW diameter, high acceleration voltages do not allow individual nanowire observation, hence, a signal over noise trade had to be made.

4.3.5.2. The irradiation effect on the EBIC profile

EBIC characterization performed on individual nanowires have shown a clear effect of the EBIC signal before and after irradiation of the sample. As it can be seen in Figure 83, a signal appears in reverse bias at the position of the junction between the p-type and the n-type AlN.

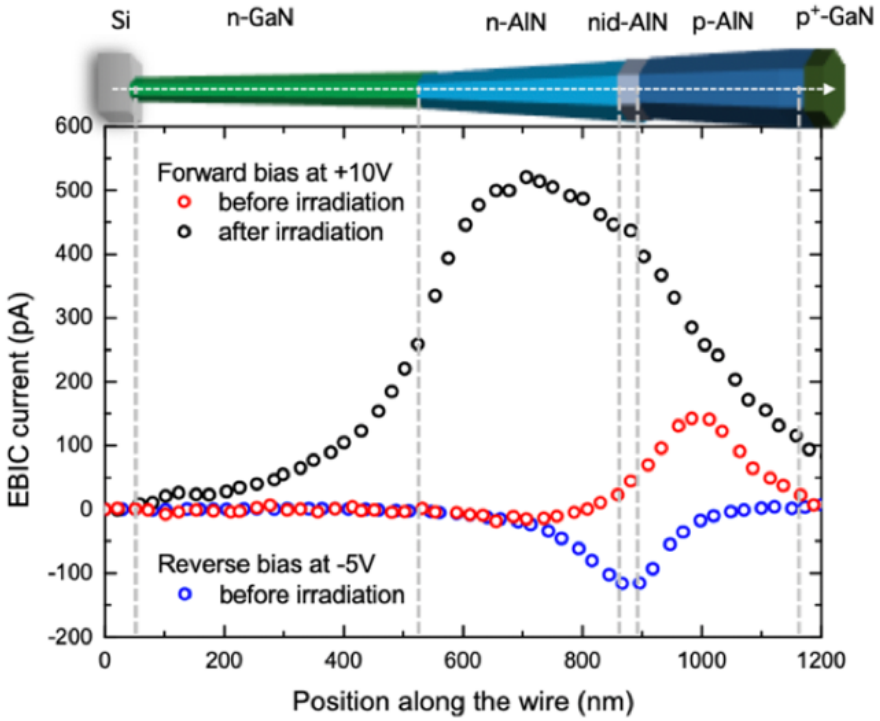

Figure 83. Individual NW schematics and corresponding electron beam induced current (EBIC) profile measured along the dashed line of the image. The EBIC profiles have been performed before irradiation under reverse (-5V) and forward (+10V) bias regime.

By irradiating the sample under the electron beam, the position of the intense signal of EBIC profile moves toward the n-type of the junction. In the following, we will essentially be focusing on the comprehension of this behavior. In forward bias, the potential drop occurs in the more resistive part of the sample whereas in reverse bias information about the intrinsic electric field at the *pin* junction can be extracted. An important investigation related to the *pin* junction was performed by considering the irradiation effect on the nanowires. In our case, the statistical study of 8 different nanowires showed the same tendency as the example given in Figure 83.

4.3.5.3. Zero bias *pn* junction proof by EBIC characterization

The EBIC signal coming from the no bias measurements on the sample corresponds to the intrinsic electric field prevailing at the *pin* junction. The EBIC signal with respect to the position along an individual AlN nanowire is profiled in Figure 84a. The alignment was done with respect to the SEM image and the structure of the sample with the different regions is illustrated below. During this study, the nanowire was not irradiated, the conditions for the EBIC experiment being limited by using quick scans.

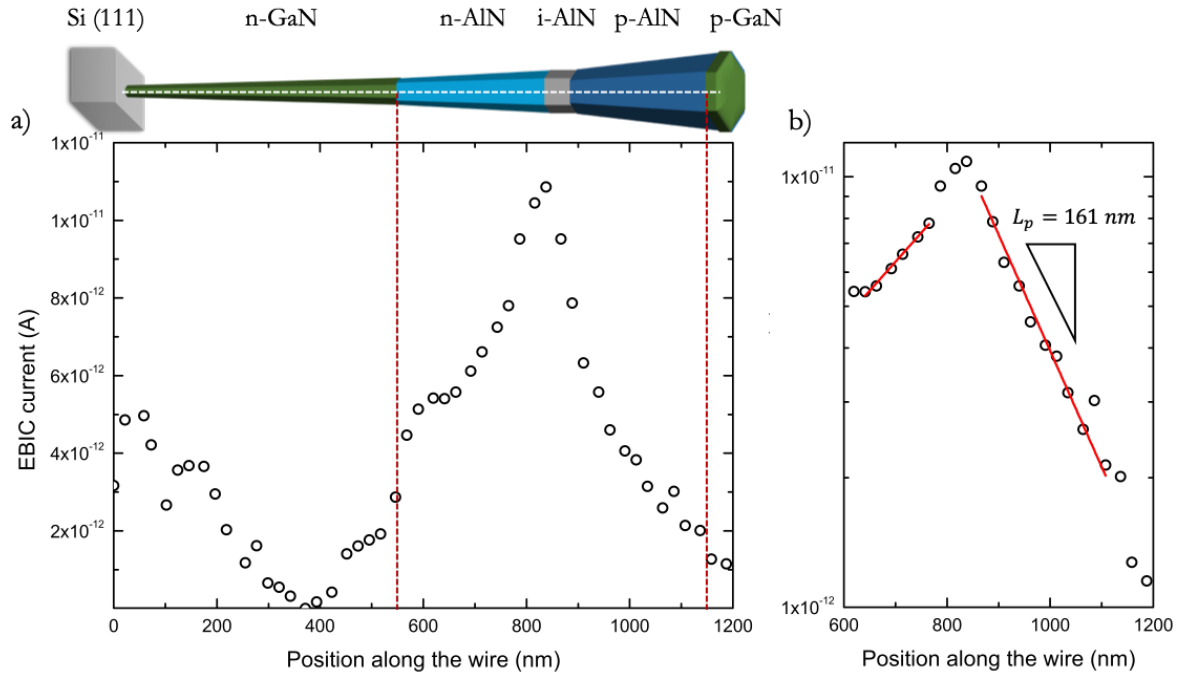

Figure 84 a) EBIC profile along the nanowire under no bias. b) EBIC profile in the pin junction region in logarithmic scale with the corresponding diffusion lengths fitting.

The beam current applied on the sample is of the order of 30 pA. The low resolution of the beam as well as the low current intensity coming from junction do not allow a clear visualization of the signal without biasing of the structure. The EBIC current is given here is absolute value. In the profile, the EBIC current is superimposed to the surface potential contrast given by the secondary electrons inside the SEM.

Nevertheless, the peak corresponding to the intrinsic field at the junction appears in Figure 84b in the corresponding AlN region, which is a proof of an intense electric field which we assign to the *pin* junction formation. The space charge region width for this nanowire under no bias is of approximately 100 nm, including the 30 nm of the intrinsic region. The minority carrier diffusion length is determined from the semi-logarithmic plot of the EBIC signal in the *pin* region (Figure 84b). The effective diffusion length of electrons on the p part of the junction extracted from these measurements was found to be of L_p=160 nm.

On the other hand, the effective diffusion length of holes on the n part of the junction gives a value of L_n=320 nm from experimental fitting. However, this value can be biased by the secondary electrons signal superimposed to the EBIC signal and is to be considered as only indicative. The fact that an EBIC signal appears at the junction prior to irradiation suggests a Mg activation in the sample which is already significant. The effective doping in the nanowire was determined to be of the order of 1×10^{18} cm^{-3}. This result is consistent with an impact ionization transport mechanism in the sample, since such doping levels are associated with a low carrier concentration.

However, in the first part of this study, we have analyzed the Mg incorporation in AlN NWs synthesized under similar conditions as sample N3209. Hence, Mg content in this sample is estimated at 1×10^{20} $at.cm^{-3}$, which means that at least 1% of the Mg has been activated in the given experimental conditions.

4.3.5.4. Mg activation by irradiation

While studying the sample under polarization, we can draw information about the electric field at the junction as well as from the space charge region width.

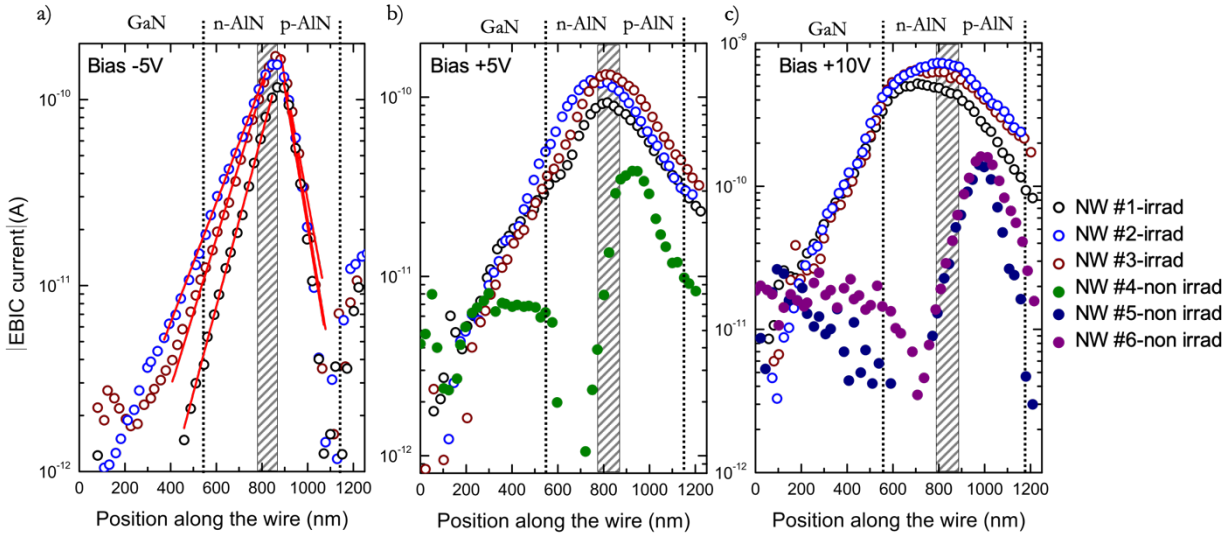

Figure 85. EBIC current profile with respect to the position along the nanowire under a) -5V polarization b) +5V polarization and c) +10 V polarization. The EBIC signature coming from the junction can be clearly observed in the middle of the AlN region (from 600 nm to 1200 nm)

Still by looking at the sample in parallel beam configuration, EBIC profiles were investigated on 6 different nanowires under different polarization conditions. To ease the understanding of the EBIC experiments, nanowire that have not been irradiated are represented with full circles whereas nanowires that underwent irradiation are illustrated by empty circles. The EBIC profiles along the nanowires is shown in Figure 85 for voltage bias of -5V (a), +5V (b) and +10V (c), respectively. The three cases will be discussed further.

An electric field appears systematically on a series of 3 nanowires at the *pin* junction of the sample under reverse bias (shown at –5V in Figure 85a). The EBIC current has been represented

in absolute value. Charge carriers created inside the NW or close to the *pin* junction are separated by the electric field localized within the *pin* junction. The linear fit of the EBIC signal allows the extraction of the space charge region as well as of the carrier diffusion length on both sides of the sample. The results are summarized in Table 14.

	L_n (nm)	L_p(nm)	W_D(nm)	Neff (cm^{-3})
NW #1	95	50	72	2.3×10^{18}
NW #2	108	55	80	1.8×10^{18}
NW #3	134	58	81	1.8×10^{18}

Table 14. Junction parameters extracted from the EBIC studies in reverse bias of -5V.

The difference between the minority carrier's diffusion lengths and space charge region for the three NWs considered in this case is small. The average diffusion lengths in the n-type of the junction is of 110 nm whereas it is of around 55 nm in the p part of the junction. The average SCR width as calculated from the three cases is of approximately 78 nm. These results clearly show a similar behavior of three nanowires from the same diode under polarization and confirms the reproducibility of the experiment. The effective doping N_{eff} can be determined from the space charge region width and was determined to be of the order of $(1.5\text{-}2.5)\times10^{18}$ cm^{-3}.

In order to check the presence of charge carriers within the structure, we performed EBIC measurements in forward regime, under a positive bias of +5V and +10V. Prior to e-beam irradiation (NW #4 for +5V - Figure 85b and NW#5 and NW#6 for +10V -Figure 85c), the EBIC signal in forward regime appears only and systematically in the p-type AlN part of the junction indicating that the voltage drop occurs in the p-type part which is more resistive than the n-type.

Interestingly, after irradiation (NW #1, NW#2 and NW#3), the EBIC signal in forward regime appears to be larger in the n-type AlN part of the sample (Figure 85b and c), indicating that the p-type part became more conducting than the n-type. This important observation can be related to the activation of Mg dopants in the p-part of the sample, shifting the EBIC signal towards the more resistive parts of the *pin* sample.

4.3.5.5. Forward bias effect on an individual nanowire

If we have a closer look at NW#1 at +5V, +10V, +20V and +30V, the EBIC current profiles are shown in Figure 86. The EBIC signals were aligned with respect to the respective SEM images and the different regions are identified and separated by the dashed lines.

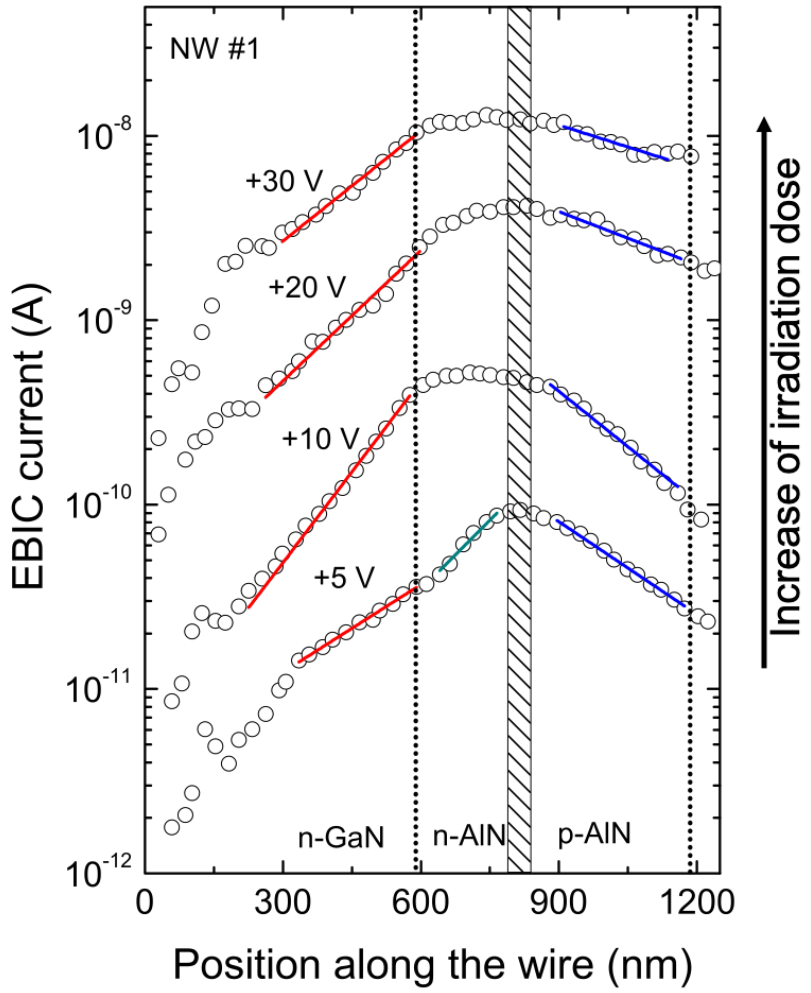

Figure 86. EBIC current profile with respect to the position along the nanowire under forward bias of +5V, +10 V, +20V and +30V. The EBIC signature coming from the junction can be clearly observed in the middle of the AlN region (from 600 nm to 1200 nm)

The EBIC profile at +5V (corresponding to a SCLC conduction mechanism) is different than the profiles at higher forward polarization. The AlN *pin* junction appears more abrupt than in the other cases, which is consistent with a change of transport mechanism for higher polarization. Moreover, at +5V the structure is not biased in forward configuration, since the threshold is at a higher voltage (around 6.2 eV). The signal appears at the junction, such as in the case of reverse bias.

If we refer to the analysis done in Section 4.3.4.2, when applying a higher bias (+10 V, +20V and +30V) the nanowire underwent a certain irradiation during the EBIC studies. Thus, the irradiation dose increases from the lower voltage towards the higher voltage and the irradiation

effect is in competition with the bias effect. Hence, by considering a low irradiation at +10V, the conduction mechanism in the nanowire is done by impact ionization. For higher voltages (+20 V and +30 V) it is then changing to a SCLC mechanism. The more resistive part of the sample appears as a voltage drop in the EBIC signal towards the n-part of the junction. This suggest that the n-type AlN could be resistive. When irradiating or applying a high voltage on the nanowires, the p-type AlN becomes more conductive than the n-type AlN due to the activation of the Mg by the e-beam.

We have considered so far, the simple case of a purely axial *pin* junction structure for the sample under study. However, the potential drop signal does not seem to be at a constant position (it is changing towards the n-type AlN), which allows us to consider the following hypothesis: an additional radial core (n-type)/shell (p-type) structure could account for additional effects observed so far. This is strongly probable, since the enhanced diffusion of metal atoms in presence of Mg is a known mechanism in the growth of nitride materials.

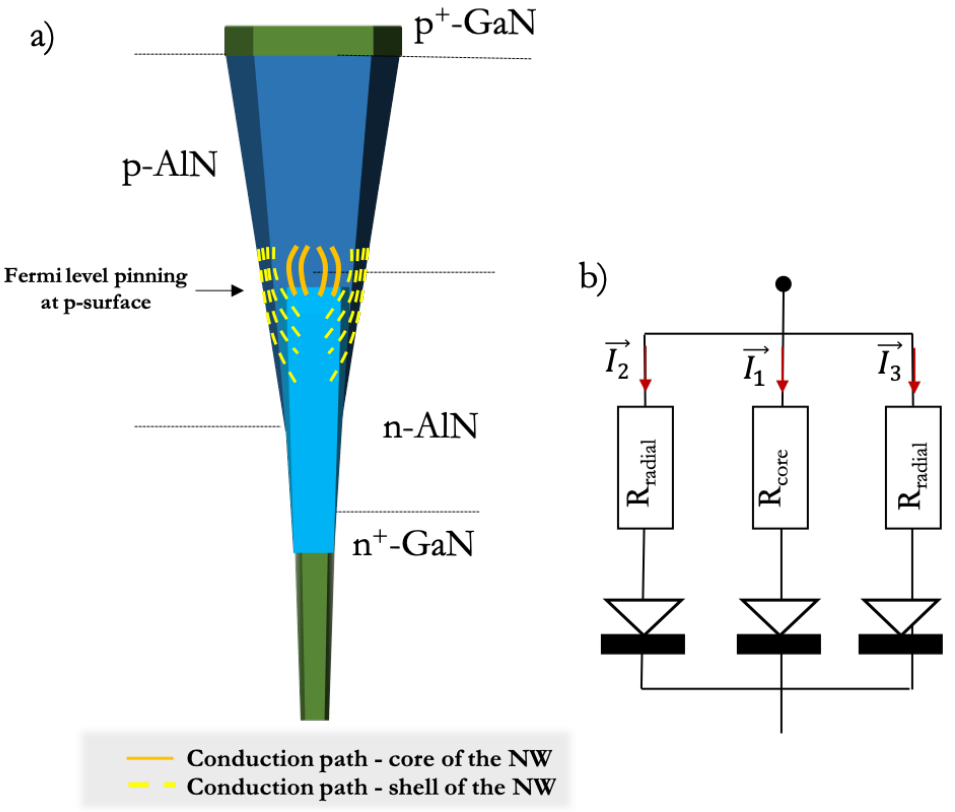

Figure 87. a) Transversal view schematization of the nanowire structure with respective conduction paths. b) Equivalent circuit (neglecting the diode threshold) with respective resistances for the n-type core/p-type shell nanowire.

Instead of considering the simple *pin* axial diode, the structure presented in Figure 87a is proposed. An important step in understanding the transport mechanisms would be the identification of the conduction paths inside the sample. If we consider the core-shell configuration, we can distinguish between two different conduction paths in competition inside the NWs:

- A core conduction inside the sample through the p-AlN/n-AlN axial junction of section surface S_{core} and resistance $R_{core} = \frac{\rho l}{S_{core}}$ (with ρ the resistivity of the material and l the length);
- A radial conduction by additional conduction paths through a thin p-type shell around nanowire of a smaller surface section S_{radial} and thus a much higher resistance expressed as $R_{radial} = \frac{\rho l}{S_{radial}}$ (with ρ the resistivity of the material and l the length).

Thus, the resistive p-type shell could be responsible of limiting the conduction mechanism, the potential drop we see in the EBIC experiment being correlated to this shell. This model has already been proposed in the literature (Tchernycheva et al. 2014).

To further evaluate this hypothesis, we have looked at the potential contrast on SEM images at different polarization bias. This technique of junction visualization by potential contrast has been shown previously in reference papers for GaN and $In_xGa_{1-x}N$/GaN junctions NW (Tchernycheva et al. 2014, 2015; Tchoulfian et al. 2014).

Figure 88b shows the potential contrast in the nanowire for different applied bias from -6V to +6V with a 2V step, at same brightness and contrast settings. The profiles were extracted from these images by image treatment and were aligned with respect to the substrate.

The 0 V signal was subtracted from the signal at different bias under the assumption that at 0V only the chemical contrast can be accounted for the SEM contrast. Nonetheless, this hypothesis is an approximation, since in various cases and on various samples, the surface contrast between n-type and p-type AlN is visible even without biasing of the sample.

The normalized contrast potential is represented in Figure 88a with respect to the position along the wires. For an easier lecture and interpretation of the data, forward bias was represented with different shades of red, whereas reverse bias appears in different shades of blue. The different regions of the structures have been evidenced by black dashed lines.

Interestingly, a potential drop appears at the junction between the Si substrate and the GaN stem of the sample. The same potential drop was also visible on the EBIC profiles, with a significantly lower intensity than in the case of the *pin* junction.

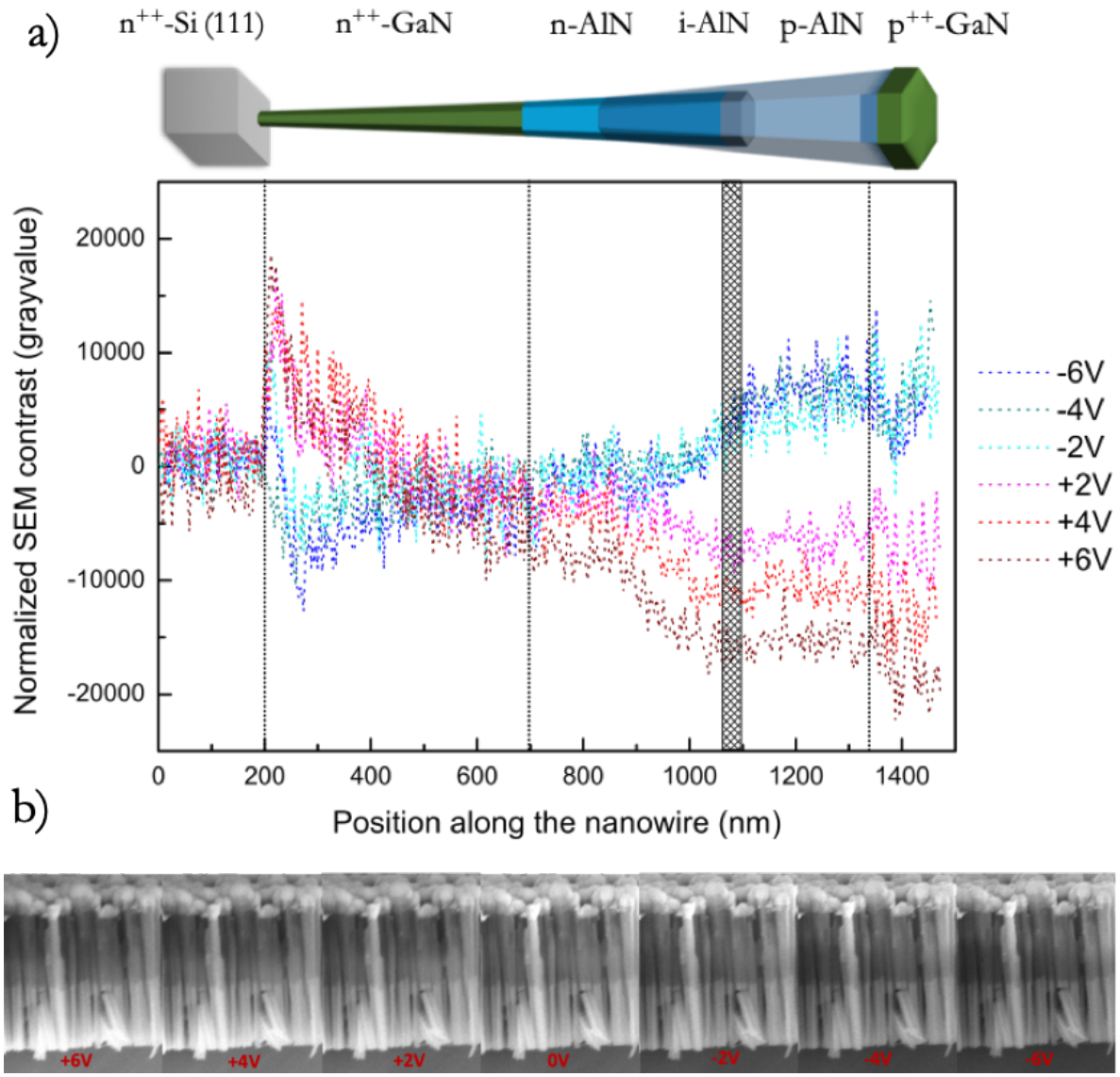

Figure 88. a) Potential contrast profile at different polarization bias as normalized with respect to the 0V bias profile. b) SEM images at different polarizations showing the potential contrast in the nanowires.

If we consider the case of a reverse bias, the contrast potential is equally distributed on the n and p sides of the samples at the position of the junction, consistent with results presented during EBIC experiments. Moreover, the potential contrast in the nanowires does not change significantly with the quantity of injected electrons, the physical position of the junction being the same whatever the applied bias. However, in forward bias, the potential drop takes place mainly in the "n-type AlN" and varies with the applied bias. By incrementing the forward bias, the potential contrast extends in the "n-type AlN", in agreement with a core-shell like structure of the AlN nanowire. Indeed, the electric field revealed by EBIC measurement in this region in forward bias being due to the potential drop induced by the conduction path through the thin p-type resistive shell. Eventually, this study confirms the presence of an external shell around the nanowire. It must be notice that this thin p-type shell could be also partly depleted due to surface pinning effect. This model is also in agreement with a SCLC current evidenced in forward regime, probably due to a hopping conduction in the p-type region.

4.3.6. Electroluminescence

The e-beam irradiation effect on the *pin* junction behavior was investigated through electroluminescence experiments in the same configuration as the EBIC experiments performed in the previous section.

The electroluminescence spectrum shown in Figure 89a a in red illustrates the electroluminescence prior to irradiation at room temperature. Then, the sample was completely irradiated at a high dose in the perpendicular beam configuration mode (as illustrated in Figure 76b) and then studied again in the parallel beam configuration mode, the electroluminescence spectrum appears in red after irradiation in Figure 89a.

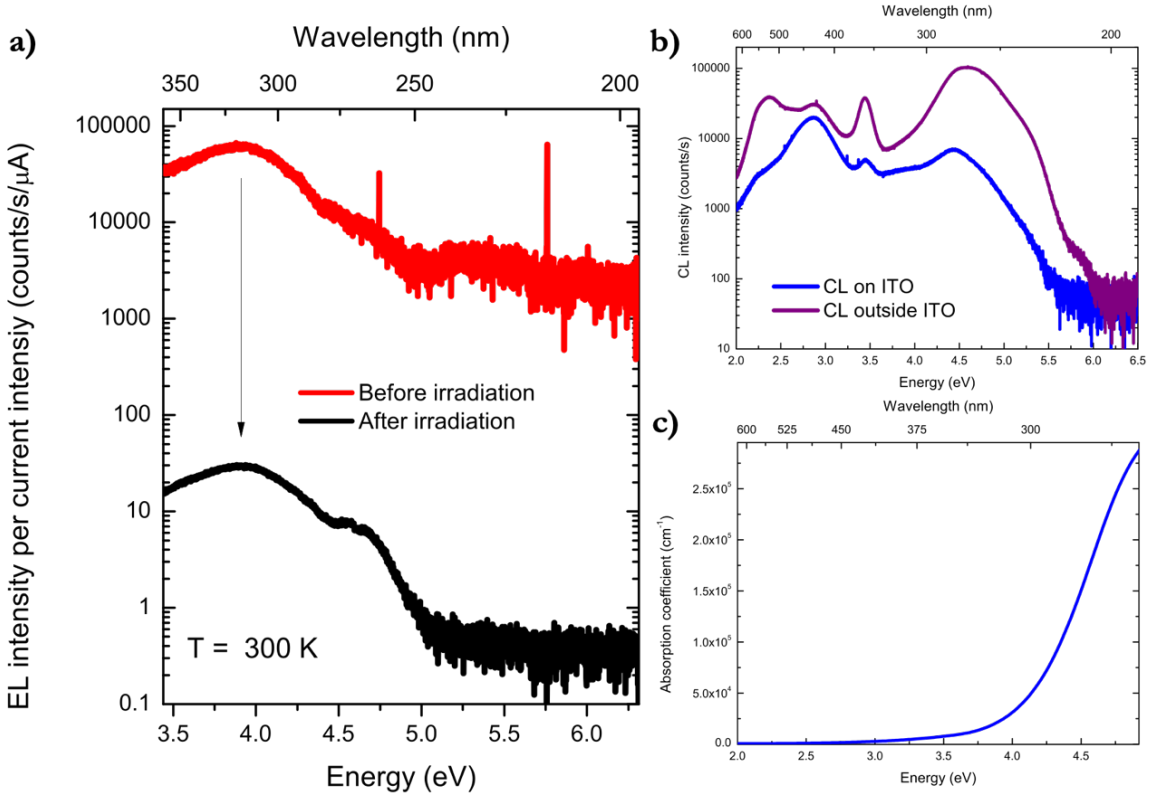

Figure 89. a) Electroluminescence spectrum of sample E recorded before and after irradiation showing deep-defect emission within p-type AlN. b) Cathodoluminescence on ITO (blue) and outside ITO (purple) explaining the lost in EL intensity for energies above 3.5 eV. c) ITO absorption coefficient variation as a function of energy.

At equivalent current excitation, the electroluminescence (EL) data shown in Figure 89 is exhibiting a drastic drop of EL intensity normalized by current intensity after e-beam irradiation. The relatively high EL intensity before e-beam irradiation, i.e. before Mg dopant activation, is consistent with the above-mentioned multiplication mechanism resulting from impact ionization. However, following Mg doping activation, the drop in EL intensity is consistent with the shift from a highly resistive regime in the p-AlN NW section to a highly conductive one and current tunneling through the *pn* junction, drastically decreasing the radiative recombination probability. Moreover, the metallic contact we have used for electrical studies have not been optimized for electroluminescence studies. Figure 89b presents the cathodoluminescence experiments performed

on the nanowires under the ITO plots (blue spectrum) and on the nanowires outside the ITO plot (purple spectrum) showing that the metal contact used for this sample is highly absorbing in the UV region. Indeed, the absorption coefficient of the ITO increases for energies higher than 3.25eV as shown in Figure 89c (König et al. 2014)(König et al. 2014).

4.4. Summary of chapter 4

Chapter 4 contains the major work done during my PhD regarding the development of AlN based DUV LEDs. I have started my research by looking and understanding the growth of $Al_xGa_{1-x}N$ *pn* junctions. However, the material characterization by HR-EDX has shown evidence of compositional fluctuations and superlattice like arrangements of AlN/GaN planes when growing high concentration p-type doped $Al_xGa_{1-x}N$ nanowires. Since the aim of this work is based on developing light emitting devices, this disordered alloy has proved detrimental to a controlled emission as shown by CL experiments. However, the realization of a *pn* junction inside the nanowire was characterized by EBIC experiments, the SCR showing a doping level of $9\times10^{16}cm^{-3}$. This investigation of $Al_xGa_{1-x}N$ nanowires has proved fruitful and opened the path in our research group toward the study of the binary alloy AlN as a candidate for DUV LEDs development.

We have further centered our research on the study of AlN based nanowires. The difficulty of p-type doping of AlN nanowires was oppressed by the efficient incorporation of Mg in a co-doping strategy, assisted by a small concentration of In. The Mg-In co-doping showed a clear increase of the Mg concentration incorporated in AlN NWs when assisted by In, achieving concentrations as high as 1.5×10^{20} at.cm^{-3}, without the formation of a ternary alloy. The quantitative results were determined by HR-EDX experiments and verified by Raman experiments. Moreover, Raman experiments have shown clear Mg-H modes appearing at high Raman scattering, coherent with Mg passivation inside the samples.

A model explaining the efficient incorporation of Mg was proposed by ab-initio theory. After discarding a purely elastic effect since both In and Mg induce a compressive strain in the AlN lattice, as well as a direct electronic interaction, we have made the hypothesis that the efficient incorporation in an Al-substitutional site is due to a complex process involving the nitrogen vacancies forming an In-V_N complex. This complex formation accommodates the related elastic deformation and also ionizes by releasing an electron, trapped by the Mg. The efficient incorporation of Mg^- in substitutional site in the growing wurzite structure with respect to the neutral Mg explains the increased Mg concentration in the samples when assisted by In.

After this successful increase of Mg incorporation, the long path towards a *pn* junction formation was still to be explained. Preliminary results on AlN nanowire *pin* junctions show a clear optical signature which was different for a p-type (Mg-In co-doped) and n-type (Si) doping as shown by CL studies. However, the electrical characteristics were pointing towards an impact ionization mechanism (with high power law variation coefficients going from 6 to 12) at high injection, and a SCLC transport at low injection. We have further investigated the effect of irradiation on the conduction mechanism showing that after complete irradiation, the samples

show an overall homogeneous SCLC transport mechanism in the samples, with 2.3 power law coefficients due to multilevel traps in the nanowires.

Further EBIC characterization on the samples have shown a first proof of a *pn* junction formation and allowed the determination of an effective doping level higher than 10^{18} cm^{-3} after study of the space charge region.

The diffusion length of minority carriers was however impacted by the resolution of the technique, since low acceleration voltages were necessary for an individual nanowire study. However, the diffusion length we have found were indicative and are of the order of L_n=110 and L_p=55 nm.

The irradiation effect on the samples was visible also on the EBIC signal under direct polarization of the samples. If the resistive part limiting the conduction inside the nanowire prior to the irradiation is the p-type AlN due to the non-activated Mg, the EBIC signal shows a potential drop in the AlN Si-doped part of the sample after irradiation. These results point towards an activation of Mg under the electron beam and we conclude that the resistive AlN n-type is in reality due to an external highly activated p-type shell. The formation of this shell is clearly visible in potential contrast experiments and allowed us to conclude on the complexity of the *pin* junction studied in this chapter.

To conclude with, no light emitting device can be considered as so without electroluminescence evidence. The EL experiments on the sample prior and after irradiation show an electroluminescence coming from deep-levels inside the Mg-doped region of the *pn* junction nanowires. If these deep-levels induced by Mg are a clear evidence of its presence, they are also detrimental to radiative recombination.

General conclusion and perspectives

The demands for efficient non-polluting UV-LEDs in view of replacing the mercury lamps used nowadays in purification systems have increased lately. Looking for deep-UV emitting materials (265 nm emission wavelength), the research groups have been focusing on the nitride materials. $Al_xGa_{1-x}N$ ternary alloys and the binary AlN and GaN materials are particularly interesting for the active region of device structures due to the emission wavelength modulation. The state-of-the-art emission of an $Al_xGa_{1-x}N$ based LED is still low, the best efficiency of a DUV LED being of 20% at 275 nm. However, significant progress is needed for further improvement of electrical properties, one of the major issues we confront with today being the difficult p-type doping of AlN and $Al_xGa_{1-x}N$ alloys. Obtaining a p-type conductivity in $Al_xGa_{1-x}N$ has been particularly difficult due to the high ionization energy of Mg dopant and the difficult incorporation of this dopant in $Al_xGa_{1-x}N$ material. Whereas n-type doping has been intensively studied for GaN nanowires. The lower ionization energy of the Si n-type dopant gives good results in terms of electrical conduction.

Finding a solution to the particular issue of the p-type doping of $Al_xGa_{1-x}N$ has been one of the objectives of my last years of research. We have focused all of our attention on working with nanowires, due to their particular geometry. These one-dimensional objects offer several advantages coming from their high surface/volume ratio, allowing strain relaxation, carrier confinement, better dopant incorporation and leading to a more efficient light emission, in the end.

Therefore, our research consisted in studying and improving the electrical properties of $Al_xGa_{1-x}N$ NW based structures for DUV light emitters. During my PhD, I tried to answer some of the essential questions regarding the III-N nanowire that I have already stated in the introduction.

Is the NW doping a specific mechanism?

n-type doping has already been intensively studied previously with the conclusion that the Si dopant tends to segregate in material systems at high doping temperatures. An advantage of these structures was the higher solubility limit of Si in GaN NW with respect to 2D layers. Regarding Mg systems, the question was still open.

By looking into Mg-doped GaN NWs by APT, the inhomogeneous radial distribution of Mg dopant inside of GaN nanowires helped us in understanding the incorporation mechanism of Mg, preferential on the m-plane side-wall. Due to the high m-plane to c-plane ratio in nanowires, it is expected to obtain higher levels of Mg doping in NWs than in their thin film counterpart.

Another take-away of this study was that the incorporation of this dopant is H assisted due to the high stability of this complex in N rich conditions. The passivation of Mg dopants by forming Mg-H complexes occurs even in MBE growth.

Moreover, positron annihilation experiments on Si and Mg doped nanowires concluded that the main vacancy defects in nanowires are V_{Ga} complexes with oxygen and hydrogen impurities. The experiment also suggested the presence of optically active defects in NWs, such as $(H_2)_{Ga}(V_N)_2$ and $(H_3)_{Ga}(V_N)_3$ complexes.

By performing EBIC experiments on an assembly of nanowires, we have concluded about the formation of a *pn* junction, however, with a lower carrier concentration on the p-side of the junction than on the n-part.

How can we incorporate acceptors in $Al_xGa_{1-x}N$…

We have investigated $Al_xGa_{1-x}N$ systems by studying the presence of acceptors in a *pn* junction at 60% Al composition. During compositional investigations, we have seen by HR-EDX, evidence of compositional fluctuations and superlattice-like arrangements of AlN/GaN planes when growing high concentration p-type doped $Al_xGa_{1-x}N$ nanowires. Cathodoluminescence results have shown a broadening of the emission line by Mg assigned deep levels in the band gap of the $Al_xGa_{1-x}N$ material, which is not favorable for efficient LEDs. However, EBIC experiment have shown an effective doping of the *pn* junction of $9x10^{16}$ cm^{-3}, a promising result for future structure optimization.

However, since the AlN material is the limiting compound of $Al_xGa_{1-x}N$ alloys, we have further investigated the Mg incorporation in this binary system. The doping incorporation has proved difficult even at high Mg fluxes during growth. However, we have managed to break the barrier of this difficult task by co-doping technique.

One of the major results of the PhD is the Mg-In co-doping of AlN nanowires. The efficient incorporation of this dopant in AlN material assisted by small concentration of In has been assessed by a series of techniques (EDX, Raman). The Mg concentration in the samples was found to be of $1.5x10^{20}$ $at.cm^{-3}$ for the highest doped samples. Ab-initio theoretical calculation have shown that the efficient incorporation in an Al-substitutional site is due to a process involving the nitrogen vacancies forming an In-V_N complex. This complex formation accommodates the related elastic deformation and also ionizes by releasing an electron, trapped by the Mg, easing its incorporation in substitutional site.

… and moreover, how can we activate them?

Another important result of this PhD was the dopant activation under e-beam irradiation. Similar to the case of GaN material, we have discovered a favorable effect of the electron beam irradiation of the samples, increasing the activation of Mg inside the samples.

How can we measure the activation and doping level?

The incorporation of Mg is one difficulty of working with high Al concentrations $Al_xGa_{1-x}N$ materials. The measurement of the activation of dopants and of the doping level is another difficult task. For that, I have used Electron Beam Induced Current (EBIC) on *pin* junctions of AlN nanowires to quantify the doping concentration inside the samples. This technique, even if not trivial due to the difficult quantification of results and experimental condition, has proven to be very efficient for dopants activation investigation. The effective doping in the nanowires was determined to be of the order of 1×10^{18} cm^{-3}. However, given the Mg concentration of atoms incorporated in the sample which is of the order of 1×10^{20} $at.cm^{-3}$, we have concluded that at least 1% of the Mg has been activated in the given experimental conditions.

What are the transport mechanisms in high Al content and AlN structures?

The electrical characteristics we had for our *pin* diodes were not compatible with a pure diode behavior, but were pointing towards a dominant impact ionization mechanism. In detail current density versus voltage characterization of samples prior to irradiation have shown an impact ionization mechanism (with high power law variation coefficients going from 6 to 12) at high injection, and a SCLC transport at low injection. After complete irradiation, the samples show an overall homogeneous SCLC transport mechanism with the presence of traps in the nanowires. These deep traps introduced by Mg incorporation were also playing a role on the emission spectrum of the samples, being responsible for deep-level electroluminescence. A complete EBIC study on the samples before and after irradiation has evidenced a potential drop in the n-type AlN. Complementary characterizations by surface potential contrast let us conclude about the presence of an external, highly activated p-type shell around the n-type AlN.

What other solutions would allow one to improve the metallic contacts for DUV LEDs?

The ITO electrodes I have used in the PhD were chosen due to the availability of the fabrication process and to the great results in previous studies. As a perspective of this project, we have started the study of a DUV transparent metallic contact on top of the AlN nanowires that would allow an easier light extraction from our samples: a **p-type diamond contact**. The p-type doping of this wide band gap semiconductor is optimized and it is possible to attain high boron doping levels of the order of 1×10^{21} $at.cm^{-3}$, inducing a metallic behavior of the contact. The preliminary steps concerning the diamond deposition on top of AlN nanowires have been already done in a collaboration with Professor Ken Haenen from IMEC group in Hasselt (Belgium). I have done the processing and conformity check of these electrodes with promising results, illustrated in Figure 90.

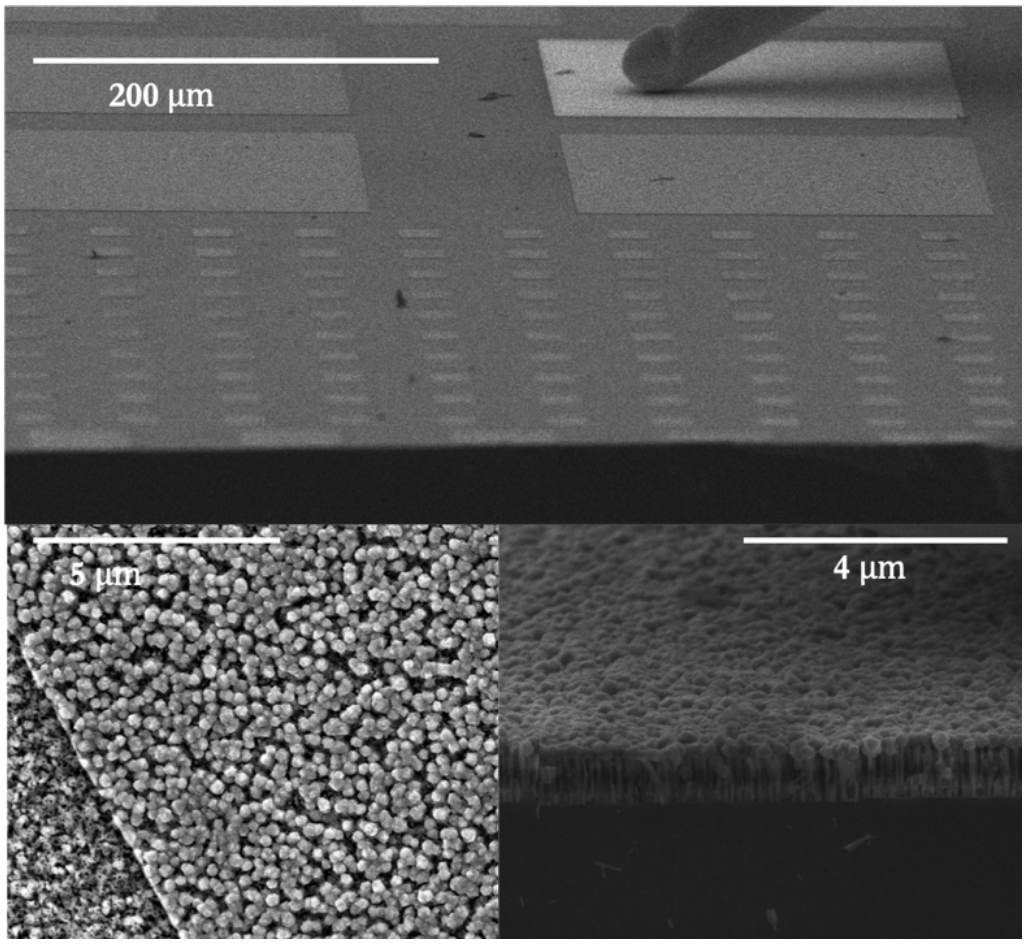

Figure 90. Diamond electrodes grown on top of AlN nanowires and contacting of the nanowires

Throughout this project, I had the great opportunity of participating at all of the steps of a light emitting device realization, from samples growth, contacting and electrical characterization. Moreover, by assisting my collaborators during several experiments, I had the occasion of becoming familiar and understanding more easily the physics behind each technique I am thankful for.

Interesting research questions for future research that can be derived from this work:

- What is the residual doping level in our AlN NWs and can we control it to fabricate intrinsic layer?
- Is it possible to achieve higher doping level in the n-type and p-type AlN, up to a metallic conduction?
- Is the incorporation process identical for the higher doping level?
- Can we activate Mg dopants in AlN using a thermal annealing instead of e-beam as in GaN ?
- Can we use and optimize the p-type shell in order to improve the performances of the NW based LED?
- What is the optimal transparent contact to reach efficient UV-LED ?

The answers to all these open questions should pave the way for the fabrication of next generation of efficient UV emitters based on nitride materials.

Scientific Communications

PUBLICATIONS

Mg and In co-doped p-type AlN nanowires for pn junction realization

Alexandra-Madalina Siladie, Gwénolé Jacopin, Ana Cros, Nùria Garro, Eric Robin, Damien Caliste, Pascal Pochet, Fabrice Donatini, Julien Pernot, Bruno Daudin*, Nano Lett. 2019, 19, 12, 8357-8364, doi.org/10.1021/acs.nanolett.9b01394*

Vacancy-type defects in GaN self-assembled nanowires probed using monoenergetic positron beam

Akira Uedono, Alexandra-Madalina Siladie, Julien Pernot, Bruno Daudin and Shoji Ishibashi, *J Appl Phys, 2019, 125:175705. doi: 10.1063/1.5088653*

Dopant radial inhomogeneity in Mg-doped GaN nanowires

Alexandra-Madalina Siladie, Lynda Amichi, Nicolas Mollard, Isabelle Mouton, Bastien Bonef, Catherine Bougerol, Adeline Grenier, Eric Robin, Pierre-Henri Jouneau, Nuria Garro, Ana Cros and Bruno Daudin *Nanotechnology, 2018, Volume 29, Number 25, doi.org/10.1088/1361-6528/aabbd6*

(PATENT) Procédé de réalisation de diode électroluminescente émettant dans l'UV et contenant une électrode conductrice en AlN dopé de type p.

Alexandra-Madalina Siladie, Gwenole Jacopin, Julien Pernot, Bruno Daudin, *PATENT PENDING, Oct. 2019*

CONFERENCES (Presenting author)

July 2019, ICNS, Seattle, Etats-Unis (oral) Problematics of p-type AlN nanowires: Mg/In codoping and activation issues

Alexandra-Madalina Siladie, Gwenole Jacopin, Ana Cros, Nuria Garro, Eric Robin, Damien Caliste, Pascal Pochet, Fabrice Donatini, Julien Pernot and Bruno Daudin

November 2018, IWN, Kanazawa, JAPON (Late news oral, Best student presentation award) The use of Mg and In co-doping for the realization of AlN NW deep UV emitters grown by molecular beam epitaxy

Alexandra-Madalina Siladie, Gwenole Jacopin, Ana Cros, Nuria Garro, Eric Robin, Fabrice Donatini, Julien Pernot and Bruno Daudin

August 2018, JMC, Grenoble, FRANCE (oral) Doping inhomogeneity in GaN and $Al_xGa_{1-x}N$ nanowires

Alexandra-Madalina Siladie, Fabrice Donatini, Gwenole Jacopin, Lynda Amichi, Catherine Bougerol, Eric Robin, Ana Cros, Nuria Garro, Julien Pernot and Bruno Daudin

July 2018, ICPS, Montpellier, FRANCE (oral) $Al_xGa_{1-x}N$ nanowire LED heterostructures: the intrinsic effect of radial doping inhomogeneity

Alexandra-Madalina Siladie, Fabrice Donatini, Gwenole Jacopin, Lynda Amichi, Catherine Bougerol, Eric Robin, Ana Cros, Nuria Garro, Julien Pernot and Bruno Daudin

June 2018, Nanowire Week, Hamilton, Ontario, CANADA (oral) Doping and electrical transport characterization of $Al_xGa_{1-x}N$ nanowire heterostructures for UV-C LEDs

Alexandra-Madalina Siladie, Fabrice Donatini, Gwenole Jacopin, Lynda Amichi, Catherine Bougerol, Eric Robin, Ana Cros, Nuria Garro, Julien Pernot and Bruno Daudin

April 2018, IUVALED Conference, Berlin, GERMANY (poster) p-n junction visualization and quantitative characterization of nanowire based $Al_xGa_{1-x}N$ LEDs

Alexandra-Madalina Siladie, Fabrice Donatini, Bruno Gayral, Julien Pernot and Bruno Daudin

November 2017, J2N Conference, Grenoble, FRANCE (oral) p-n junction visualization and quantitative characterization on single $Al_xGa_{1-x}N$ nanowires

Alexandra-Madalina Siladie, Matthias Belloeil, Fabrice Donatini, Luiz Tizei, Mathieu Kociak, Ana Cros, Nuria Garro, Bruno Gayral, Julien Pernot and Bruno Daudin

July 2017, ICNS-12 Conference, Strasbourg, FRANCE (oral) p-n junction visualization and quantitative characterization on $Al_xGa_{1-x}N$ single nanowires

Alexandra-Madalina Siladie, Matthias Belloeil, Fabrice Donatini, Zihua Fang, Luiz Tizei, Mathieu Kociak, Ana Cros, Nuria Garro, Bruno Gayral, Julien Pernot and Bruno Daudin

July 2017, ICNS-12 Conference, Strasbourg, FRANCE (oral) LATE NEWS: Radial dopant segregation in Mg-doped GaN nanowires

Alexandra-Madalina Siladie, Lynda Amichi, Nicolas Mollard, Eric Robin, Catherine Bougerol, Adeline Grenier, Isabelle Mouton, Pierre-Henri Jouneau, Ana Cros, Nuria Garro and Bruno Daudin

Bibliography

Agrawal R, Bernal RA, Isheim D, Espinosa HD (2011) Characterizing Atomic Composition and Dopant Distribution in Wide Band Gap Semiconductor Nanowires Using Laser-Assisted Atom Probe Tomography. J Phys Chem C 115:17688–17694

Ajay A (2018) GaN/AlGaN nanowires for quantum devices. Université Grenoble Alpes

Ajay A, Lim CB, Browne DA, et al (2017) Effect of doping on the intersubband absorption in Si- and Ge-doped GaN/AlN heterostructures. Nanotechnology 28:405204. https://doi.org/10.1088/1361-6528/aa8504

Aledia (2019) Aledia - Aledia. https://www.aledia.com/. Accessed 12 Sep 2019

Amano H, Kito M, Hiramatsu K, Akasaki I (1989) P-Type Conduction in Mg-Doped GaN Treated with Low-Energy Electron Beam Irradiation (LEEBI). Jpn J Appl Phys 28:L2112. https://doi.org/10.1143/JJAP.28.L2112

Angerer H, Brunner D, Freudenberg F, et al (1997) Determination of the Al mole fraction and the band gap bowing of epitaxial AlxGa1−xN films. Appl Phys Lett 71:1504–1506. https://doi.org/10.1063/1.119949

Auzelle T (2015) GaN/AlN nanowires : nucleation, polarity and quantum heterostructures. Phdthesis, Université Grenoble Alpes

Auzelle T, Haas B, Minj A, et al (2015) The influence of AlN buffer over the polarity and the nucleation of self-organized GaN nanowires. J Appl Phys 117:245303. https://doi.org/10.1063/1.4923024

Baliga BJ (2008) Fundamentals of power semiconductor devices. Springer, New York, NY

Ban K, Yamamoto J, Takeda K, et al (2011) Internal Quantum Efficiency of Whole-Composition-Range AlGaN Multiquantum Wells. Appl Phys Express 4:052101. https://doi.org/10.1143/APEX.4.052101

Bandić ZZ, Bridger PM, Piquette EC, McGill TC (1998) Minority carrier diffusion length and lifetime in GaN. Appl Phys Lett 72:3166–3168. https://doi.org/10.1063/1.121581

Beeler M, Hille P, Schörmann J, et al (2014) Intraband Absorption in Self-Assembled Ge-Doped GaN/AlN Nanowire Heterostructures. Nano Lett 14:1665–1673. https://doi.org/10.1021/nl5002247

Belloeil M (2017) Growth and optical properties of AlGaN/GaN nanowire heterostructures emitting in the ultraviolet. Université Grenoble Alpes

Belloeil M, Gayral B, Daudin B (2016) Quantum Dot-Like Behavior of Compositional Fluctuations in AlGaN Nanowires. Nano Lett 16:960–966. https://doi.org/10.1021/acs.nanolett.5b03904

Belosevic M, Craik SA, Stafford JL, et al (2001) Studies on the resistance/reactivation of Giardia muris cysts and Cryptosporidium parvum oocysts exposed to medium-pressure ultraviolet radiation. FEMS Microbiol Lett 204:197–203. https://doi.org/10.1111/j.1574-6968.2001.tb10885.x

Bois FY, Fahmy T, Block J-C, Gatel D (1997) Dynamic modeling of bacteria in a pilot drinking-water distribution system. Water Res 31:3146–3156. https://doi.org/10.1016/S0043-1354(97)00178-4

Bonard J, Ganière J (1996) Quantitative analysis of electron-beam-induced current profiles across p–n junctions in GaAs/Al0.4Ga0.6As heterostructures. J Appl Phys 79:6987–6994. https://doi.org/10.1063/1.361464

Bondokov RT, Mueller SG, Morgan KE, et al (2008) Large-area AlN substrates for electronic applications: An industrial perspective. J Cryst Growth 310:4020–4026. https://doi.org/10.1016/j.jcrysgro.2008.06.032

Bonef B, Cramer R, Speck JS (2017) Nanometer scale composition study of MBE grown BGaN performed by atom probe tomography. J Appl Phys 121:225701. https://doi.org/10.1063/1.4984087

Brandt MS, Ager JW, Götz W, et al (1994) Local vibrational modes in Mg-doped gallium nitride. Phys Rev B 49:14758–14761. https://doi.org/10.1103/PhysRevB.49.14758

Bremser MD, Perry WG, Nam OH, et al (1998) Acceptor and donor doping of AlxGa1−xN thin film alloys grown on 6H-SiC(0001) substrates via metalorganic vapor phase epitaxy. J Electron Mater 27:229–232. https://doi.org/10.1007/s11664-998-0392-9

Brochen S, Brault J, Chenot S, et al (2013) Dependence of the Mg-related acceptor ionization energy with the acceptor concentration in p-type GaN layers grown by molecular beam epitaxy. Appl Phys Lett 103:032102. https://doi.org/10.1063/1.4813598

Bryan I, Bryan Z, Mita S, et al (2016) The role of surface kinetics on composition and quality of AlGaN. J Cryst Growth 451:65–71. https://doi.org/10.1016/j.jcrysgro.2016.06.055

Calarco R, Marso M, Richter T, et al (2005) Size-dependent Photoconductivity in MBE-Grown GaN−Nanowires. Nano Lett 5:981–984. https://doi.org/10.1021/nl0500306

Calarco R, Stoica T, Brandt O, Geelhaar L (2011) Surface-induced effects in GaN nanowires. J Mater Res 26:2157–2168. https://doi.org/10.1557/jmr.2011.211

Cancho B, Ventura F, Galceran M, et al (2000) Determination, synthesis and survey of iodinated trihalomethanes in water treatment processes. Water Res 34:3380–3390. https://doi.org/10.1016/S0043-1354(00)00079-8

Carlos Rojo J, Slack GA, Morgan K, et al (2001) Report on the growth of bulk aluminum nitride and subsequent substrate preparation. J Cryst Growth 231:317–321. https://doi.org/10.1016/S0022-0248(01)01452-X

Carnevale SD, Kent TF, Phillips PJ, et al (2013) Mixed Polarity in Polarization-Induced p–n Junction Nanowire Light-Emitting Diodes. Nano Lett 13:3029–3035. https://doi.org/10.1021/nl400200g

Caro Bayo M (2013) Theory of elasticity and electric polarization effects in the group-III nitrides. University College Cork

Charak S, Shandilya M, Tyagi G, Mehrotra R (2012) Spectroscopic and molecular docking studies on chlorambucil interaction with DNA. Int J Biol Macromol 51:406–411. https://doi.org/10.1016/j.ijbiomac.2012.06.012

Chen GD, Smith M, Lin JY, et al (1996) Fundamental optical transitions in GaN. Appl Phys Lett 68:2784–2786. https://doi.org/10.1063/1.116606

Chernyak L, Osinsky A, Fuflyigin V, Schubert EF (2000) Electron beam-induced increase of electron diffusion length in p-type GaN and AlGaN/GaN superlattices. Appl Phys Lett 77:875–877. https://doi.org/10.1063/1.1306910

Chevrefils G, Ing B, Caron É, et al (2006) UV Dose Required to Achieve. 8

Chichibu SF, Onuma T, Hazu K, Uedono A (2010) Major impacts of point defects and impurities on the carrier recombination dynamics in AlN. Appl Phys Lett 97:201904. https://doi.org/10.1063/1.3517484

Chine Z, Rebey A, Touati H, et al (2006) Stress and density of defects in Si-doped GaN. Phys Status Solidi A 203:1954–1961. https://doi.org/10.1002/pssa.200521107

Christensen NE, Gorczyca I (1994) Optical and structural properties of III-V nitrides under pressure. Phys Rev B 50:4397–4415. https://doi.org/10.1103/PhysRevB.50.4397

Clancy JL, Bukhari Z, Hargy TM, et al (2000) Using UV to inactivate Cryptosporidium. J - Am Water Works Assoc 92:97–104. https://doi.org/10.1002/j.1551-8833.2000.tb09008.x

Contreras S, Konczewicz L, Peyre H, et al (2017) High Temperature Annealing of MBE-grown Mg-doped GaN. J Phys Conf Ser 864:012018. https://doi.org/10.1088/1742-6596/864/1/012018

Coughlan C, Schulz S, Caro MA, O'Reilly EP (2015) Band gap bowing and optical polarization switching in AlGaN alloys. Phys Status Solidi B 252:879–884. https://doi.org/10.1002/pssb.201451593

Cuscó R, Artús L, Pastor D, et al (2004) Local vibrational modes of H complexes in Mg-doped GaN grown by molecular beam epitaxy. Appl Phys Lett 84:897–899. https://doi.org/10.1063/1.1645668

Cuscó R, Domènech-Amador N, Artús L, et al (2012) Temperature dependence of Mg-H local vibrational modes in heavily doped InN:Mg. J Appl Phys 112:053528. https://doi.org/10.1063/1.4749266

Dadgar A, Bläsing J, Diez A, Krost A (2011) Crack-Free, Highly Conducting GaN Layers on Si Substrates by Ge Doping. Appl Phys Express 4:011001. https://doi.org/10.1143/APEX.4.011001

Dan Y, Seo K, Takei K, et al (2011) Dramatic Reduction of Surface Recombination by in Situ Surface Passivation of Silicon Nanowires. Nano Lett 11:2527–2532. https://doi.org/10.1021/nl201179n

Daudin B, Feuillet G, Hübner J, et al (1998) How to grow cubic GaN with low hexagonal phase content on (001) SiC by molecular beam epitaxy. J Appl Phys 84:2295–2300. https://doi.org/10.1063/1.368296

De Geuser F, Gault B, Bostel A, Vurpillot F (2007) Correlated field evaporation as seen by atom probe tomography. Surf Sci 601:536–543. https://doi.org/10.1016/j.susc.2006.10.019

Demichel O, Heiss M, Bleuse J, et al (2010) Impact of surfaces on the optical properties of GaAs nanowires. Appl Phys Lett 97:201907. https://doi.org/10.1063/1.3519980

Deslattes RD, Kessler Jr. G, Indelicato P, et al (2005) X-Ray Transition Energies Database | NIST. https://www.nist.gov/pml/x-ray-transition-energies-database. Accessed 15 Sep 2019

Djavid M, Mi Z (2016) Enhancing the light extraction efficiency of AlGaN deep ultraviolet light emitting diodes by using nanowire structures. Appl Phys Lett 108:051102. https://doi.org/10.1063/1.4941239

Dmitriev AV, Oruzheinikov AL (1996) Radiative recombination rates in GaN, InN, AlN and solid solutions. Mater Res Soc Symp Proc 423:5

Donolato C (1994) Reciprocity theorem for charge collection by a surface with finite collection velocity: Application to grain boundaries. J Appl Phys 76:959–966. https://doi.org/10.1063/1.357774

Dridi Z, Bouhafs B, Ruterana P (2003) First-principles investigation of lattice constants and bowing parameters in wurtzite AlxGa1−xN, InxGa1−xN and InxAl1−xN alloys. Semicond Sci Technol 18:850. https://doi.org/10.1088/0268-1242/18/9/307

Duff AI, Lymperakis L, Neugebauer J (2014) Understanding and controlling indium incorporation and surface segregation on InGaN surfaces: An ab initio approach. Phys Rev B 89:085307. https://doi.org/10.1103/PhysRevB.89.085307

El Kacimi A, Pauliac-Vaujour E, Eymery J (2018) Flexible Capacitive Piezoelectric Sensor with Vertically Aligned Ultralong GaN Wires. ACS Appl Mater Interfaces 10:4794–4800. https://doi.org/10.1021/acsami.7b15649

Elsner J, Jones R, Heggie MI, et al (1998) Deep acceptors trapped at threading-edge dislocations in GaN. Phys Rev B 58:12571–12574. https://doi.org/10.1103/PhysRevB.58.12571

Ertekin E, Greaney PA, Chrzan DC, Sands TD (2005) Equilibrium limits of coherency in strained nanowire heterostructures. J Appl Phys 97:114325. https://doi.org/10.1063/1.1903106

Fang Z, Donatini F, Daudin B, Pernot J (2018) Axial p–n junction and space charge limited current in single GaN nanowire. Nanotechnology 29:01LT01. https://doi.org/10.1088/1361-6528/aa9a0e

Fang Z, Robin E, Rozas-Jiménez E, et al (2015) Si Donor Incorporation in GaN Nanowires. Nano Lett 15:6794–6801. https://doi.org/10.1021/acs.nanolett.5b02634

Fernández-Garrido S, Grandal J, Calleja E, et al (2009) A growth diagram for plasma-assisted molecular beam epitaxy of GaN nanocolumns on Si(111). J Appl Phys 106:126102. https://doi.org/10.1063/1.3267151

Fernández-Garrido S, Kaganer VM, Sabelfeld KK, et al (2013) Self-Regulated Radius of Spontaneously Formed GaN Nanowires in Molecular Beam Epitaxy. Nano Lett 13:3274–3280. https://doi.org/10.1021/nl401483e

Flynn C, Lee W (2014) The dependence of Raman scattering on Mg concentration in Mg-doped GaN grown by MBE. Mater Res Express 1:025901. https://doi.org/10.1088/2053-1591/1/2/025901

Francis RW, Worrell WL (1976) High Temperature Electrical Conductivity of Aluminum Nitride. J Electrochem Soc 123:430–433. https://doi.org/10.1149/1.2132844

Fritze S, Dadgar A, Witte H, et al (2012) High Si and Ge n-type doping of GaN doping - Limits and impact on stress. Appl Phys Lett 100:122104. https://doi.org/10.1063/1.3695172

Gault B (ed) (2012) Atom probe microscopy. Springer, New York, NY

Gault B, Saxey DW, Ashton MW, et al (2016) Behavior of molecules and molecular ions near a field emitter. New J Phys 18:033031. https://doi.org/10.1088/1367-2630/18/3/033031

Glas F (2006) Critical dimensions for the plastic relaxation of strained axial heterostructures in free-standing nanowires. Phys Rev B 74:. https://doi.org/10.1103/PhysRevB.74.121302

Goldstein JI, Newbury DE, Echlin P, et al (2003) Generation of X-Rays in the SEM Specimen. In: Goldstein JI, Newbury DE, Echlin P, et al. (eds) Scanning Electron Microscopy and X-ray Microanalysis: Third Edition. Springer US, Boston, MA, pp 271–296

Goldstein JI, Newbury DE, Michael JR, et al (2017) Scanning Electron Microscopy and X-Ray Microanalysis. Springer

Gonzalez JC, Bunker KL, Russell PE (2001) Minority-carrier diffusion length in a GaN-based light-emitting diode. Appl Phys Lett 79:1567–1569. https://doi.org/10.1063/1.1400075

Grandjean N, Massies J, Semond F, et al (1999) GaN evaporation in molecular-beam epitaxy environment. Appl Phys Lett 74:1854–1856. https://doi.org/10.1063/1.123691

Grandusky JR, Chen J, Gibb SR, et al (2013) 270 nm Pseudomorphic Ultraviolet Light-Emitting Diodes with Over 60 mW Continuous Wave Output Power. Appl Phys Express 6:032101. https://doi.org/10.7567/APEX.6.032101

Grandusky JR, Gibb SR, Mendrick MC, et al (2011) High Output Power from 260 nm Pseudomorphic Ultraviolet Light-Emitting Diodes with Improved Thermal Performance. Appl Phys Express 4:082101. https://doi.org/10.1143/APEX.4.082101

Grazzi C, Albrecht M, Strunk HP, et al (2001) Minority Carrier Diffusion Lengths in Silicon Doped Gallium Nitride Thin Films Measured by Electron Beam Induced Current. Solid State Phenom 82–84:807–0. https://doi.org/10.4028/www.scientific.net/SSP.82-84.807

Gupta C, Enatsu Y, Gupta G, et al (2016) High breakdown voltage p–n diodes on GaN on sapphire by MOCVD. Phys Status Solidi A 213:878–882. https://doi.org/10.1002/pssa.201532554

Gurwitz R, Shalish I (2011) Method for electrical characterization of nanowires. Nanotechnology 22:435705. https://doi.org/10.1088/0957-4484/22/43/435705

Haller C, Carlin J-F, Jacopin G, et al (2018) GaN surface as the source of non-radiative defects in InGaN/GaN quantum wells. Appl Phys Lett 113:111106. https://doi.org/10.1063/1.5048010

Han J, Crawford MH, Shul RJ, et al (1998) AlGaN/GaN quantum well ultraviolet light emitting diodes. Appl Phys Lett 73:1688–1690. https://doi.org/10.1063/1.122246

Harima H, Inoue T, Nakashima S, et al (1999) Local vibrational modes as a probe of activation process in p-type GaN. Appl Phys Lett 75:1383–1385. https://doi.org/10.1063/1.124701

Hartwigsen C, Goedecker S, Hutter J (1998) Relativistic separable dual-space Gaussian pseudopotentials from H to Rn. Phys Rev B 58:3641–3662. https://doi.org/10.1103/PhysRevB.58.3641

Hasegawa S (2012) Reflection High Energy Electron Diffraction. In: Characterization of Materials. John Wiley & Sons, Inc., p 14

Held PG (2001) Nucleic acid purity assessement using A260/A280 ratios

Hellman ES (1998) The Polarity of GaN: a Critical Review. Mater Res Soc Internet J Nitride Semicond Res 3:. https://doi.org/10.1557/S1092578300000831

Helmenstine A (2016) Colorful Periodic Table with 118 Element Names. In: Sci. Notes Proj. https://sciencenotes.org/2016-2017-colorful-periodic-table-118-element-names/. Accessed 4 Sep 2019

Henry TA, Armstrong A, Allerman AA, Crawford MH (2012) The influence of Al composition on point defect incorporation in AlGaN. Appl Phys Lett 100:043509. https://doi.org/10.1063/1.3679681

Herman M, Sitter H (2012) Molecular Beam Epitaxy: Fundamentals and Current Status, 2nd Edition. Springer Science & Business Media

Hestroffer K (2012) Croissance et caractérisation de nanofils de GaN et d'hétérostructures filaires de GaN/AlN. Grenoble

Hestroffer K, Leclere C, Bougerol C, et al (2011) Polarity of GaN nanowires grown by plasma-assisted molecular beam epitaxy on Si(111). Phys Rev B 84:245302. https://doi.org/10.1103/PhysRevB.84.245302

Hijnen WAM, Beerendonk EF, Medema GJ (2006) Inactivation credit of UV radiation for viruses, bacteria and protozoan (oo)cysts in water: A review. Water Res 40:3–22. https://doi.org/10.1016/j.watres.2005.10.030

Hille P, Müßener J, Becker P, et al (2014) Screening of the quantum-confined Stark effect in AlN/GaN nanowire superlattices by germanium doping. Appl Phys Lett 104:102104. https://doi.org/10.1063/1.4868411

Himwas C, den Hertog M, Dang LS, et al (2014) Alloy inhomogeneity and carrier localization in AlGaN sections and AlGaN/AlN nanodisks in nanowires with 240–350 nm emission. Appl Phys Lett 105:241908. https://doi.org/10.1063/1.4904989

Hirayama H (2018) Recent Progress in AlGaN Deep-UV LEDs. Light-Emit Diode - Outlook Empir Featur Its Recent Technol Adv. https://doi.org/10.5772/intechopen.79936

Hirayama H, Maeda N, Fujikawa S, et al (2014) Recent progress and future prospects of AlGaN-based high-efficiency deep-ultraviolet light-emitting diodes. Jpn J Appl Phys 53:100209. https://doi.org/10.7567/JJAP.53.100209

Høiaas IM, Liudi Mulyo A, Vullum PE, et al (2019) GaN/AlGaN Nanocolumn Ultraviolet Light-Emitting Diode Using Double-Layer Graphene as Substrate and Transparent Electrode. Nano Lett 19:1649–1658. https://doi.org/10.1021/acs.nanolett.8b04607

Huang W-C, Chu C-M, Wong Y-Y, et al (2016) Investigations of GaN growth on the sapphire substrate by MOCVD method with different AlN buffer deposition temperatures. Mater Sci Semicond Process 45:1–8. https://doi.org/10.1016/j.mssp.2016.01.008

Iida D, Tamura K, Iwaya M, et al (2010) Compensation effect of Mg-doped a- and c-plane GaN films grown by metalorganic vapor phase epitaxy. J Cryst Growth 312:3131–3135. https://doi.org/10.1016/j.jcrysgro.2010.07.038

Inazu T, Fukahori S, Pernot C, et al (2011) Improvement of Light Extraction Efficiency for AlGaN-Based Deep Ultraviolet Light-Emitting Diodes. Jpn J Appl Phys 50:122101. https://doi.org/10.1143/JJAP.50.122101

Isamu Akasaki, Hiroshi Amano, Masahiro Kito, Kazumasa Hiramatsu (1991) Photoluminescence of Mg-doped p-type GaN and electroluminescence of GaN p-n junction LED. J Lumin 48–49:666–670. https://doi.org/10.1016/0022-2313(91)90215-H

Ishibashi S, Tamura T, Tanaka S, et al (2007) Ab initio calculations of electric-field-induced stress profiles for diamond-cBN (110) superlattices. Phys Rev B 76:153310. https://doi.org/10.1103/PhysRevB.76.153310

Ishibashi S, Uedono A (2014) First-principles calculation of positron states and annihilation parameters for group-III nitrides. J Phys Conf Ser 505:012010. https://doi.org/10.1088/1742-6596/505/1/012010

Jiang H, Zhao GY, Ishikawa H, et al (2000) Determination of exciton transition energy and bowing parameter of AlGaN alloys in AlGaN/GaN heterostructure by means of reflectance measurement. J Appl Phys 89:1046–1052. https://doi.org/10.1063/1.1334923

Joyce BA, Dobson PJ, Neave JH, et al (1986) RHEED studies of heterojunction and quantum well formation during MBE growth — from multiple scattering to band offsets. Surf Sci 168:423–438. https://doi.org/10.1016/0039-6028(86)90873-3

Kaczmarczyk G, Kaschner A, Hoffmann A, Thomsen C (2000) Impurity-induced modes of Mg, As, Si, and C in hexagonal and cubic GaN. Phys Rev B 61:5353–5357. https://doi.org/10.1103/PhysRevB.61.5353

Kamimura J, Bogdanoff P, Ramsteiner M, et al (2017) p-Type Doping of GaN Nanowires Characterized by Photoelectrochemical Measurements. Nano Lett 17:1529–1537. https://doi.org/10.1021/acs.nanolett.6b04560

Kanaya K, Okayama S (1972) Penetration and energy-loss theory of electrons in solid targets. J Phys Appl Phys 5:43–58. https://doi.org/10.1088/0022-3727/5/1/308

Karpov SYu, Makarov YN (2002) Dislocation effect on light emission efficiency in gallium nitride. Appl Phys Lett 81:4721–4723. https://doi.org/10.1063/1.1527225

Karpov SYu, Talalaev RA, Makarov YuN, et al (2000) Surface kinetics of GaN evaporation and growth by molecular-beam epitaxy. Surf Sci 450:191–203. https://doi.org/10.1016/S0039-6028(00)00055-8

Kaschner A, Siegle H, Kaczmarczyk G, et al (1999) Local vibrational modes in Mg-doped GaN grown by molecular beam epitaxy. Appl Phys Lett 74:3281–3283. https://doi.org/10.1063/1.123320

Kaufmann U, Schlotter P, Obloh H, et al (2000) Hole conductivity and compensation in epitaxial GaN:Mg layers. Phys Rev B 62:10867–10872. https://doi.org/10.1103/PhysRevB.62.10867

Kibria MG, Zhao S, Chowdhury FA, et al (2014) Tuning the surface Fermi level on p-type gallium nitride nanowires for efficient overall water splitting | Nature Communications. Nat Commun 5:. https://doi.org/DOI: 10.1038/ncomms4825

Kingham DR (1982) The post-ionization of field evaporated ions: A theoretical explanation of multiple charge states. Surf Sci 116:273–301. https://doi.org/10.1016/0039-6028(82)90434-4

Kinoshita A, Hirayama H, Ainoya M, et al (2000) Room-temperature operation at 333 nm of Al0.03Ga0.97N/Al0.25Ga0.75N quantum-well light-emitting diodes with Mg-doped superlattice layers. Appl Phys Lett 77:175–177. https://doi.org/10.1063/1.126915

Kinoshita T, Hironaka K, Obata T, et al (2012) Deep-Ultraviolet Light-Emitting Diodes Fabricated on AlN Substrates Prepared by Hydride Vapor Phase Epitaxy. Appl Phys Express 5:122101. https://doi.org/10.1143/APEX.5.122101

Kirste R, Hoffmann MP, Tweedie J, et al (2013) Compensation effects in GaN:Mg probed by Raman spectroscopy and photoluminescence measurements. J Appl Phys 113:103504. https://doi.org/10.1063/1.4794094

Kneissl M, Rass J (eds) (2016) III-Nitride Ultraviolet Emitters. Springer International Publishing, Cham

Kneissl M, Seong T-Y, Han J, Amano H (2019) The emergence and prospects of deep-ultraviolet light-emitting diode technologies. Nat Photonics 13:233–244. https://doi.org/10.1038/s41566-019-0359-9

Kneissl M, Yang Z, Teepe M, et al (2007) Ultraviolet semiconductor laser diodes on bulk AlN. J Appl Phys 101:123103. https://doi.org/10.1063/1.2747546

Koelling S, Li A, Cavalli A, et al (2017) Atom-by-Atom Analysis of Semiconductor Nanowires with Parts Per Million Sensitivity. Nano Lett 17:599–605. https://doi.org/10.1021/acs.nanolett.6b03109

König TAF, Ledin PA, Kerszulis J, et al (2014) Electrically Tunable Plasmonic Behavior of Nanocube–Polymer Nanomaterials Induced by a Redox-Active Electrochromic Polymer. ACS Nano 8:6182–6192. https://doi.org/10.1021/nn501601e

Koppe T, Hofsäss H, Vetter U (2016) Overview of band-edge and defect related luminescence in aluminum nitride. J Lumin 178:267–281. https://doi.org/10.1016/j.jlumin.2016.05.055

Krause-Rehberg R, Leipner HS (1999) Positron Annihilation in Semiconductors: Defect Studies. Springer Science & Business Media

Krueger JG, Wolfe JT, Nabeya RT, et al (1995) Successful ultraviolet B treatment of psoriasis is accompanied by a reversal of keratinocyte pathology and by selective depletion of intraepidermal T cells. J Exp Med 182:2057–2068

Kumakura K, Makimoto T, Kobayashi N, et al (2005) Minority carrier diffusion length in GaN: Dislocation density and doping concentration dependence. Appl Phys Lett 86:052105. https://doi.org/10.1063/1.1861116

Kwok-Keung A, LeChevallier MW (2013) Water treatment and pathogen control Process efficiency in achieving safe drinking-water. WHO, Genf

Kyle ECH, Kaun SW, Young EC, Speck JS (2015) Increased p-type conductivity through use of an indium surfactant in the growth of Mg-doped GaN. Appl Phys Lett 106:222103. https://doi.org/10.1063/1.4922216

Landré O, Fellmann V, Jaffrennou P, et al (2010) Molecular beam epitaxy growth and optical properties of AlN nanowires. Appl Phys Lett 96:061912. https://doi.org/10.1063/1.3315943

Landré O, Songmuang R, Renard J, et al (2008) Plasma-assisted molecular beam epitaxy growth of GaN nanowires using indium-enhanced diffusion. Appl Phys Lett 93:183109. https://doi.org/10.1063/1.3013840

Largeau L, Galopin E, Gogneau N, et al (2012) N-Polar GaN Nanowires Seeded by Al Droplets on Si(111). Cryst Growth Des 12:2724–2729. https://doi.org/10.1021/cg300212d

Le BH, Zhao S, Liu X, et al (2016) Controlled Coalescence of AlGaN Nanowire Arrays: An Architecture for Nearly Dislocation-Free Planar Ultraviolet Photonic Device Applications. Adv Mater 28:8446–8454. https://doi.org/10.1002/adma.201602645

Lee I-H, Choi I-H, Lee C-R, et al (1998) Stress relaxation in Si-doped GaN studied by Raman spectroscopy. J Appl Phys 83:5787–5791. https://doi.org/10.1063/1.367501

Leroux M, Vennéguès P, Dalmasso S, et al (2002) Structural Defects and Relation with Optoelectronic Properties in Highly Mg-Doped GaN. Phys Status Solidi Appl Res 192:394–400. https://doi.org/10.1002/1521-396X(200208)192

Leroux M, Vennéguès P, Dalmasso S, et al (2004) Pyramidal defects in highly Mg-doped GaN: atomic structure and influence on optoelectronic properties. Eur Phys J Appl Phys 27:259–262. https://doi.org/10.1051/epjap:2004119-2

Levinshtein ME, Rumyantsev SL, Shur MS (2001) Properties of Advanced Semiconductor Materials: GaN, AIN, InN, BN, SiC, SiGe. John Wiley & Sons

Li J, Nam KB, Nakarmi ML, et al (2003) Band structure and fundamental optical transitions in wurtzite AlN. Appl Phys Lett 83:5163–5165. https://doi.org/10.1063/1.1633965

Li KH, Liu X, Wang Q, et al (2015) Ultralow-threshold electrically injected AlGaN nanowire ultraviolet lasers on Si operating at low temperature. Nat Nanotechnol 10:140–144. https://doi.org/10.1038/nnano.2014.308

Lin ME, Xue G, Zhou GL, et al (1993) p-type zinc-blende GaN on GaAs substrates. Appl Phys Lett 63:932–933. https://doi.org/10.1063/1.109848

Liu Z, Fu B, Yi X, et al (2016) Co-doping of magnesium with indium in nitrides: first principle calculation and experiment. RSC Adv 6:5111–5115. https://doi.org/10.1039/C5RA24642C

Lopez-Haro M, Bayle-Guillemaud P, Mollard N, et al (2014) Obtaining an accurate quantification of light elements by EDX: K-factors vs. Zeta-factors. In: 18th International Microscopy Congress Czechoslovak Microscopy Society. Prague

Lyons JL, Janotti A, Van de Walle CG (2014) Effects of carbon on the electrical and optical properties of InN, GaN, and AlN. Phys Rev B 89:035204. https://doi.org/10.1103/PhysRevB.89.035204

Lyons JL, Janotti A, Van de Walle CG (2012) Shallow versus Deep Nature of Mg Acceptors in Nitride Semiconductors. Phys Rev Lett 108:156403. https://doi.org/10.1103/PhysRevLett.108.156403

Madhukar A (1983) Far from equilibrium vapour phase growth of lattice matched III–V compound semiconductor interfaces: Some basic concepts and monte-carlo computer simulations. Surf Sci 132:344–374. https://doi.org/10.1016/0039-6028(83)90547-2

Mahan JE, Geib KM, Robinson GY, Long RG (1990) A review of the geometrical fundamentals of reflection high energy electron diffraction with application to silicon surfaces. 10

Mancini L, Amirifar N, Shinde D, et al (2014) Composition of Wide Bandgap Semiconductor Materials and Nanostructures Measured by Atom Probe Tomography and Its Dependence on the Surface Electric Field. J Phys Chem C 118:24136–24151. https://doi.org/10.1021/jp5071264

Marini J, Leathersich J, Mahaboob I, et al (2016) MOCVD growth of N-polar GaN on on-axis sapphire substrate: Impact of AlN nucleation layer on GaN surface hillock density. J Cryst Growth 442:25–30. https://doi.org/10.1016/j.jcrysgro.2016.02.029

Matoussi A, Boufaden T, Guermazi S, et al (2003) Minority carrier diffusion lengths and optical self-absorption coefficient in undoped GaN. Phys Status Solidi B 240:160–168. https://doi.org/10.1002/pssb.200301870

Mattila T, Nieminen RM (1997) Point-defect complexes and broadband luminescence in GaN and AlN. Phys Rev B 55:9571–9576. https://doi.org/10.1103/PhysRevB.55.9571

Maya C, Beltrán N, Jiménez B, Bonilla P (2003) Evaluation of the UV disinfection process in bacteria and amphizoic amoebae inactivation. Water Sci Technol Water Supply 3:285–291. https://doi.org/10.2166/ws.2003.0074

McLaurin M, Mates TE, Speck JS (2005) Molecular-beam epitaxy of p-type m-plane GaN. Appl Phys Lett 86:262104. https://doi.org/10.1063/1.1977204

Mi Z, Zhao S, Connie A, Dastjerdi MHT (2015) High efficiency AlGaN deep ultraviolet light emitting diodes on silicon. International Society for Optics and Photonics, p 937306

Mi Z, Zhao S, Woo SY, et al (2016) Molecular beam epitaxial growth and characterization of Al(Ga)N nanowire deep ultraviolet light emitting diodes and lasers. J Phys Appl Phys 49:364006. https://doi.org/10.1088/0022-3727/49/36/364006

Miceli G, Pasquarello A (2016) Self-compensation due to point defects in Mg-doped GaN. Phys Rev B 93:165207. https://doi.org/10.1103/PhysRevB.93.165207

Mickevičius J, Tamulaitis G, Shur M, et al (2012) Internal quantum efficiency in AlGaN with strong carrier localization. Appl Phys Lett 101:211902. https://doi.org/10.1063/1.4767657

Mickevičius J, Tamulaitis G, Shur M, et al (2013) Correlation between carrier localization and efficiency droop in AlGaN epilayers. Appl Phys Lett 103:011906. https://doi.org/10.1063/1.4813259

Minj A, Cros A, Garro N, et al (2015) Assessment of Polarity in GaN Self-Assembled Nanowires by Electrical Force Microscopy. Nano Lett 15:6770–6776. https://doi.org/10.1021/acs.nanolett.5b02607

Mireles F, Ulloa SE (1998) Acceptor binding energies in GaN and AlN. Phys Rev B 58:3879–3887. https://doi.org/10.1103/PhysRevB.58.3879

Moe CG, Garrett GA, Rotella P, et al (2012) Impact of temperature-dependent hole injection on low-temperature electroluminescence collapse in ultraviolet light-emitting diodes. Appl Phys Lett 101:253512. https://doi.org/10.1063/1.4772506

Moldovan G, Kazemian P, Edwards PR, et al (2007) Low-voltage cross-sectional EBIC for characterisation of GaN-based light emitting devices. Ultramicroscopy 107:382–389. https://doi.org/10.1016/j.ultramic.2006.10.002

Musolino M, Tahraoui A, Fernández-Garrido S, et al (2015) Compatibility of the selective area growth of GaN nanowires on AlN-buffered Si substrates with the operation of light emitting diodes. Nanotechnology 26:085605. https://doi.org/10.1088/0957-4484/26/8/085605

Nakamura S, Mukai T, Senoh M (1992a) Si- and Ge-Doped GaN Films Grown with GaN Buffer Layers. Jpn J Appl Phys 31:2883. https://doi.org/10.1143/JJAP.31.2883

Nakamura S, Mukai T, Senoh M, Iwasa N (1992b) Thermal Annealing Effects on P-Type Mg-Doped GaN Films. Jpn J Appl Phys 31:L139. https://doi.org/10.1143/JJAP.31.L139

Nam KB, Nakarmi ML, Li J, et al (2003) Mg acceptor level in AlN probed by deep ultraviolet photoluminescence. Appl Phys Lett 83:878–880. https://doi.org/10.1063/1.1594833

Namkoong G, Doolittle WA, Brown AS (2000) Incorporation of Mg in GaN grown by plasma-assisted molecular beam epitaxy. Appl Phys Lett 77:4386–4388. https://doi.org/10.1063/1.1334942

Neugebauer J, Van de Walle CG (1999) Chemical trends for acceptor impurities in GaN. J Appl Phys 85:3003–3005. https://doi.org/10.1063/1.369619

Nguyen HPT, Cui K, Zhang S, et al (2012a) Controlling Electron Overflow in Phosphor-Free InGaN/GaN Nanowire White Light-Emitting Diodes. Nano Lett 12:1317–1323. https://doi.org/10.1021/nl203860b

Nguyen HPT, Djavid M, Cui K, Mi Z (2012b) Temperature-dependent nonradiative recombination processes in GaN-based nanowire white-light-emitting diodes on silicon. Nanotechnology 23:194012. https://doi.org/10.1088/0957-4484/23/19/194012

Nichia C (2019) NICHIA CORPORATION. In: UV-LED. http://www.nichia.co.jp/en/product/uvled.html. Accessed 12 Sep 2019

Niquet YM, Priester C, Mariette H (1997) Influence of the inhomogeneous strain relaxation on the optical properties of etched quantum wires. Phys Rev B 55:R7387–R7390. https://doi.org/10.1103/PhysRevB.55.R7387

Nishida T, Saito H, Kobayashi N (2001) Efficient and high-power AlGaN-based ultraviolet light-emitting diode grown on bulk GaN. Appl Phys Lett 79:711–712. https://doi.org/10.1063/1.1390485

Northrup JE (2008) Hydrogen and magnesium incorporation on c-plane and m-plane GaN surfaces. Phys Rev B 77:045313. https://doi.org/10.1103/PhysRevB.77.045313

Nötzel R, Däweritz L, Ploog K (1992) Topography of high- and low-index GaAs surfaces. Phys Rev B 46:4736–4743. https://doi.org/10.1103/PhysRevB.46.4736

NS Nanotech (2019) NS Nanotech. https://www.nsnanotech.com/. Accessed 12 Sep 2019

Ochalski TJ, Gil B, Lefebvre P, et al (1999) Photoreflectance investigations of the bowing parameter in AlGaN alloys lattice-matched to GaN. Appl Phys Lett 74:3353–3355. https://doi.org/10.1063/1.123342

Okumura H, Misawa S, Okahisa T, Yoshida S (1994) Epitaxial growth of cubic and hexagonal GaN by gas source molecular beam epitaxy using a microwave plasma nitrogen source. J Cryst Growth 136:361–365. https://doi.org/10.1016/0022-0248(94)90440-5

Okumura H, Misawa S, Yoshida S (1991) Epitaxial growth of cubic and hexagonal GaN on GaAs by gas-source molecular-beam epitaxy. Appl Phys Lett 59:1058–1060. https://doi.org/10.1063/1.106344

Okumura H, Ohta K, Feuillet G, et al (1997) Growth and characterization of cubic GaN. J Cryst Growth 178:113–133. https://doi.org/10.1016/S0022-0248(97)00084-5

Orton JW, Blood P (1990) The electrical characterization of semiconductors : measurement of minority carrier properties. Academic Press Limited, London

Ozawa M, Ferenczi K, Kikuchi T, et al (1999) 312-nanometer Ultraviolet B Light (Narrow-Band UVB) Induces Apoptosis of T Cells within Psoriatic Lesions. J Exp Med 189:711–718

Parish CM, Russell PE (2006) On the use of Monte Carlo modeling in the mathematical analysis of scanning electron microscopy–electron beam induced current data. Appl Phys Lett 89:192108. https://doi.org/10.1063/1.2385212

Perdew JP (1996) Generalized Gradient Approximation Made Simple. Phys Rev Lett 77:3865–3868. https://doi.org/10.1103/PhysRevLett.77.3865

Perea DE, Wijaya E, Lensch-Falk JL, et al (2008) Tomographic analysis of dilute impurities in semiconductor nanostructures. J Solid State Chem 181:1642–1649. https://doi.org/10.1016/j.jssc.2008.06.007

Perkowitz S (2012) Optical Characterization of Semiconductors: Infrared, Raman, and Photoluminescence Spectroscopy. Elsevier

Pernot C, Kim M, Fukahori S, et al (2010) Improved Efficiency of 255–280 nm AlGaN-Based Light-Emitting Diodes. Appl Phys Express 3:061004. https://doi.org/10.1143/APEX.3.061004

Pernot J, Donatini F, Tchoulfian P (2014) Doping and Transport. In: Consonni V, Feuillet G (eds) Wide Band Gap Semiconductor Nanowires 1. John Wiley & Sons, Inc., Hoboken, NJ, USA, pp 99–123

Pierret A (2013) Propriétés structurales et optiques de nanostructures III-N semiconductrices à grand gap : nanofils d'AlxGa1-xN synthétisés par épitaxie par jets moléculaires et nanostructures de nitrure de bore. Phdthesis, Université Pierre et Marie Curie - Paris VI

Pierret A, Bougerol C, Gayral B, et al (2013a) Probing alloy composition gradient and nanometer-scale carrier localization in single AlGaN nanowires by nanocathodoluminescence. Nanotechnology 24:305703. https://doi.org/10.1088/0957-4484/24/30/305703

Pierret A, Bougerol C, Murcia-Mascaros S, et al (2013b) Growth, structural and optical properties of AlGaN nanowires in the whole composition range. Nanotechnology 24:115704. https://doi.org/10.1088/0957-4484/24/11/115704

Ploog K, Trankle G, Weimann G (2000) Compound Semiconductors 1999: Proceedings. Institute of Physics Publishing, Bristol UK

Ptak AJ, Myers TH, Romano LT, et al (2001) Magnesium incorporation in GaN grown by molecular-beam epitaxy. Appl Phys Lett 78:285–287. https://doi.org/10.1063/1.1339255

Qu Y, Duan X (2012) One-dimensional homogeneous and heterogeneous nanowires for solar energy conversion. J Mater Chem 22:16171. https://doi.org/10.1039/c2jm32267f

Rastogi RP, Richa, Kumar A, et al (2010) Molecular Mechanisms of Ultraviolet Radiation-Induced DNA Damage and Repair. J Nucleic Acids 2010:1–32. https://doi.org/10.4061/2010/592980

Reshchikov MA, Morkoç H (2005) Luminescence properties of defects in GaN. J Appl Phys 97:061301. https://doi.org/10.1063/1.1868059

Richter T, Meijers HLR, Calarco R, Marso M (2008) Doping concentration of GaN nanowires determined by opto-electrical measurements. Nano Lett 8:3056–3059. https://doi.org/10.1021/nl8014395

Rigutti L (2015) Semiconducting nanowires. Wiley Encycl Electr Electron Eng. https://doi.org//10.1002/047134608X.W8215

Rigutti L, Mancini L, Hernández-Maldonado D, et al (2016) Statistical correction of atom probe tomography data of semiconductor alloys combined with optical spectroscopy: The case of Al0.25Ga0.75N. J Appl Phys 119:105704. https://doi.org/10.1063/1.4943612

Robin E, Mollard N, Guilloy K, et al (2016) Quantification of dopants in nanomaterial by SEM/EDS. Lyon, France

Romanov AE, Baker TJ, Nakamura S, et al (2006) Strain-induced polarization in wurtzite III-nitride semipolar layers. J Appl Phys 100:023522. https://doi.org/10.1063/1.2218385

Rosa AL, Neugebauer J, Northrup JE, et al (2002) Adsorption and incorporation of silicon at GaN(0001) surfaces. Appl Phys Lett 80:2008–2010. https://doi.org/10.1063/1.1452785

Rose A (1955) Space-Charge-Limited Currents in Solids. Phys Rev 97:1538–1544. https://doi.org/10.1103/PhysRev.97.1538

Sánchez-Páramo J, Calleja JM, Sánchez-García MA, Calleja E (2001) Optical investigation of strain in Si-doped GaN films. Appl Phys Lett 78:4124–4126. https://doi.org/10.1063/1.1379063

Sanford NA, Robins LH, Blanchard PT, et al (2013) Studies of photoconductivity and field effect transistor behavior in examining drift mobility, surface depletion, and transient effects in Si-doped GaN nanowires in vacuum and air. J Appl Phys 113:174306. https://doi.org/10.1063/1.4802689

Schroder DK (2015) Semiconductor Material and Device Characterization. John Wiley & Sons

Schubert EF (2006) Light-emitting diodes, 2nd edn. Cambridge University Press

Schuck PJ, Mason MD, Grober RD, et al (2001) Spatially resolved photoluminescence of inversion domain boundaries in GaN-based lateral polarity heterostructures. Appl Phys Lett 79:952–954. https://doi.org/10.1063/1.1390486

Shatalov M, Sun W, Bilenko Y, et al (2010) Large Chip High Power Deep Ultraviolet Light-Emitting Diodes. Appl Phys Express 3:062101. https://doi.org/10.1143/APEX.3.062101

Shatalov M, Sun W, Lunev A, et al (2012) AlGaN Deep-Ultraviolet Light-Emitting Diodes with External Quantum Efficiency above 10%. Appl Phys Express 5:082101. https://doi.org/10.1143/APEX.5.082101

Shen PH, Sampath A, Garrett G, Wraback M (2006) Mechanisms of Enhanced Luminescence In Nanoscale Compositionally Inhomogeneous AlGaN. ECS Trans 3:181–187. https://doi.org/10.1149/1.2357207

Siladie A-M, Amichi L, Mollard N, et al (2018) Dopant radial inhomogeneity in Mg-doped GaN nanowires. Nanotechnology 29:255706. https://doi.org/10.1088/1361-6528/aabbd6

Siladie A-M, Jacopin G, Cros A, et al (2019) Mg and In Codoped p-type AlN Nanowires for pn Junction Realization. Nano Lett 19:acs.nanolett.9b01394. https://doi.org/10.1021/acs.nanolett.9b01394

Sobanska M, Fernández-Garrido S, Zytkiewicz ZR, et al (2016) Self-assembled growth of GaN nanowires on amorphous Al x O y : from nucleation to the formation of dense nanowire ensembles. Nanotechnology 27:325601. https://doi.org/10.1088/0957-4484/27/32/325601

Sommer R, Cabaj A, Sandu T, Lhotsky M (1999) Measurement of UV radiation using suspensions of microorganisms. J Photochem Photobiol B 53:1–6. https://doi.org/10.1016/S1011-1344(99)00113-X

Song Y, Guo ZX, Yang R (2004) Influence of selected alloying elements on the stability of magnesium dihydride for hydrogen storage applications: a first-principles investigation. Phys Rev B 69:094205

Sproul AB (1994) Dimensionless solution of the equation describing the effect of surface recombination on carrier decay in semiconductors. J Appl Phys 76:2851–2854. https://doi.org/10.1063/1.357521

Stampfl C, Neugebauer J, Van de Walle CG (1999) Doping of AlxGa1−xN alloys. Mater Sci Eng B 59:253–257. https://doi.org/10.1016/S0921-5107(98)00347-X

Stringfellow GB (2012) Organometallic Vapor-Phase Epitaxy: Theory and Practice. Elsevier

Sugahara T, Saito H, Hao M, et al (1998) Direct Evidence that Dislocations are Non-Radiative Recombination Centers in GaN. Jpn J Appl Phys 37:L398. https://doi.org/10.1143/JJAP.37.L398

Sun Q, Selloni A, Myers TH, Doolittle WA (2006) Energetics of Mg incorporation at GaN(0001) and (000-1) surfaces. Phys Rev B 73:155337. https://doi.org/10.1103/PhysRevB.73.155337

Sun W, Adivarahan V, Shatalov M, et al (2004) Continuous Wave Milliwatt Power AlGaN Light Emitting Diodes at 280 nm. Jpn J Appl Phys 43:L1419. https://doi.org/10.1143/JJAP.43.L1419

Suzuki M, Uenoyama T, Yanase A (1995) First-principles calculations of effective-mass parameters of AlN and GaN. Phys Rev B 52:8132–8139. https://doi.org/10.1103/PhysRevB.52.8132

Takano T, Mino T, Sakai J, et al (2017) Deep-ultraviolet light-emitting diodes with external quantum efficiency higher than 20% at 275 nm achieved by improving light-extraction efficiency. Appl Phys Express 10:031002. https://doi.org/10.7567/APEX.10.031002

Tang, F., Moody, M.P., Martin, T.L., et al (2015) Practical Issues for Atom Probe Tomography Analysis of III-Nitride Semiconductor Materials. Microsc Microanal 21:544

Taniyasu Y, Kasu M, Makimoto T (2006) An aluminium nitride light-emitting diode with a wavelength of 210 nanometres. Nature 441:325–328. https://doi.org/10.1038/nature04760

Tchernycheva M, Lavenus P, Zhang H, et al (2014) InGaN/GaN Core–Shell Single Nanowire Light Emitting Diodes with Graphene-Based P-Contact. Nano Lett 14:2456–2465. https://doi.org/10.1021/nl5001295

Tchernycheva M, Neplokh V, Zhang H, et al (2015) Core–shell InGaN/GaN nanowire light emitting diodes analyzed by electron beam induced current microscopy and cathodoluminescence mapping. Nanoscale 7:11692–11701. https://doi.org/10.1039/C5NR00623F

Tchoulfian P, Donatini F, Levy F, et al (2014) Direct Imaging of p–n Junction in Core–Shell GaN Wires. Nano Lett 14:3491–3498. https://doi.org/10.1021/nl5010493

Thompson SS, Jackson JL, Suva-Castillo M, et al (2003) Detection of infectious human adenoviruses in tertiary-treated and ultraviolet-disinfected wastewater. Water Environ Res Res Publ Water Environ Fed 75:163–170

Tran NH, Le BH, Zhao S, Mi Z (2017) On the mechanism of highly efficient p-type conduction of Mg-doped ultra-wide-bandgap AlN nanostructures. Appl Phys Lett 110:032102. https://doi.org/10.1063/1.4973999

Tuomisto F, Makkonen I (2013) Defect identification in semiconductors with positron annihilation: Experiment and theory. Rev Mod Phys 85:1583–1631. https://doi.org/10.1103/RevModPhys.85.1583

Uedono A, Ishibashi S, Oshima N, Suzuki R (2013) Positron Annihilation Spectroscopy on Nitride-Based Semiconductors. Jpn J Appl Phys 52:08JJ02. https://doi.org/10.7567/JJAP.52.08JJ02

Uedono A, Siladie A-M, Pernot J, et al (2019) Vacancy-type defects in GaN self-assembled nanowires probed using monoenergetic positron beam. J Appl Phys 125:175705. https://doi.org/10.1063/1.5088653

Uedono A, Takashima S, Edo M, et al (2018) Carrier Trapping by Vacancy-Type Defects in Mg-Implanted GaN Studied Using Monoenergetic Positron Beams. Phys Status Solidi B 255:1700521. https://doi.org/10.1002/pssb.201700521

Uedono A, Takashima S, Edo M, et al (2015) Vacancy-type defects and their annealing behaviors in Mg-implanted GaN studied by a monoenergetic positron beam. Phys Status Solidi B 252:2794–2801. https://doi.org/10.1002/pssb.201552345

Uedono A, Tenjinbayashi K, Tsutsui T, et al (2012) Native cation vacancies in Si-doped AlGaN studied by monoenergetic positron beams. J Appl Phys 111:013512. https://doi.org/10.1063/1.3675270

United Nations (2010) The human right to water and sanitation

United Nations (2017) Minamata convention on mercury

Van de Walle CG (1997) Interactions of hydrogen with native defects in GaN. Phys Rev B 56:R10020–R10023. https://doi.org/10.1103/PhysRevB.56.R10020

Van de Walle CG, Limpijumnong S, Neugebauer J (2001) First-principles studies of beryllium doping of GaN. Phys Rev B 63:. https://doi.org/10.1103/PhysRevB.63.245205

Van de Walle CG, Neugebauer J (2004) First-principles calculations for defects and impurities: Applications to III-nitrides. J Appl Phys 95:3851–3879. https://doi.org/10.1063/1.1682673

Vennéguès P, Benaissa M, Dalmasso S, et al (2002) Influence of high Mg doping on the microstructural and optoelectronic properties of GaN. Mater Sci Eng B 93:224–228. https://doi.org/10.1016/S0921-5107(02)00046-6

Vurgaftman I, Meyer JR (2003) Band parameters for nitrogen-containing semiconductors. J Appl Phys 94:3675–3696. https://doi.org/10.1063/1.1600519

Wang H, Chen A-B (2000) Calculation of shallow donor levels in GaN. J Appl Phys 87:7859–7863. https://doi.org/10.1063/1.373467

Watanabe M, Williams DB (2006) The quantitative analysis of thin specimens: a review of progress from the Cliff-Lorimer to the new ζ-factor methods. J Microsc 221:89–109. https://doi.org/10.1111/j.1365-2818.2006.01549.x

Wei CH, Xie ZY, Li LY, et al (2000) MOCVD growth of cubic GaN on 3C-SiC deposited on Si (100) substrates. J Electron Mater 29:317–321. https://doi.org/10.1007/s11664-000-0070-z

World Health Organization, UNICEF (2017) Progress on drinking water, sanitation and hygiene: 2017 update and SDG baselines.

Wright AF, Grossner U (1998) The effect of doping and growth stoichiometry on the core structure of a threading edge dislocation in GaN. Appl Phys Lett 73:2751–2753. https://doi.org/10.1063/1.122579

Wu Y, Clevenger T, Deng B (2005) Impacts of Goethite Particles on UV Disinfection of Drinking Water. Appl Environ Microbiol 71:4140–4143. https://doi.org/10.1128/AEM.71.7.4140-4143.2005

Xie J, Ni X, Fan Q, et al (2008) On the efficiency droop in InGaN multiple quantum well blue light emitting diodes and its reduction with p-doped quantum well barriers. Appl Phys Lett 93:121107. https://doi.org/10.1063/1.2988324

Xu T, Nys JP, Grandidier B, et al (2008) Growth of Si nanowires on micropillars for the study of their dopant distribution by atom probe tomography. J Vac Sci Technol B Microelectron Nanometer Struct Process Meas Phenom 26:1960–1963. https://doi.org/10.1116/1.3021371

Yacobi BG, Holt DB (1986) Cathodoluminescence scanning electron microscopy of semiconductors. J Appl Phys 59:R1–R24. https://doi.org/10.1063/1.336491

Yamada K, Furusawa Y, Nagai S, et al (2014) Development of underfilling and encapsulation for deep-ultraviolet LEDs. Appl Phys Express 8:012101. https://doi.org/10.7567/APEX.8.012101

Yoshizawa M, Kikuchi A, Mori M, et al (1997) Growth of Self-Organized GaN Nanostructures on Al2O3(0001) by RF-Radical Source Molecular Beam Epitaxy. Jpn J Appl Phys 36:L459. https://doi.org/10.1143/JJAP.36.L459

Yun F, Reshchikov MA, He L, et al (2002) Energy band bowing parameter in AlxGa1−xN alloys. J Appl Phys 92:4837–4839. https://doi.org/10.1063/1.1508420

Zhao S, Connie AT, Dastjerdi MHT, et al (2015a) Aluminum nitride nanowire light emitting diodes: Breaking the fundamental bottleneck of deep ultraviolet light sources. Sci Rep 5:srep08332. https://doi.org/10.1038/srep08332

Zhao S, Connie AT, Le BH, et al (2015b) p-Type AlN nanowires and AlN nanowire light emitting diodes on Si. In: 2015 IEEE Summer Topicals Meeting Series (SUM). pp 131–132

Zhao S, Djavid M, Mi Z (2015c) Surface Emitting, High Efficiency Near-Vacuum Ultraviolet Light Source with Aluminum Nitride Nanowires Monolithically Grown on Silicon. Nano Lett 15:7006–7009. https://doi.org/10.1021/acs.nanolett.5b03040

ANNEXE 1

Excess carrier generation in AlN material

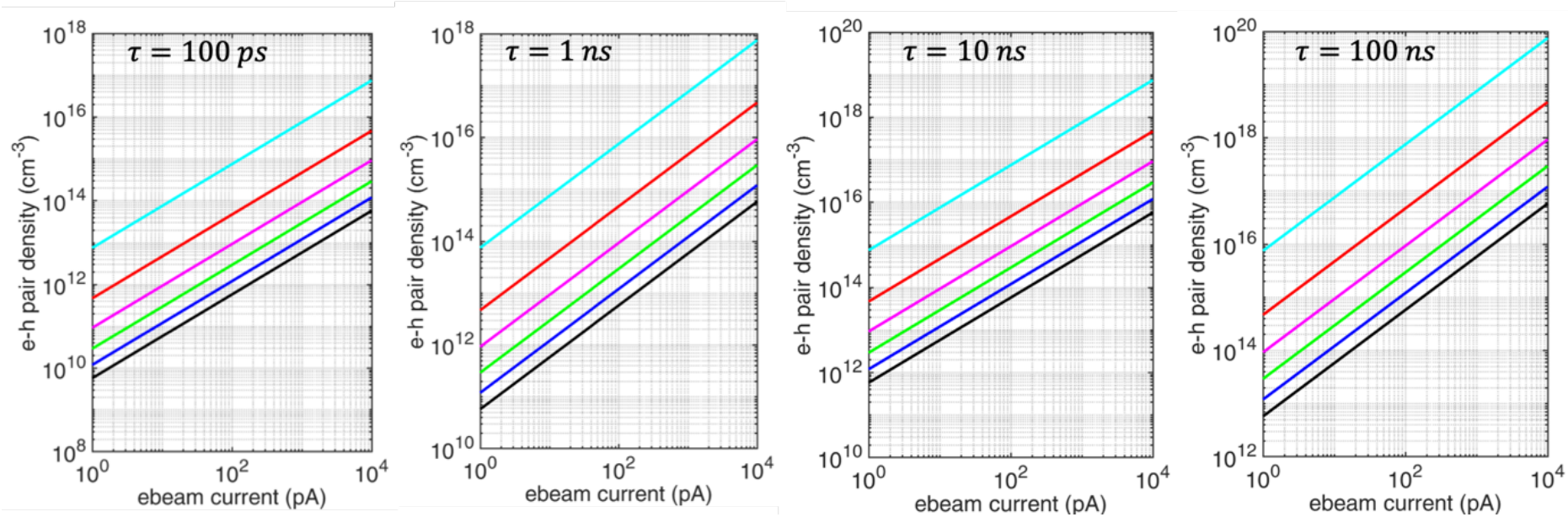

Excess carrier generation in $Al_{0.6}Ga_{0.4}N$ material